Investigating the Performance of Reinforced Glulam Beams Under Shock Tube Induced Blast Loading

Laith Ismail Ahmad Gharaibeh

Thesis submitted to the University of Ottawa

in partial fulfillment of the requirements for the degree of

Doctor of Philosophy

in Civil Engineering

uOttawa

Department of Civil Engineering

Faculty of Engineering

University of Ottawa

Abstract

Glulam beams are widely used in timber construction due to their strength and versatility; however, they are prone to brittle failure under flexural loading, particularly in the tension zone. This study explores the effectiveness of Near-Surface Mounted (NSM) reinforcement using steel rebars and plates as a retrofit strategy to improve the structural performance of glulam beams, especially under extreme dynamic loads such as blast events. The reinforcement was applied by embedding steel elements into pre-cut grooves along the tension face of the beams and bonding them with epoxy. Three reinforcement ratios (0.8%, 1.6%, and 2.5%) were examined using 10M, 15M, and 20M rebars, respectively. In addition, steel plates were employed with a reinforcement ratio equivalent to the 15M configuration. Variations in plate positioning were investigated to assess the impact of horizontal versus vertical placement, offering practical solutions where side access to beams is limited.

A total of sixteen reinforced beams were tested under both static four-point bending and dynamic blast loading, the latter simulated using a shock tube device at the University of Ottawa Structural Laboratory. The experimental results revealed that NSM reinforcement significantly enhanced the load-carrying capacity, stiffness, and ductility of the beams. Strength increases ranged from 23.0% to 83.3%, while stiffness improvements were between 7.8% and 38.1%. Ductility ratios improved substantially, ranging from 1.1 to 7.2, and failure modes transitioned from brittle tensile rupture to more ductile compression crushing, indicating enhanced energy absorption and deformation capacity.

The epoxy bonding system showed excellent performance, with no significant debonding or slippage observed during testing, except near ultimate failure. While some plate-reinforced specimens exhibited slip failures at the wood–epoxy or plate–epoxy interface, overall bonding integrity was maintained throughout the critical stages of loading. In dynamic tests, the reinforced beams exhibited higher resistance compared to unreinforced controls, confirming the potential of NSM systems for blast-resistant timber design.

An analytical model based on layered-section analysis was developed to simulate the behavior of the reinforced beams. The model accounted for elastic, inelastic, and plastic hinge stages and treated the steel reinforcement as concentrated elements. Analytical predictions demonstrated strong agreement with experimental data, accurately capturing trends in strain, displacement, and force response.

Overall, this research confirms that NSM reinforcement using steel rebars and plates is an effective and practical technique for improving the structural performance and blast resistance of glulam beams. The results contribute valuable insights into the design, application, and modeling of timber reinforcement systems under both static and extreme dynamic loading conditions.

Acknowledgements

I would like to express my deepest gratitude to my supervisor, **Professor Ghasan Doudak**, for his invaluable support and guidance throughout my PhD journey. His expertise in wood design and blast engineering has been instrumental in shaping the direction and depth of this research. I am sincerely thankful for his mentorship and encouragement.

I am also grateful to **Professor Christian Viau**, whose insights and guidance, especially through his experience as a former student of Professor Doudak, have been of great assistance to me. His constructive feedback and support were truly appreciated.

My sincere thanks go to my colleagues and fellow PhD students **Antoine, Dalu, Fernanda, Bita**, and **Esmaeil** for their help, collaboration, and companionship throughout this journey.

I would also like to thank the people I worked with at the **University of Ottawa**. Special thanks to **Professor Anfreé Skaff**, whose sense of humor and positive energy will never be forgotten. I am also grateful to **Luc Cloutier**, our exceptional administration officer in the department, for his consistent support and dedication.

Special thanks to my friend at the University of Ottawa, **Professor Nour Kadri**, for his kind support and encouragement, and to my best friend, **Mohammad Shaheen**, for always being there with sincere advice and friendship.

Most importantly, I would like to thank my family for their unwavering love and support. A special thank you goes to my father, **Professor Ismail Gharaibeh**, whose background in physics and lifelong academic dedication have always inspired me. His encouragement and belief in me played a vital role in completing this work.

Finally, I extend my heartfelt appreciation to my **lovely wife, Hala Chakra**, for her endless patience, understanding, and unwavering support throughout this journey. Her presence and encouragement have been a constant source of strength.

Contents

List of Figures

List of Tables

CHAPTER ONE: INTRODUCTION

1.1 Research needs

Timber in general, and glued laminated timber (Glulam) in particular, has been successfully used for decades in heavy timber construction, especially in Europe and North America. Examples of important structures containing a significant amount of structural timber are the "Brock Commons Tallwood House", in Canada, and, the Ascent MKE building in Milwaukee, USA, and the "Mjøstårnet" in Norway. Glulam is formed of several segments of lumber that have been stress-graded separately and attached to each other via glue and finger-joints. This helps minimize continuous defects found in solid-sawn lumber and allows for better control of the lamination's characteristics to attain assemblies with more desired and anticipated features in comparison with those found in solid timber. The structural performance of glulam beams subjected to out-plane-lateral loads is typically described as brittle with little to no post-peak behaviour (Lacroix and Doudak, 2018a). Attempts to improve the material performance and attain ductile failure modes in flexure have been achieved, for example, by reinforcing the tension side of the beam (eg., Gentile et al., 2002). This also helped initiate crushing failure mode at the compression face which in turn facilitated the increase in the overall energy dissipation capabilities of the beam elements. The reinforcement can take many forms including rebar or rod as investigated by (Gentile et al., 2002; Raftery and Whelan, 2014; Raftery and Kelly, 2015; Yang et al., 2016a), or using laminates or strips (Alhayek and Svecova, 2012; Biscaia et al., 2017). Additionally, reinforcement sheets or fabric attached to the tension surface of the beam (Borri et al., 2013; Corradi et al., 2020; Bakalarz & Kossakowski, 2022) or embedded reinforcement between the layers of the beam (Raftery and

Harte, 2011; Rescalvo et al., 2021; He et al., 2022) have also been investigated. However, these investigations have been limited to static loading.

Blast forces resulting from explosions can greatly affect and harm buildings. In the past two decades, designing buildings and protecting them against blast load has become necessary due to the increase in the number of intentional or accidental explosions nowadays (Van Der Woerd, 2022). Blast or impact load includes a load period near milliseconds which is significantly smaller than that attained under seismic loads where the load event is determined in the range of seconds. It is well-established that materials generally gain strength, and possibly stiffness, as a function of the strain rate increase. In design for blast loading, this increase in strength is generally referred to as a dynamic increase factor (DIF) and is applied to adjust the static stiffness and strength of the material to consider the strain rate effects (e.g., UFC 3-340-02 (Unified Facilities Criteria Program, 2008); ASCE/SEI 59-22, 2022). Extensive studies can be found on materials such as steel and concrete structures, and their behaviour has been well documented (e.g., Nassr et al., 2012; Burrell et al., 2015; Algassem et al., 2017; Jacques and Saatcioglu, 2019; Lee et al., 2020; Hammoud et al., 2021; Njeem et al., 2022; Li and Aoude, 2023). However, the design and retrofitting options for timber structures subjected to a blast threat are still lacking. With the advent of engineered wood products (EWP), mid and high-rise wood structures have become feasible. As these buildings grow in volume and height, they increasingly serve functions similar to those of concrete and steel. There is also a growing trend toward using wood in construction to reduce greenhouse gas (GHG) emissions and promote the environmental sustainability of buildings. Previous studies have been conducted using the Shock Tube facility at the University of Ottawa, which can simulate far-field blast loads. These studies have investigated on wood studs (Jacques, et al., 2014), light

frame stud wall (Lacroix and Doudak 2015), cross-laminated-timber (CLT) panels (Poulin et al, 2017), glulam beams and columns (Lacroix and Doudak, 2018b).

During explosive events, buildings can be damaged in different forms. As the shock wave is Fand cladding and create hazards for the occupants from flying debris. However, the more dangerous effects occur when the shockwave causes damage to or failure of beams or columns, especially at the first storey, which can affect the overall stability of the building and may lead to progressive collapse of the whole structure (FEMA, 2011). There are several approaches to safeguarding buildings from the consequences of explosions. One method is to place rigid barriers around the structures intended to redirect some of blast forces or increase a secure distance from possible explosive hazards (FEMA, 2011). Limitation of available space may restrict options. In such situations, reinforcing the building structural components may be necessary. Reinforcing wood structural elements against blast loads were examined at the shock-tube laboratory at the University of Ottawa, e.g., replacing the typical sheathing for light frame stud wall with steel sheet (Lacroix et al., 2014) or to a limited degree timber-composite assemblies using steel wires (Viau and Doudak, 2016a), as well as using Fiber-Reinforced Polymer (FRP) sheet to reinforce CLT panels (Lopez-Molina and Doudak, 2019) or glulam beams (Lacroix and Doudak, 2018c), or using connections to dissipate energy (McGrath and Doudak, 2021; Viau and Doudak, 2021a).

1.2 Near-Surface-Mounting (NSM) Technique

The current study aims to investigate possible retrofit techniques to reinforce glulam beams against blast loading using the near-surface-mounting (NSM) technique by utilizing steel rebar and plate reinforcements. This method involves coring out grooves at the beam's surface where the

reinforcements are attached using an epoxy compound. The NSM method itself is not novel, however, its application to timber used to resist blast effects is unique. For reinforcement, steel material is employed, since it provides sufficient strength and stiffness to enhance the material properties of the wood structural elements, particularly in the post-peak region. Steel material also has great ductility, which in turn enhances the structural response of the wood elements under static and blast loading. The main disadvantage of using steel is the potential for corrosion and oxidation. This issue can be addressed by applying a coating such as epoxy, galvanizing, or using stainless steel. For this study, epoxy is used, which mainly serves as a bonding agent and secondarily as a coating material to protect the steel from deterioration. Various reinforcing materials, including GFRP and CFRP, can be utilized to enhance glulam beams with NSM rebars. Nonetheless, GFRP's reduced stiffness diminishes its performance as a reinforcement material, while CFRP, though offering superior stiffness, is associated with higher expense. Furthermore, the choice of NSM method may also help in preventing delamination issues observed in FRP sheets applied at the material surface as observed by (Lacroix and Doudak, 2018c). These issues could be prevented by means of confinement, but that solution may be hindered by lack of access to the sides and top of the beam. Finally, the NSM method may provide a better aesthetic appearance compared to FRP sheets since the rod and plates can be hidden. The NSM method has been successfully used to reinforce timber beams using FRP rods, strips and plate (e.g, Gentile et al., 2002; Raftery and Kelly, 2015; Yang et al., 2016a; Bakalarz et al., 2020, Yeboah and Gkantou, 2021) or using steel reinforcement rebars (Yang et al., 2016a; Alkhudery et al., 2023).

1.3 Research objectives

In the current study, the glulam beams were reinforced against static and blast loading using the NSM technique and utilizing steel rebar and plate reinforcements. The application of this method to timber structures against blast load effects is unique. The results from the static and dynamic tests were also compared, which provides valuable information on the dynamic behaviour of such composite systems, including the strain rate effects in the wood and steel materials. The steel reinforcements contribute to bridging the defects in the wood element and thereby delaying the failure in the beams. As a result, the stiffness and strength capacity of the beam are further increased. In addition, steel reinforcement is expected to change the failure mode of the beam from being primarily brittle tension failure to a failure involving ductile compression crushing failure. The post-peak behavior and ductility of the beams are also expected to be enhanced using steel reinforcements. The effects of different rebar sizes and reinforcement ratios were investigated under both static and dynamic loads. In addition, this is the first study that includes a direct comparison between rebar and plate reinforcements.

The overarching objective of the current research is to investigate and enhance the performance of glulam elements subjected to blast loading, using NSM rebar and plate reinforcements. More specifically, the objectives are to:

1. Evaluate the effectiveness and validity of the NSM as a strengthening technique for wood glulam beams using steel rebar and plate reinforcements.
2. Examine the failure modes and behaviour of reinforced glulam beams with NSM rebars and plates when subjected to a static four-point bending test.
3. Investigate the structural response of reinforced glulam beams when subjected to dynamic blast loading using the shock tube device.

4. Investigate parameters affecting the behaviour of reinforced glulam beams in order to optimize the performance, especially related to the post-peak behaviour.
5. Provide, where needed, recommendations on design and analysis of the NSM approaches.

1.4 Methodology

The objectives of the study are achieved through the following steps, which contain both experimental and analytical components:

- Detailed review of dynamic and blast analysis methods, blast shock wave characteristics, and recent blast design guidelines for wood buildings.
- A detailed review of the application of NSM reinforcement method with rebar, plates or other reinforcement forms or shapes.
- Review on the response of wood material subjected to loading that causing high strain rates and the use of steel as a retrofit option for wood elements.
- Testing sixteen reinforced glulam beams under static and dynamic loads.
- Investigating the effect of rebar and plate reinforcement using the NSM strengthening technique on the static and dynamic response of reinforced glulam beams.
- Discussing the output findings by comparing the results data theoretically and experimentally.
- Providing recommendations on design and analysis methods for glulam beams reinforced with NSM techniques.

1.5 Layout

The thesis is structured in chapters containing the following:

Chapter 1 establishes the research needs and presents the key objectives and methodology followed in this research project.

Chapter 2 provides a detailed literature review covering the behavior of wood under static and dynamic loading, the effects of reinforcement especially the NSM strengthening method, and the use of steel rebars and plates as reinforcement for glulam elements.

Chapter 3 covers the methodology used in the experimental research program and provides detailed information on the specimens and the test setups.

Chapter 4 presents the experimental results from the static and dynamic blast tests for the reinforced glulam beams.

Chapter 5 presents the analytical data results for both static and dynamic tests, for different variables such as displacement and resistance.

Chapter 6 provides the discuss of the results between static and dynamic results, while Chapter 7 provides the conclusions of the study and recommendations for future works.

Appendix A presents analytical parameters. Appendix B and C present the results of the static test and presents the results of the dynamic test, respectively, while Appendix D presents a parametric study for the material parameters. Appendix E presents equations for the analytical models.

CHAPTER TWO: LITERATURE REVIEW

2.1 Wood as Construction Material

Wood is sawn and processed from harvested trees to produce a specific-sized product known as dimensional lumber used to create joists, beams, columns and light framed-walls. The drawbacks of traditional lumber and timber products are their limited sizes, variability associated with their mechanical properties, and waste generated during their production process. To overcome these issues, Engineered Wood Products (EWP) have been developed which expand size possibilities and provides more precise and less variable strength and mechanical properties (Thelandersson and Larsen, 2003). EWPs typically consist of small dimension lumber joined together using glue, nails, or dowels to create larger and stronger products. EWP products are available in different sizes and specifications such as oriented strand board (OSB), laminated veneer lumber (LVL), cross-laminated timber (CLT), glued laminated timber (Glulam), I-joist, etc. The engineering wood products can be used together to form large structure. Nowadays, timber is used in multi- and high-story buildings, as well as long-span bridges. The Brock Commons Tallwood House in Vancouver, British Columbia and ORIGINE in Quebec City are examples of tall mass timber buildings in Canada. These buildings demonstrate the increasing use of mass timber for mid- and high-rise construction, supported by advancements in EWP. Countries like Canada have developed their own specifications for designing wood for residential and commercial applications such as (Engineering Design in Wood CSA O86, 2024) mentored and developed by the Canadian Wood Council (CWC). The CWC plays a key role in developing and promoting the necessary guidelines for EWP products and tall mass timber buildings. Figure 2.1 shows one of the heavy mass timber buildings constructed in Canada.

a) Outside the building

b) Inside the building

Figure 2.1: Heavy mass buildings (https://www.nordic.ca/fr/projets).

2.2 Timber reinforcement background

2.2.1 Properties of Wood

Wood is a viscoelastic material, which means its behaviour is affected by creep, and loading rate. Wood is also considered as an orthotropic material that has different mechanical properties in each of the longitudinal, tangential and radial directions (Ross, 2010). In most applications, wood is preferably loaded in the longitudinal direction to fully utilize the strength of the fibres such as in axial loads in column members running along the vertical axis, parallel to the fiber grain, or a bending load on beam members where bending stress acts in the longitudinal direction. The stress-strain diagram for clear wood in the longitudinal direction has been studied earlier by (Glos, 1978; Bazan, 1980). Bazan (1980) proposed a bilinear curve with a descending branch representing the crushing of wood compression fibers, while in tension, wood exhibits linear behavior with brittle failure. The wood stress-strain diagram has been modified by Buchanan (1990) to include lumber grades and their size effects, based on Weibull theory (Weibull, 1939). The stress-strain diagram for wood in compression and tension is shown in Figure 2.2.

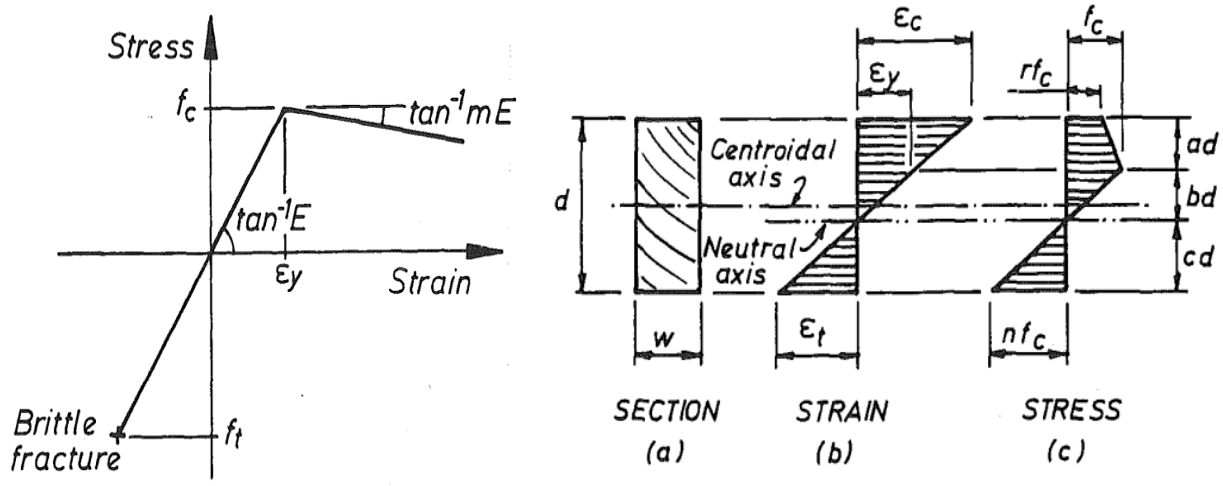

Figure 2.2: Stress-strain diagram for wood (reproduced from Buchanan, 1990).

Dimensional lumber naturally has defects such as knots or insect damage. Defects may also occur during the drying process as the wood is vulnerable to swelling and shrinkage, primarily in the tangential and radial directions which in turn can lead to warping and splitting of the wood boards. Moreover, some defects may occur due to improper sawing during wood board production (Ross, 2010). The wood boards after production should be maintained at constant moisture contents to prevent cracks caused by changes in moisture levels. As the wood board sizes increase, the likelihood of defects appearing also increases. Moreover, wood lumbers are classified according to their species such as Douglas fir and spruce-pine-fir (SPF). Furthermore, the wood species is further classified into grading types based on their quality, presence of defects and other factors. The size factor for different wood species, influencing mechanical properties such as tensile and compressive strengths can be found on the Canadian lumber handbook (Barrett and Lau, 1994). The strength of the wood can be adjusted from one size to another through statistical and probabilistic means using the size factors. The material inputs for the wood stress-strain diagram in Figure 2.2 must be adjusted to the proper size factors before being implemented in the analysis. This wood material model was also used in several studies to simulate the behaviour of the reinforced timber beams (Gentile et al., 2002, Yang et al., 2016a and Lacroix and Doudak, 2018c) and was used in a similar manner to this study, as presented in Chapter 5.

2.2.2 Reinforcement background

Reinforcing wood in construction was initially investigated during the mid-19th century with the use of aluminum alloys bonded to the outside of timber beams (Mark, 1963). The disadvantage of using aluminum was its low modulus of elasticity. This shortcoming was rectified when steel bars were successfully used (e.g., Lantos, 1970 and Bulleit et al., 1989). Bulleit et al., (1989) used steel

bars with serrated surfaces to provide more interaction between the structural elements and placed them on the tension side of the timber beam. The rebar was embedded inside a flakeboard, and an increase in the stiffness for reinforced beam was reported. A prestress technique was applied to glulam beams using steel cables (Bohannan, 1964) and high strength steel strip (Peterson, 1965). Both studies reported an increase in the strength of the reinforced beams and less variability in the strength results. Borgin et al. (1968) reinforced glulam beams with steel strips embedded inside the beams at the top and bottom. The authors reported significant increase in the stiffness of the reinforced beams. Steel plate reinforcement was also placed between the wood laminations in the vertical direction as reported by (Stern and Kumar, 1973; Coleman and Hurst, 1974).

Other reinforcement materials included glass fiber-reinforced polymer (GFRP), which was used to reinforce timber beams (Biblis, 1965). Theakston (1965) reinforced laminated timber beams with GFRP and demonstrated an increase in strength for the reinforced beams. Plevris and Triantafillou (1992) reinforced wood beams and beam-column elements using carbon fiber-reinforced polymer (CFRP) sheets. The authors reported increases in the stiffness, strength, and ductility of the beams. An analytical model was developed to predict the response of the beam and to include the interaction between bending and axial load for the beam-column elements. Triantafillou and Deskovic (1992) also used FRP sheets to reinforce the timber beams with the inclusion of prestress. Triantafillou (1997) reinforced timber beams with CFRP sheets as shear reinforcement. The sheet was attached to the shear zone area. Johns and Lacroix (2000) reinforced timber beams with FRP sheets at the tension side, showing an increase in the strength of the reinforced timber beams compared to unreinforced ones.

2.2.3 External Reinforcement

Fiorelli and Dias (2003) examined the flexural behavior of timber beams reinforced with CFRP and GFRP sheets. The sheets were placed at the tension side of the beams. The results indicated that the reinforcement was able to increase the stiffness and moment capacity of the beams. The reinforced beam was able to reach higher capacity, as the top compression fibers of the beam were crushed, which also helped increase the ductility of the beams. The beam reached higher strain values and the probability of failure occurring at a defect was reduced. Corradi et al. (2016) reinforced softwood timber beams with unbonded GFRP plates. The plates were fixed to the beam with different configurations and arrangements using screws, bolts and steel brackets. The results showed that the flexural strength and bending stiffness of the reinforced beams were increased by up to 58.9% and 98.9%, respectively.

Glišović et al., (2016) reinforced glulam beams with CFRP plates at a reinforcement ratio of 0.46% attached to the tension side of the beam. The results showed that the stiffness of the beam was increased by 18.1%, while the moment strength improved by 54.3%. Unlike the unreinforced beams, the reinforced beams showed an engagement of compression failure resulting in a more ductile failure compared to the unreinforced beam. Yusof and Rahman (2017) reinforced timber beams with CFRP plates. The results showed that the maximum load capacity of the reinforced beams increased by 31.8% to 44.5%, while stiffness improved by 32.6% to 87.6%, depending on the reinforcement ratio, which ranged from 0.15% to 0.42%. Additionally, the study demonstrated effective bonding between the CFRP and the timber beams. Brunetti et al (2019) reinforced glulam beams with CFRP sheets using two different CFRP types. The results showed that the moment capacity increased between 45% and 57%, when compared to unreinforced beams. In addition, the ductility for the reinforced beams was improved, while the unreinforced beams showed brittle

failure. The results further confirmed that the mono-component polyurethane glue can be used effectively to bond the CFRP sheet to the wood surface.

Shekarchi et al. (2020) reinforced timber beams with flat, L-shaped, and U-shaped pultruded GRFP plates. The plates were glued either at tension side or at both tension and compression sides. The results showed that the flexural rigidity and modulus of rupture of the reinforced beams were increased by up to 59% and 61%, respectively, compared to unreinforced beams, while the absorbed energy increased by up to 209%. The results also showed that flat plate was vulnerable to premature debonding, unlike L-shaped and U-shaped plates, as those shapes can provide some confinement for the reinforcement. Bakalarz and Kossakowski (2022) reinforced laminated veneer lumber (LVL) beams with CFRP sheets having different configurations. The CFRP were placed in a U-shape to provide confinement. The results showed that the average improvement in moment strength for the reinforced beams ranged from 42% to 58% and from 15% to 43% for bending stiffness, when compared to unreinforced beams. Additionally, the CFRP sheets effectively shifted the failure mode from brittle tension to a more ductile compression failure mode.

Shu et al. (2022) reinforced timber beams using aluminum plates of varying thicknesses and connection methods, including screws and epoxy. The study examined the impact of connection type, comparing screw-only, glue-only, and a combination of both. All aluminum plates were affixed to the bottom surface of the beams. The reinforced beams demonstrated an average increase of 30% in flexural capacity, with a maximum improvement of 57%. Furthermore, the flexural stiffness of the reinforced beams increased by up to 109%, with an average increase of 55%. The findings indicated that the most effective approach was to combine screws and glue, while using

screws alone resulted in the lowest performance. Bakalarz (2024) reinforced timber beams with varying reinforcement ratios and arrangements, examining their performance. The results demonstrated that a 1.7% reinforcement ratio increased stiffness by 35% and maximum load by 46%. The authors highlighted that the key to achieving more efficient reinforcing lies in increasing the reinforcement ratio and maximizing the surface area of the timber covered by reinforcement. Additionally, ductile compression failure was observed in the reinforced beams.

Gul et al. (2024) reinforced glulam beams with cold-formed steel (CFS) sections on the tension side, investigating both flat and channel (C-shaped) steel sections. The steel sections were bonded to the wood beams using epoxy. Additional configurations were also examined incorporating screws and steel straps placed along the length of the beams. The results demonstrated significant improvements in load-bearing capacity, with an increase of 25% for flat sections with epoxy connections and up to 106% for C-shaped sections with epoxy and steel strap connections, compared to unreinforced beams. The study also revealed that the reinforced beams exhibited nearly double the stiffness of the unreinforced ones.

2.2.4 NSM Reinforcement

Gentile et al. (2002) reinforced half and full-scale timber beams using the Near-Surface-Mounted (NSM) method with GFRP rebars. The rebars were inserted at the tension side of the beam, with a reinforcement ratio of 0.27% to 0.82% as shown in Figure 2.3. The authors reported an increase in bending strength by 18% to 46% for reinforced beams when compared to those without reinforcement. The research outcomes indicate that using NSM GFRP bars to reinforce the wood beams improved the moment capacity and reduced issues associated with defects. Moreover, the failure shifted from brittle to ductile compression failure, and the ductility of the reinforced beams was greatly increased when compared to unreinforced one as shown in Figure 2.4 for half-scale beams configuration, where the HS0 beam represents the unreinforced reference beam, while HS41 and HS82 represent beams reinforced with 0.41% and 0.82% respectively.

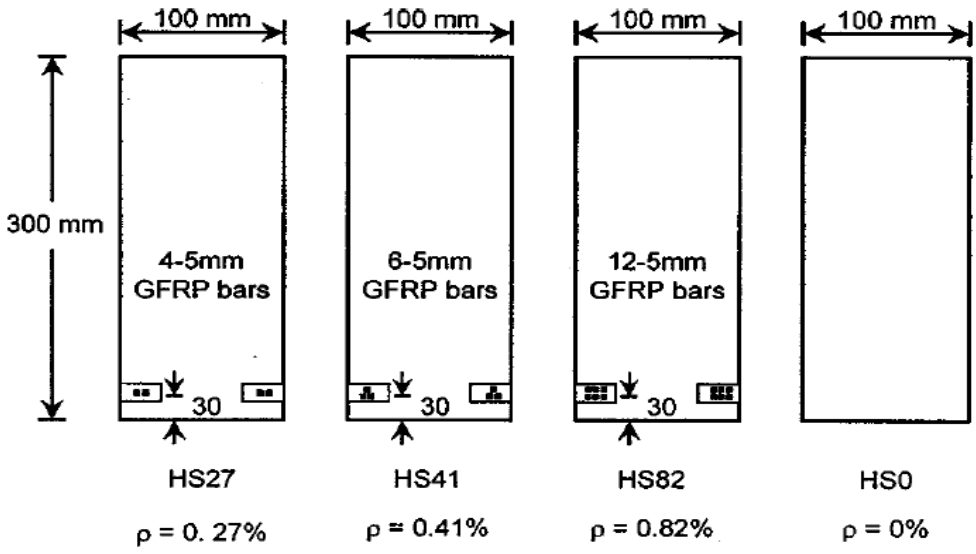

Figure 2.3: Reinforced timber beams (reproduced from Gentile et al., 2002).

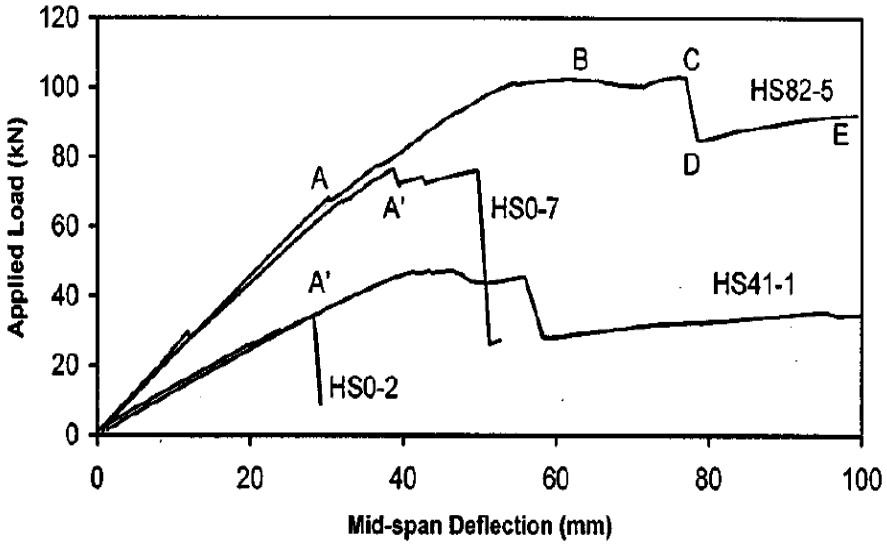

Figure 2.4: Reinforced timber beams (reproduced from Gentile et al., 2002).

Johnsson et al. (2006) studied the strengthening of spruce Glulam beams with 10 mm square section CFRP rods using three different configurations including single and double bars with full length, as well as single reduced length bar. The average increase in maximum load capacity for reinforced beams was between 49% and 63%. Barragán and Jacob (2007) analyzed a wide range of reinforcement ratios for glulam beams reinforced at the tension face of the beam with a CFRP plate having a modulus of elasticity of 300 GPa. The study showed that reinforcing the beam beyond the 2% reinforcement ratio was inefficient since a higher level of reinforcement could lead to shear failure prior to the ultimate bending strength being attained. The study also showed that the increase in the moment capacity for reinforced beams was from 57% to 96%, and stiffness increased from 80% to 107% compared to those of the unreinforced beams. Alam et al. (2009) strengthened fractured timber beams using steel, GFRP and CFRP reinforcements with different configurations. The reinforcements were placed inside grooves at the bottom, top and both sides. The results of the study showed that steel and CFRP reinforcements were very efficient in improving bending strength, and that the reinforced beams' fracture behavior depended on the

properties of the glue and reinforcement location. The results also showed that steel reinforcement had the most significant impact on enhancing beam stiffness, while using CFRP produced the highest increase in strength. Yusof and Saleh (2010) reinforced timber beams with GFRP rods. The reinforced beams were classified based on their reinforcement ratios. The increase in stiffness and maximum load capacity ranged from 24% to 60% and 20% to 30%, respectively. De Luca and Marano (2011) reinforced timber beams using a single steel bar on both the tension and compression sides, achieving a reinforcement ratio of 0.82%. They also investigated the effect of pre-tensioning on the bottom bar. The results indicated that, for non-prestressed reinforced beams, load capacity, stiffness, and ductility increased by 48.1%, 25.9%, and 43.8%, respectively. For prestressed reinforced beams, these increases were 37.9%, 40.2%, and 79.1%, respectively. Xu et al. (2012) investigated reinforced timber beams, including beams strengthened with NSM CFRP bars. The test configurations involved mounting NSM CFRP bars at the outer tension face. Anchorage using steel wire and strip U-shaped anchors were also investigated for NSM CFRP bars. The flexural capacity of the tested beams was increased on average by 47%.

Raftery and Whelan (2014) reinforced low-grade timber using GFRP rebar. The research explored the impact of various groove patterns and different sizes of GFRP rods, utilizing both tension-face reinforcements only as well as tension-and-compression faces reinforcements. With a 1.4% as reinforcement ratio, the results showed that the increase in maximum moment was 68%, while using a 2.8% reinforcement ratio distributed equally between tension and compression reinforcements, enhanced the maximum moment with 98.5% compared to unreinforced ones. The authors also studied the effect of using smaller-diameter rebar size to increase the bond surface of

the reinforcement, as shown in Figure 2.5. However, this technique didn't offer an advantage. Figure 2.5 also shows the reinforcement on the compression side of the beam.

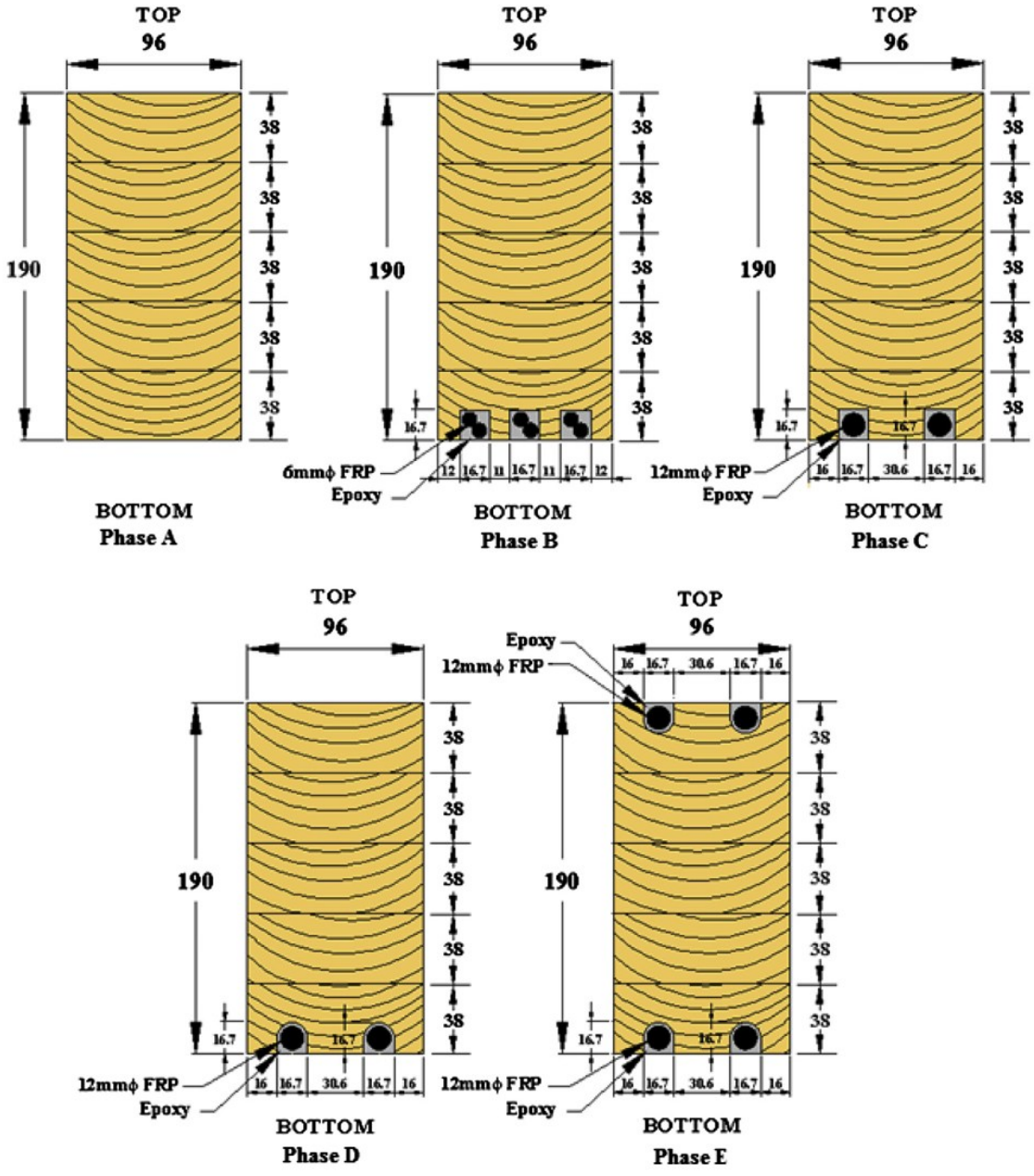

Figure 2.5: Reinforced Glulam beams (reproduced from Raftery and Whelan, 2014).

Raftery and Kelly (2015) reinforced low-quality glulam beams by inserting basalt FRP bars using a reinforcement ratio of 1.4% at the bottom of the beam. The results showed that the increase in mean maximum moment was 23% relative to those of unreinforced ones, while the increase in mean stiffness was 10.3% and 8.4% for local and global ones, respectively. The effectiveness of the reinforcements was also demonstrated by the strain profile along the depth of the reinforced beams. Yang et al., (2016a) reinforced glulam beam specimens using reinforcement steel and GFRP rebars as well as GFRP and CFRP plates at the tension and compression faces of the beam with different reinforcement ratios. The results of the study showed that the average increases in bending stiffness and strength were 27.5% and 56.3% for reinforced beams, respectively. Moreover, the ductility of the reinforced beams was improved. The authors also concluded that as the reinforcement ratio increases, the ductility is further enhanced as shown in Figure 2.6, for the reference unreinforced beams and the reinforced beams with 1.79% steel reinforcement ratios. Moreover, the bending stiffness and strength of the reinforced beams were accurately predicted using an analytical model.

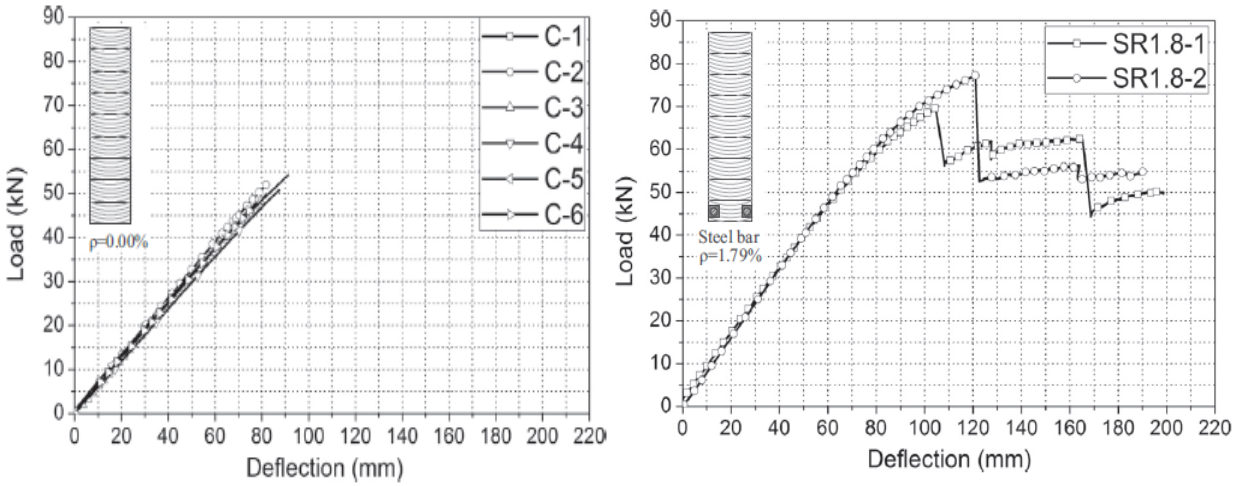

a) un-reinforced beams b) reinforced beams

Figure 2.6: Force-displacement curve for glulam beams (reproduced from Yang et al., 2016a).

Yang et al. (2016b) reinforced glulam beams by embedding prestressed CFRP bars in grooves. The resulting increases in moment capacity were between 64.8% and 131%, with a maximum increase in flexural stiffness of 42.0%. Nianqiang and Weixing (2017) reinforced timber beams with CFRP sheets, steel rebars, or both. The reinforced beams were tested under four-point bending test to examine their mechanicals properties. The results showed an effective improvement in bending stiffness, strength, and ductility of the reinforced beams compared to unreinforced ones. The results also showed that strengthening the wood beam with rebars and FRP sheet together can enhance the behaviour of the beam significantly. Gand et al. (2018) reinforced timber beams using basalt FRP bars with the NSM method. The reinforced beams were subjected to three-point bending tests with another three unreinforced beams as a reference. The results showed that the average enhancement for reinforced beams in load capacity was 16% while the maximum increase reached 60% relative to unreinforced ones. Bakalarz et al. (2020) reinforced laminated veneer lumber (LVL) beams with a 0.62% reinforcement ratio of CFRP strip reinforcement. The CFRP plates were attached to pre-drilled slots with the aid of epoxy adhesive at the bottom of the beam. The reinforcement primarily improved the maximum moment capacity and stiffness of the beam. The results from strain gauges showed a greater usage of compression side of the reinforced beam than the un-reinforced one. The reinforced beam also showed non-linear behaviour in force-displacement curve before the failure of the beam. Yeboah and Gkantou (2021) reinforced timber beams using NSM Glass and basalt FRP rebars with reinforcement ratios of 0.67% and 1%. Twenty beams were tested under a bending setup test, including four unreinforced beams. The authors reported an increase in stiffness increased of up to 33% while the load capacity by up to 69%, compared to those of unreinforced beams. The deflection at the midpoint of the reinforced beam was greater than that of the unreinforced ones, on average by 34%.

Livas et al. (2022) reinforced glulam beams using passive reinforcement with a single steel plate and active reinforcement with a prestressed steel rod. The reinforcement ratio was 1.28% for the steel plate and 1.34% for the active reinforcements. The study revealed that passive reinforcement improved the beams' strength, stiffness, and ductility by 26%, 30%, and 90%, respectively. In contrast, active reinforcement led to increases of 39%, 11%, and 75%, respectively. Additionally, the reinforcements altered the failure mode from brittle tension to ductile compression. He et al., (2022) tested 18 glulam beams including unreinforced and reinforced beams. The CFRP sheets were placed inside the beams' layups near the tension side of the beam. The purpose of the study was to examine the reinforcement ratio, CFRP configuration, and their modulus of elasticity on behavior of reinforced beams. The results showed that, for beam with reinforcement ratio of 0.04%, the increase for maximum deflection and moment capacity was increased by 12.02% and 6.51%, respectively. The results also showed that the compression part of the beam was more engaged in the presence of the CFRP reinforcements. As a result, the reinforced beams showed a ductile behavior compared to unreinforced beams. Furthermore, analytical models were also created using both conventional methods and finite element model to predict and examine the experimental results of the reinforced beams successfully. Alkhudery et al. (2023) strengthened ten glulam beams using steel bar reinforcements. The first group of beams was reinforced in both the tension and compression zones with various configurations while maintaining the same bar size. The second group included the reinforcements from the first group, along with CFRP sheets as shear reinforcement spaced along the length of the beam. The beams were subjected to testing with a four-point bending load configuration. The results demonstrated significant improvements in the structural performance of the reinforced glulam beams, with maximum load strength increasing between 16% and 49% compared to the unreinforced beams. Additionally, shear

reinforcement contributed to a modest increase in maximum load of only 2% to 7%. Furthermore, the study results showed that as the reinforcement ratio at the tension side increased, the load capacity and ductility were also improved. The study concluded that the NSM reinforcing method using steel bars is an effective approach to enhance the strength and flexural capacity of glulam beams.

Wdowiak-Postulak et al. (2023) reinforced glulam beams with two pre-stressed basalt FRP bars placed on the tension side of the beams having reinforcement ratio of 1.2%. In a second configuration, an additional bar without prestressing was added to the compression side for further investigation having a total reinforcement ratio of 1.9%. The results demonstrated that the reinforced beams had increased stiffness and maximum load by 23% and 36%, respectively, compared to unreinforced beams, while also mitigating failure and crack propagation. The study found that beams reinforced on both the tension and compression sides showed even greater improvements. The numerical analysis closely aligned with the experimental results. Mathuros et al. (2024) reinforced timber beams with GFRP bars with a reinforcement ratio of 0.59%, 0.88%, and 1.32%. The GFRP bars were placed in grooves at the tension side of the beams, with the addition of one steel rebar at the compression side of the reinforced beams. The unreinforced and reinforced beams were tested using monotonic and cyclic loads under four-point bending tests. The results showed that the stiffness of the reinforced beams increased between 58 %to 71%, while the ultimate load increased between 20 % to 61%. On the other hand, the stiffness and ultimate load increased between 58% to 90 % and 22% to 75%, respectively when the reinforced beams were subjected to cyclic load tests. The results also showed that the energy absorption for the timber beams increased significantly after reinforcement.

2.2.5 Reinforcement length and end attachments

The majority of research studies have used full-length reinforcement along the beam length (e.g. Barragán and Jacob 2007; Raftery and Whelan, 2014). However, it is more convenient to place the reinforcement away from the face of the support to facilitate the application of the NSM reinforcement, as done by (Johnsson et al., 2006; Bakalarz et al., 2020). This option can also reduce the amount of epoxy required. However, De Jesus et al., (2012) showed that the application of reinforcements shorter than the beam spans can lead to significant stress concentration in the interface (adhesive layer) between the reinforcement and the beam surface, especially at the end of the reinforcement. The shear and peeling (normal) stresses are mainly responsible for delamination, resulting in a reduction in the capacity of reinforced beams. Johnsson et al., (2006) studied the bond strength between CFRP reinforcements and wood beam and examined the distribution of the shear bond stress between the reinforcement CFRP bars and the surface of the timber beams. The authors did not report any delamination failure until the beams reached their ultimate capacity.

Barragán and Jacob (2007) investigated two types of epoxies and mentioned that the viscosity of the epoxy has a significant impact on constructing the reinforced beam, where it was found that more viscous epoxy was easier to handle, especially for narrow slot widths. However, high viscos epoxy led to lower shrinkage during the curing process because of the grain particles in the epoxy. The shape of the groove can also affect the structural response of the reinforced timber elements. Raftery and Whelan (2014) concluded that a circular groove shape reduces the stress concentration at the edge and could lead to an increased capacity of the section.

2.3 Blast Loading

2.3.1 Blast Wave Characteristics

Explosions occur when there is a rapid and intense release of a substantial amount of energy, which could be physical, chemical, or nuclear, etc. An explosion of an overheated and pressurized container is considered a physical explosion. Rapid oxidation of trinitrotoluene (TNT) that generates heat and detonation pressure shock wave is considered as exothermic chemical reactions. The generated waves spread and travel faster than the speed of sound (Krauthammer, 2008). The shockwaves travel and propagate in a spherical form. However, when the charge is on the ground, the wave is redirected and spreads in hemispherical forms (FEMA, 2011). The pressure wave will spread uniformly through the atmosphere until it reaches a building surface and reflects off it. This reflection may lead to the wave undergoing diffraction or amplification, especially in the presence of complex building shapes or geometries. Consequently, further analysis may be required to address these interactions. The effects of explosives can be represented by the scale distance, Z, in terms of charge weight (W) and stand-off distance (R), as demonstrated in Equation 2.1.

$$Z = \frac{R}{W^{1/3}} \qquad Eq.\,2.1$$

This implies that two explosive charges may exhibit the same scaled distance or similar effect on the structural element, even if they have different magnitudes and stand-off distances.

Shock waves are defined using pressure-time record functions. The intensity and duration of the pressure in these functions depend on how far the explosion is from the source as well as the size of the explosion. Figure 2.7 shows a typical far-field shock wave as a pressure-time history.

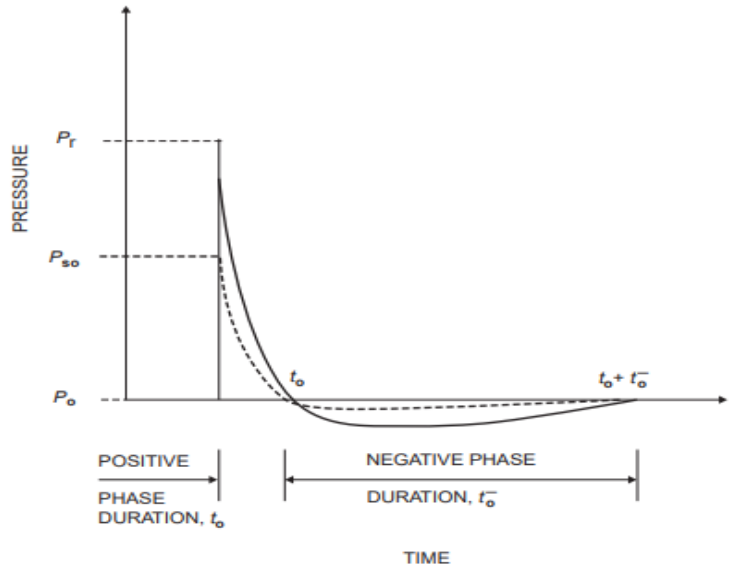

Figure 2.7: Idealization of pressure (Dusenberry, 2010).

The negative pressure is generated due to air particles created during the positive phase. As a result, a suction force is developed since the pressure is less than the ambient pressure. In most cases, the effect of the negative phase is disregarded since it has lower pressure relative to the positive phase (UFC 3-340-02). The pressure versus time curve can be represented using idealized Friedlander equation. The equation is represented by a sudden rise in pressure then it is dropped by exponential decrease. The pressure and impulses versus time can be calculated by using Equation 2.2 through Equation 2.4. The integral or the area under the curve is referred to as the impulse (I).

$$P(t) = P_{so} e^{-\frac{ct}{t_o}} \left(1 - \frac{t}{t_o}\right) \qquad Eq. 2.2$$

$$I^+ = \int_{t_A}^{t_A + t_o} P(t)\, dt \qquad Eq. 2.3$$

$$I^+ = \int_{t_A}^{t_A + t_o + t_O^-} P(t)\, dt \qquad Eq. 2.4$$

where P_{so} is the incident peak overpressure, t_A is the arrival time of the front of the shock, $t_O and\ t_O^-$ is the positive and negative phase duration respectively, and c is the parameter of blast waveform.

2.3.2 Dynamic Analysis for Blast

Due to the uncertainty and unpredictability related to blast loading, simplified analysis methods are typically used to predict the behavior of structural elements under blast loading. This includes the equivalent single-degree-of-freedom (SDOF) method. A description on how to use and apply this simplified method can be found in (e.g., UFC 3-340-02). The method includes converting the structural behavior of a real structure into an equivalent system that has a predefined degree of freedom (DOF). The transformation is generally achieved by using the integral of deflected shape function that considers the boundary conditions and the actual distribution of the mass of the structure as well as the load distribution (Biggs, 1964). Equation 2.5 presents the equation of motion with transformation factors.

$$K_{LM}\, m\, \ddot{u} + c\dot{u} + k\, u = P(t) \qquad Eq.\,2.5$$

Where m, c, and k represent the mass, damping, and stiffness of the structural element, while u, $\dot{u}$ and $\ddot{u}$ are the displacement, velocity, and acceleration of the prescribed degree of freedom.

The values of the transformation factors are based on the deflected shape of the beam (Biggs, 1964). The transformation factors for mass (K_M), load (K_L), and resistance (K_R) are considered in the equation of motion. The deflected shape depends on the applied load configurations

(concentrated or distributed), and the boundary condition (simply supported or fixed). The K_M and K_L factors can be calculated using Equations 2.6 and 2.7, respectively.

$$K_M = \frac{\int_0^L \overline{m}(x)\emptyset^2(x)dx}{\int_0^L \overline{m}(x)dx} \qquad Eq.2.6$$

$$K_L = \frac{\int_0^L f(x,t)\ \emptyset(x)dx}{\int_0^L f(x,t)\ dx} \qquad Eq.2.7$$

In general, the resistance factor (K_R) is equal to the load factor (K_L), because the resistance of the system acts in opposition to the applied loads. The load and mass factors can be combined into a load-mass factor (K_{LM}). This can be done by dividing the mass factor by the load factor. More information about these factors and their values is available in the literature (Biggs, 1964). It should be noted that the SDOF may only be feasible for simple structures. For more complicated structures, and in order to enhance the accuracy, multi-degree-of-freedom (MDOF) system or Finite Element Analysis (FEA) can be used.

2.4 Blast Loading effects on timber

2.4.1 Blast load effect light-frame wood

Jacques, et al. (2014) tested thirty wood studs under static and blast loading with four-point bending loads configuration setup. The simulated blast load tests were conducted at the shock-tube facility at the University of Ottawa. The purpose of the test was to examine the effects of strain rate for the modulus of elasticity (MOE) and modulus of rupture (MOR). The results showed that the MOE did not exhibit any dynamic increase, while a DIF of 1.41 could be assumed for the MOR. Lacroix and Doudak (2015) tested full-scale light-frame stud walls under simulated blast

loading using the shock tube device. Two types of sheathing and thickness were examined for the walls. The walls had simply supported boundary conditions. Moreover, the walls were subjected to static bending load with the same configuration and boundary condition as the dynamic test in order to validate the DIF in strength and stiffness. A total of twenty light-frame walls were tested in static and dynamic tests. The DIF was found to be 1.18 and 1.40 on the stiffness and force resistance, respectively, and the response of the walls was predicted using a SDOF system. Figure 2.8 shows one of the tests on stud walls using the shock tube device.

a) Stud wall before the test b) Stud wall after the test

Figure 2.8: Stud walls (reproduced from Lacroix and Doudak, 2015).

In an attempt to strengthen the stud walls and reduce sheathing debris at high blast pressures, Lacroix et al. (2014) tested four different retrofitted wall options by adding thicker sheathing, adding extra flat-wise stud or using corrugated steel panels as sheathing. The retrofit options showed enhancement in the response of walls. Moreover, the responses of the retrofitted wall were studied using a SDOF model. In addition, pressure-impulse (P-I) diagrams were generated using SDOF system that describe the damage of the wall using defined ductility ratios. Figure 2.9 shows an example of the tested walls with a flatwise stud and corrugated steel panel.

a) Flat wise stud b) Steel panel

Figure 2.9: Stud walls (reproduced from Lacroix and Doudak, 2014).

Viau and Doudak (2016a) conducted tests on wood stud walls using the same shock tube device. The authors employed two different types and thicknesses of sheathing. The study showed that thicker sheathing and additional screws enhanced the ability to transfer greater force to the studs before the sheathing failed. Additionally, a welded wire mesh was used to contain sheathing debris and increase the strength of the sheathing. An SDOF analytical model was utilized to predict the system's response successfully. Viau and Doudak (2016b) tested wood stud walls under realistic boundary conditions that simulate those used in construction to protect against seismic and wind loads. The study investigated different connection types, including nails, joist hangers, and steel angle connections, and reported various types of failure for each connection type. The study showed that connections relying solely on nails performed poorly and may fail before the stud wall reached its capacity, while joist hangers and angles demonstrated adequate performance. However, the authors highlighted the necessity of developing more sophisticated analytical models beyond the SDOF approach to accurately simulate the effects of damage in the connections. Viau et al. (2016) performed an assessment of light-frame stud walls that were tested under blast loading. In total 33 walls were subjected to 48 blast shots. With the aid of a SDOF analytical model system, the PI-diagrams were generated to describe the damage of the stud walls using the ductility ratio. The results also showed that a ductility ratio of a maximum of 2 was more suitable for the design purposes for light-frame stud walls, and the code design values were overestimating this value.

Lacroix et al. (2021) reinforced individual wood studs using GFRP fabric sheets in four different configurations: longitudinal layers, U-shaped layers, longitudinal layers with wrapping as confinement, and U-shaped layers with warping. The number of longitudinal layers was varied from one to three. These configurations aimed to optimize the performance of the reinforced studs.

The reinforced studs were tested under a four-point static bending test, where all configurations except the single-layer configuration without confinement outperformed the unreinforced studs and were able to alter the failure into ductile compression, unlike unreinforced studs having brittle behaviour. Reinforced studs showed increases by 1.8 and 2.4 times in stiffness and strength, respectively, compared to unreinforced studs, and ductility ratios ranging between 1.4 to 3.9. In a subsequent study, Lacroix et al. (2021) tested six full-scale light-frame stud walls reinforced with GFRP and subjected to dynamic blast testing using a shock tube device. Individual studs within these walls were reinforced with either simple tension layers or U-shaped fabric, both with and without confinement. The GFRP-reinforced stud walls showed up to 2.6 times increase in energy resistance under blast loading compared to unreinforced walls, while over-reinforcing the stud walls increased the resistance energy but altered the failure mode from flexural to shear. Figure 2.10 illustrates the failure modes observed in each reinforced light-frame stud wall after the dynamic blast test.

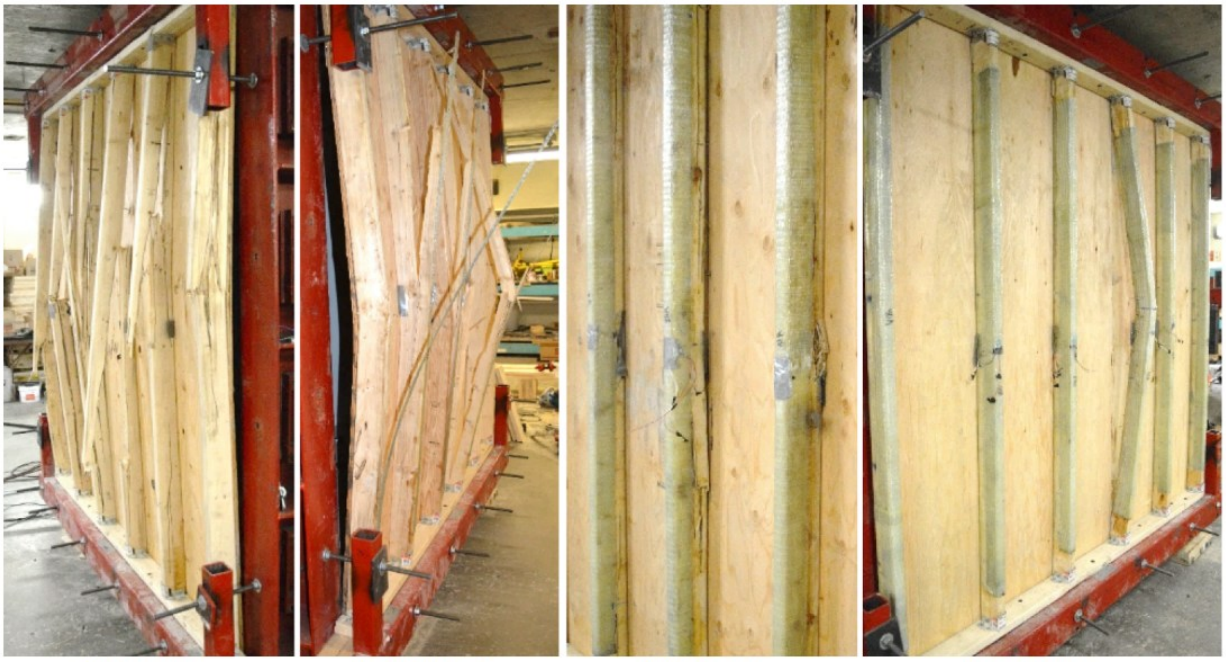

(a) Wall 1 (b) Wall 3 (c) Wall 4 (d) Wall 5

Figure 2.10 Stud walls (reproduced from Lacroix et al., 2021).

As shown in Figure 2.10, after the blast shots occurred, reinforced walls 4 and 5, with studs strengthened with U-shaped FRP sheets, sustained less damage than unreinforced wall 1, as well as wall 2, which was reinforced with a single-layer sheet.

2.4.2 Blast load effect on CLT

Poulin et al. (2017) performed static and dynamic blast load tests on eighteen CLT panels. Two thicknesses of panels were used in the test as 3 and 5 layers. Four-point bending load setup was used in the out-of-plane direction for static and dynamic tests. Flexural failure mode was reported in most of the CLT slabs. However, rolling shear failure was observed in the CLT's panels near the ultimate failure. The study established a DIF for this type of structural element and investigated the failure modes. The study noted an average DIF of 1.28 in flexure strength, with no reported

enhancement in stiffness. Moreover, a SDOF system model was used to predict the displacement-time history for the CLT panels. The ductility ratio was reported to be up to 2.5 for all tests. Côté and Doudak (2019) investigated the impact of different connection types placed at the top and bottom of CLT panels subjected to blast loading using a shock tube device. Various connection types were tested to evaluate their performance, with thirteen wall panels examined under a four-point bending load configuration. The study highlighted distinct failure modes and behavioral responses for each connection type. Results showed that conventional screw connections were ineffective, leading to early failure, whereas steel angle connections performed better by effectively dissipating energy. The authors concluded that more advanced models are needed to accurately predict the effects of connections on slab response, as existing SDOF analytical models proved insufficient.

Lopez-Molina and Doudak (2019) investigated the response of reinforced CLT panels using the shock tube device. The CLT panels were subjected to a four-point bending load configuration. The authors used both steel straps and GFRP fabric to strengthen the CLT panels. For the steel straps, the number of straps and straps arrangements were studied, while, for GFRP, the lay-up arrangements and direction of fibre were examined. A total of seventeen reinforced CLT panels were investigated. These strengthening techniques increased the stiffness of the panel between of 10 % to 28 % compared to the data of un-reinforced CLT reference panels. No additional increase in stiffness was obtained when the reinforced panels were tested in the shock tube facility. In addition, a great enhancement in strength, post-peak force and ductility ratio was achieved. Figure 2.11 shows one of the panels reinforced with GFRP sheet.

Figure 2.11: CLT panels (reproduced from Lopez-Molina and Doudak, 2019).

Viau and Doudak (2019) examined the blast response of CLT panels with varying boundary connections. Two types of connections were examined, representing thin and thick angles, and these were attached to wood with screw fasteners. Small-scale wood component tests were conducted to examine the behavior of connections independently, followed by full-scale tests with CLT panel assemblies. Findings showed that the DIF were notable for connections where wood crushing and angle bending occurred, whereas no increase in DIF was observed when failure was due to screw yield and rupture alone. A two-degree-of-freedom analytical software model was developed and validated against experimental results, providing displacement and time-history response outputs. Van Le et al. (2020) explored the response of Radiata pine CLT panels in the out-of-plane direction subjected to simulated blast loading using the shock-tube device. The study showed the output of eight blast load tests on two CLT panels, measuring 130 mm and 145 mm in

thickness. The maximum reflected pressure ranged from 60 kPa to 240 kPa and remained within the elastic range of the panels. The response of the panels was examined using numerical models and a SDOF system. The data from the dynamic tests were compared to the static properties to find the DIF for the stiffness of the panels. Notably, the SDOF analysis found DIF values ranging from 1.12 to 1.57, while the numerical simulation estimated DIF values between 1.05 and 1.43.

2.4.3 blast load effect on Glulam

Lacroix and Doudak (2018a) tested glulam beams with different cross-sections and from multiple suppliers using the shock tube device to investigate their DIF. The result showed that a DIF of 1.14 was obtained for beams having staggered finger joints across the lamination, while no enhancement was observed for glulam beams where the finger joints were closely spaced on the lamination surface. Moreover, all glulam beams showed a linear-brittle behavior. In addition, SDOF system was used to capture the dynamic response of the glulam while incorporating the DIF. Furthermore, under blast loading, a brash crack occurred when the beam failed, in contrast to the splintering crack seen during static tests for beams having only one full laminate at the bottom of the beam. Furthermore, a combined axial and bending loading applied on the glulam beams was also investigated by Lacroix and Doudak (2018b). An analytical SDOF model was developed based on the concept of composite resistance curves to simulate the effects of the loss in axial load as the specimen underwent into lateral deflection. Figure 2.12 shows a sample of damaged specimens after the blast test using shock tube device.

a) Beam specimen b) Column specimen c) Column specimen close-up

Figure 2.12: Glulam blast test (reproduced from Lacroix and Doudak, 2018b).

Lacroix and Doudak (2018c) investigated the structural response of reinforced glulam beams using FRP sheets, including the reinforcement of previously damaged beams. The study explored various beam configurations with FRP sheets, incorporating multiple FRP layers and different layouts along the beam's length. The effects of FRP confinement were also examined. The results showed that the maximum increases in strength and mid-span displacement were 1.66 and 1.62 times, respectively. Additionally, the FRP reinforcements enhanced the ductility of the glulam beams. FRP confinement effectively prevented premature debonding of the reinforcement. The FRP reinforcement with confinement was also able to recover some of the stiffness and strength of the damaged beams. An analytical model was developed to account for the effects of FRP

reinforcement and generate the resistance-displacement curve for the reinforced beams. Figure 2.13 shows one of the damaged, reinforced beams after blast testing.

a) Reinforced beam b) Close-up for mid region

Figure 2.13: Reinforced glulam using FRP sheet (reproduced from Lacroix and Doudak, 2018c).

Lacroix and Doudak (2018d) reinforced glulam beams with FRP sheets in various layout configurations and tested two beam sizes, as shown in Figure 2.14. In addition, the fibers were oriented at angle of 45 degrees. The reinforced beams were subjected to shock-tube testing using a four-point bending setup. The results indicated that the reinforcement significantly improved the

beams' behavior, achieving ductility ratios between 2.30 and 3.61. The bidirectional fiber reinforcement effectively delayed failure and increased the wood's tensile strain by an average of 1.21 times. Furthermore, an analytical model was developed to predict the resistance-displacement curve, showing good agreement with the experimental data. Additionally, an SDOF analysis model was used to predict the displacement-time response curve of the reinforced beams under blast loads, closely matching the experimental results.

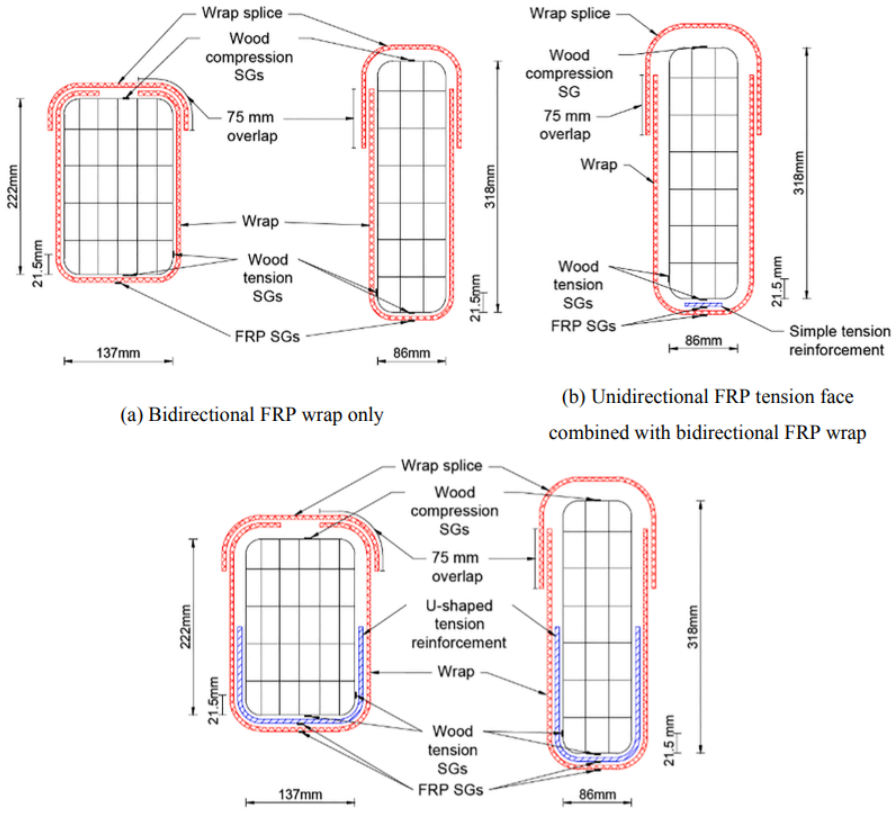

Figure 2.14: Reinforced beam with FRP sheets (reproduced from Lacroix and Doudak, 2018d).

McGrath and Doudak (2021a) investigated the response of steel bolt connections in glulam beams under simulated blast loads using a shock tube device. Two bolt diameters and wood block sizes were tested to control failure modes, focusing on either wood crushing or bolt yielding. The study also examined the effects of applying blast loads either aligned parallel or perpendicular to the

wood grain. Static tests were conducted to assess the dynamic increase factor (DIF). The results showed that allowing the bolts to yield is essential for achieving ductile behavior and preventing brittle failure from wood crushing alone. Additionally, the DIF was limited when the bolts yielded, compared to cases dominated by wood crushing. The results also showed that reinforcing the connections with self-tapping screws effectively prevented premature splitting. A two-degree-of-freedom model was used to simulate the connection's response under blast load successfully.

Viau and Doudak (2021a) investigated the effect of bolted connections on glulam beams subjected to blast loads using a shock tube device. The connections were placed at the top and bottom of the beams as boundary conditions. Various bolt configurations and arrangements were tested in full-scale beam experiments. The findings revealed that allowing the bolts to yield resulted in improved performance, as the yielding facilitated energy dissipation, unlike overdesigned connections that limited such behavior. Viau and Doudak (2021b) investigated the performance of EACs in glulam and CLT beam members through full-scale testing with a shock tube device. The results demonstrated that EACs effectively absorbed and dissipated energy, outperforming idealized simply supported connections. Additionally, these connections enhanced the ductility of the glulam and CLT members under loading. The system's response was also predicted using a two-degree-of-freedom model. Figure 2.15 illustrates a connection-glulam beam assembly during testing with the shock tube device.

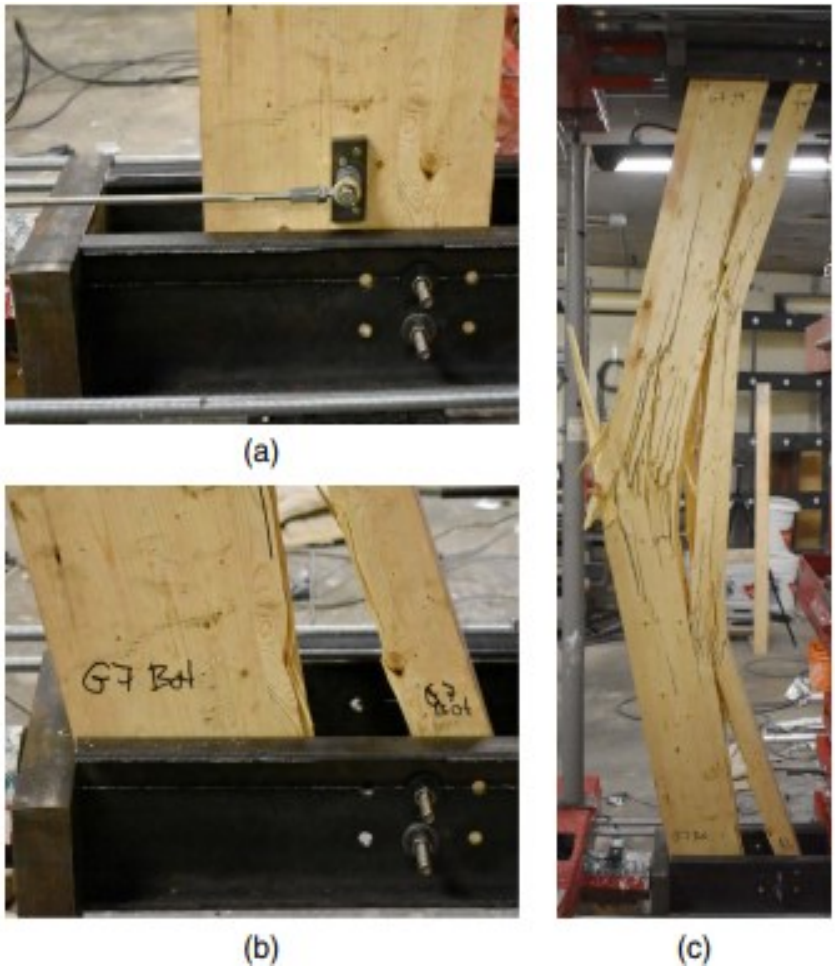

a) Connection before test b) Connection after test c) Glulam beam assembly

Figure 2.15: Glulam assembly test (reproduced from Viau and doudak, 2020a).

Oliveira et al. (2023b) tested three samples of glulam beams and CLT panels using the shock tube device. The beams were subjected to multiple blast shots to examine the effect of accumulative damage. Flexure failure mode was observed with rolling shear also observed in the CLT members. An SDOF model was utilized to obtain the displacement and time responses of the beams. Oliveira et al (2023a) employed finite element method with a 3D model to acquire the responses of glulam and CLT beams subjected to simulated blast loading using the shock-tube device and to mimic the accumulative damage on the sample due to the multiple shots. The ABAQUS program with a

numerical subroutine was developed and employed to predict the response. The data from the finite element model matched the experimental response results. Figure 2.16 shows on of the predicted damages for glulam beam using the finite element method.

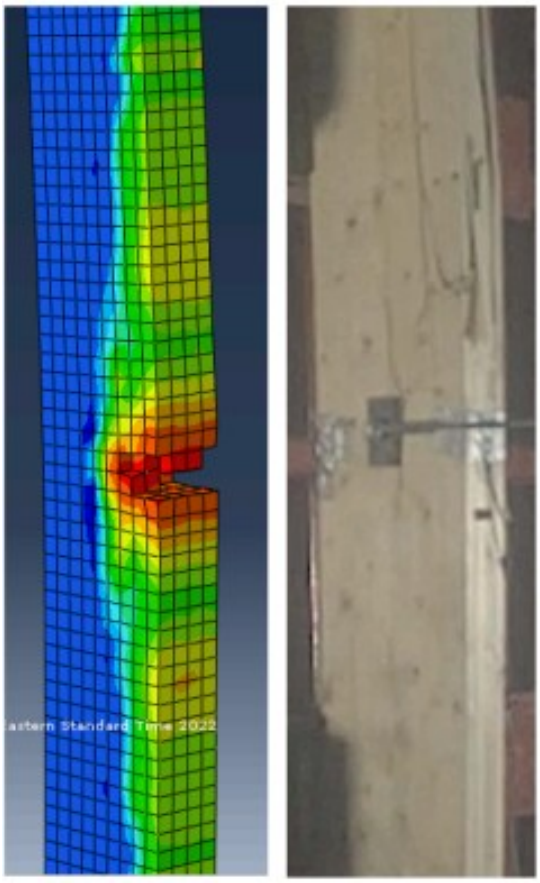

Figure 2.16: Glulam beam damage (reproduce from Oliveira et al., 2023a)

Bérubé and Doudak (2023) investigated the structural performance of energy-absorbing connections (EACs) in various configurations, including angled and circular sections. The EACs were subjected to both static loading and dynamic blast loading using a shock tube device. The results demonstrated that EACs effectively dissipated energy and could enhance the performance of timber connection assemblies under blast loads. The analysis indicated that EACs could

potentially increase the reflected peak pressure of timber assemblies by 55% and improve their energy absorption capacity by 247%. Bérubé and Doudak (2024) investigated the performance of energy-absorbing connections (EACs) in full-scale static flexural beam tests. Allowing EACs to yield demonstrated significant displacement and energy absorption prior to beam failure. Furthermore, a SDOF analysis showed that integrating EACs into beam assemblies enhanced energy dissipation by approximately 5 to 6 times compared to assemblies with idealized simply supported boundary conditions.

Wight et al., (2024) tested nine glulam beams under quasi-static and dynamic loads. The dynamic tests were conducted with a four-point bending setup utilizing a weight impact testing facility. The research simulated impact conditions within a strain-rate range of 0.67 to 1.05 s^{-1}. Both static and dynamic flexural tests indicated a linear brittle response for the force resistance-displacement curves. The results indicated substantial DIFs, with values of 1.20 for stiffness and 1.13 for maximum resistance. A SDOF model was developed and verified using the experimental test data, showing precise predictions of the time and displacement responses. Thevarajah et al. (2025) reinforced LVL beams and subjected them to impact loading with a 100 kg free-fall hammer in a three-point bending setup. Reinforcements using CFRP, GFRP, and steel plates were shown to improve the beams' stiffness, load resistance, and ductility.

CHAPTER THREE: EXPERIMENTAL PROGRAM

3.1 Introduction

An experimental program has been designed to evaluate the performance of glulam beams reinforced with steel plates and rebars under static and simulated blast loading. Steel reinforcement is chosen due to its proven ability to provide adequate stiffness, strength, and ductility, which is expected to enhance the behavior of the beam elements, particularly in the post-peak region where inelastic energy dissipation is critical. Epoxy primer and paste were utilized in this study as bonding agents between wood and steel, as well as coating materials for steel reinforcement.

3.2 Material

3.2.1 Steel

Three different sizes of steel reinforcement rebars, namely 10M, 15M, and 20M, in accordance with the CSA G30.18-21 - 400W (CSA, 2021), as well as 6.35 mm thick and 31.75 mm wide smooth steel plate according to the CSA G40.21 - 44W (CSA, 2013), were used as reinforcement. Three coupon samples were taken from each rebar and plate reinforcement and tested under axial tension, except for the 20M bars, where only two samples were considered due to sample limitations. The tests were performed using the Galdabini Universal Testing Machine (UTM) in the Structural Lab, as shown in Figure 3.1, following the procedures outlined in ASTM A370 to determine the mechanical properties of the steel. The obtained properties were used as input parameters in the analytical model. Table 3.1 presents the average summary of the mechanical properties of the steel reinforcement rebars and plates, including the experimental yield stress (σ_y) and strain (ϵ_y), modulus of elasticity of steel (E_s), ultimate stress (σ_u), and ultimate strain (ϵ_u).

The stress–strain diagram for one representative sample of each steel rebar and plate is shown in Figure 3.2.

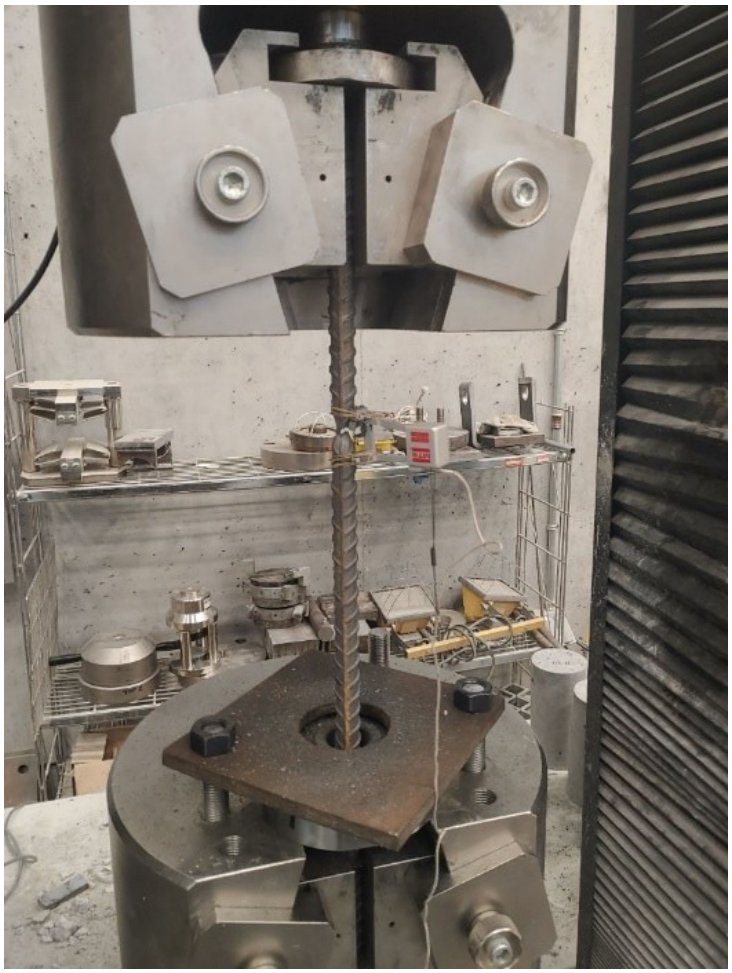

Figure 3.1: Steel sample under test.

Table 3.1: Material steel properties.

Member	$\epsilon_y\ (10^{-3})$	$\sigma_y\ (MPa)$	$E_s\ (MPa)$	COV	ϵ_u	COV	$\sigma_u\ (MPa)$	COV
10 M	2.3	491	211019	(0.042)	0.121	(0.024)	587	(0.016)
15 M	2.2	403	186130	(0.037)	0.144	(0.108)	561	(0.001)
20 M	2.3	480	208696	(0.044)	0.084	(0.091)	573	(0.007)
Plate	1.6	323	207828	(0.067)	0.189	(0.025)	448	(0.004)

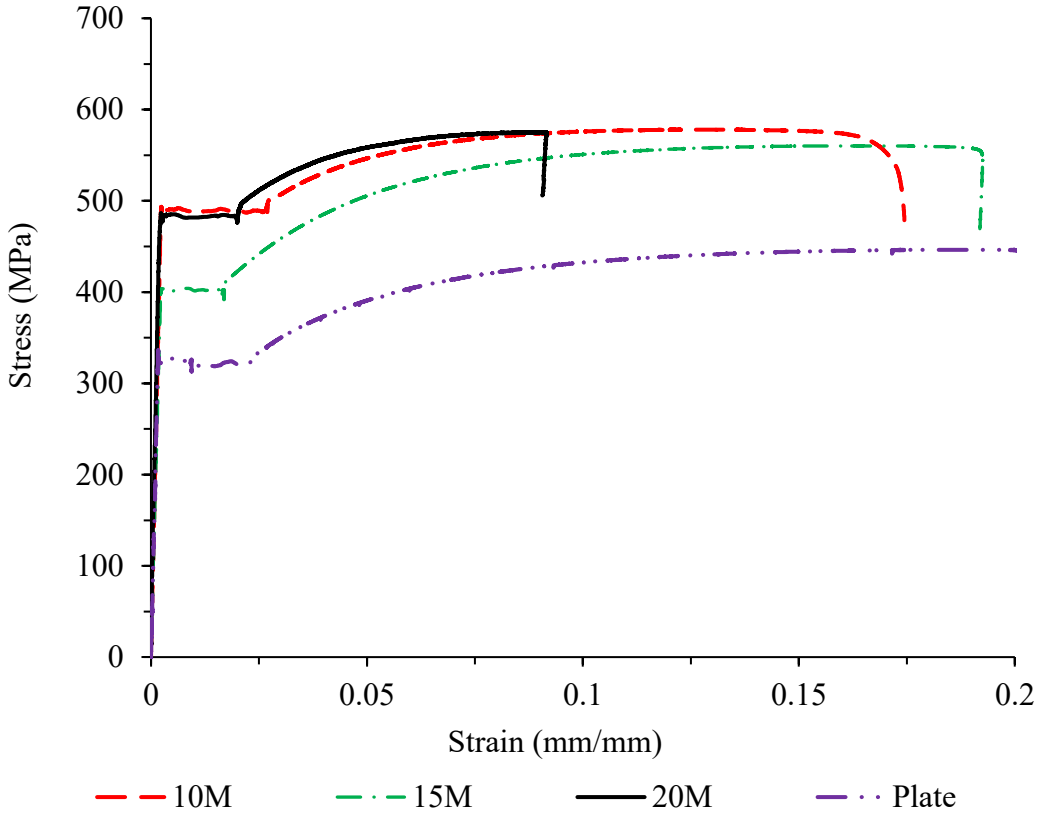

Figure 3.2: Tension test for steel samples.

3.2.2 Glulam beams

The glulam beams used in the experimental program consisted of SPF species (black spruce) with grade 24F-ES/NPG (NORDIC LAM+), manufactured by Nordic Structures Inc. The beams have homogeneous layup, which means that they consist of the same grade of laminations across their depth. The nominal dimensions of the beams' cross-section were 137 mm x 191 mm, while the average measured dimensions were 136 mm x 189.5 mm. Although the difference between nominal and actual dimensions was small, the actual dimensions were used in Chapters 4 and 5 as inputs in the analyses. The length of the beams was 2.5 m, which represents a depth-to-width and length-to-depth ratios of 1.4:1 and 12:1, respectively. Such beam dimensions promote flexural failure modes, which are at the core of the current investigation.

3.2.3 Epoxy

Two types of epoxies were used in this study, namely CSS-ES Epoxy Primer and Saturant and CSS-EP Epoxy Paste and Filler, produced by Simpson Strong-Tie Inc. These epoxy types are suitable and effective for this application due to their slow setting time of around one hour, which provides sufficient time to install the reinforcement before it hardens. The epoxy primer has low viscosity and is used as the first coat for the wood before placing the epoxy paste, since wood is a porous material and needs a low-viscous epoxy agent.

3.3 NSM installation method

The NSM reinforcement installation was undertaken by routing slots along the length of the beam after which the epoxy mix is cast, and the reinforcements are installed. After that the excess epoxy is flushed with the surface of the wood. The installation process is shown in Figure 3.3.

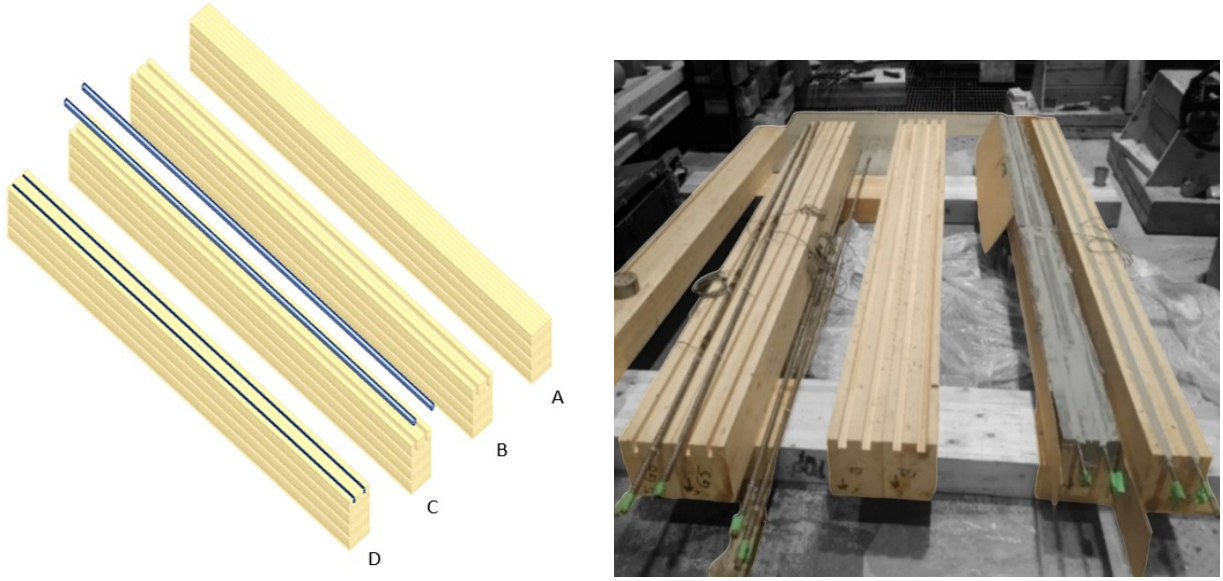

a) NSM construction process. b) Beams under reinforcement

Figure 3.3: The NSM process during the specimen construction.

A router was used to cut grooves along the surface of the wood as shown in Figure 3.4, with widths of 16 mm, 22 mm, and 27 mm for the 10M, 15M, and 20M rebars, respectively, and 12 mm for the plate reinforcement. This provided approximately 2 mm of clearance between the ribs of the rebar and the edge surface of the groove for better constructability and to provide access when the rebar is placed inside the grooves. Moreover, a 2 mm aluminum wire was used around the rebar to hold the rebar in position during the casting of the epoxy and to maintain a constant epoxy thickness. Moreover, to account for rebar straightness and sagging imperfections and to ensure complete epoxy coverage, groove depths of 20 mm, 25 mm, and 30 mm were used for the 10M, 15M, and 20M rebars, respectively. The grooves were sanded with 120-grit sandpaper before placing the epoxy in order to roughen the surface and increase the bond strength between the epoxy and the wood.

a) Before cutting b) After cutting

Figure 3.4: Grooves the construction process.

As shown in Figure 3.4, two rail guides were used to ensure straight grooves. Clamps were used to hold the beam in position while drilling. Figure 3.5 shows the glulam beams after drilling the grooves for 10M and 15M rebars and plate reinforcements.

Figure 3.5: Glulam beams after drilling the grooves.

The reinforcement rebars and plates were cleaned with a steel wire brush and stripping disc, respectively, to remove rust accumulation on the surface. Subsequently, the surface of the steel was roughened with aluminum-oxide shot blasting for the rebars, while fiber disc with 120-grits was used for the plates. Furthermore, the steel was cleaned with acetone and left to dry before the application of the epoxy. For the process of applying the strain gauges, the wood surface was sanded with 120-grit sandpaper to roughen the surface and then cleaned using air pressure to remove debris. The strain gauges and adhesive were sourced from. Hoskin Scientific, with resistances of 120 ohms for static tests and 350 ohms for dynamic tests. An example of the application of strain gauges on the glulam beams is shown in Figure 3.6.

Figure 3.6: Strain gauge application (wood).

For the wood applications, a layer of polyurethane coating was applied to the strain gauge in order to protect it from potential adverse effects from the surrounding environment. Similar procedures were employed for applying strain gauges to steel. However, for reinforcement rebars with ribs, the surface was smoothed using a grinder, subsequently, the surface was sanded with 120-grit sandpaper using a rotary machine. An example of the application of strain gauges on the steel is shown in Figure 3.7.

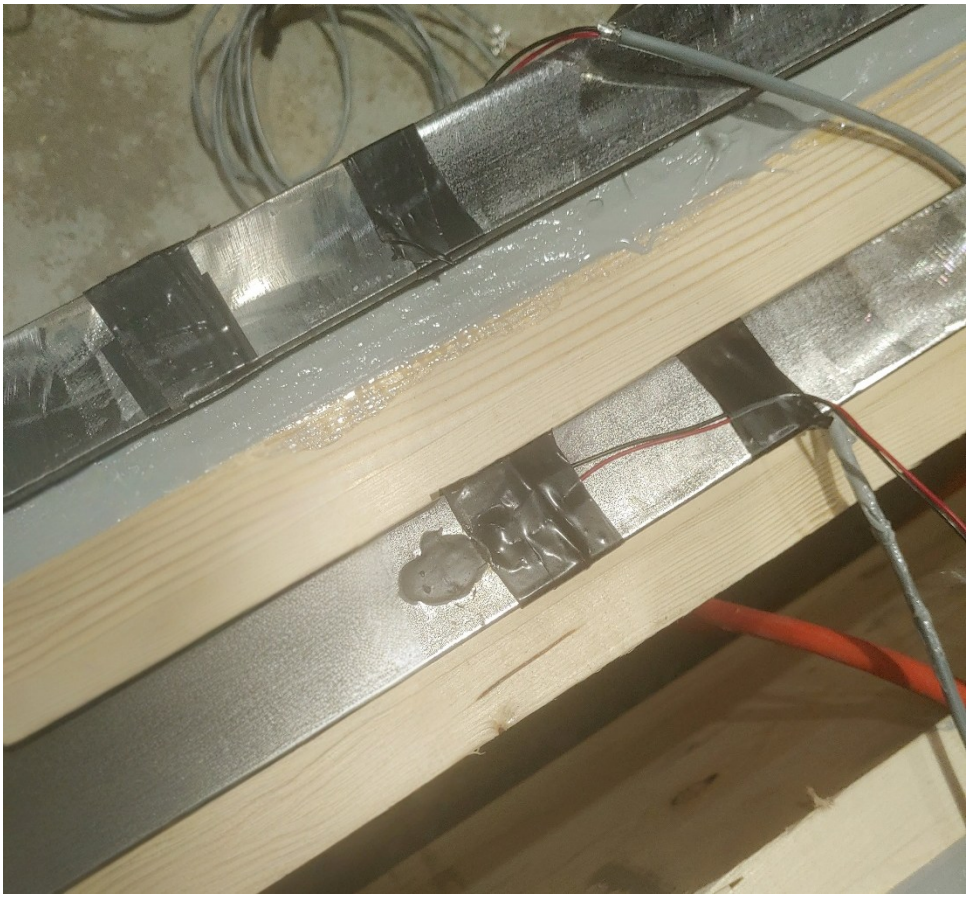

Figure 3.7: Strain gauge application (steel).

The process of applying the epoxy was initiated by placing the epoxy primer (liquid epoxy) inside the groove and leaving it for 15 min, followed by the epoxy paste, which was mixed and poured

into the groove. The steel was inserted into the groove and slightly rotated to fill the voids and release air bubbles. The final step involved flushing the excess epoxy to align with the outer surface of the wood. In accordance with the manufacturer's instructions, the epoxy was left for seven days to cure and achieve its full strength after casting. The completed specimens are shown in Figure 3.8, following the casting of the epoxy and placement of the strain gauges.

a) Bottom view b) Top view

Figure 3.8: Reinforced glulam beam.

3.4 Beam configurations and test set-up

A total of eight glulam specimens were reinforced and tested statically with steel rebar and plate reinforcements. The 15M rebar and plate reinforcements were selected to have almost similar cross-sectional areas, resulting in nearly identical reinforcement ratios. This selection is meant to reduce the variability between the configurations and focus the findings on the effect of the reinforcement shape. The reinforcement ratios were determined by dividing the area of the steel by that of the glulam cross-section, while considering the reduction in cross-section due to the grooves area from the total glulam beam section, as reported in Table 3.2.

Table 3.2: Reinforcement ratio.

Reinforcement	Cross-sectional area (mm^2)	Reinforcement ratios (ρ)
10M	100	0.8%
15M/Plate	200 mm^2	1.6%
20M	300 mm^2	2.5%

Although the reinforcement ratio exceeded the maximum efficient reinforcement of 2% recommended by (Barragán and Jacob, 2007) in order to limit the possibility of shear failure, the selected value was investigated to validate this concept and detect whether shear failure would occur. Investigating higher reinforcement ratios or rebar sizes may not be feasible while keeping adequate spacing between rebars as well as the edge distance between the rebar and wood. The configurations for the tested beams are shown in Figure 3.9, where the nomenclature followed in the naming of the specimens includes assigning reinforced beams a letter R for the static beams group, while the letters B or S indicate whether the location of the reinforcement is at the bottom (tension face) or side of the beam, respectively. The nomenclature for rebar is represented by letter

"M", followed by the rebar diameter size as 10, 15 and 20 mm, while for the plate, it is "PL". A similar number of glulam beams were reinforced with rebar and plates reinforcements, and these specimens were assigned to the letter D instead of R for the dynamic beams group. The reinforcement summary for all beams is shown Table 3.3.

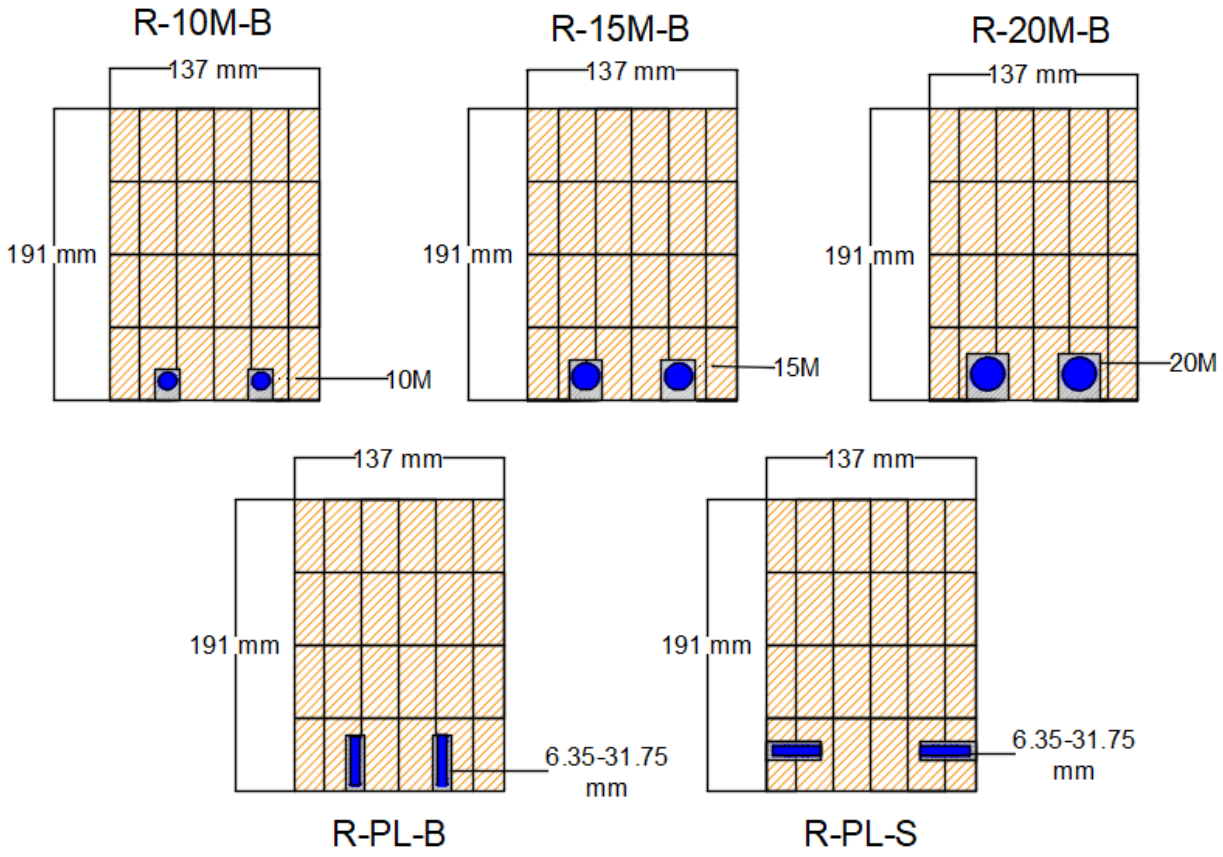

Figure 3.9: Glulam beam configuration.

Table 3.3: Reinforcement summary for all reinforced beams.

Cross Section	Specimen ID	Reinforcement Type	Reinforcement Size	Total Reinforcement Area (mm²)	Reinforcement Ratio (ρ)
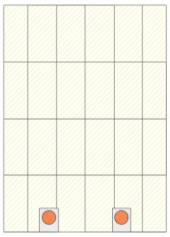	R-10M-B	10M Rebar	10M	100 mm²	0.8 %
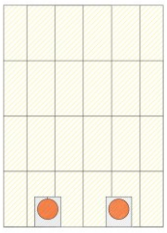	R-15M-B	15M Rebar	15M	200 mm²	1.6 %
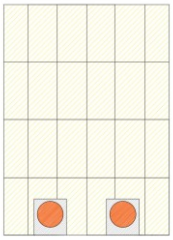	R-20M-B	20M Rebar	20M	300 mm²	2.5 %
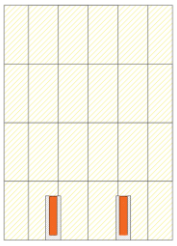	R-PL-B	Steel Plate (vertical)	6.35 × 31.75 mm	200 mm²	1.6 %
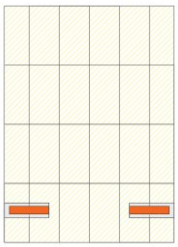	R-PL-S	Steel Plate (horizontal)	6.35 × 31.75 mm	200 mm²	1.6 %

The test setup consisted of a four-point bending, and the boundary conditions were simply supported, which was reproduced by using metal plates and rollers. The load was implemented at the one-third point of the span using a transfer steel I-beam section and manual hydraulic jack. The distance between the two supports was 2235 mm, which allows for sufficient bearing for the 2.5 m long beams and makes this dimension consistent with what is required in the shock tube facility. The load was measured using a load cell, while the mid-span and third-point deflections were measured using displacement cable transducer (DCT), Celesco Model SP2 type. Strain gauges were attached along the steel reinforcements and around the perimeter of the wood section in order to obtain the strain distribution. A data acquisition system (DAS), StrainSmart system 5000 model type, was used to collect and store the data while testing at a rate of one measurement per second. The static test setup is shown in Figure 3.10.

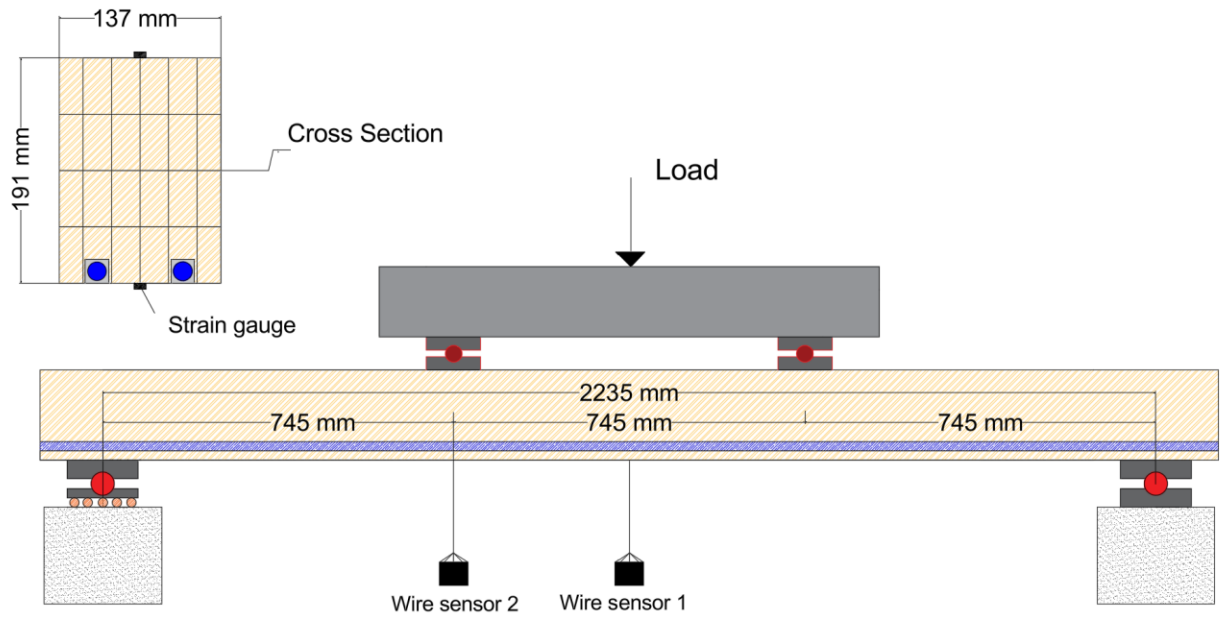

a) Static setup test

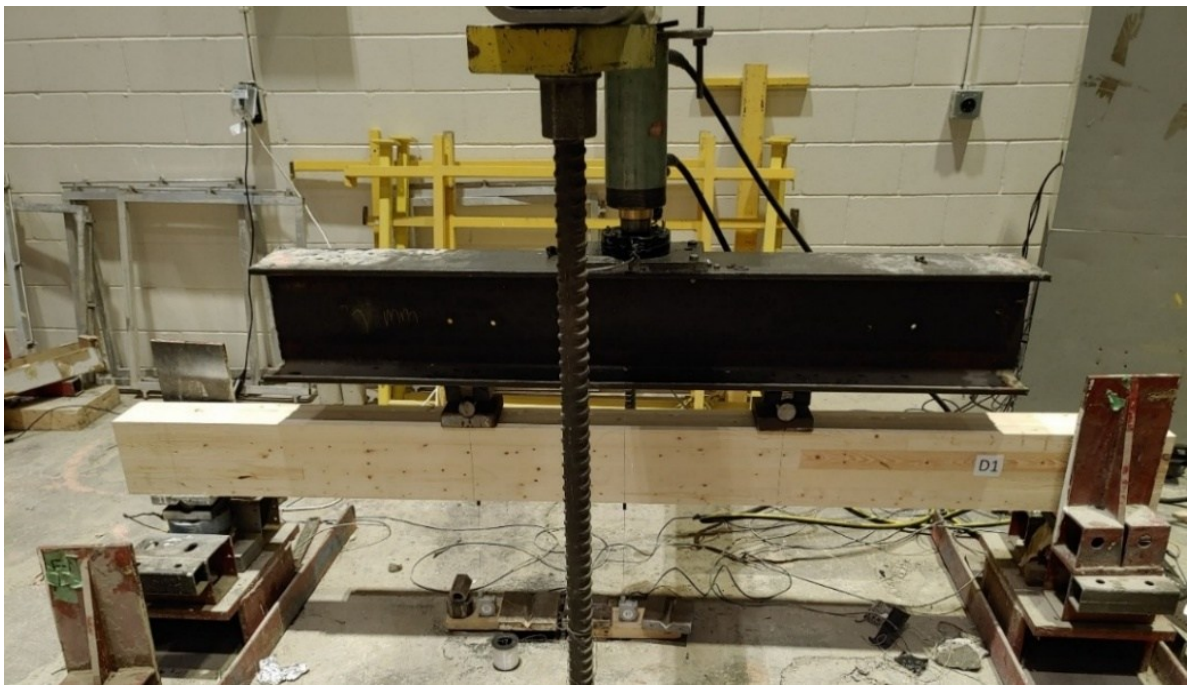

b) Beam under test

Figure 3.10: Static setup test for glulam beam.

3.5 Dynamic Test Set-Up

The dynamic test was conducted using the Shock Tube facility at the University of Ottawa. This apparatus can generate shock waves similar to those resulting from the far-field live detonations of explosives with a reflected pressure of up to 100 kPa and impulse of 2200 $kPa-ms$. The Shock Tube device is made up of three major sections: the driver, diaphragm, and expansion sections, as shown in Figure 3.11. The length of the driver section can range from 305 mm to 5185. Increasing the driver length increases the impulse of the blast shot, such that multiple pressure-impulse combinations can be achieved. After conducting an initial analysis, it was found that a 9ft (2730 mm) driver section would be appropriate to achieve the required pressure and impulse ranges needed in this study. The diaphragm is used as a trigger to release the pressure and create detonation. Two aluminum foil layers (1000-series aluminum type) were used, one at the front and one at the back of the diaphragm, and when the air pressure in the diaphragm is depleted, the air pressure in the driver ruptures the aluminum foils and propagates along the expansion section. The intensity of pressure in the driver section can be controlled by the numbers and thicknesses of foils that are used in each layer. The shock tube is equipped with air pressure vents at the front to release pressure, prevent internal reflections, and generate negative pressure. A load transfer device (LTD) in the front of the shock tube' collects the pressure and transfers it to the mounted specimen. This setup and load pattern was successfully used in several studies examining the effect of blast loading on different types of structures such as concrete (Algassem et al., 2017; Njeem et al., 2022; Li and Aoude, 2023), masonry (Ciornei, 2012; Gandia, 2019) and timber structures (Jacques et al. 2014; Viau and Doudak, 2016a; Cote and Doudak, 2019; Lacroix and Doudak, 2018c; Viau and Doudak, 2021b).

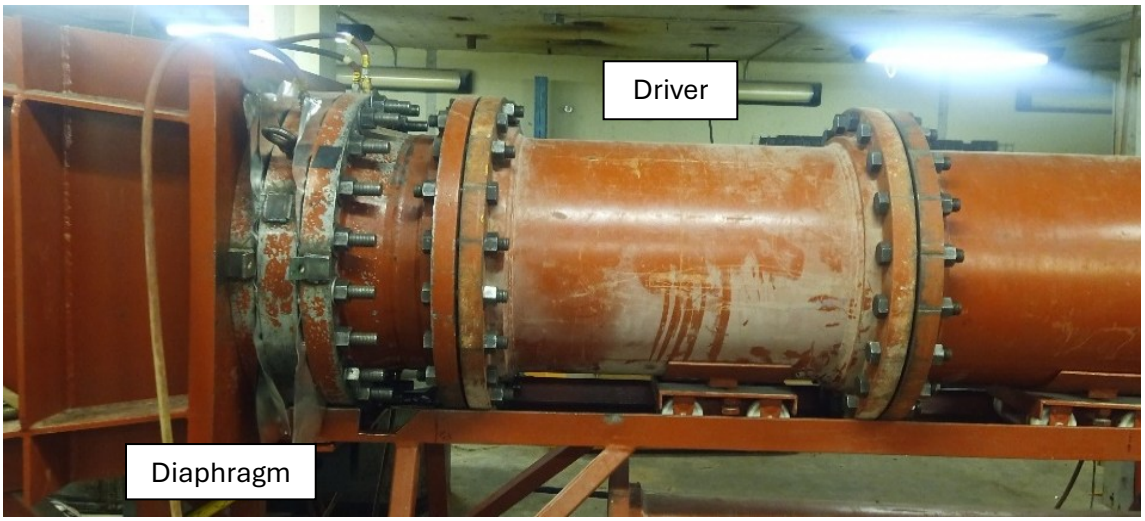

a) Driver and diaphragm.

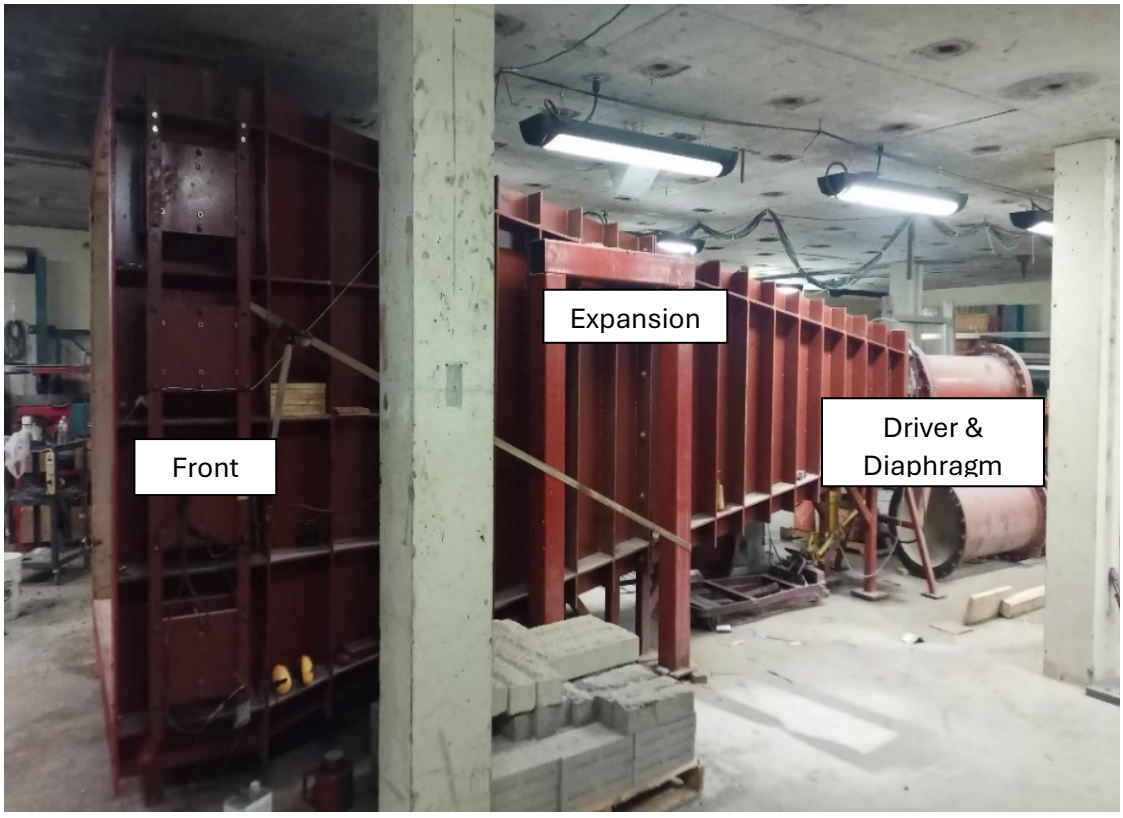

b) Side view

Figure 3.11**:** Shock Tube device components.

The clear spans of the beams were 2235 mm, and the loading pattern was consistent with that used in the static test, as shown in Figure 3.12 through Figure 3.14. The beams were attached to the shock tube device using HSS sections. Threaded rods were used to attach the HSS steel members to the end frame. Steel plates and rollers are used at all loading and support points in order to avoid local crushing of the wood and to allow free rotations at those points. The mid-span and third-point deflections were measured using high-speed linear displacement sensors (LDS), model CLWG-300-NC4. The movement of the shock tube device was also measured to eliminate such movement from the displacement of the beams. The reflected pressure-time history of the shock tube wave was recorded using two piezoelectric pressure sensors placed on the bottom and side of the shock tube opening. Furthermore, the measured data were captured utilizing a high-speed DAS system (Yokogawa SL1000 model) operating at a sampling rate of 100,000 samples per second. Moreover, two high-speed cameras, with a recording frequency of 2000 frames per second, were used to observe the structural response and identify the beam's failure mode. The cameras were controlled with Phantom Camera Control (PCC) software. The cameras were also connected to the piezoelectric pressure sensors through the DAS system. When the shock wave reaches the front of the shock tube, the pressure sensor acts as a trigger and sends a signal to the DAS system to start recording the displacement and reaction responses.

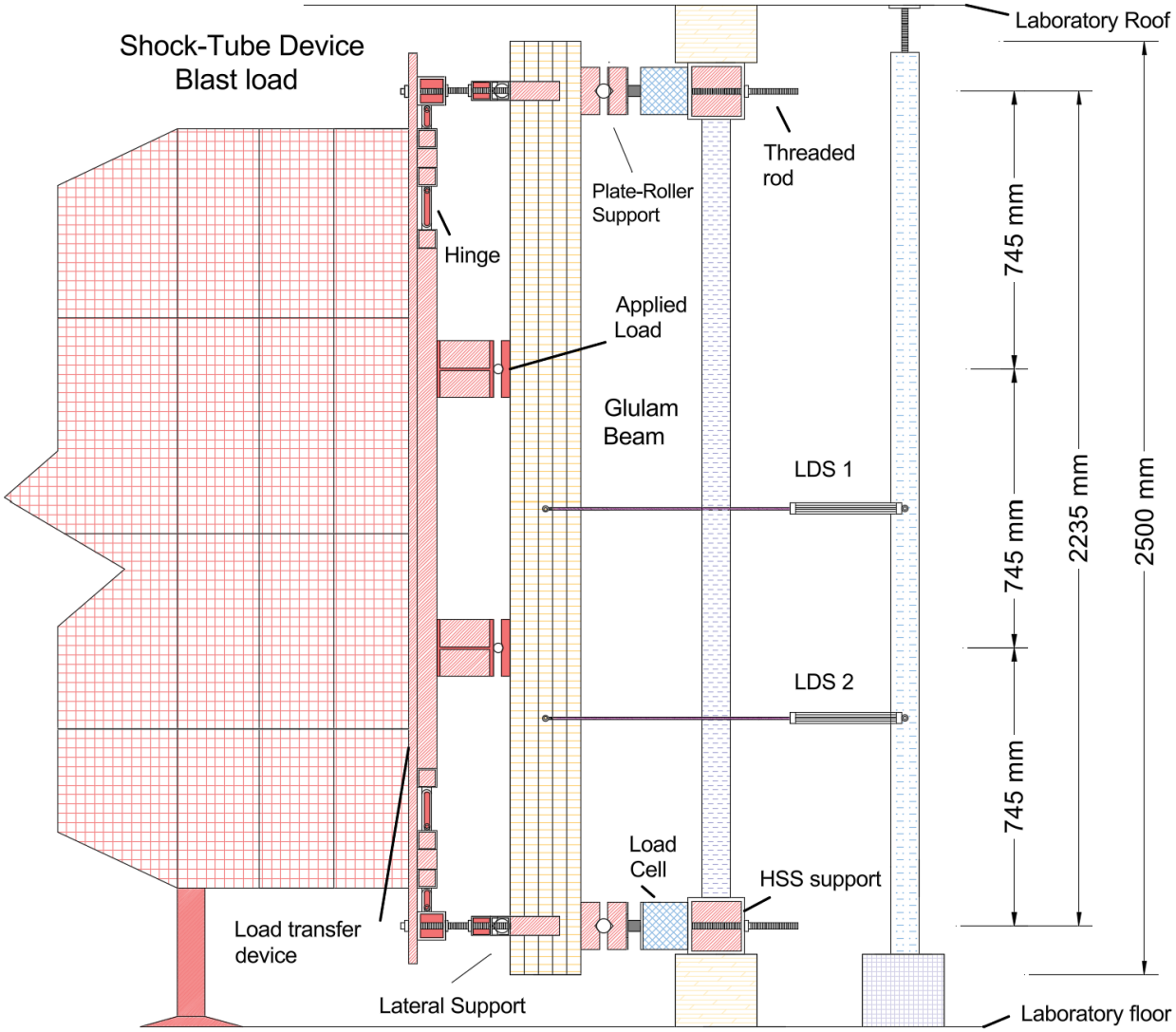

Figure 3.12: Side-view shock tube set-up

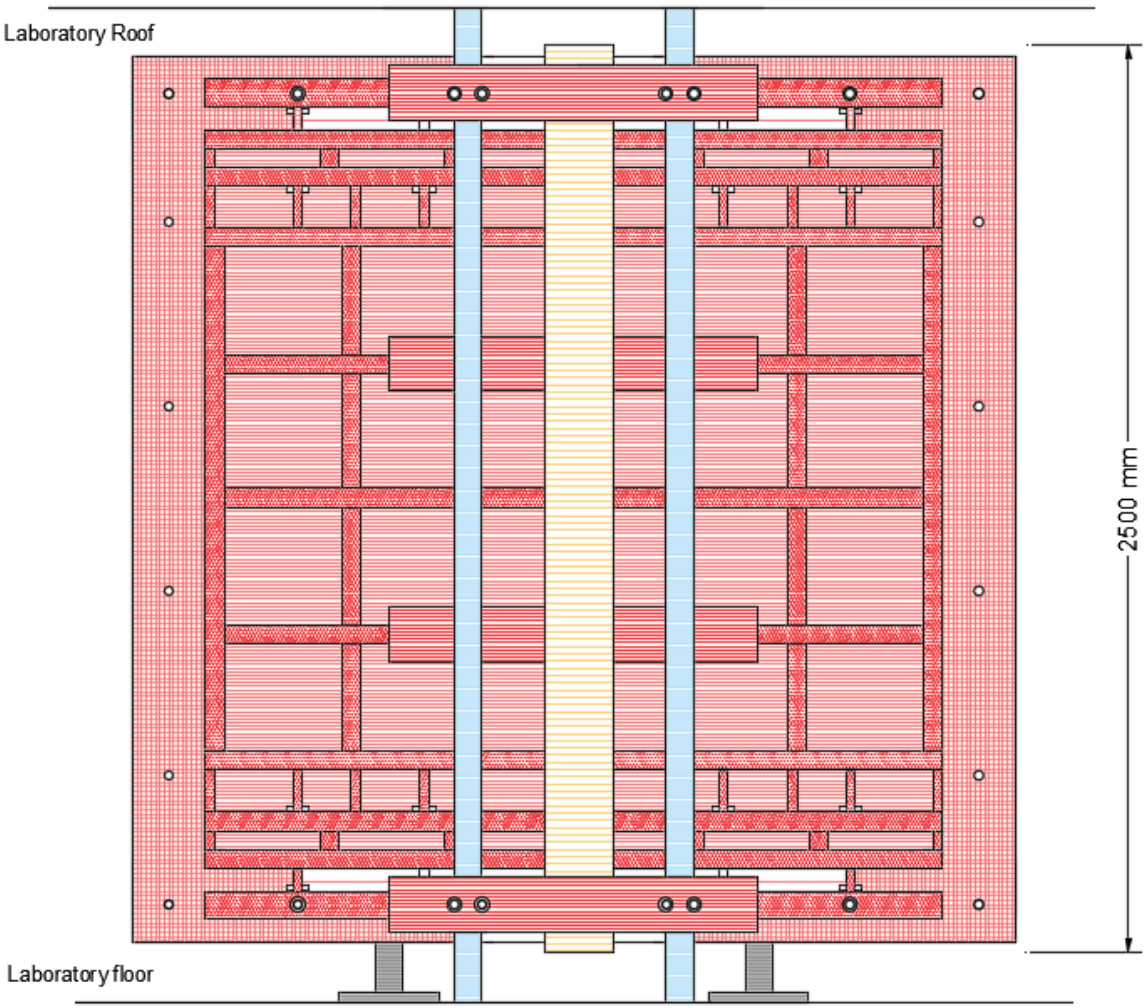

Figure 3.13: Front-view shock tube set-up

Figure 3.14: Full-view shock tube set-up

As illustrated in Figure 3.14, wood blocks and two steel posts were used to securely position and stabilize both the load cells. The supports were tightened using two screws at the ends of each steel columns. Steel brackets were used as protective covers for the displacement sensor to prevent damage

CHAPTER FOUR: EXPERIMENTAL RESULTS

4.1 General

This chapter presents the results of the non-destructive tests conducted prior to the reinforcement of the glulam beams, as well as the outcomes of the destructive tests carried out after the beams were reinforced. The experimental results, such as displacements, forces, and strains from the static and dynamic tests, are presented in this chapter. The detailed data for the static and dynamic destructive tests are presented in Appendices B and C, respectively.

4.2 Static test results

Prior to testing the specimens to failure, non-destructive static tests were performed on all specimens before reinforcing them. The results of these tests are reported in Table 4.1 and include the stiffness (*K*) of the beam as well as the apparent modulus of elasticity (MOE).

Table 4.1: MOE of the beams.

Beams	K (N/mm)	MOE (MPa)
Unreinforced	4323	11105
R-10M-B1	4697	12067
R-10M-B2	4388	11273
R-15M-B1	4708	12095
R-15M-B2	4990	12820
R-PL-B1	4582	11771
R-PL-B2	4848	12455
R-PL-S1	4775	12268
R-20M-B1	4741	12180
Average		12004
COV		0.045

The beams were loaded within the elastic range to determine the MOE. The MOE was determined by obtaining stiffness from the experimental force-displacement curves using Equation 4.1. The average value of MOE obtained from the glulam beam specimens was 12004 MPa with a coefficient of variation (COV) of 0.045. The value of MOE is observed to be close to that reported by the manufacturer value which equals 12400 MPa, while the average experimental shear-free modulus of elasticity (E_{sr}) is 13326 MPa as illustrated in Appendix A. The determination of the K for the beams before reinforcement is used to compare the stiffness of the beam after reinforcement and E_{sr} is meant to improve knowledge about input material parameters for the model introduced in Chapter 5.

$$MOE = \frac{23\ (K)L^3}{1296\ I} \qquad Eq.4.1$$

Here, K represents the stiffness derived from the experimental load-deflection curve. L denotes the clear span length. I stand for the beam's moment of inertia.

The resulting force-displacement curves for beams reinforced with rebars and plates, as well as for the unreinforced beam, are shown in Figure 4.1.

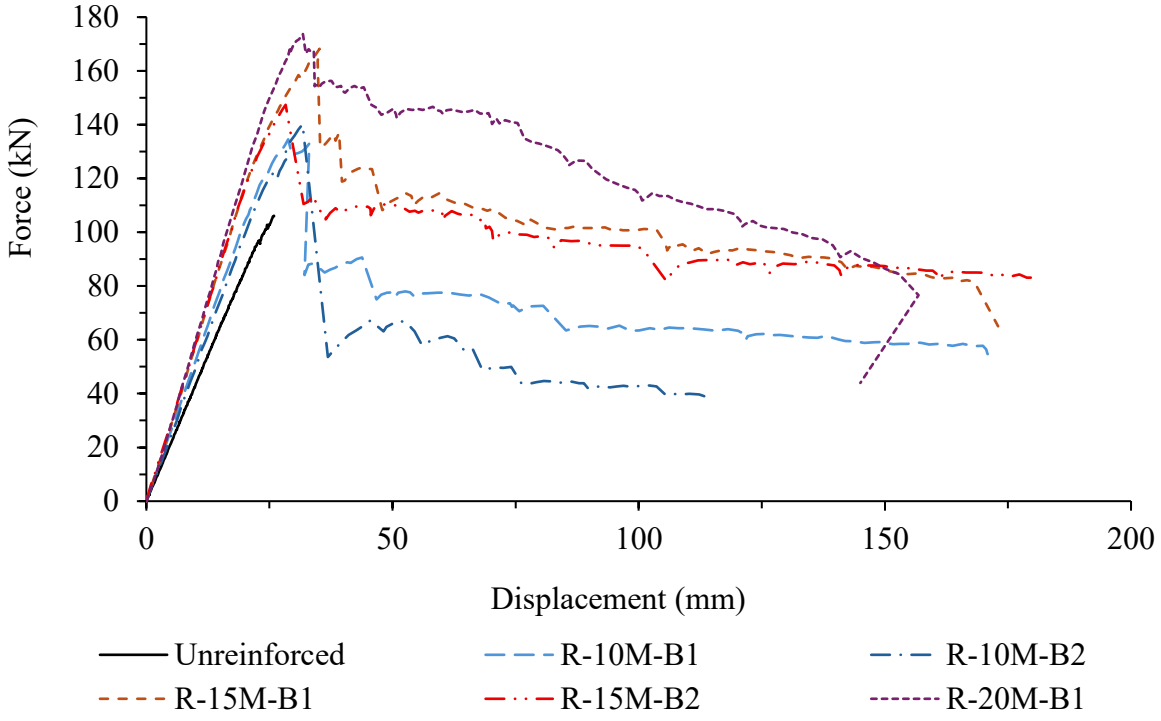

a) Rebars

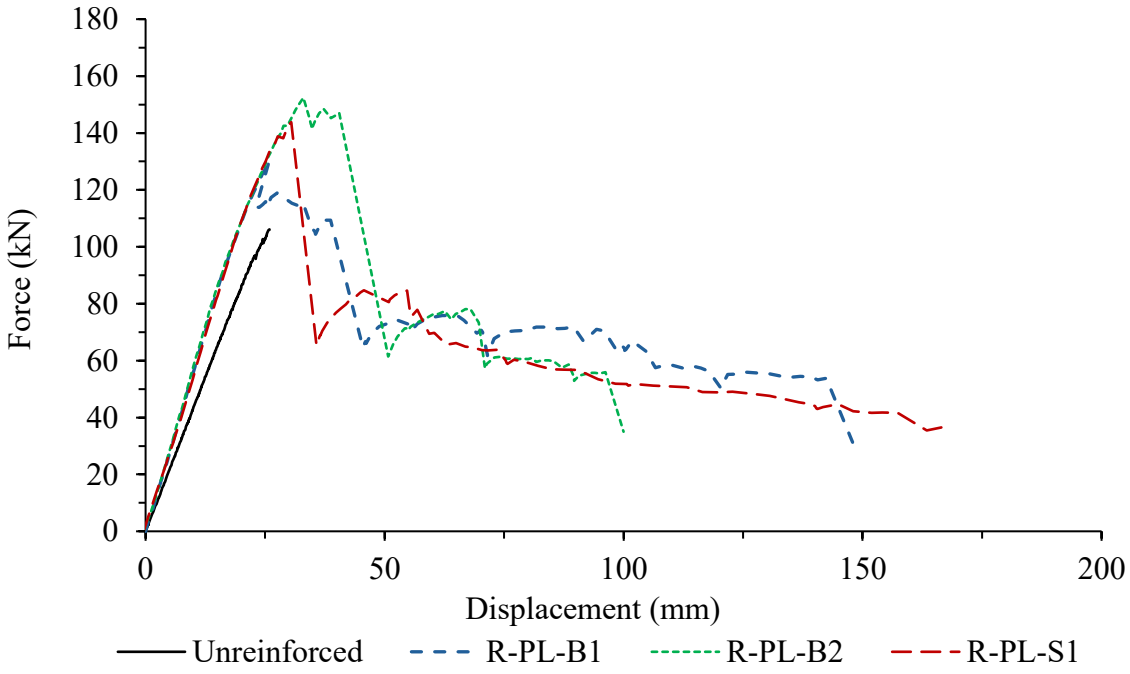

b) Plates

Figure 4.1: Force-displacement curve for reinforced beams.

At the initial region of the force displacement curve, the reinforced beam behaved linearly, similar to the unreinforced beam, however, prior to reaching the maximum force, a nonlinearity was observed, as shown in Figure 4.1. This highlights that the compression fibers at the top of the beam exceeded their crushing stress, followed by the occurrence of tensile cracks leading to a sudden drop in load capacity. Furthermore, as the beam displaces further beyond its maximum resistance, the damage at the compression side of the beam becomes more pronounced. The reinforced beams demonstrated a significantly higher deformation capacity and exhibited crushing or wrinkling of wood fibers on the compression side of the beam compared to the unreinforced ones. This resulted in a shift of the failure mode towards a more ductile failure at the compression face. Figure 4.2 shows the damage at the compression side of the reinforced beams.

a) Before test

b) During test

Figure 4.2: Reinforced beam before and after the test.

Unlike the reinforced beam with steel rebar and plate reinforcements, the unreinforced beam exhibited brittle failure and mainly failed due to a tension crack developed at the bottom surface and propagated along the depth of the beam. The comparison in the failure modes between unreinforced and reinforced beams is shown in Figure 4.3.

a) Damaged unreinforced beam

b) Damaged reinforced beam

Figure 4.3: Failure mode comparisons.

4.2.1 R-10M-B

For specimens reinforced with 10M rebars, the maximum force capacity were reached 134.6 kN and 140.2 kN for specimens R-10M-B1 and R-10M-B2, respectively, while the displacement at maximum resistance reached 28.8 mm and 31.7 mm. Specimens R-10M-B1 exhibited flexural failure mode nearly at the mid of the beam within the applied two-point loads region, while specimen R-10M-B2, where the failure at maximum resistance initiated with a shear crack. Moreover, cracks were also observed to occur at finger joints in some cases. Cracks were also observed to occur along the glue line of the beam mainly near the mid span of the beam. The epoxy material performed well, with no de-bonding or slippage observed between the wood and rebar at the beam ends during the test. Any form of debonding was observed to occur near the ultimate failure of the specimens. The failure modes for specimens R-10M-B are shown in Figure 4.4.

a) R-10M-B1

b) R-10M-B2

Figure 4.4: Failure mode for R-10M-B.

4.2.2 R-15M-B

Specimens reinforced with 15M rebars achieved maximum force capacities of 168.2 kN and 147.4 kN for R-15M-B1 and R-15M-B2, respectively, with corresponding displacements at maximum force of 35.2 mm and 28.3 mm. Similar to the R-10M-B specimens, the beams reinforced with 15M rebars exhibited a flexural failure mode near mid-span within the two-point load application region. Cracks were also observed in some instances at the finger joints and along the glue line, primarily near mid-span. After testing, epoxy debris in the form of chunk pieces was noted. Figure 4.5 illustrates the failure modes for specimens R-15M-B.

a) R-15M-B1

b) R-15M-B2

Figure 4.5: Failure mode for R-15M-B.

Specimens R-15M-B exhibited highly ductile failure modes, characterized by flexural and compression failures, including crushing, wrinkling, and buckling of wood fibers on the compression side of the beam, as illustrated in Figure 4.5. In specimen R-15M-B2, slip failure occurred near the ultimate failure, initiating at the beam's end and propagating along the glue line, as shown in Figure 4.6. The rebar slips at the end of R-15M-B2 reached 13.6 mm.

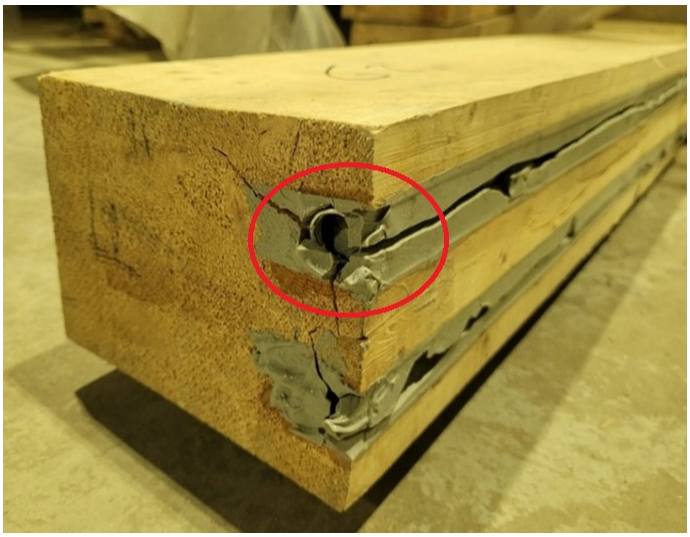

Figure 4.6: Slip failure for R-15M-B2.

4.2.3 R-20M-B

Specimen R-20M-B achieved a maximum force of 173.7 kN, with a displacement at the peak force of 31.8 mm. During testing, the specimen exhibited substantial damage and deformation capacity, particularly on the compression side, where crushing, wrinkling, and buckling of wood fibers were prominently observed. Figure 4.7 shows the damage sustained by specimen R-20M-B1 on the tension and compression sides of the beam. Although initially expected to fail in shear due to its high reinforcement ratio, the specimen reached full capacity and failed in a flexural compression

mode, as shown in the figure. The epoxy material performed effectively, with no evidence of slippage between the wood and rebar at the beam ends.

a) Compression side

b) Tension side

c) Front view

Figure 4.7: Failure mode for R-20M-B1.

4.2.4 R-PL-B & S

For specimens reinforced with plates, the maximum force capacities reached 130.5 kN, 152.4 kN, and 143.8 kN for specimens R-PL-B1, R-PL-B2, and R-PL-S1, respectively, with corresponding displacements at maximum force of 25.9 mm, 33.5 mm, and 30.9 mm. Similar to beams reinforced with rebars, specimens R-PL-B exhibited a flexural compression failure mode on the top side, with fiber crushing and buckling near mid-span within the two-point load region. Additionally, cracks were observed in some cases at the finger joints and along the glue line, primarily near mid-span. After testing, epoxy debris was observed in chunk pieces after the test. Figure 4.8 illustrates the failure modes for specimen R-PL-B1.

a) Front view

b) Compression side

Figure 4.8: Failure mode for R-PL-B1.

In contrast to the other beams reinforced with plates (specimens R-PL-B), specimen R-PL-S1 exhibited a shear crack failure at the point of maximum resistance. Following this, the beam continued to deflect as cracks developed on both the tension and compression sides. The deformation of specimen R-PL-S1 is depicted in Figure 4.9.

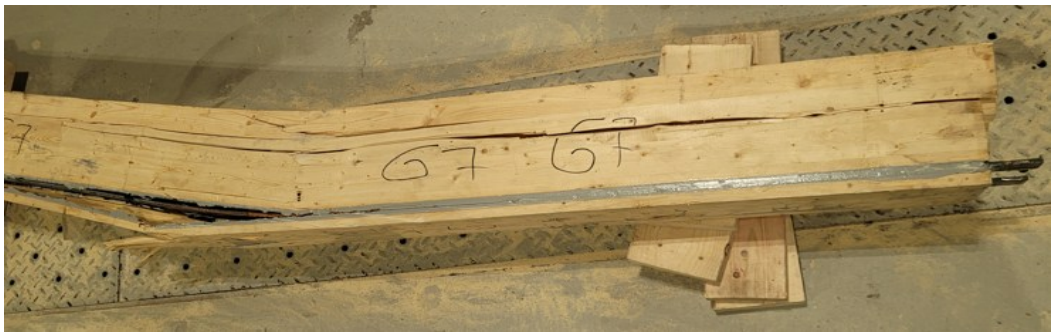

a) Top view

b) Side-front view

Figure 4.9: Failure mode for R-PL-S1.

All beams reinforced with plates also exhibited slip damage and failure between the reinforcement and the wood or between the reinforcement and epoxy layer at the end sides of the beam near ultimate failure. Figure 4.10 shows the slip failure for specimens R-PL-B.

a) Specimen R-PL-B1

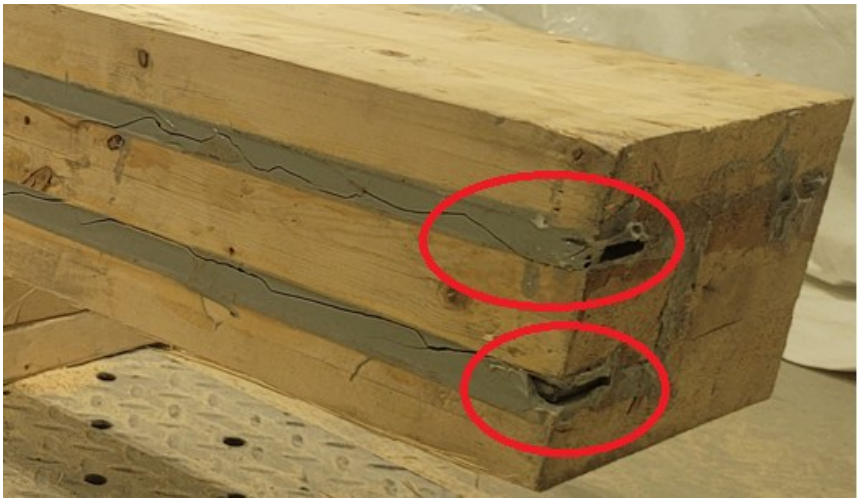

b) Specimen R-PL-B2

Figure 4.10: Slip failure beams reinforced with plates.

The slip for beams reinforced with plates ranged from 3.6 mm for specimen R-PL-S1 to 36.6 mm for specimen R-PL-B1. Beams reinforced with plates were more prone to slip failure compared to those reinforced with rebars. This is likely attributable to the ribbed surface of the rebar, which enhances bond strength through mechanical interlock.

4.3 Static test summary

The results from the destructive static tests are presented in Table 4.2, and include maximum force, stiffness, displacement, and strains data. The K_s represents the stiffness derived from 10% to 40% of the experimental load-deflection curve. The modulus of rupture (MOR) of the unreinforced beam tested in this study is equal to 48.6 MPa, which closely aligns with the average MOR of 45.6 MPa reported by Lacroix and Doudak (2018b) for glulam beams of a similar grade. The MOR is calculated using Equation 4.2.

$$MOR = \frac{R_{max} L}{6\, S} \qquad Eq.\,4.2$$

Where R_{max} is the maximum force, and S is the section modulus of the beam.

Table 4.2: Summary of the static destructive test.

Specimen	$R_{\max}{}^{a}$ (kN)	$\Delta_R{}^{b}$ (mm)	$\Delta_{at\ 50\%}{}^{c}$ (mm)	μ^{d}	$K_s{}^{e}$ (N/mm)	$R+^{f}$ %	K_s+^{g} %
Unreinforced	106.1	25.9	-	-	4323	-	-
R-10M-B1	134.6	28.8	82.9	2.9	5212	26.8	11.0
R-10M-B2	140.2	31.7	35.3	1.1	5126	32.1	16.8
R-15M-B1	168.2	35.2	158.3	4.5	5951	58.5	26.4
R-15M-B2	147.4	28.3	180.8	6.4	5787	38.9	16.0
R-PL-B1	130.5	25.9	104.1	4.0	5660	23.0	23.5
R-PL-B2	152.4	33.5	68.6	2.1	5818	43.6	20.0
R-PL-S1	143.8	30.9	58.6	1.9	5304	35.5	11.1
R-20M-B1	173.7	31.8	149.2	4.7	6286	63.7	32.6

a: Maximum force b: Displacement at $R_{\max}$ c: Displacement at 50% of $R_{\max}$ d: Ductility ratio

e: Stiffness f: Increase in strength g: Increase in stiffness

As shown from Table 4.2, from the results obtained for both rebars and plates, it can be observed that the increase in strength for the reinforced glulam beams ranged between 26.8% and 63.7% compared to the unreinforced reference beams. The stiffness for the reinforced beams also increased by 11.0% to 32.6% relative to the stiffness of each beam before reinforcement. The highest increase in stiffness and strength was for the beam reinforced with 20M rebar with a value of 63.7% and 32.6% for strength and stiffness, respectively, followed by beam reinforced with 15M rebar (R-15M-B1) with 58.5% and 26.4% as increase in strength and stiffness, respectively, while the highest increase in strength and stiffness for beams reinforced with plates was 43.6% and 23.5% for specimens R-PL-B2 and R-PL-B1 respectively. For the beam reinforced with 10M rebar, the highest increase in strength and stiffnesses was 32.1% and 16.8%, respectively, while the lowest increase in strength was for specimen R-PL-B1 with a value of 26.8%, and while the lowest increase in stiffness was for specimen R-10M-B1 with a value of 11.0%.

The post-peak behaviour and ductility ratio for the reference beam were negligible since the reduction in strength after reaching peak strength was more than 75%. In contrast, the reinforced beams exhibited significant improvement in the post-peak behaviour. The ductility of the reinforced beams was calculated by dividing the post-peak displacement at 50% of maximum force by the displacement at the peak load of the beam. The choice of using the peak load was made since “yield” point was very close to the peak and more uncertainty was expected to be associated with this value. The 50% threshold was proposed by (Lacroix and Doudak, 2018c) for reinforced beam configurations with GFRP. Based on this definition, the ductility of the reinforced beams ranged between 1.1 and 6.4. Specimen R-15M-B2 showed the highest ductility ratio over all the reinforced beams with a value of 6.4 followed by specimens R-20M-B1 and R-15M-B1 with

ductility ratios of 4.7 and 4.5, respectively. Beams reinforced with plates showed less ductility than beams reinforced with 15M rebar, even though they have the same steel cross-sectional area, with a maximum value of 4.0 for specimen R-PL-B1 followed by specimen R-PL-B2 with a value of 2.1. Specimen R-10M-B1 reinforced with 10M rebar showed ductility with a value of 2.9, while R-10M-B2 was the lowest with a value of 1.1 only.

4.4 Dynamic test results

This section presents the dynamic results of the reinforced beams. Similar to the static beam group, non-destructive static tests were conducted on the dynamic specimens prior to reinforcement to evaluate the increase in stiffness after reinforcement. The results of these tests, including the MOE of the beams before reinforcement, are summarized in Table 4.3.

Table 4.3: MOE of beams tested dynamically.

Beams	K (N/mm)	MOE (MPa)
D-10M-B1	4801	12334
D-10M-B2	4890	12563
D-15M-B1	4361	11205
D-15M-B2	4664	11982
D-PL-B1	4637	11913
D-PL-B2	4588	11787
D-PL-S1	4417	11349
D-20M-B1	4311	11074
Average		11776
COV		0.045

The reinforced beams were subjected to high pressure and impulse using a shock tube device to investigate strain rate effects and evaluate the effectiveness of the NSM reinforcement method for glulam beams under dynamic loading. During the tests, reflected pressure, dynamic force reaction, and displacement were recorded using sensors, as detailed in Chapter 3. Figure 4.11 presents an example of the reflected pressure versus time recorded during a blast shot, along with the corresponding integrated impulse, as described in Chapter 2.

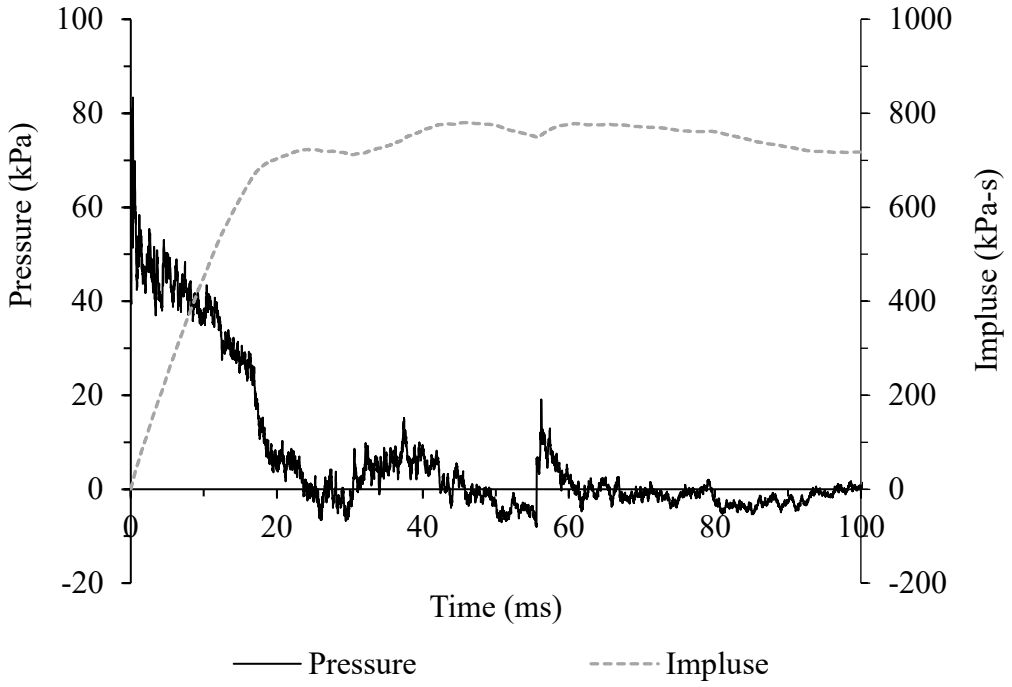

Figure 4.11: Reflected pressure and impulse time history.

Figure 4.12 shows the average dynamic reaction from load cells and displacement versus time for specimen D-10M-B1 recorded during the test, while Figure 4.13 shows the strains recording in tension and compression versus time. Moreover, Figure 4.14 shows the strain recording along with dynamic reaction versus time.

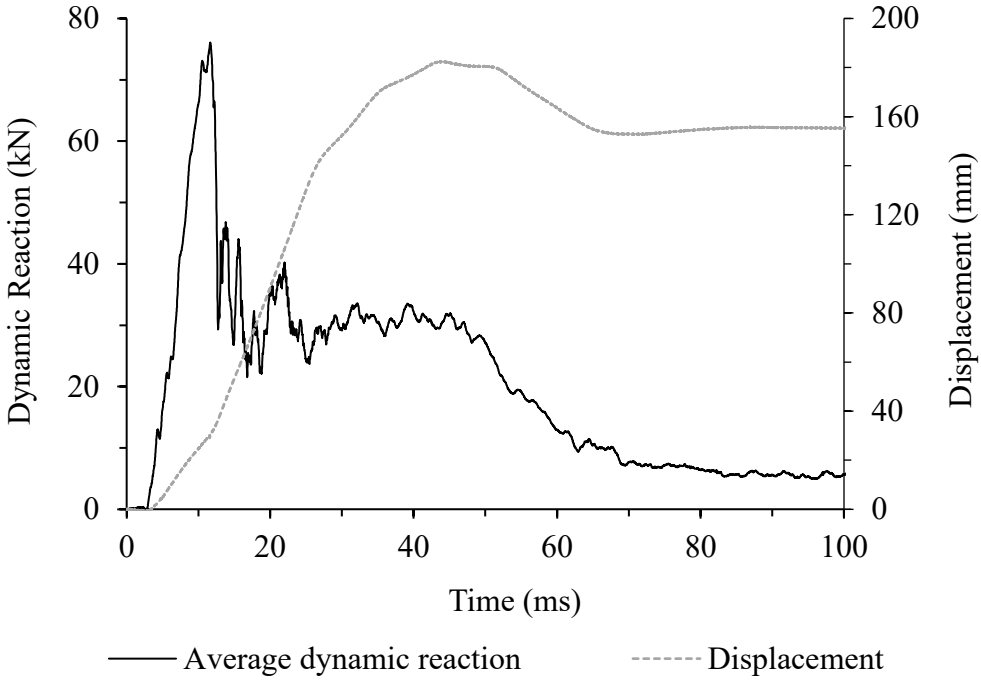

Figure 4.12: Dynamic reaction and displacement time history.

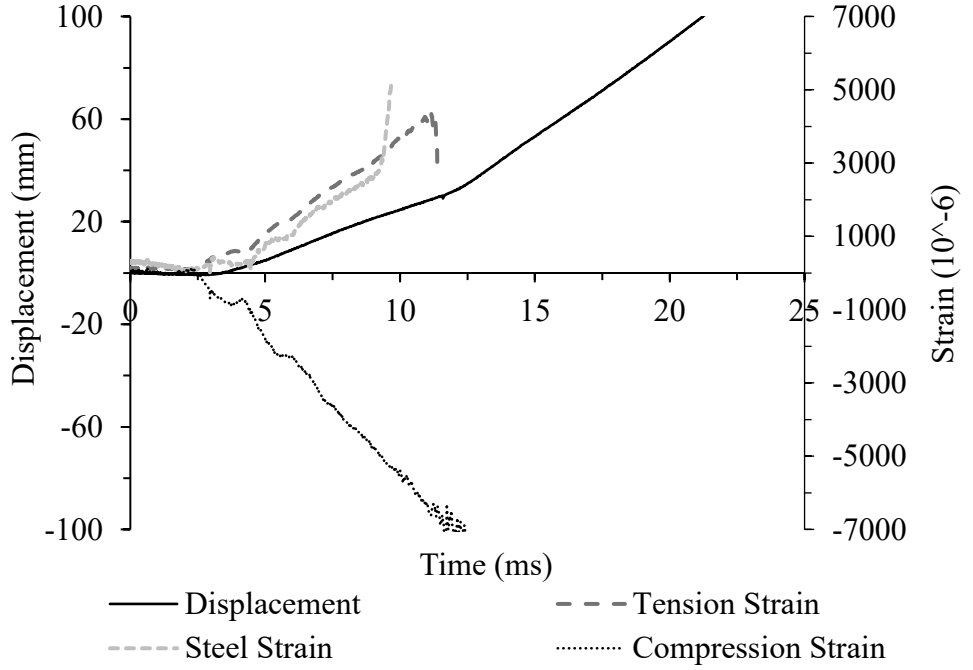

Figure 4.13: Displacement and strain time history.

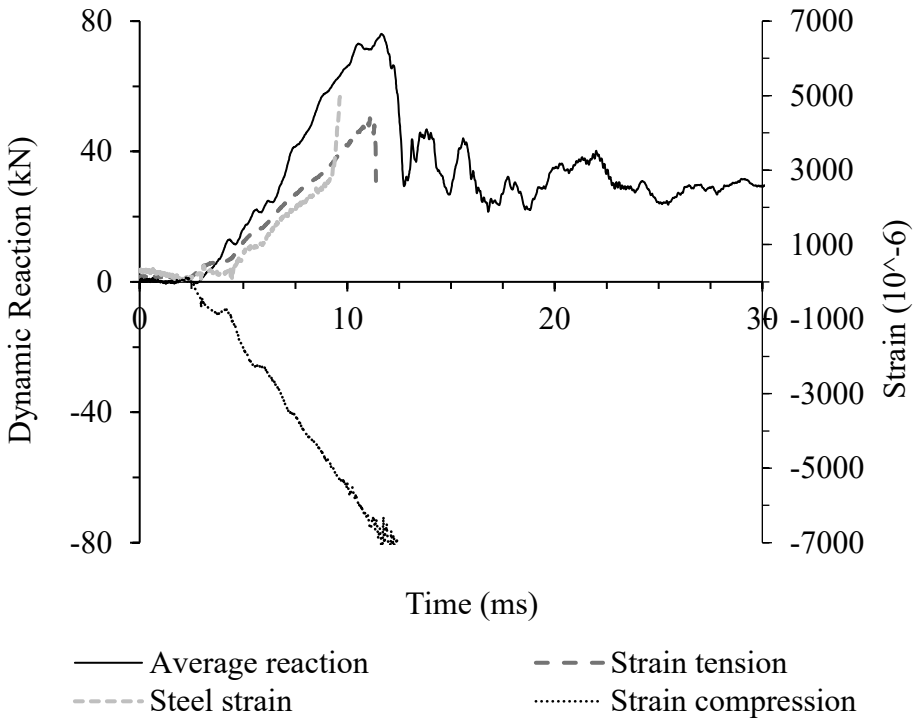

Figure 4.14: Response records sample D-10M-B1.

As illustrated in the above figures, blast loads occur within a fraction of a second, resulting in dynamic responses such as reaction forces, displacements, and strain histories being measured over milliseconds (ms), as shown in Figure 4.14. The dynamic responses for the other reinforced beams are provided in Appendix C. For the dynamic resistance of the beam, the inertia forces should be included in the equilibrium. A simplified method using the SDOF model can be found in (Biggs, 1964). For the shock tube device, the load transfer device (LTD) is also incorporated in the inertia force since its weight is significant compared to the weight of the beam. Equations 4.3 and 4.4 are used to find the dynamic resistance of the beam and derived using an idealized system and dynamic equilibrium by taking the moment where the equivalent inertia force acts. The derivation of these equations can be found in (Lacroix, 2017).

$$R(t) = \frac{6}{L}\left(v(t)x_{eq} + \frac{F(t)}{2}\left(\frac{L}{3} - x_{eq}\right)\right) \qquad Eq.4.3$$

$$x_{eq} = \frac{0.102\,\bar{m}L^2 + 0.290\,m_c\,L}{0.319\,\bar{m}L + 0.870\,m_c} \qquad Eq.4.4$$

Where v(t) is the dynamic reaction, $F(t)$ is the applied force, and L is the clear span. x_{eq} is the distance from the support to the point of application of the equivalent inertia force, where $\bar{m}$ is the mass per length of the sample and m_c is half of the mass of the LTD. The applied force F(t) was found by multiplying the reflected pressure-time history $P(t)$ by the effective tributary area (A) for the LTD, taken as $3.55\ m^2$ (Jacques, 2016).

Figure 4.15 shows the resistance-displacement curves for reinforced beams with rebar and plate reinforcements along with the unreinforced beam obtained from the static beam test and adjusted using a DIF of 1.1, as per CSA S850:23 to account for dynamic strain effects.

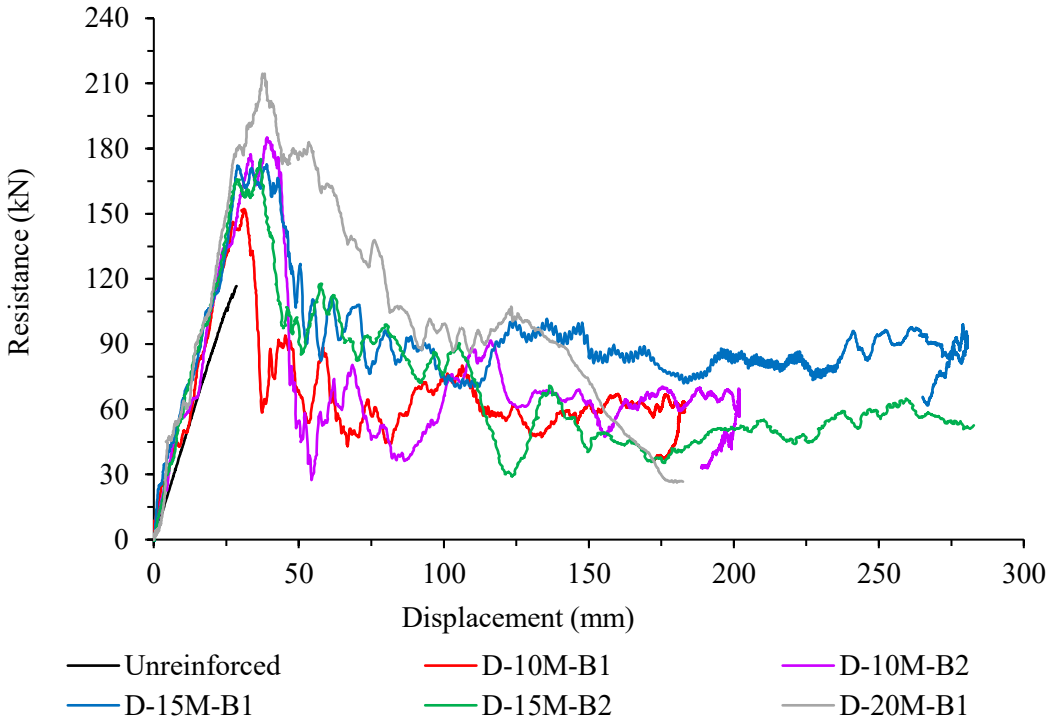

a) Beams reinforced with rebars

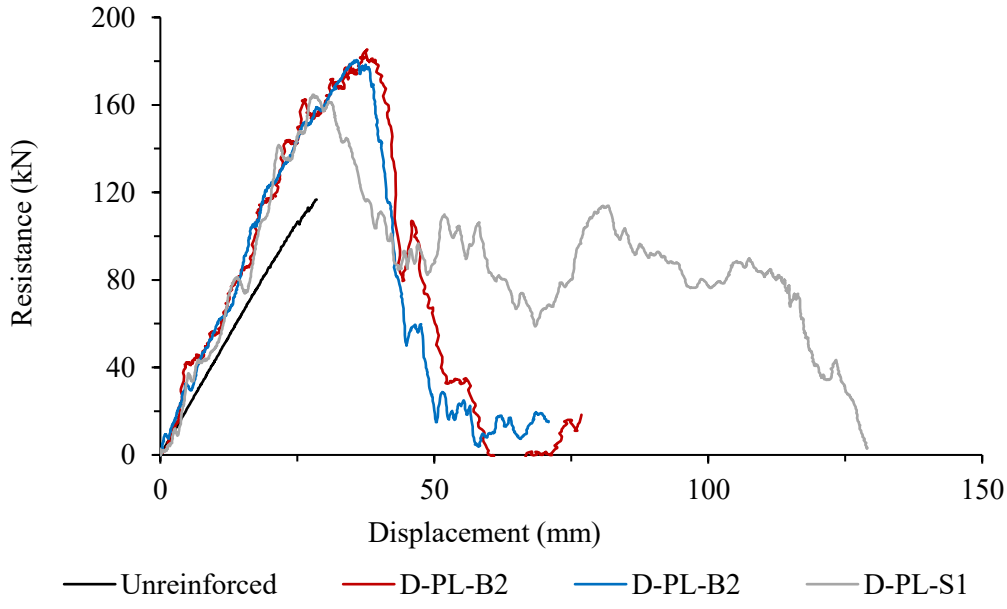

b) Beams reinforced with plates

Figure 4.15: Force-displacement curve for reinforced beams tested dynamically.

All beams were subjected to a single high-intensity blast shot to reach their full-strength capacity, avoiding cumulative damage from multiple shots, which is difficult to detect or analyze. Both reinforced beams with rebars and plates demonstrated significant deformation capacity, with crushing, buckling, and wrinkling of wood fibers on the compression side, ultimately failing in a flexural mode. Detailed results for each specimen are presented below.

4.3.1 Specimens D-10M-B

For specimens reinforced with 10M rebars, specimens D-10M-B1 and D-10M-B2 were subjected to driver pressure of 530.9 kPa and 620.5 kPa, respectively, which resulted in reflected pressure of 83.3 and 88.8 kPa, respectively, and impulse of 780.5 $kPa\text{-}ms$ and 912.4 $kPa\text{-}ms$, respectively. The maximum resistances were $152.1\ kN$ and $185.2\ kN$ for specimens D-10M-B1 and D-10M-B2, respectively, while the time at maximum resistance was $11.7\ ms$ and $11.9\ ms$, respectively, and the displacements at the maximum resistance reached $31.1\ mm$ and $39.1\ mm$ for specimens D-10M-B1 and D-10M-B2, respectively. Figure 4.16 shows specimen D-10M-B1 within the setup before and after the test, while Figure 4.17 also shows the damage to specimen D-10M-B2 after the dynamic test.

a) Before test

b) After test

c) Damaged beam

Figure 4.16: Failure for specimen D-10M-B1.

a) Side view

b) Back view

c) Damaged beam

Figure 4.17: Failure for specimen D-10M-B2.

As presented in Figures 4.16 and 4.17, specimens D-10M-B1 and D-10M-B2 exhibited high deformation capacity, characterized by pronounced crushing, buckling, and wrinkling of wood fibers on the compression side, ultimately leading to flexural failure. On the tension side, failure was accompanied by fracture at the finger joint. Figure 4.18 illustrates the displacement response of specimen D-10M-B1 during a blast test conducted using the shock tube device. The rapid displacement of the beam was recorded with a high-speed camera, as detailed in Chapter 3.

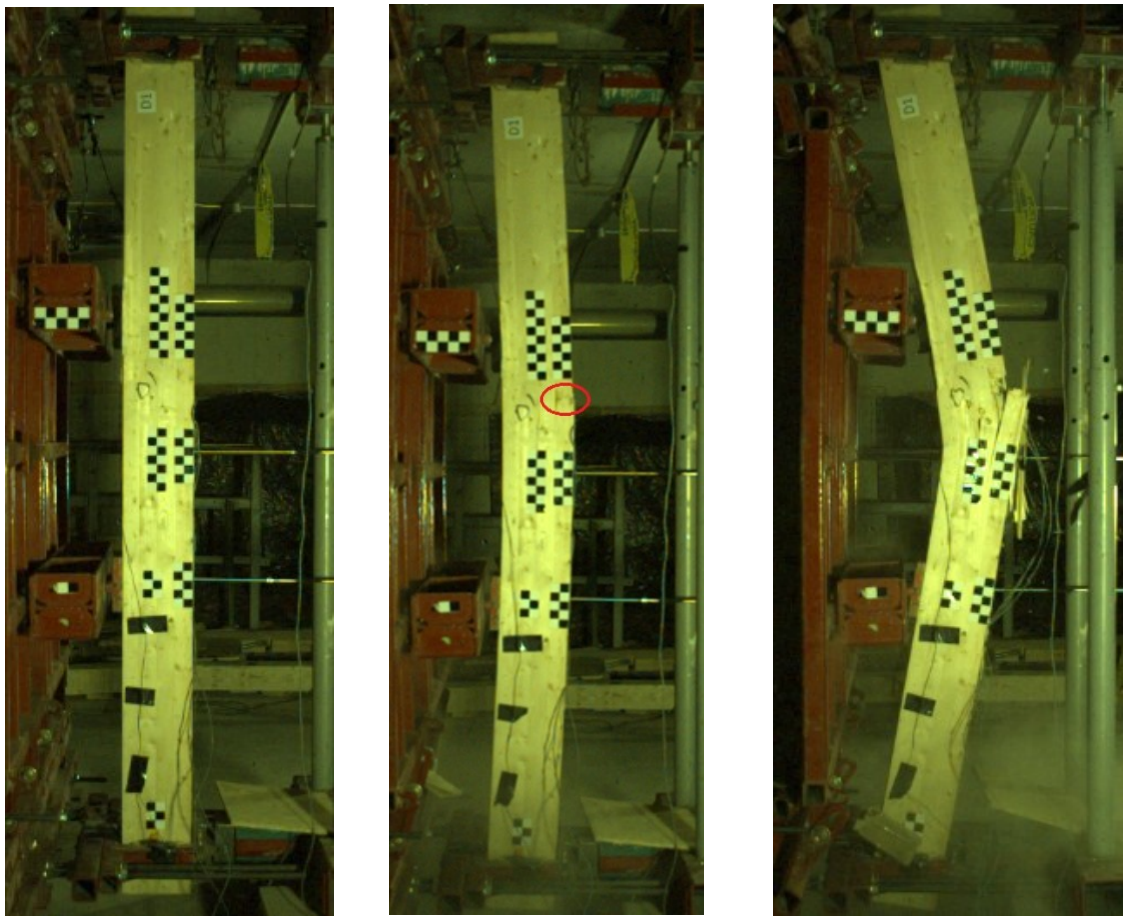

a) At Rest b) At R_{max} c) During the shot

Figure 4.18: Dynamic test pictures for D-10M-B1.

4.3.2 Specimens D-15M-B

For specimens reinforced with 15M rebars, specimens D-15M-B1 and D-15M-B2 were subjected to driver pressure of 758.4 kPa and 717.1 kPa, respectively, which resulted in reflected pressure of 89.3 and 99.9 kPa, respectively and impulse of 1007.4 $kPa\text{-}ms$ and 1012.0 $kPa\text{-}ms$, respectively, The maximum resistances were $172.9\,kN$ and$175.1\,kN$ for specimens D-15M-B1 and D-15M-B2, respectively, while the time at maximum resistance was $10.8\,ms$ for both reinforced beams, and the displacements at the maximum resistance reached $38.9\,mm$ and $36.9\,mm$ for specimens D-15M-B1 and D-15M-B2, respectively.

Consistent with the behavior of the D-10M-B specimens, both D-15M-B1 and D-15M-B2 demonstrated high deformation capacity. Clear signs of crushing, buckling, and wrinkling of wood fibers were observed on the compression side, leading to flexural failure. On the tension side, cracks developed at the finger joints in some cases, with additional cracking propagating along the glue line. Post-test inspections revealed fragmented epoxy debris. Figure 4.19 illustrates the damage sustained by specimen D-15M-B2 following dynamic testing. In general, the epoxy performed effectively, with no evidence of de-bonding or slippage between the wood and rebar, consistent with the response of rebar-reinforced beams tested under static conditions. An exception was observed in specimen D-15M-B2, where a rebar plug-out failure occurred on one side of the beam during the post-peak phase, as shown in Figure 4.20.

a) Side view

b) Back view

c) After test

Figure 4.19: Failure for specimen D-15M-B2.

a) Top view

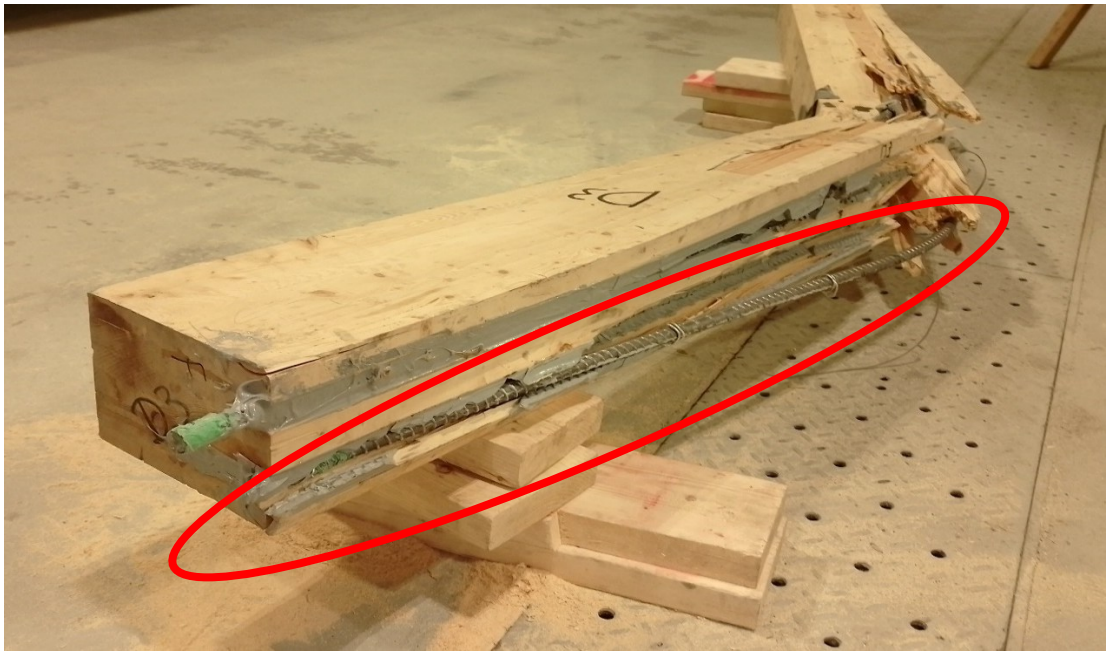

b) Side view

Figure 4.20: Failure of specimen D-15M-B2.

The rebar plug-out failure happened nearly after 110 mm, which associated with a sudden drop in the force resistance as shown in Figure 4.15 for beams reinforced with rebars. The rebar plug-out failure happened due to bonding failure between steel, epoxy, and wood surfaces.

4.3.3 Specimens D-20M-B1

Specimen D-20M-B1 was subjected to high blast pressure to ensure that the beam would fail from the first blast shot with a driver pressure of 758.4 kPa, which resulted in reflected pressure of 105.7 kPa, and impulse of 961.6 $kPa\text{-}ms$. The maximum resistance for specimen D-20M-B1 were reached 214.5 kN. Specimen D-20M-B1 was expected to fail in shear due to its high reinforcement ratio. However, the specimens failed in flexural failure mode as shown in Figure 4.21.

a) Side view b) Back view

Figure 4.21: Failure of specimen D-20M-B1.

As shown in Figure 4.21, specimen D-20M-B1 exhibited high deformation capacity, particularly on the compression side of the beam, as well as crushing and wrinkling of wood fibers. Additionally, cracks were noted along the glue line of the beam. A close view along the depth of specimen D-20M-B1 after the test is shown in Figure 4.22.

Figure 4.22: Failure of specimen D-20M-B1.

4.3.4 Specimens D-PL-B & S

For specimens reinforced with plates, specimens D-PL-B1, D-PL-B2 and D-PL-S1 were subjected to driver pressure of 561.2 kPa, 482.6 kPa and 517.1 kPa, respectively, which resulted in reflected pressure of 72.0 kPa, 78.8 kPa and 73.2 kPa respectively, with impulse of 795.9 $kPa\text{-}ms$, 712.4 $kPa\text{-}ms$, and 755.0 $kPa\text{-}ms$, respectively. The maximum resistances were reached 185.3 kN, 180.5 kN and 164.6 kN for specimens D-PL-B1, D-PL-B2 and D-PL-S1, respectively, while the time at maximum resistance was 12.9 ms, 13.8 ms and 11.8 ms, respectively. Beams reinforced with plates also exhibited high deformation capacity and a ductile flexure failure mode as shown in Figure 4.23 for specimen D-PL-B1.

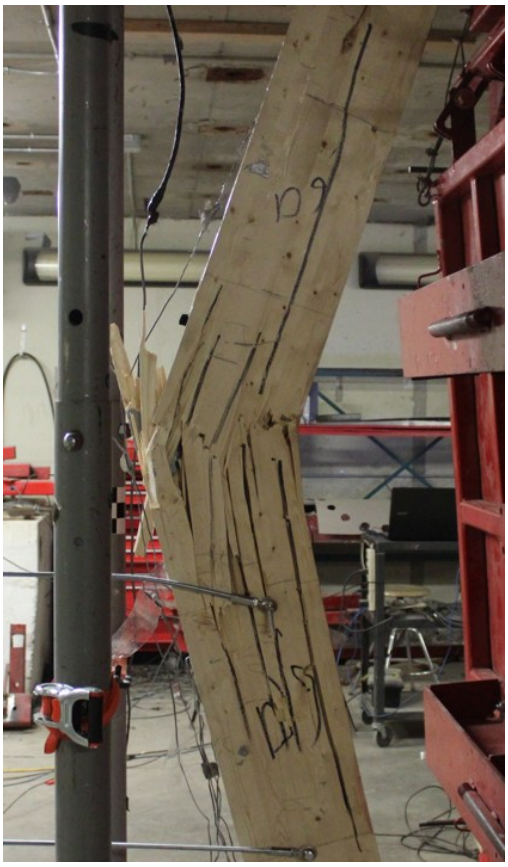

a) Side view

b) Back view

c) After test

Figure 4.23: Failure mode for specimen D-PL-B1.

Beams reinforced with vertical and horizontal plates showed a slip failure at the end sides of the beam as shown in Figure 4.24 for specimens D-PL-B1 and D-PL-B2.

a) D-PL-B1

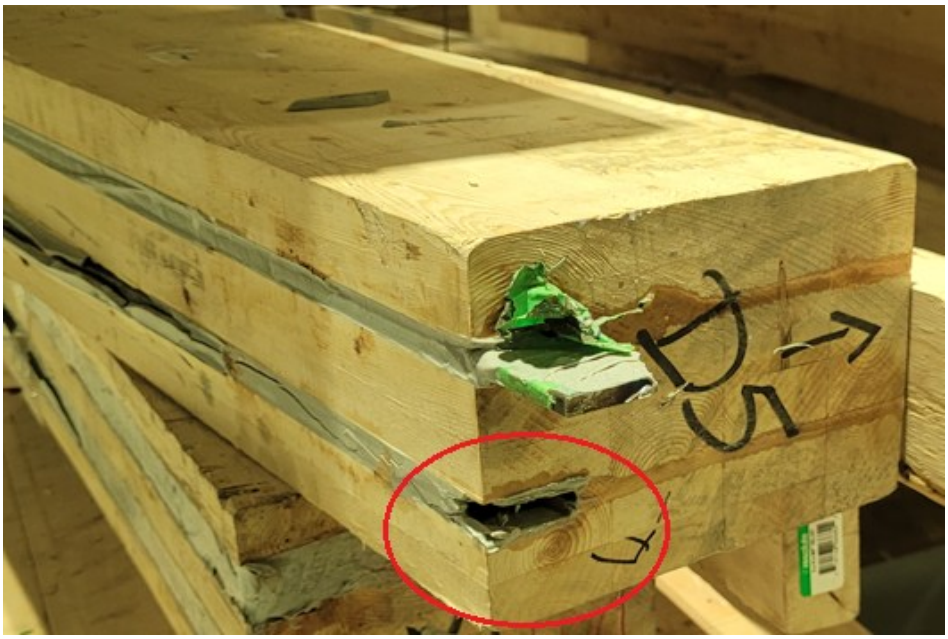

b) D-PL-B2

Figure 4.24: Slip failure mode for beams tested dynamically.

The ultimate slip for beams reinforced with plates, tested dynamically, ranged from 23 mm to 95 mm. Due to limitations in the setup and challenges in tracking slip measurements during the test, it is unclear when the slip occurred for D-PL-B1 and D-PL-B2, during the test. However, it is

likely that the slip happened immediately after the maximum resistance was reached, as indicated by a sudden drop to nearly zero resistance, followed by a slight increase in resistance, as shown in Figure 4.15. On the other hand, beam D-PL-S1, with horizontal plates exhibited better post-peak behavior. The deformation for specimen D-PL-S1 is illustrated in Figure 4.25.

a) Front view

b) Back view

Figure 4.25: Failure mode for specimen D-PL-S1.

It is noteworthy that the damage pattern observed in specimen D-PL-S1 differed from that of the other reinforced beams. This variation is attributed to the slot grooves being routed along the beam's sides, without discontinuity at the bottom surface. As a result, the bottom layer of the beam

detached from the steel reinforcement as an intact unit. A summary of the dynamic test data is presented in Section 4.2.5.

4.5 Dynamic results summary

Table 4.4 presents a summary of the dynamic destructive tests using the shock-tube device including reflected pressure, impulse, maximum resistance, displacements, stiffness, time at maximum resistance, strain in tension and strain rate.

Table 4.4: Summary of the dynamic destructive test.

Specimen	Pa^a (kPa)	I^b $(kPa-ms)$	${R_{\max}}^c$ (kN)	${\Delta_R}^d$ (mm)	${\Delta_{at\,50\%}}^e$ (mm)	${t_{max}}^f$ (mm)	$k^g(N/mm)$	${\epsilon_t}^h$ 10^{-4}	${\dot{\epsilon_t}}^i$ (s^{-1})
Un-reinf.	-	-	116.7	28.5	-	-	-	-	-
D-10M-B1	83.3	780.5	152.1	31.1	60.2	11.4	5174	43.9	0.40
D-10M-B2	88.8	912.4	185.2	39.1	46.6	11.9	5305	66.4	0.56
D-15M-B1	89.3	1007.4	172.9	38.9	280.7	10.8	5623	50.1	0.53
D-15M-B2	99.9	1012.0	175.1	36.9	105.5	10.8	5727	43.0	0.48
D-PL-B1	72.0	795.9	185.3	37.8	47.4	12.9	5846	45.3	0.37
D-PL-B2	78.8	712.4	180.5	35.8	42.7	13.8	5643	48.1	0.35
D-PL-S1	73.2	755.0	164.6	31.0	111.8	11.8	5590	52.8	0.45
D-20M-B1	105.7	961.6	214.5	38.2	85.2	10.8	5954	-	-

a: Reflected pressure b: Impulse c: Maximum Resistance d: Displacement at $R_{\max}$ e: Displacement at 50% of $R_{\max}$
f: Time at $R_{\max}$ g: Stiffness h: Rupture tensile strain i: Tension strain rate

Table 4.5 presents the dynamic test results, including the increase in resistance and stiffness due to the reinforcement, as well as ductility ratios.

Table 4.5: Summary of the dynamic destructive test results.

Beams	μ^a	$R+^b$ %	$k+^c$ %
D-10M-B1	1.9	30.3	7.8
D-10M-B2	1.2	58.7	8.5
D-15M-B1	7.2	48.1	28.9
D-15M-B2	2.9	50.0	22.8
D-PL-B1	1.3	58.8	26.1
D-PL-B2	1.2	54.7	23.0
D-PL-S1	3.6	41.0	26.5
D-20M-B1	2.2	83.8	38.1

a: Ductility ratio b: Increase in strength c: Increase in stiffness

As shown in Table 4.5, the stiffness and strength of reinforced beams with rebars and plates have been greatly increased when compared to the unreinforced beam. The increase in strength ranged from 30.3% to 83.8%, while stiffness increased from 7.8% to 38.1% relative to the beam before reinforcement. The highest increase in stiffness and strength was for specimen D-20M-B1 with 20M rebar with a value of 83.8% and 38.1% for strength and stiffness, respectively, followed by specimens D-PL-B1 and D-10M-B2 with 58.8% and 58.7%, respectively, as increase in strength, while the highest increase for beams reinforced with 15M rebar was 50.0%. The highest increase in stiffness after specimen D-20M-B1 was for specimen D-15M-B1 with a value of 28.9%, while the lowest increase was for D-10M-B1 with 30.3% and 7.8% as increase in strength and stiffness, respectively.

The post-peak behavior of the reinforced beams showed significant improvement compared to the unreinforced beam. The ductility ratio for beams reinforced with rebars and plates ranged from 1.2 to 7.2. The highest ductility value was observed at D-15M-B1 at 7.2, followed by D-PL-S1 and D-

15M-B2 at 3.6 and 2.9, respectively. In contrast, beams reinforced with 10M rebars and vertical plates, D-10M-B2 and D-PL-B2, had ductility values around 1.2. Specimens D-PL-B1 and D-PL-B2 exhibited lower performance compared to their counterparts reinforced with 15M rebar, as their resistance dropped suddenly to zero after reaching maximum capacity, as shown in Figure 4.15. Meanwhile, specimen D-PL-S1, reinforced with horizontal plates on both sides, displayed ductility behavior similar to those reinforced with rebars.

CHAPTER FIVE: ANALYSIS RESULTS

5.1 Material Models

The analytical model developed in this study is based on layered-section analysis. This method divides the beam cross-section into strips in order to determine the moment-curvature relationship for the composite beam. After establishing the moment-curvature relationship, the displacement of the beam is generated by integrating the curvature using the moment area or conjugated beam method. The wood material model used in this study is presented in Figure 5.1, where f_{wc} and f_{wt} are the maximum compressive and tensile stresses, respectively, while ε_{wc} and ε_{wt} are the corresponding strains, respectively. ε_{uc} and f_{uc} are the ultimate compressive strain and stress, respectively. m is the slope of the descending curve until ε_{uc} is reached. E_w is the modulus of elasticity of the wood.

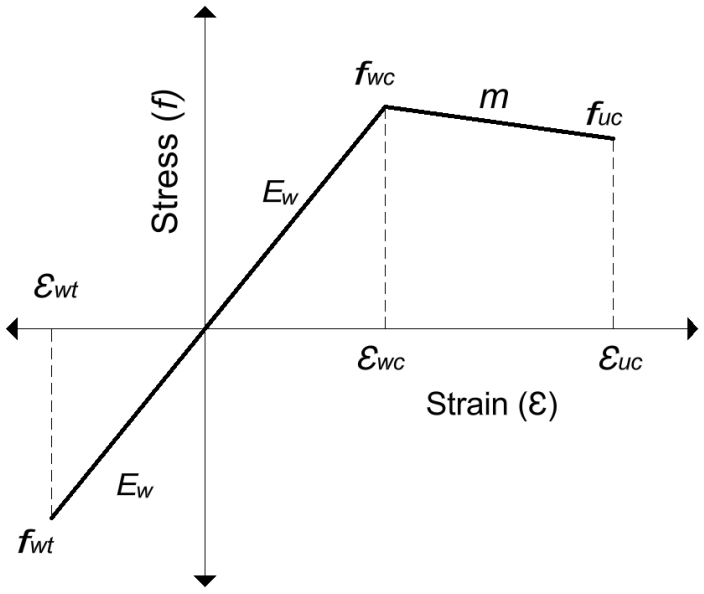

Figure 5.1: Wood material model.

An elasto-plastic material model was implemented for steel, as shown in Figure 5.2, where ε_y and f_y is the yield strain and stress, respectively.

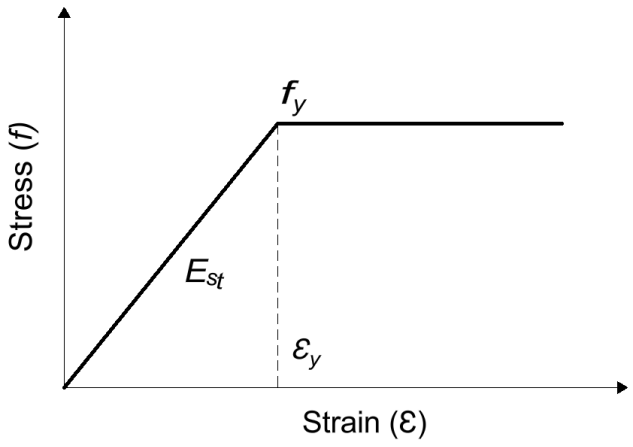

Figure 5.2: Steel material model.

An incremental strain procedure was used to establish the moment-curvature relationship, where at each increment, the strain at depth (z) is obtained using Equation 5.1. The value in Equation 5.1 can be positive or negative depending on whether the material is in compression or tension.

$$\varepsilon(t) = \frac{(c - z)\varepsilon_{top}}{c} \qquad Eq.5.1$$

Where $\varepsilon(t)$ is the strain along the depth, ε_{top} is the top strain, and c is the depth of the neutral axis. The strain at the top of the beam was increased by 0.0001 at each step, and the initial value for neutral axis depth (c) is assumed to be at the mid-height of the beam. According to the Euler-Bernoulli beam theory, the strain distribution throughout the depth of the beam is linear based on the assumption that plane sections remain plane. After calculating the strain values, the stress is determined at each layer based on the wood material model in Figure 5.1. After determining the

stress in the wood and steel sections, the force at each layer is calculated by multiplying the area of the layer strip by the average stress. For steel reinforcement, the force is calculated as a concentrated point load based on the strain at the center of the reinforcement. The sum of the forces from entire wood strips in tension and compression as well as the tension force in the reinforcement must be in equilibrium. If the equilibrium is not satisfied, a new value for c is created, and the procedure is repeated. An Excel solver function was used to perform the iterative procedure. The curvature is calculated by dividing the top strain by the depth (c), and the moment for each layer strip is calculated by multiplying the average force of the strip by the distance from the center of the strip to the location of the neutral axis.

The accuracy of the analysis depends on the incremental strain interval, however, increasing the moment-curvature points also increases the time required to complete the analysis. The calculation process is demonstrated in Figure 5.3. After determining the moment-curvature relationship, the curvature is distributed along the beam and integrated using the moment area method to calculate the maximum displacements at the mid-span of the beam at each value of the incremental moment. The model also considered the shear deflection (Δ_s), detailed in Appendix A.

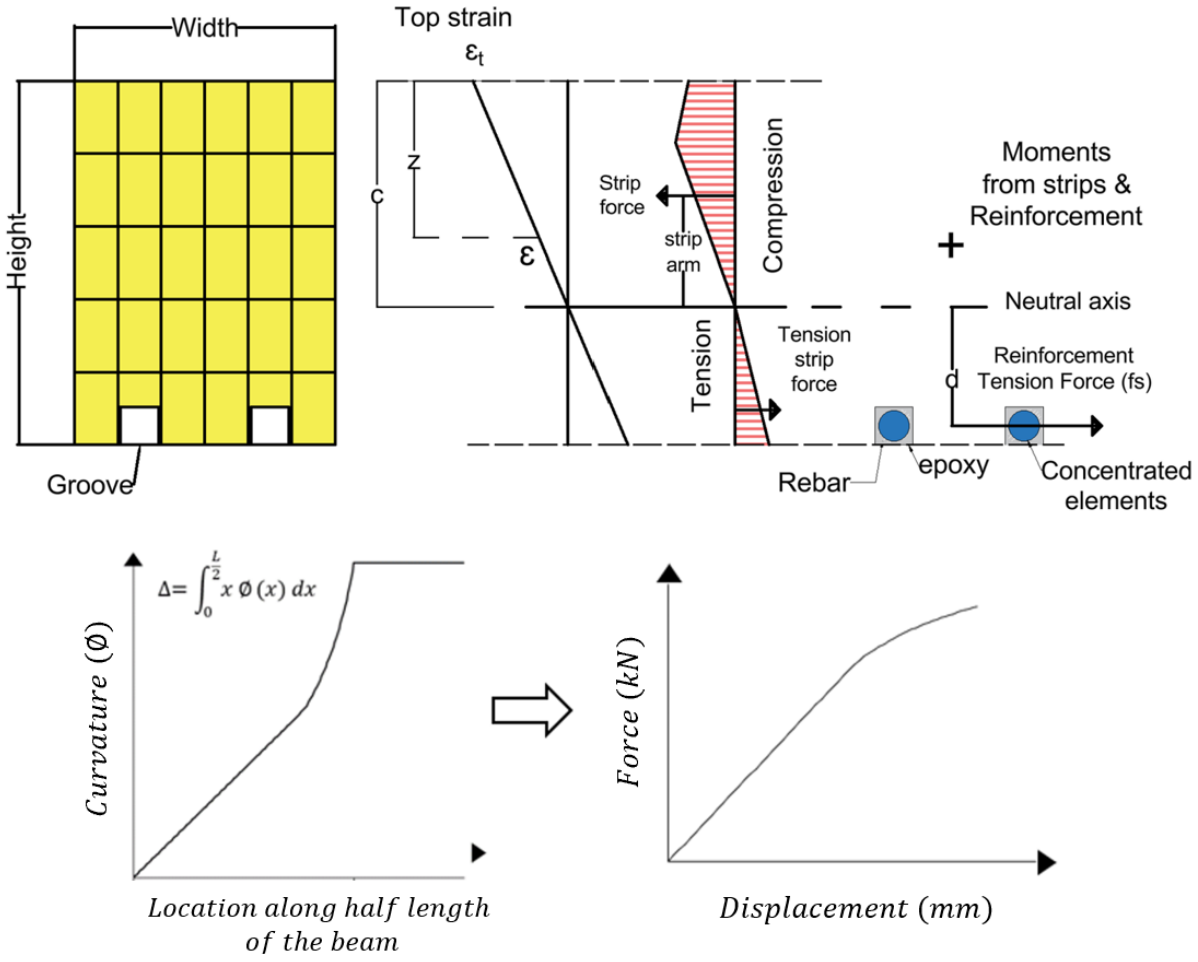

Figure 5.3: Sectional analysis and displacement calculations.

5.2 Analysis results

A software code was created using MATLAB and Excel VBA programs and used to obtain the analysis results for the reinforced glulam beams. A typical moment-curvature relationship is presented in Figure 5.4 for beam R-15M-B2. Figure 5.4 also shows the location where the steel started to yield, and the wood reached its maximum compressive stress.

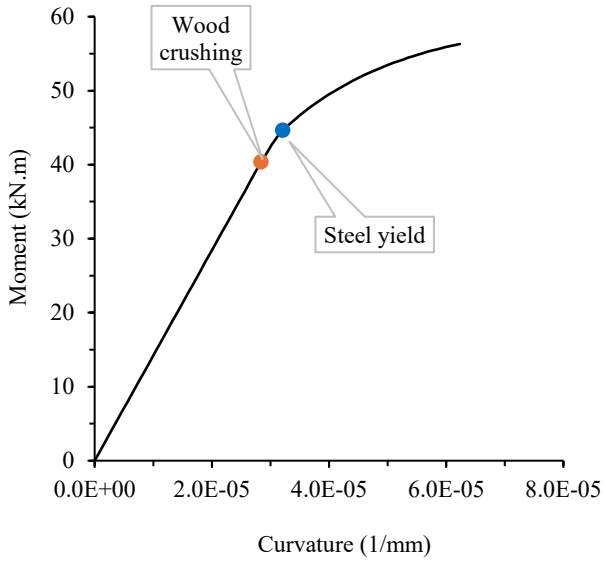

Figure 5.4: Moment and curvature.

For the descending slope in compression (m) (see Figure 5.1), a value of 0.1 was used based on the experimental data of wood samples with similar grade (Lacroix, 2017). A similar value was also found by (Yang et al., 2016a) for Douglas fir glulam and was used by (He et al., 2022). The value of f_{wc} and f_{wt} stresses were based on the coupon experimental test of glulam with a similar grade (Lacroix and Doudak, 2018b). In bending, the extreme fiber tensile stress (f_{wb}) exceeds axial tension (f_{wt}) (Buchanan, 1990). Due to challenges in strain gauge accuracy near failure, f_{wb} was determined by incrementally adjusting strain at f_{wt}, incorporating the experimental E_{sr}, until reaching the failure load of the unreinforced beam, consistent with the methodology followed by (Lacroix and Doudak, 2018b). The material input for wood is shown in Table 5.1, The prediction of the unreinforced beam tested in this study is shown in Figure 5.5.

Table 5.1: Wood strength inputs.

Stress	MPa
f_{wc}	41.9
f_{wt}	43.3
f_{wb}	49.2

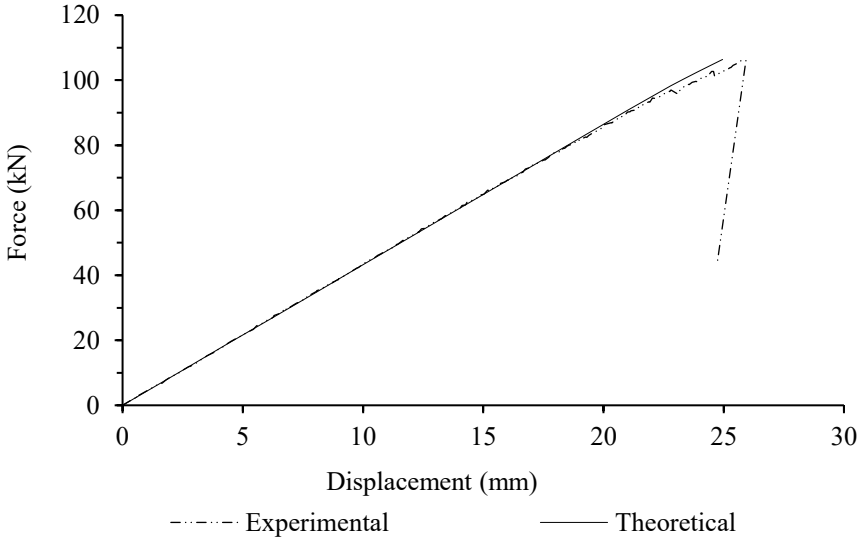

Figure 5.5: Force-displacement curve prediction for unreinforced beam.

In reinforced beams, reinforcement contributes to bridging defects and delaying the failure of the beam. Consequently, the maximum bending stress f_{wb} is increased by a constant factor (α) to account for this improvement (e.g., Gentile et al., 2002; Yang et al. 2016a, and Lacroix and Doudak, 2018c). The value for α varies based on wood quality, reinforcement type, beam stiffness, and adhesive properties. The average value of α for all reinforced beams tested statically was 1.26. Due to challenges in obtaining reliable and accurate data from strain gauges, often caused by premature failure, the theoretical values closely matched the results of only three beams: R-10M-B2, R-15M-B1, and R-15M-B2. Their corresponding theoretical values were 1.25, 1.46, and 1.23, respectively, compared to experimental values of 1.28, 1.44, and 1.27. Previous studies, including

(Gentile et al., 2002) and (Yang et al., 2016a), found a value of α equal to 1.3 for beams reinforced with GFRP or steel rebars, while CFRP plate reinforcement resulted in a higher value of 1.49. In general, greater force capacity in reinforced beams corresponds to higher α values. Figure 5.6 shows the force-displacement curve prediction for specimens R-10M-B2 and R-15M-B2, representing an average prediction for the analytical model.

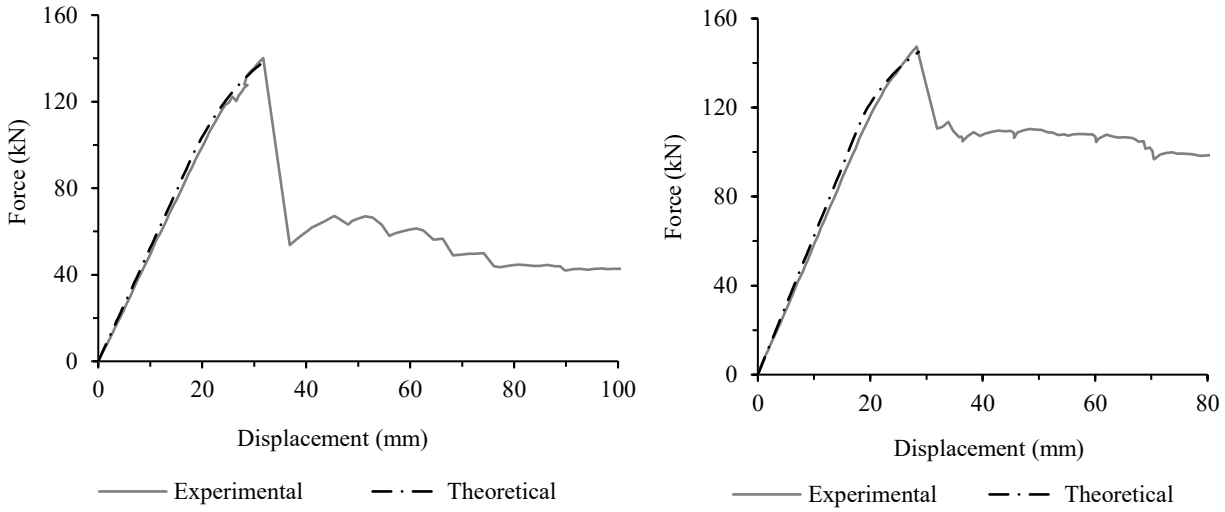

a) R-10M-B2 b) R-15M-B2

Figure 5.6: Force-displacement curve.

As shown in Figure 5.6, the analytical model shows very reasonable agreement with the experimental results based on the overall behaviour of the tested specimens. It can be seen that the strength capacity is predicted with high accuracy, while for the stiffness, the proposed model represents a reasonable agreement. This result is expected since stiffness is notoriously more difficult to predict in wood specimens. The comparison between theoretical and experimental results for reinforced beams is shown in Figure 5.7 for maximum force and its corresponding displacement data, respectively.

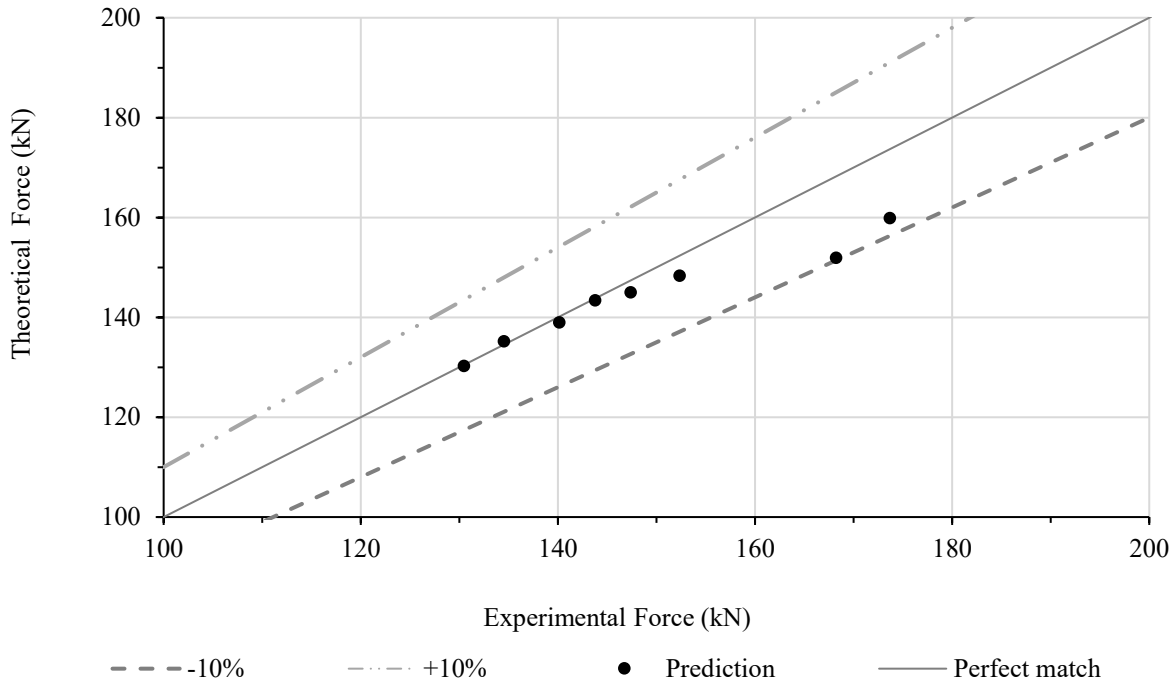

a) Force model comparison

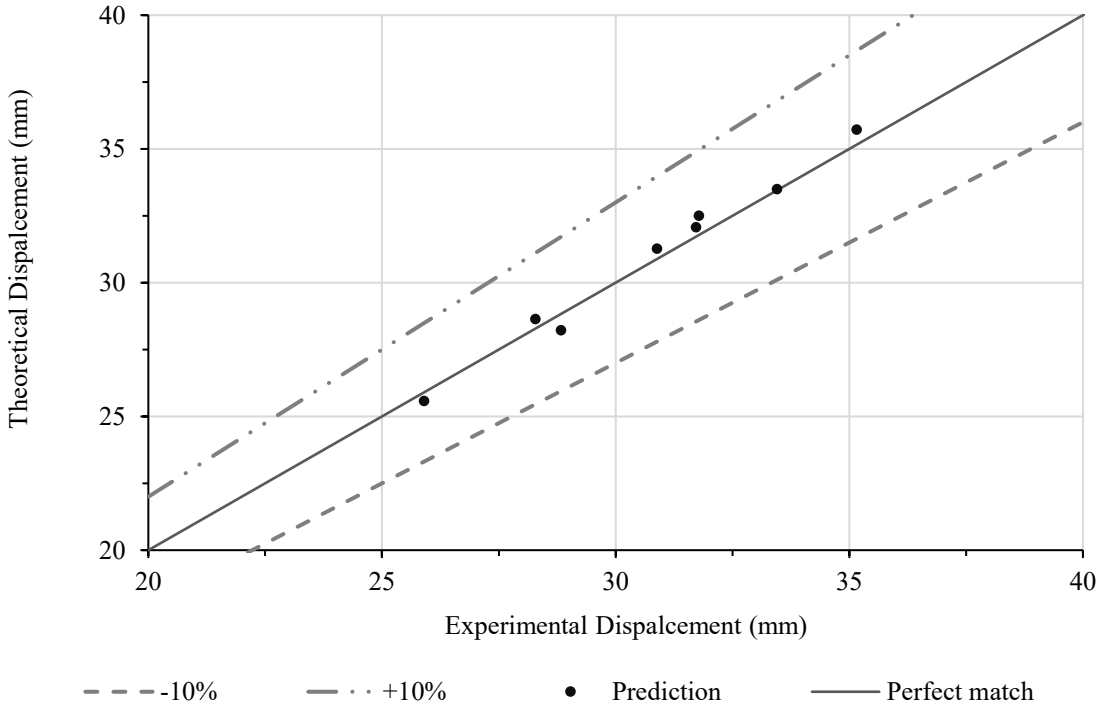

b) Displacement model comparison

Figure 5.7: Displacement model comparison.

The comparison between theoretical and experimental results presents a reasonable match with average prediction ratios of 0.97 and 1.01 and coefficients of variation (COV) of 0.04 and 0.01 for force and displacement, respectively. The good match in the result is partially attributed to the data obtained from the non-destructive tests as well as the determination of the tensile and compressive strain measured experimentally in the beam specimens. The strain-displacement curves comparison between theoretical and experimental results are shown in Figure 5.8 for R-15M-B beams.

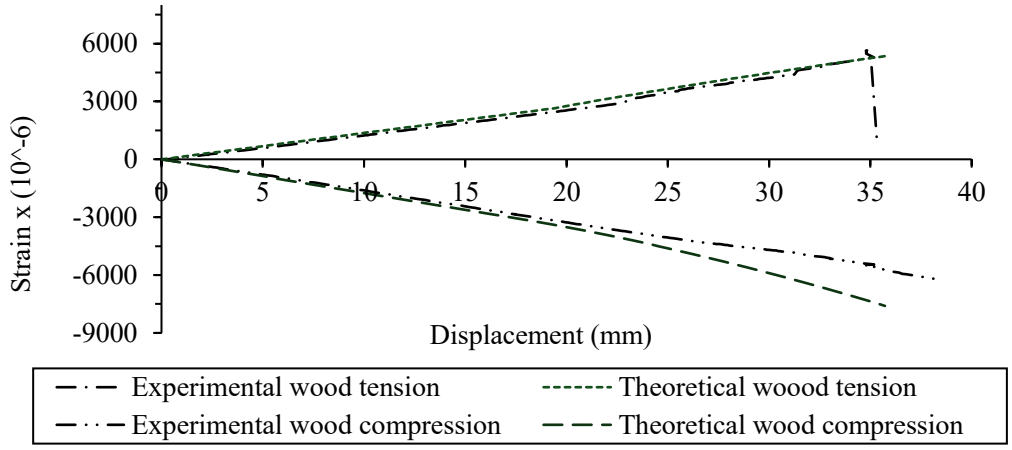

a) R-15M-B1

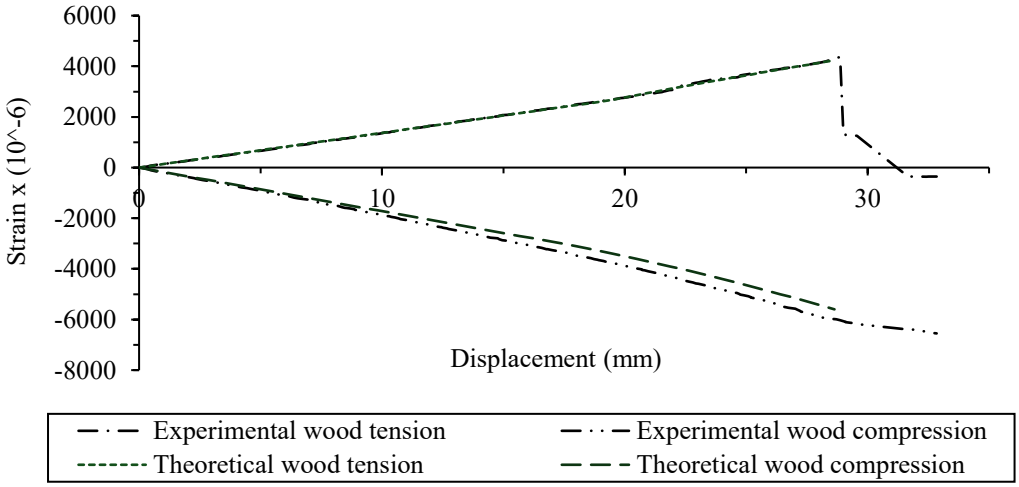

b) R-15M-B2

Figure 5.8: Strain-displacement curves prediction.

5.3 Analysis model for the post-peak behaviour

Three-stage analyses are considered in this study, where first a linear-elastic analysis is conducted, followed by the prediction of the maximum force capacity and associated deflection, and finally, a post-peak analysis was performed to predict the behaviour of the beam after it reached its maximum load-carrying capacity. This analysis employed a simplified method commonly applied to reinforced concrete sections (e.g., Algassem et al., 2019), where plastic hinge formation typically occurs due to the yielding of steel reinforcement, accompanied by crack development on the tension face and compression crushing at the top of the beam. A comparable mechanism can occur in timber beams reinforced with NSM steel rebars, where the ductile steel provides rotational capacity and the timber undergoes localized cracking and compression crushing. The development of this plastic hinge behavior in the tested beams is illustrated in Figure 5.9.

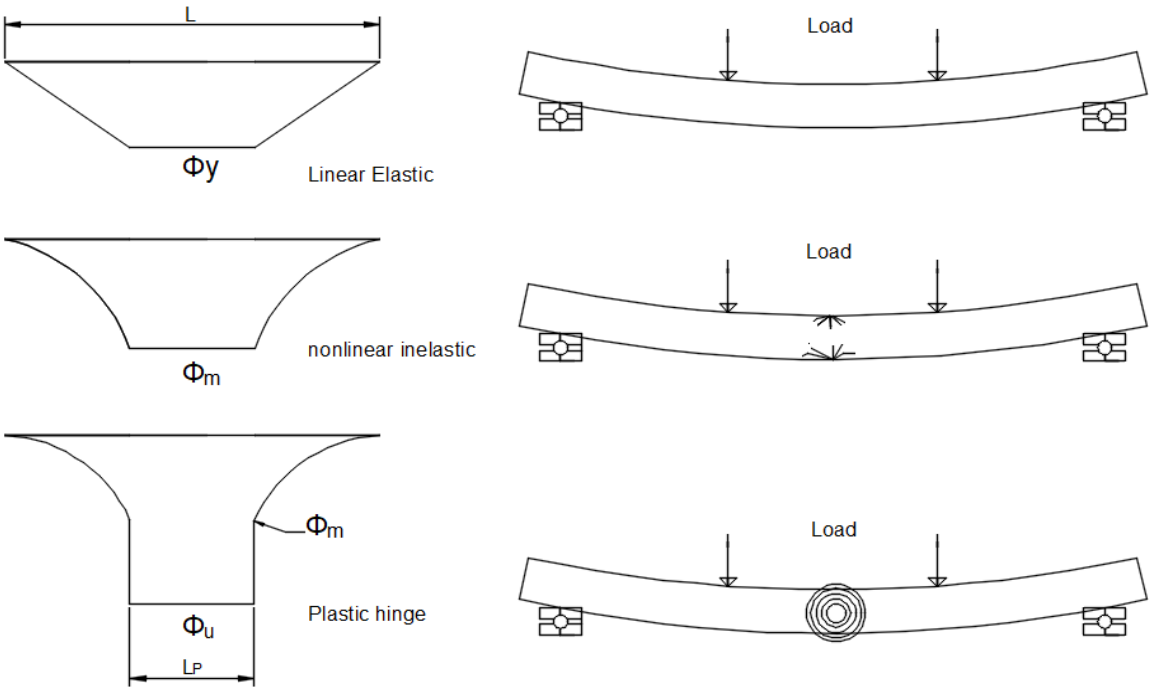

Figure 5.9: Analysis stages.

The variables $\emptyset_y, \emptyset_m \; and \; \emptyset_u$ represent the yielding, maximum, and ultimate curvatures, respectively. L is the length of the beam, and L_P represents the plastic hinge length. Equation 3 is used to calculate the deflection at the plastic hinge location (e.g., Algassem et al., 2019). The implementation of Equation 5.2 to calculate the deflection of the beam is illustrated in Figure 5.10 for half of the beam due to symmetry.

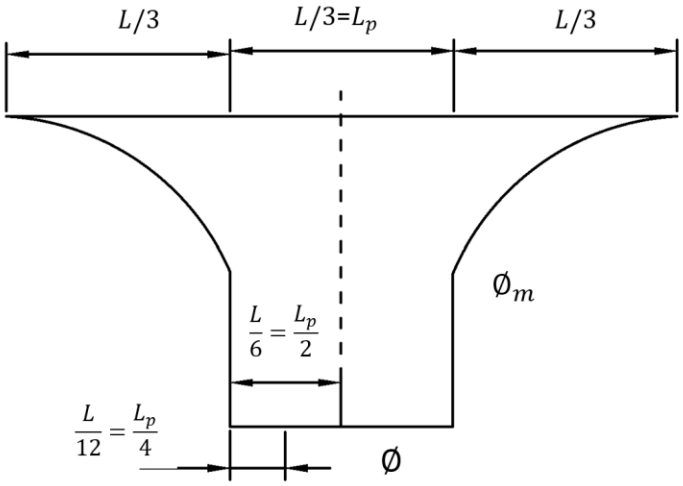

Figure 5.10: Ultimate deflection calculation.

$$\Delta = u_m + \frac{(\emptyset - \emptyset_m)L_p}{2}\left(\frac{L}{2} - \frac{L_p}{4}\right) \qquad Eq.5.2$$

Where Δ and $\emptyset$ represent deflection and curvature after the occurrence of the plastic hinge, and u_m is the displacement at the maximum resistance. The deflection is calculated at each increment value of the curvature until $\emptyset_u$ is reached.

Most of the studies in the literature analyze the behaviour of reinforced timber beams near or up to the maximum force. The compression stress-strain diagram from the previous stage, described in section 5.2, was extended to simulate the post-peak behaviour. The compressive stress for wood under direct compression decreases after reaching the maximum crushing stress, and may subsequently exhibit more ductile behavior (Buchanan, 2017). This decrease in stress is assumed in this study to be linear until it reaches zero. In contrast, for tension, the stress-strain diagram demonstrates a linear brittle failure (Buchanan, 2017), similar to the earlier stage outlined in Section 5.2. Differently from the behaviour on the compression side, as the maximum tensile stress is reached, it drops to zero, indicating the initiation of a tensile crack. Figure 5.11 presents the wood stress-strain diagram for the R-15M-B1 specimen.

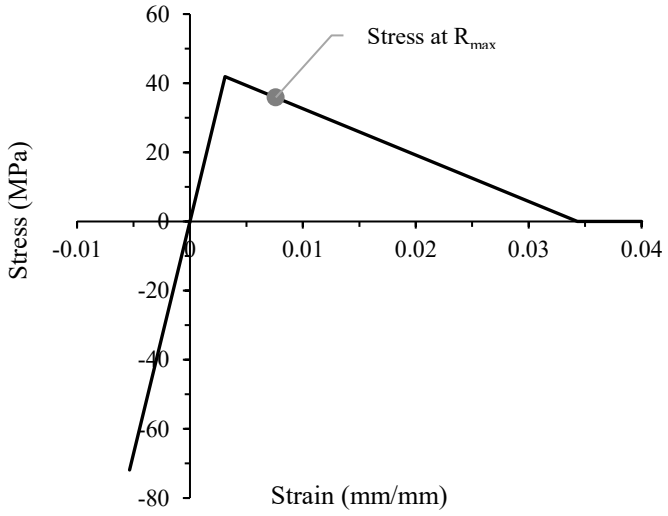

Figure 5.11: Extended wood stress-strain diagram for R-15M-B1.

The stress-strain relationship proposed by Park & Paulay (1975) is used to model the full curve of the steel reinforcement plate and rebars, as illustrated in Equation 5.3.

$$f_s = \begin{bmatrix} E_{st}\varepsilon_s & 0 < \epsilon_s < \epsilon_y \\ f_y & \epsilon_y < \epsilon_s < \epsilon_{sh} \\ f_y\left[\dfrac{m(\varepsilon_s - \varepsilon_{sh}) + 2)}{60(\varepsilon_s - \varepsilon_{sh}) + 2)} + \dfrac{(\varepsilon_s - \varepsilon_{sh})(60 - m)}{2(30r + 1)^2}\right] & \epsilon_y < \epsilon_s < \epsilon_{sh} \end{bmatrix}$$

$$r = (\varepsilon_u - \varepsilon_{sh})$$

$$m = \frac{\left(\frac{f_u}{f_y}\right)(30r + 1)^2 - 60r - 1}{15r^2} \qquad Eq.5.3$$

Where ϵ_s is the steel strain, f_s is the steel stress, and ϵ_{sh} refers to strain hardening, ϵ_{su}. An example of the stress-strain curve for 15M is presented in Figure 5.12.

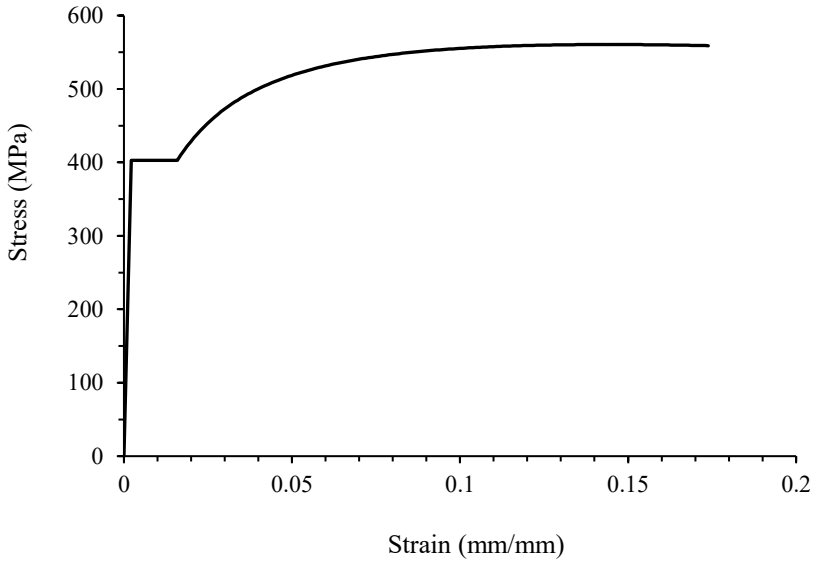

Figure 5.12: Extended steel stress-strain diagram.

The result of the post-peak analysis for beam reinforced with rebars and plates are shown Figure 5.13 and Figure 5.14, respectively.

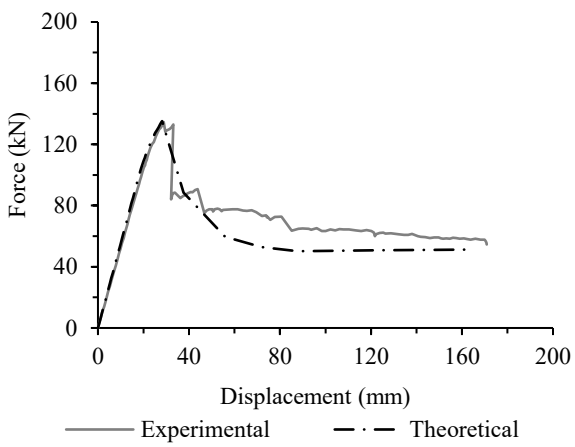

a) R-10M-B1

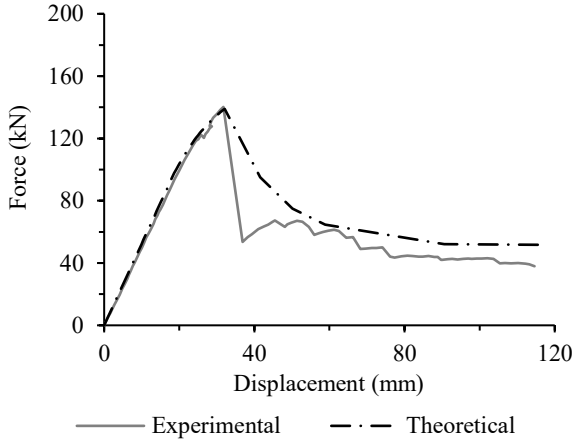

b) R-10M-B2

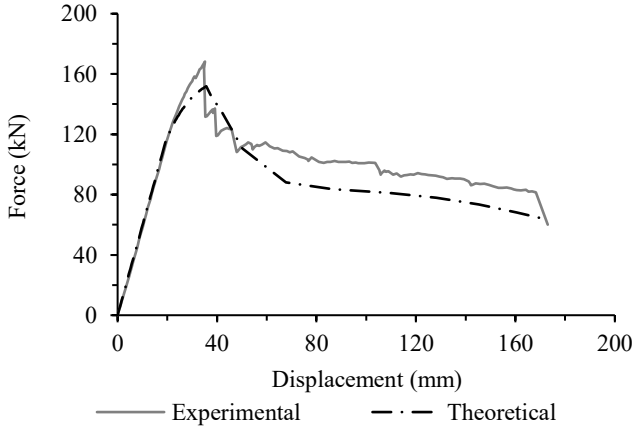

c) R-15M-B1

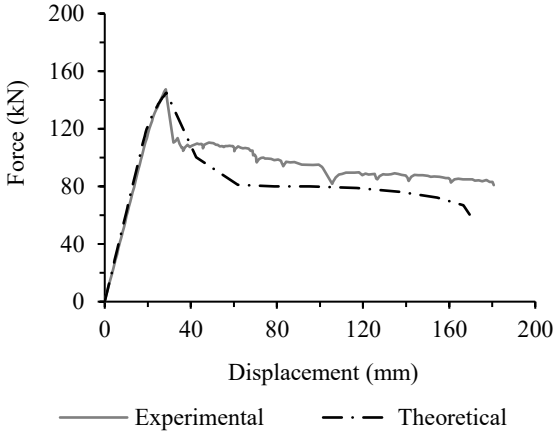

d) R-15M-B2

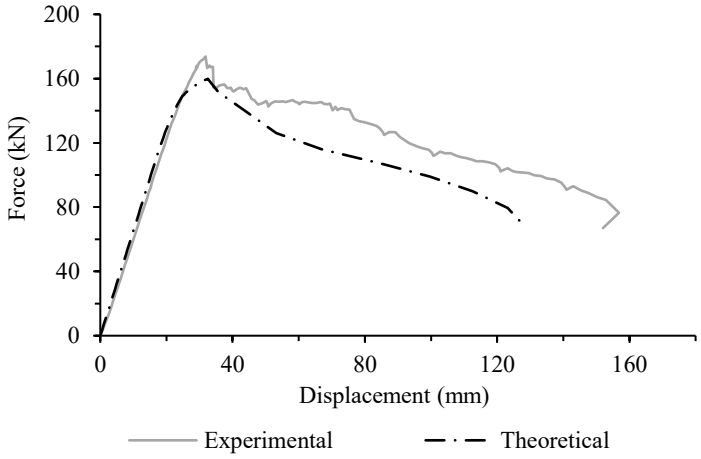

e) R-20M-B1

Figure 5.13: Post-peak displacements for reinforced beams with rebars.

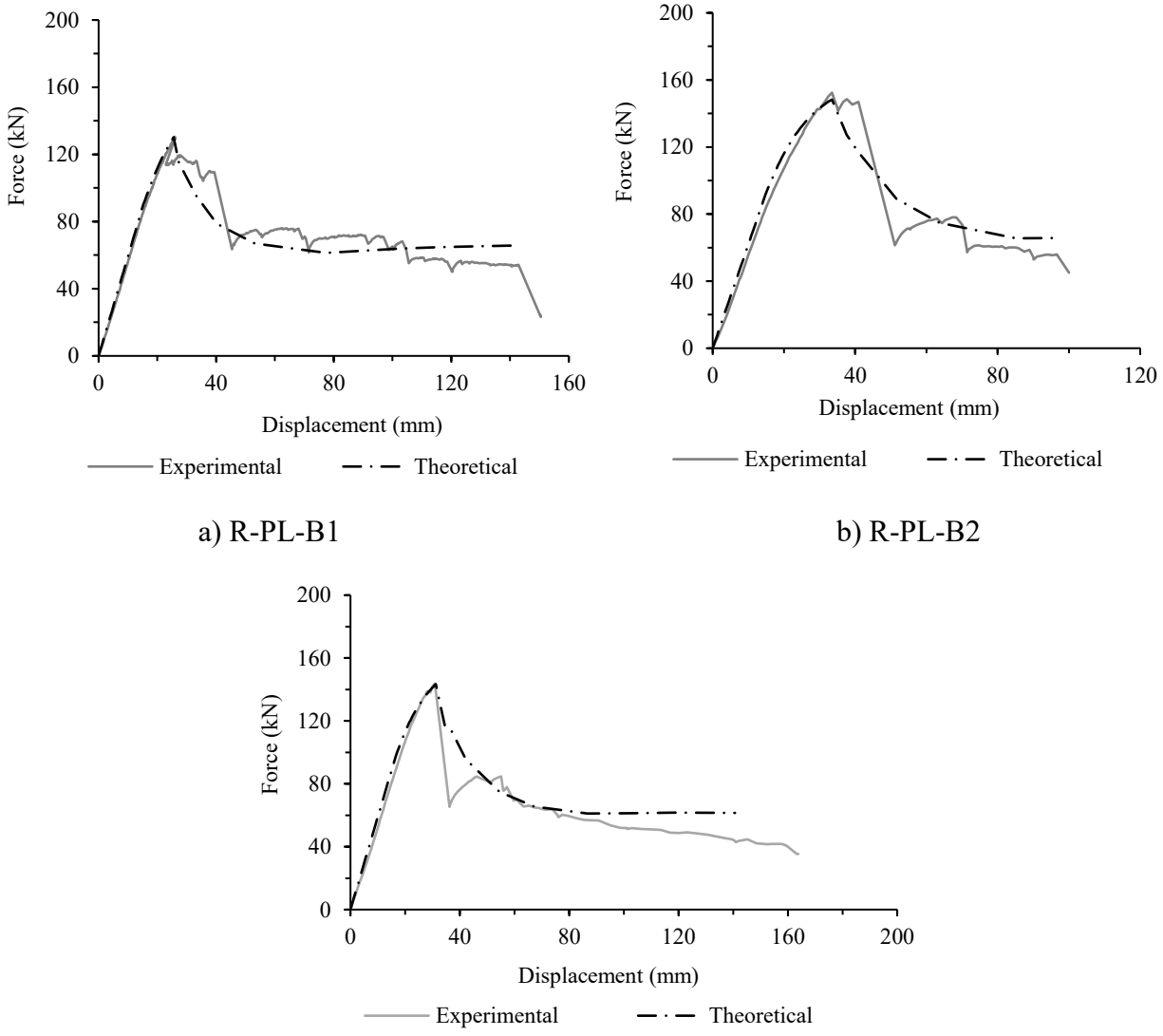

Figure 5.14: Post-peak displacements for reinforced beams with plates.

As shown in Figures 5.14 and 5.15, a good match between experimental and theoretical post-peak force-displacement results was obtained using the proposed analysis method for both beams reinforced with rebars and plates.

5.4 Dynamic test results

The analytical data for the dynamic tests using the shock-tube device are presented in this section. More analytical data for reinforced beams tested dynamically can be found in Appendix C. The analytical procedure in section 5.1 to simulate the static force-displacement curves, was also used to simulate the dynamic resistance curves. However, for the wood and steel materials the stress-strain diagrams should be modified by the DIF to simulate the effect of the strain rates as illustrated in Chapter 2. The values of dynamic increase factor for the materials under flexural behavior were taken from the CSA S850:23. For glulam, it is 1.1 for tension and compression stresses. For steel reinforcement rebar (400 MPa), it is 1.3 for yielding stress and 1.1 for ultimate stress, while for the steel plate (300 MPa), it is 1.25 for yielding stress and 1.1 for ultimate stress. Figure 5.15 and Figure 5.16 show one of the stress-strain diagrams for wood for the D-15M-B1 beam, and for steel reinforcements with DIFs, respectively.

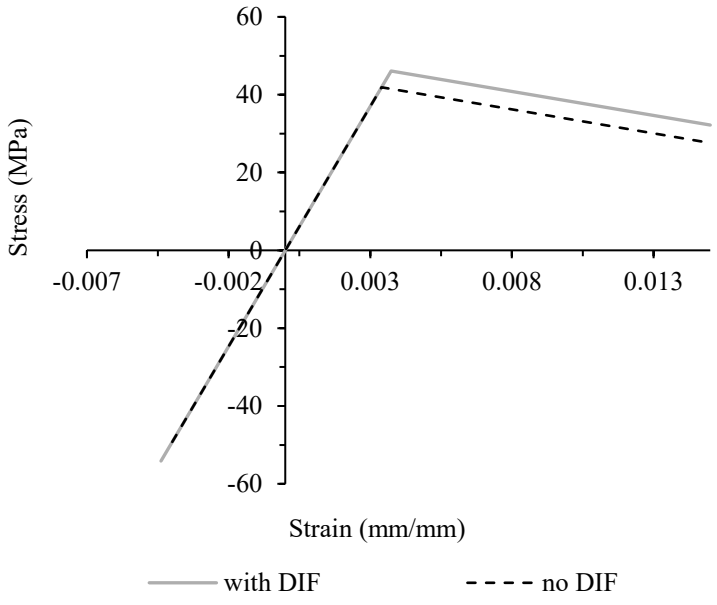

Figure 5.15: Wood stress-strain diagram for D-15M-B1.

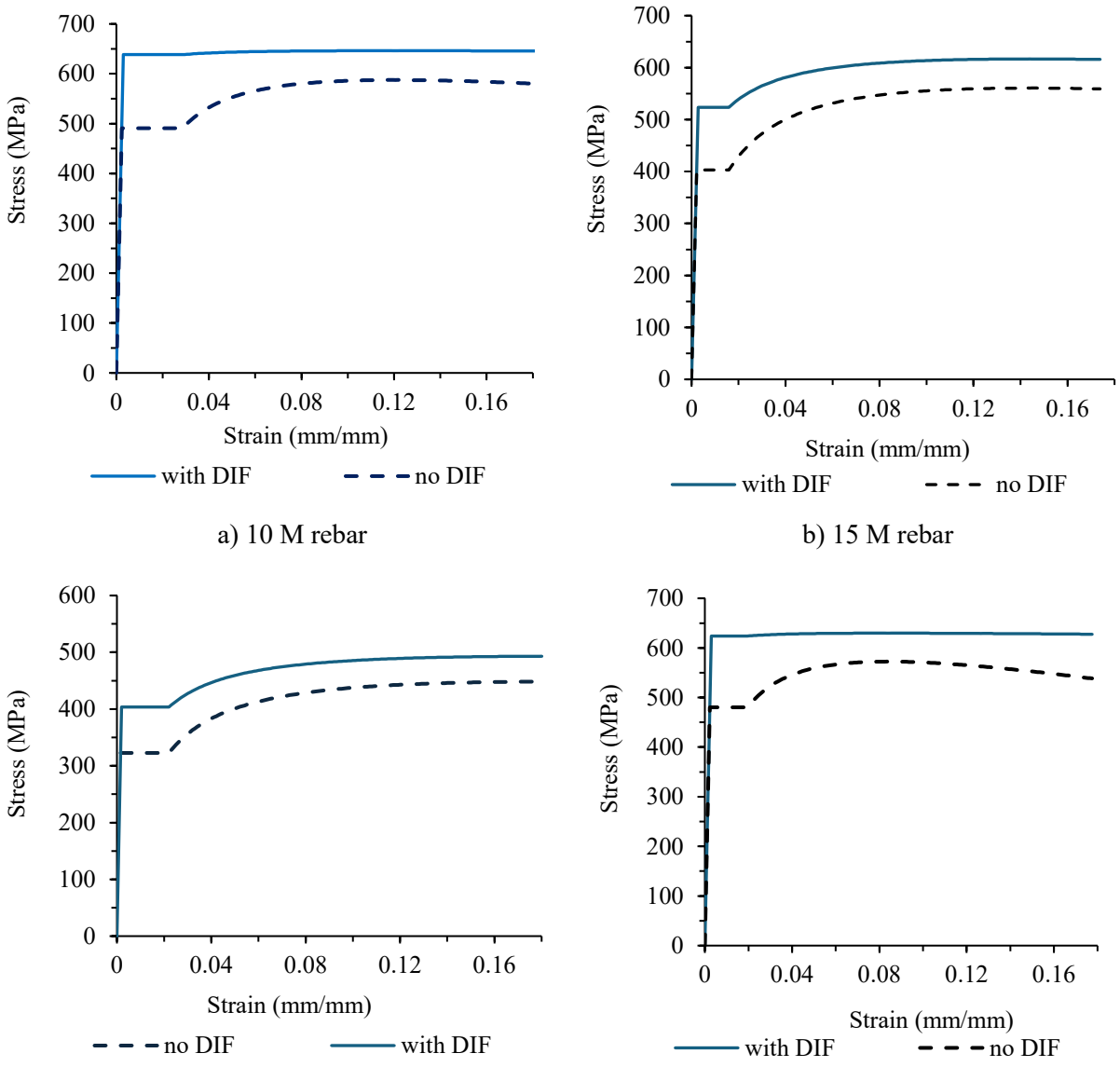

Figure 5.16: Steel stress-strain diagram for steel reinforcements.

Similar to the static results, strain gauge data at peak loads were unreliable due to vibration, noise, and potential gauge failure. Therefore, α values were calculated by adjusting the wood bending strength until the model matched experimental displacement near failure. The average α from dynamic tests was 1.27. which is very close to the previous value observed during static testing.

The detailed values are presented in Appendix A. Figure 5.17 and Figure 5.18 show the prediction for the force-displacement curve for the D-10M-B1 and D-PL-B1, respectively.

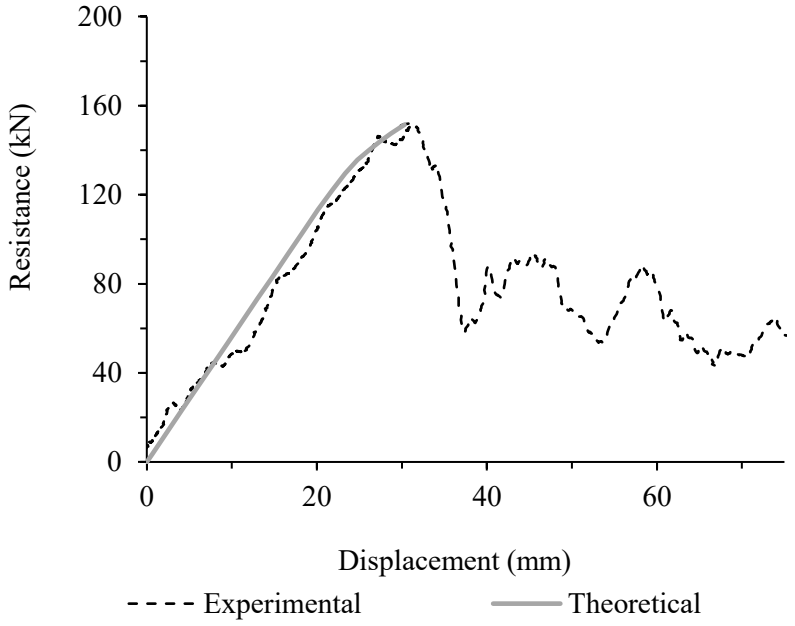

Figure 5.17: Force-displacement curve prediction for D-10M-B1.

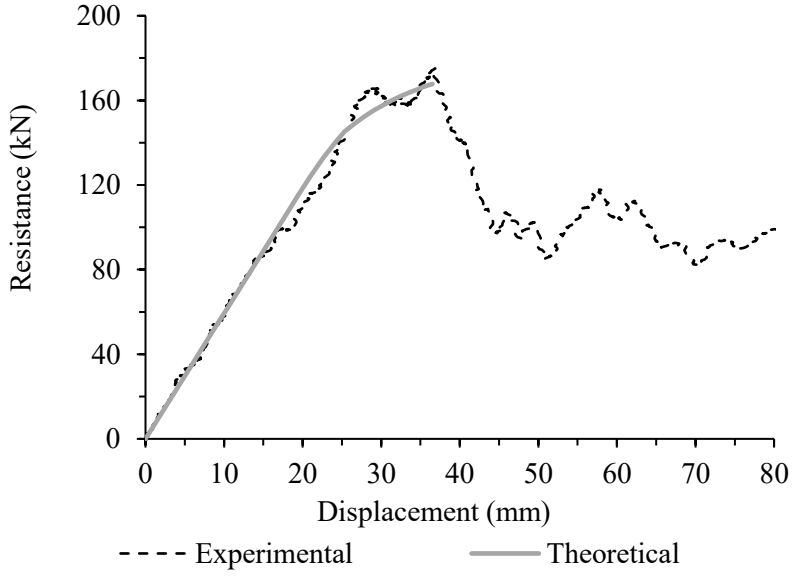

Figure 5.18: Force-displacement curve prediction for D-PL-B2.

The comparison between theoretical and experimental results for reinforced beams under dynamic testing is shown in Figure 5.19 and Figure 5.20 for maximum resistance and its corresponding displacement data, respectively.

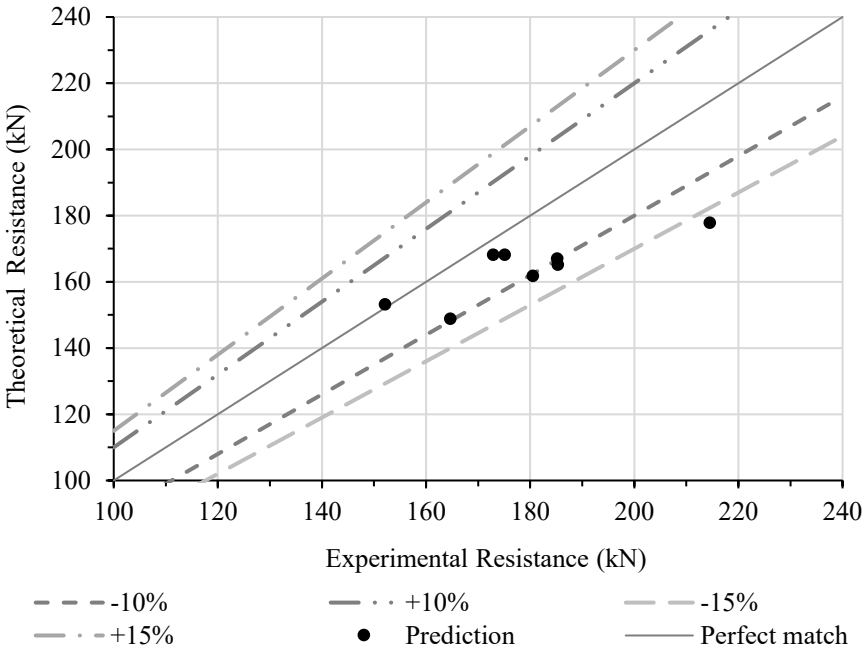

Figure 5.19: Dynamic force model comparison.

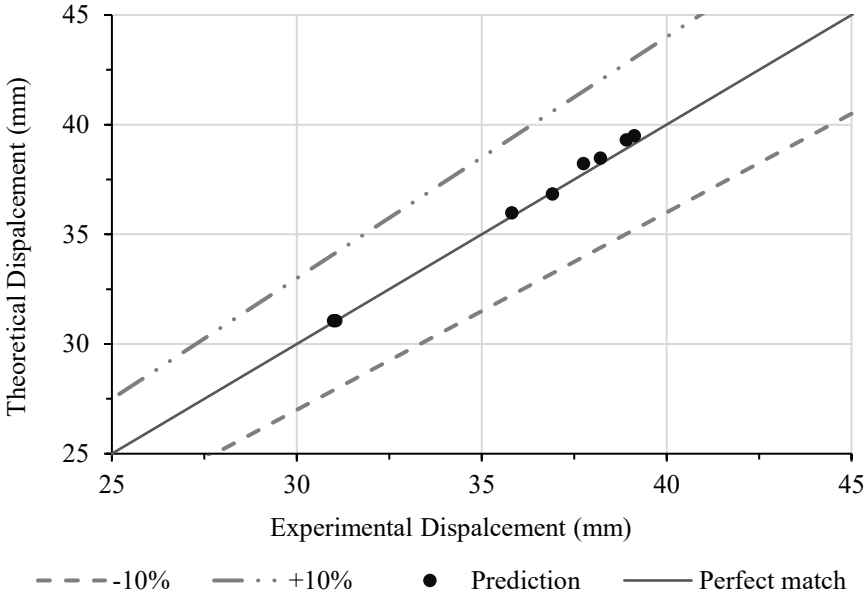

Figure 5.20: Dynamic displacement model comparison.

The analytical model closely aligns with experimental results in terms of overall specimen behaviour, although it slightly underestimates peak resistance. The average theoretical-to-experimental resistance ratio was 0.92 (COV = 0.06), likely due to uncertainties in dynamic increase factors (DIFs) for wood, size effects in scaling material properties, and differences in glulam characteristics compared to previous study (Lacroix and Doudak, 2018b). For displacement comparison, the average prediction ratio between theoretical data to experimental one is 1.01 with a COV of 0.01.

The strain-displacement curve results form the experimental and theoretical dynamic data were also compared to each other as shown in Figure 5.21 for specimens D-10M-B2 and D-PL-S1, detailed in Appendix C.

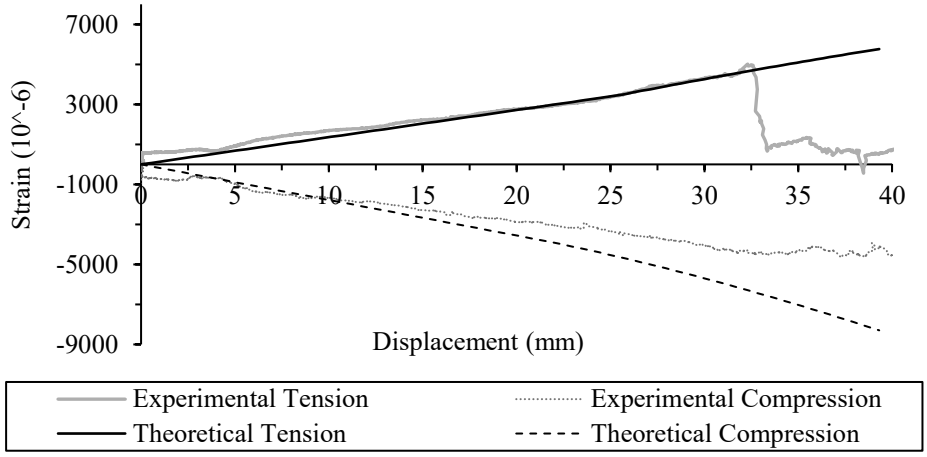

a) D-PL-S1

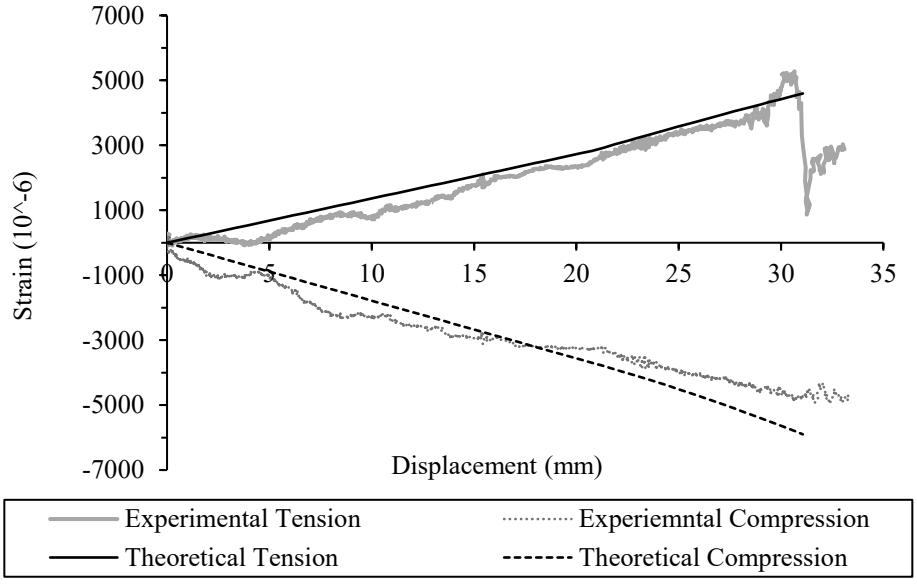

b) D-10M-B2

Figure 5.21: Strain-displacement curves prediction (dynamic beams).

As shown in Figure 5.21, a reasonable agreement was found for the strain-displacement curves comparison. For predicting the time-displacement curve at the maximum resistance, the RC blast program was used (Jacques, 2014). This program operates under the assumption of SDOF system as detailed in Chapter 2, disregarding damping effects for blast loads due to their negligible impact

on the initial peak displacement (Biggs 1964; UFC 3-340-02). Equation 5.4 presents the SDOF equation system.

$$K_{LM}\, m\, \ddot{u}(t) + k\, u(t) = A\, P(t) \qquad Eq.5.4$$

The load and mass factor (K_{LM}) was taken as 0.87 for four-point bending load pattern (Biggs, 1964), while m is the mass of the LTD with a value of $283.6\ kg$ (Jacques, 2016), plus the mass of the specimen, described in Chapter 3, while *A* is the effective tributary area for the LTD taken as $3.55\ m^2$ (Jacques, 2016). This program was also successfully used to predict the behaviour of wood structural elements subjected to blast loading such as studs (Jacques, et al., 2014) or for Cross Laminated Timber (CLT) panels such as (Poulin et al., 2017), as well as for reinforced concrete beams such as (e.g., Algassem et al., 2019). It is important to note that the program accurately predicts displacement only up to the point of peak resistance. Beyond that, the sudden drop in resistance leads to rapid deflection, which the model does not capture. Figure 5.22 presents RCblast program's output for specimen D-10M-B1, including the applied pressure–time history, theoretical resistance–displacement curves, and the predicted displacement–time response of the reinforced beam. Similarly, Figure 5.23 illustrates the displacement–time responses for specimens D-15M-B2 and D-PL-S1.

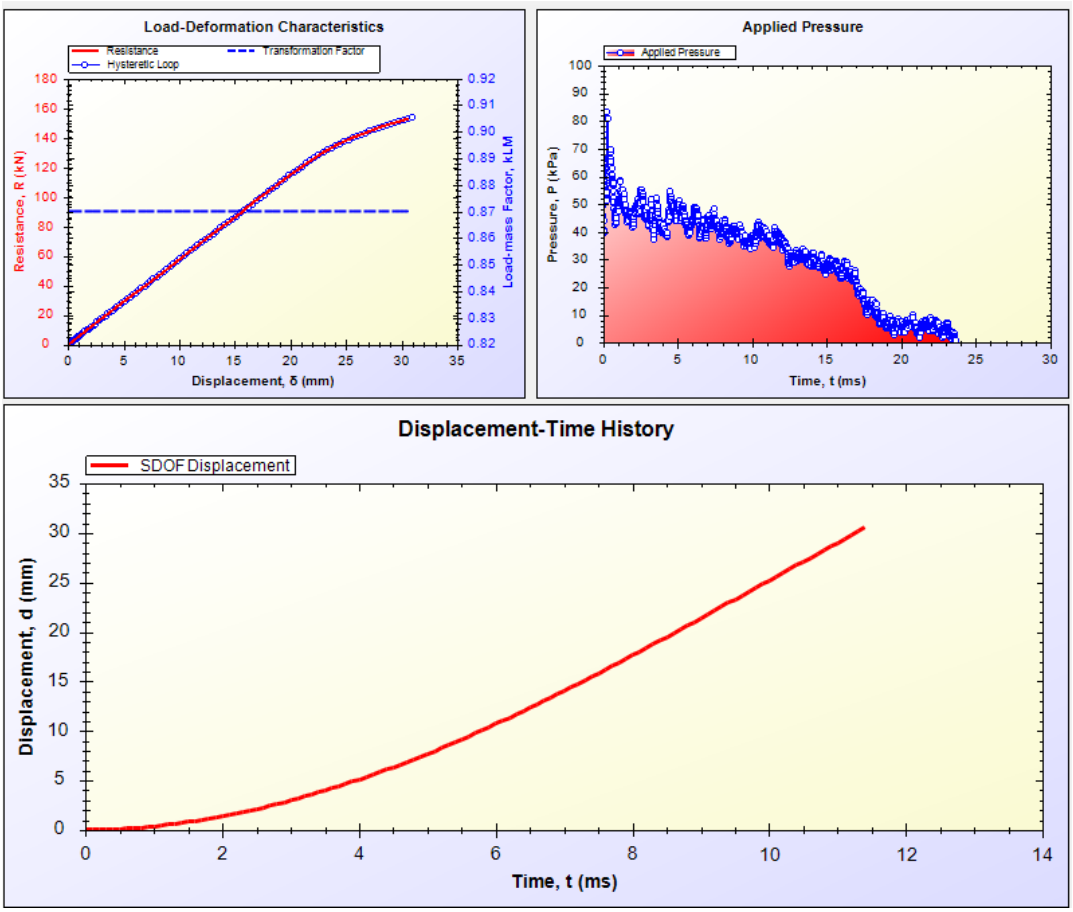

Figure 5.22: RC blast program's window.

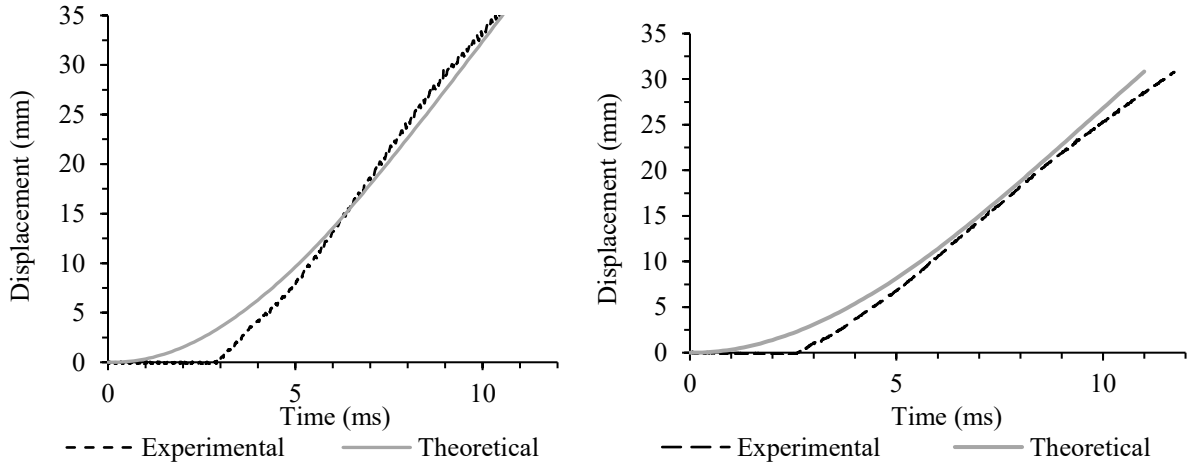

a) D-15M-B2 b) D-PL-S1

Figure 5.23: Displacement-time curves prediction.

As shown in Figure 5.23, a very good match was found for displacement-time curves comparison. The comparison between theoretical and experimental results for reinforced beams using the RC blast program is shown in Figure 5.24 and Figure 5.25 for displacement and time at maximum resistance, respectively.

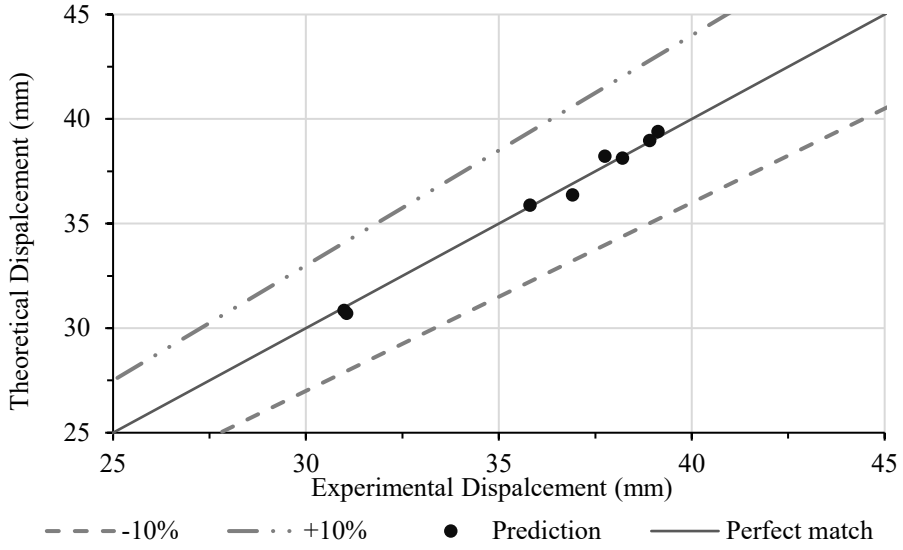

Figure 5.24: RC blast displacement prediction.

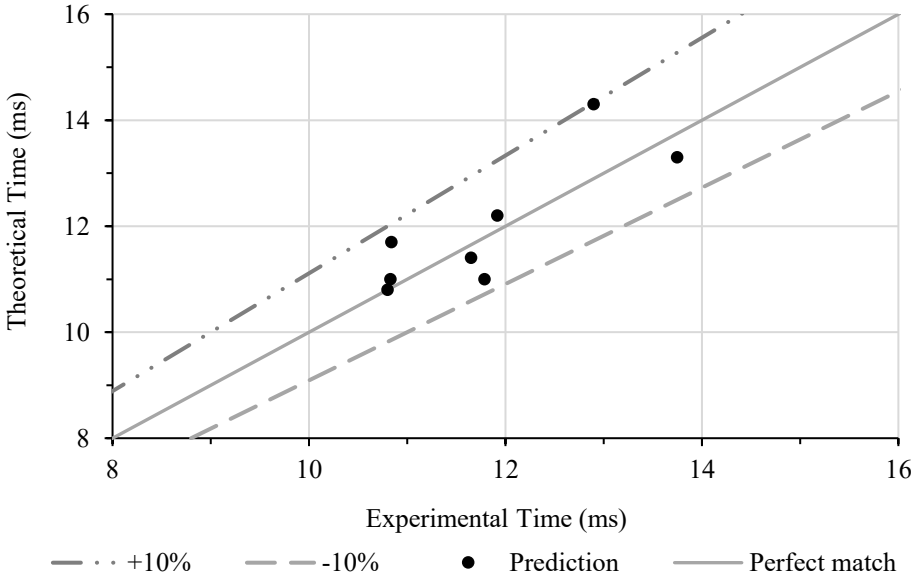

Figure 5.25: RC blast time prediction.

As shown in Figures 5.24 and 5.25, the difference in the prediction of the displacement and time at the maximum resistance is within 10%. The average prediction ratio between theoretical data to experimental one was 1.00 and 1.01, with a COV of 0.01 and 0.06 for displacement and time, respectively. Similar to the post-peak of force-displacement curves for beams tested statically, the post peak dynamics curves were generated using the same procedure used earlier with the incorporation of DIF factors to include strain rate effects. The results of the post-peak analysis for beams reinforced with rebars and plates tested dynamically are shown in Figure 5.26 and Figure 5.27, respectively.

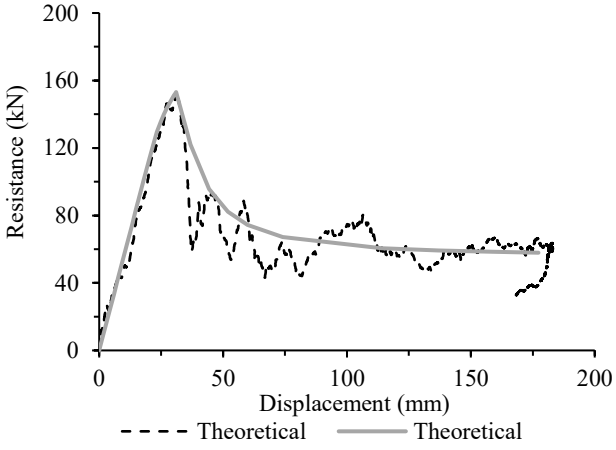

a) D-10M-B1

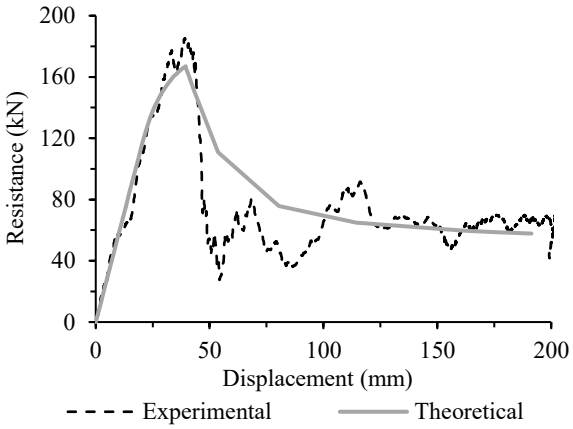

b) D-10M-B2

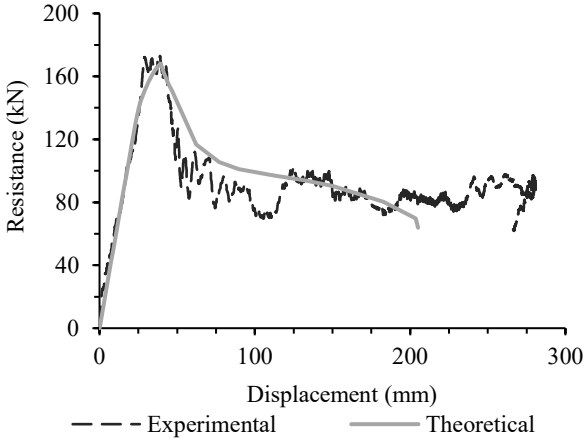

c) D-15M-B1

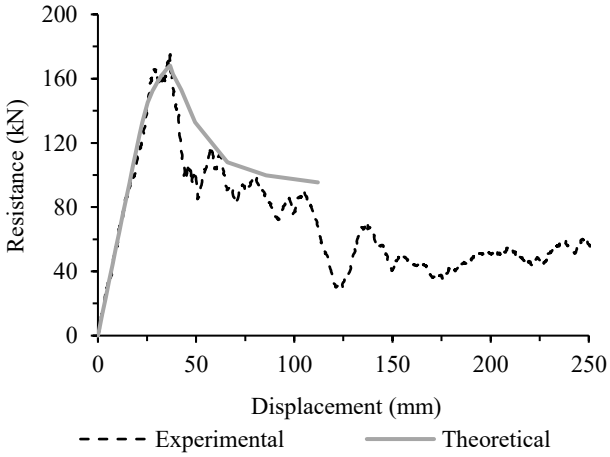

d) D-15M-B2

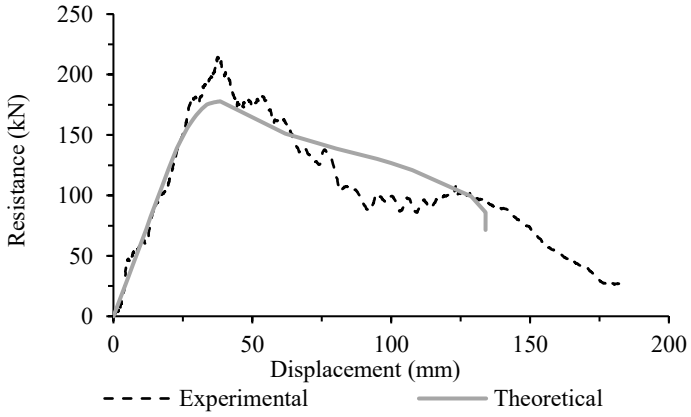

e) D-20M-B1

Figure 5.26: Post-peak resistance-displacement dynamic curves (rebars).

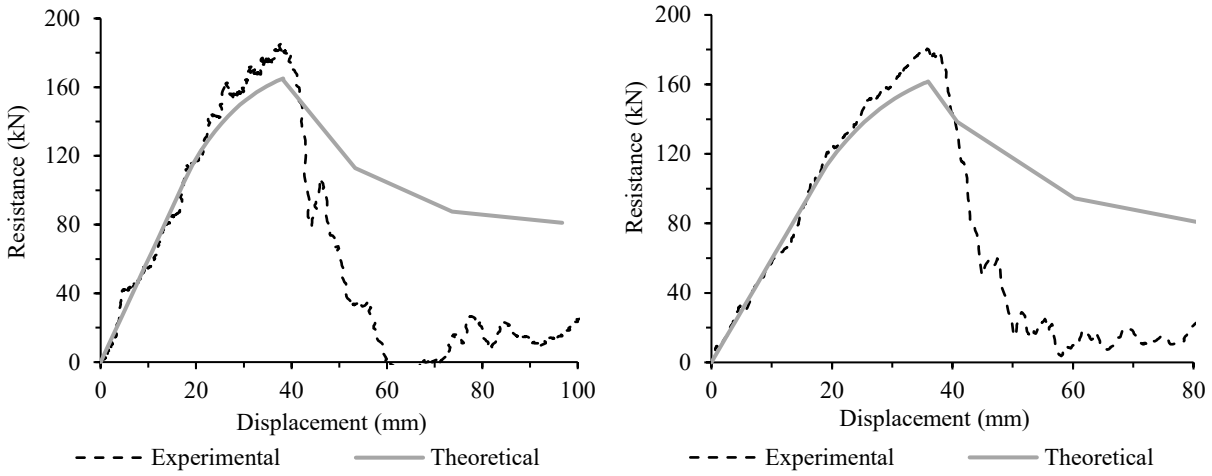

a) D-PL-D1

b) D-PL-D2

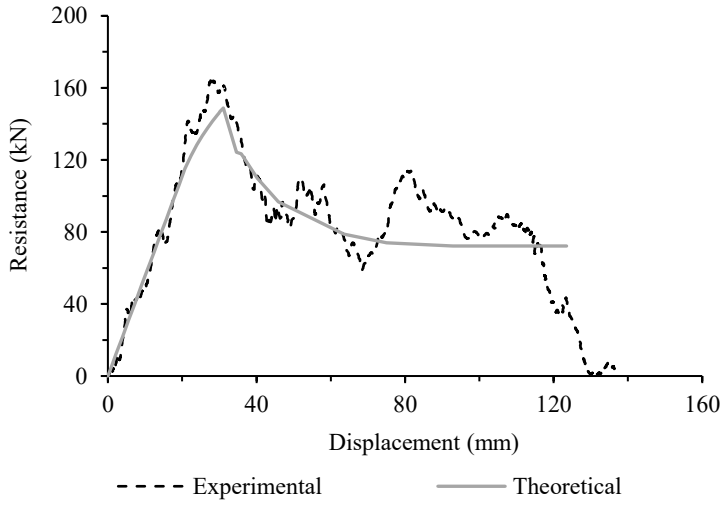

c) D-PL-S1

Figure 5.27: Post-peak resistance-displacement dynamic curves (plates).

As shown in Figures 5.26 and 5.27, good match was found for the post-peak resistance-displacement curves comparison between experimental and theoretical data using the simplified procedure for post-peak analysis.

CHAPTER SIX: DISCUSSION

6.1 Introduction

The study investigates the reinforcement of glulam beams against static and blast loading using the NSM technique with steel rebar and plate reinforcements. As explained in Chapter 3, the dynamic test was conducted using the shock tube device at the University of Ottawa. Eight reinforced beams were used for each static and dynamic test. Both have the same nomenclature except that static beams start with the letter R while the dynamic ones start with letter D. Results from static and dynamic tests are compared in this chapter, offering insights into improving stiffness, strength, and post-peak behavior and strain rate effects.

6.2 Unreinforced beam

For unreinforced beam, the beams' moment strength was determined following the guidelines outlined in CSA (2024) similar to the procedure applied by (Goodwin et al, 2022). For glulam beam, this standard specifies that the moment resistance (M_r) should be calculated as the minimum strength between Equations 6.1 and 6.2.

$$M_r = \phi F_b \; S \, K_x \, K_{zbg} \qquad Eq.6.1$$

$$M_r = \phi F_b \, S \, K_x \, K_L \qquad Eq.6.2$$

$Where$

$$S = \frac{bd^2}{6}$$

$$K_{zbg} = \left(\frac{130}{b}\right)^{0.1} \left(\frac{610}{d}\right)^{0.1} \left(\frac{9100}{L}\right)^{0.1} \leq 1.3 \qquad Eq.6.3$$

The reduction factor ϕ is set to 1 to find the mean moment capacity, while F_b stands for the bending strength and equals to of 30.7 MPa according to the manufacturer, multiplied by a load duration factor (K_D) of 1.15 since the load will not last more than 7 days. The curvature factor, K_x, is assumed to be 1 for straight beams. and K_L. denotes a lateral stability factor, set to 1. S and K_{zbg} is the section modulus and size factor, respectively, while b and d are the width and depth of the beam cross-section, and L is the clear span of the beam.

The value of K_{zbg} is 1.287 for the beam used in this study, and S is 813965.7 mm^3. The value of F_b should be also adjusted by a factor K to modify from specified strength to mean strength according to Annex B of CSA (2024)., using Equation 6.4:

$$K = \frac{1}{1 - (1.65)(COV)} \qquad Eq.6.4$$

Where COV is the coefficient of variation, equals to 0.16 for glulam, which yields a K value of 1.36. This will result in a bending strength and moment capacity of 48.0 MPa and 39.1 $kN.m$, respectively, as well as a load capacity of 104.9 kN based on a four-point loading configuration with equal spans of 0.745 m. It should be noted that this value is very close to the capacity of the unreinforced beam tested on this study with a value of 106.1 kN.

Both reinforced beams in each static and dynamic test showed increase in strength and stiffness, as well as improvement in the post-peak behaviour. The comparison between both tests is presented in the next section.

6.3 Reinforced beams

The comparison between the reinforced beams tested statically and dynamically are shown in Figure 6.1 through Figure 6.5, where the static test curves were drawn along with their dynamic test curves counterpart.

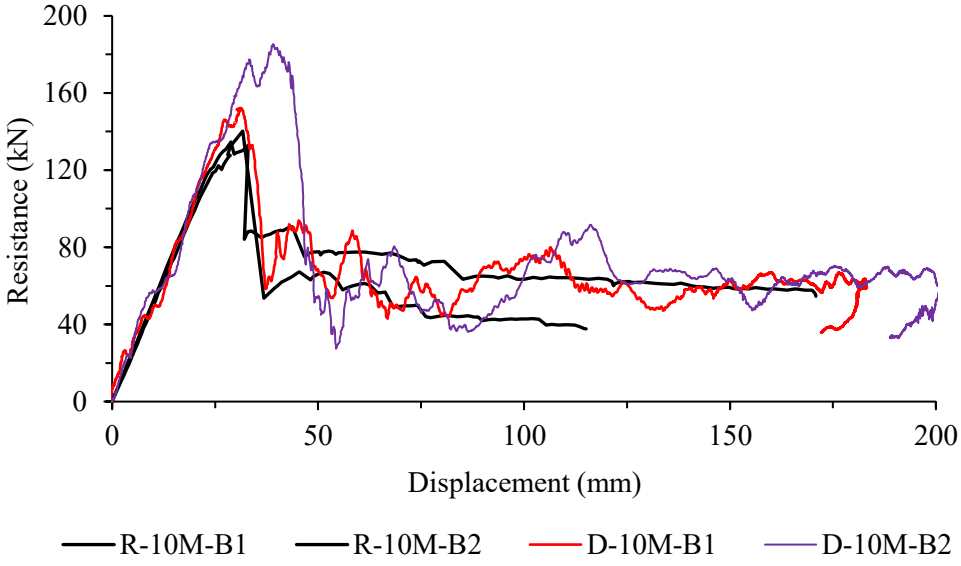

Figure 6.1: Static and dynamic resistance curve (10M).

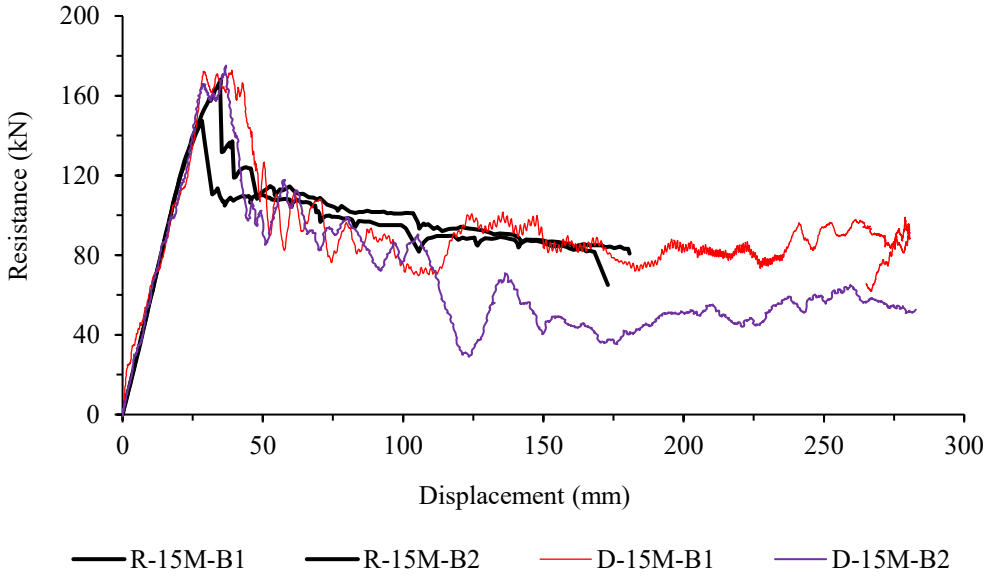

Figure 6.2: Static and dynamic resistance curve (15M).

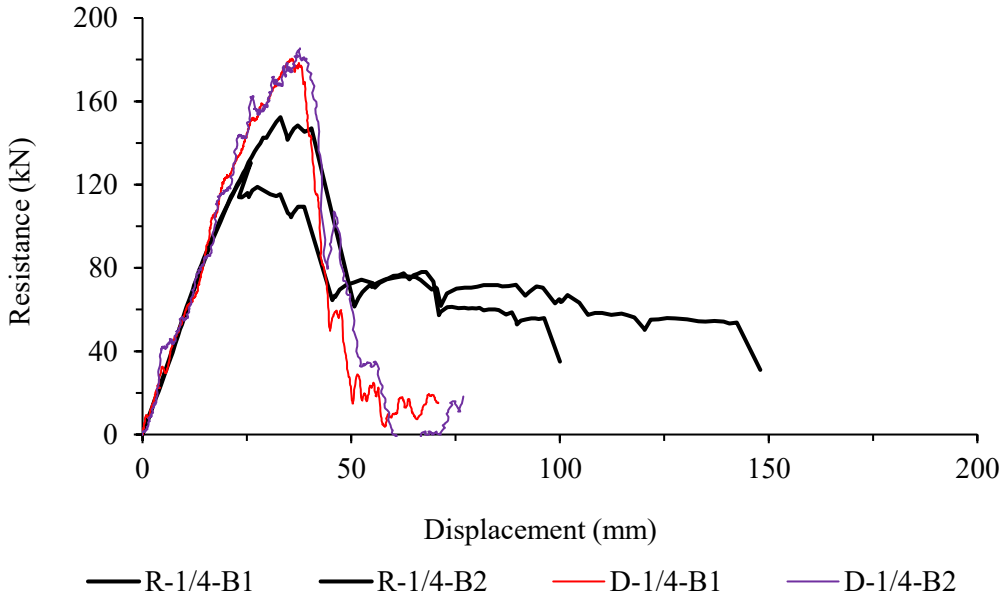

Figure 6.3: Static and dynamic resistance curve (Plate B).

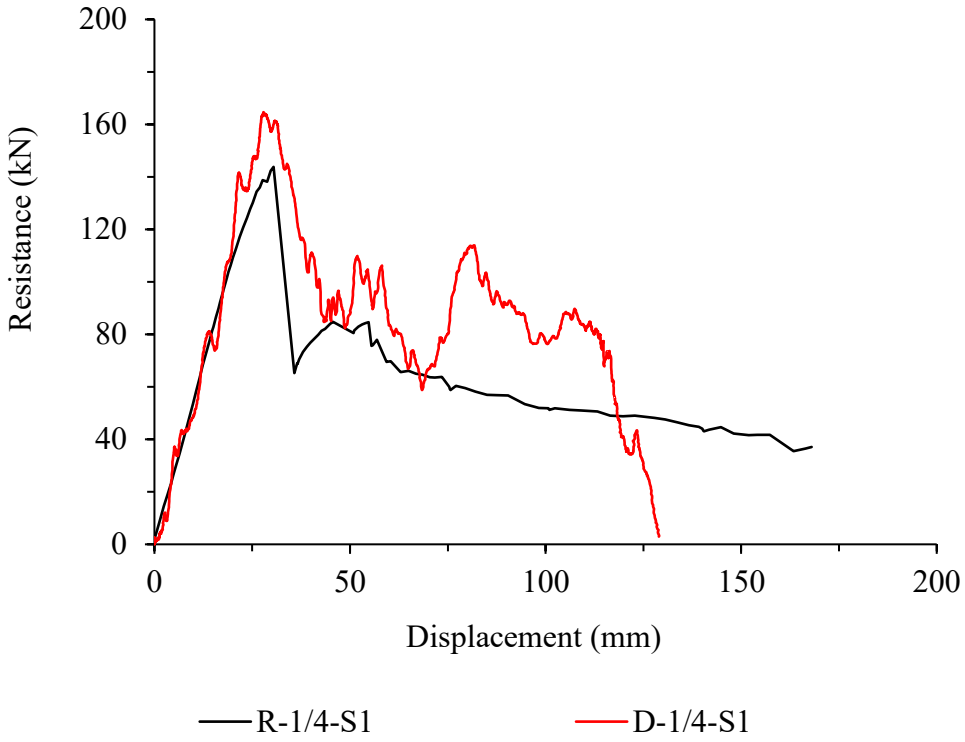

Figure 6.4: Static and dynamic resistance curve (Plate S).

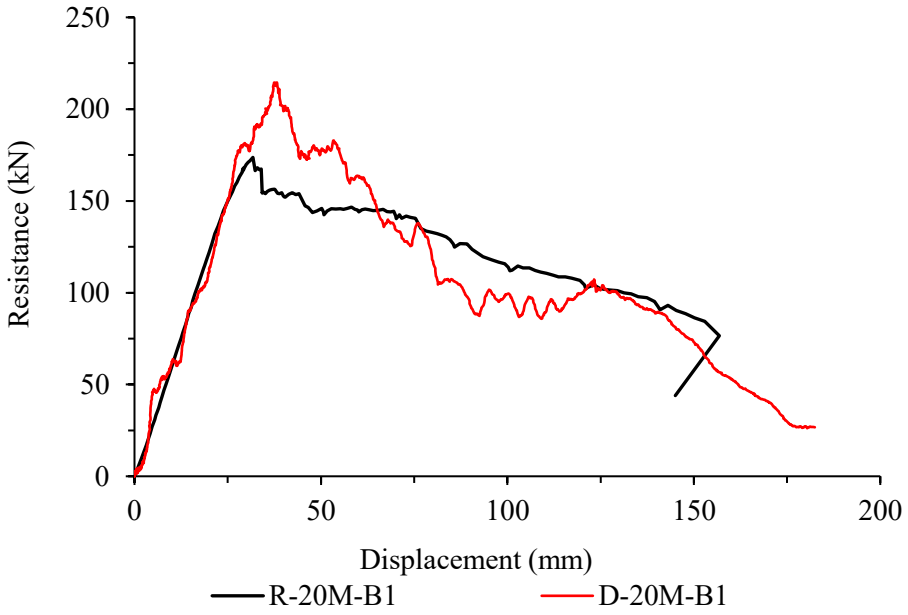

Figure 6.5: Static and dynamic resistance curve comparison for (20M).

As shown in Figures 6.1 through 6.5, the static resistance-displacement curves are more uniform and smother than the dynamics one. This is because if the vibrating and variability nature of the dynamic loads. The average ratio between dynamic resistance and static force is 1.23, 1.10, 1.29, 1.14 and 1.24 in Figures 6.1 through 6.5, respectively, with average of 1,2 (COV of 0.06). It is important to highlight that beam categorized under D-PL-B exhibited distinct behavior compared to their counterparts in the R-PL-B group within the static analysis, as shown in Figure 6.3. Notably, the force resistance of D-PL-B beams sharply diminishes to zero after reaching their peak resistance. Such behavior is undesirable, particularly in blast or seismic-prone regions where residual strength is essential for safeguarding buildings against collapse following an event. The comparison between beams reinforced with 15M bars versus those reinforced with plates is shown in Figure 6.6 and Figure 6.7 for beams tested statically and dynamically, respectively.

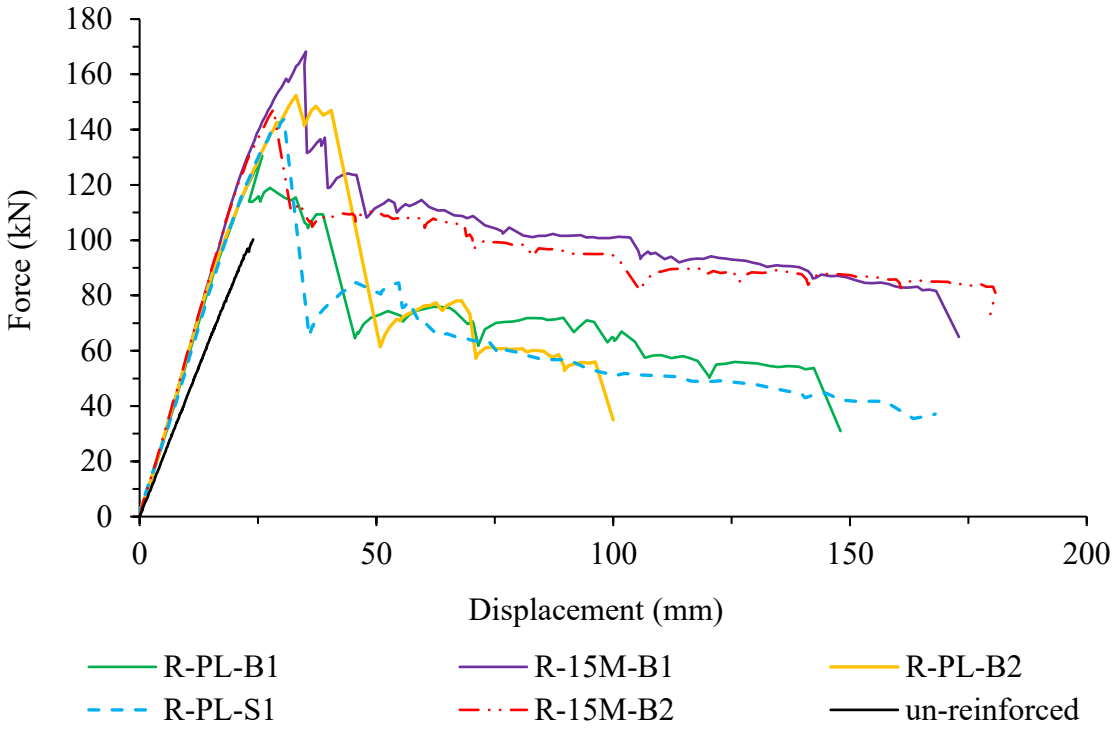

Figure 6.6: Beams reinforced with 15M rebar versus those with plates (static).

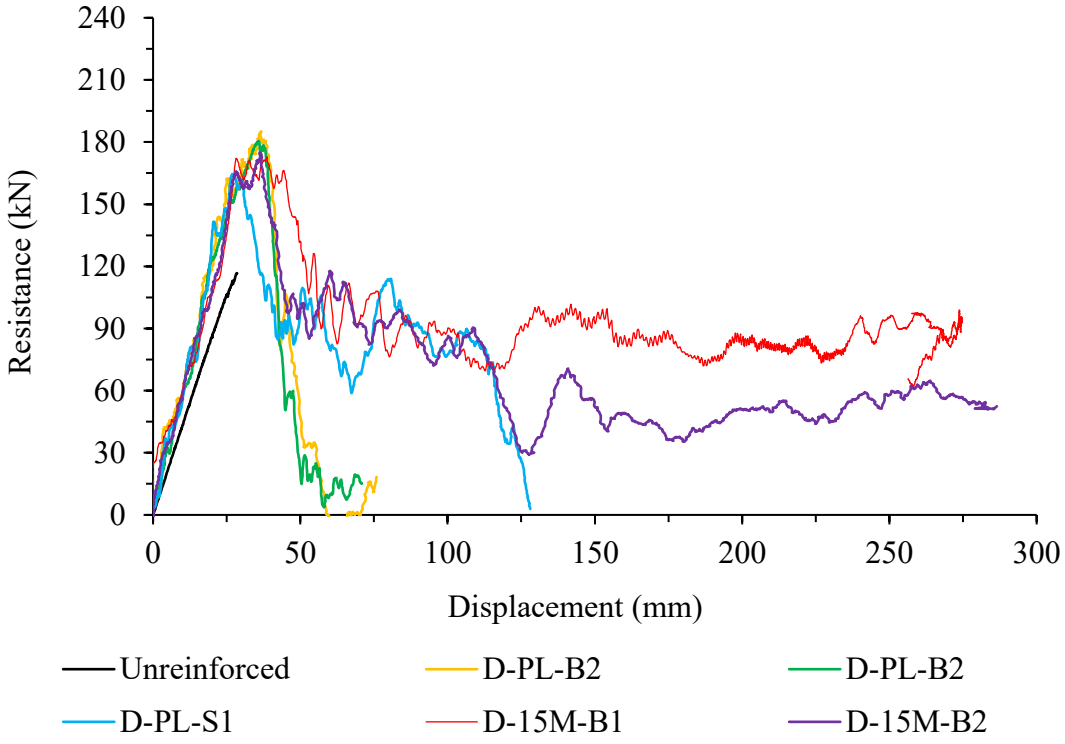

Figure 6.7: Beams reinforced with 15M rebar versus those with plates (dynamic).

As shown in Figures 6.6 and 6.7, beams reinforced with 15M rebars and those reinforced with plates exhibited comparable increases in strength and stiffness. However, in terms of ductility and post-peak response, beams reinforced with 15M rebars demonstrated better performance compared to those reinforced with plates. The compassion between the average increase in strength between beams tested statically and dynamically relative to those of unreinforced beams are shown in Figure 6.8. For the average increase in strength and stiffness, it is applied for all beams type except for specimens reinforced with 20M rebar (20M-B1) and horizontal plates (PL-S1), since they were not duplicated, and a single specimen was used in each static and dynamic test as illustrated in Chapter 3.

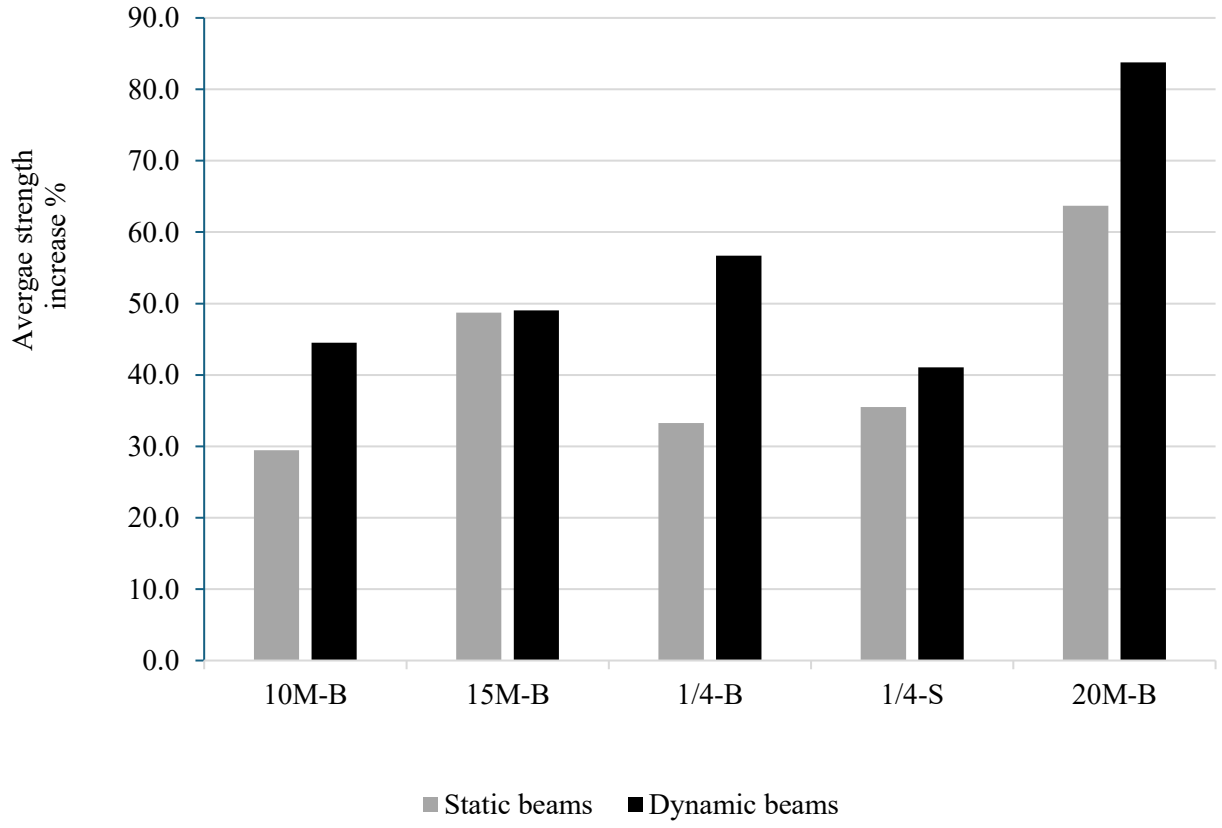

Figure 6.8: Average strength increases comparisons.

As shown in Figure 6.8, both reinforced beams tested statically and dynamically show an increase in strength over unreinforced beams. In general, a higher increase in strength was observed for beams tested dynamically than those tested statically. The discrepancy in results can be seen in Figure 6.8 especially in the dynamics one. The highest increase was for specimens reinforced with 20M rebars (R-20M-B1 and D-20M-B1) with a value of 63.7% and 83.3%, respectively, followed by specimens R-15M-B for static beams and D-PL-B for dynamic beams with a value of 48.7% and 56.7%, respectively, while the lowest increase in strength was for beams tested statically with 10M rebars (R-10M-B) with a value of 29.4%. Besides, for the dynamic's beams, the lowest increase was for specimen D-PL-S1 with a value of 41.0%. The increase in stiffness for both reinforced beams tested statically and dynamically relative to their stiffness before reinforcement is shown in Figure 6.9, while the comparison for ductility ratio between static and dynamic beam groups is shown in Figure 6.10.

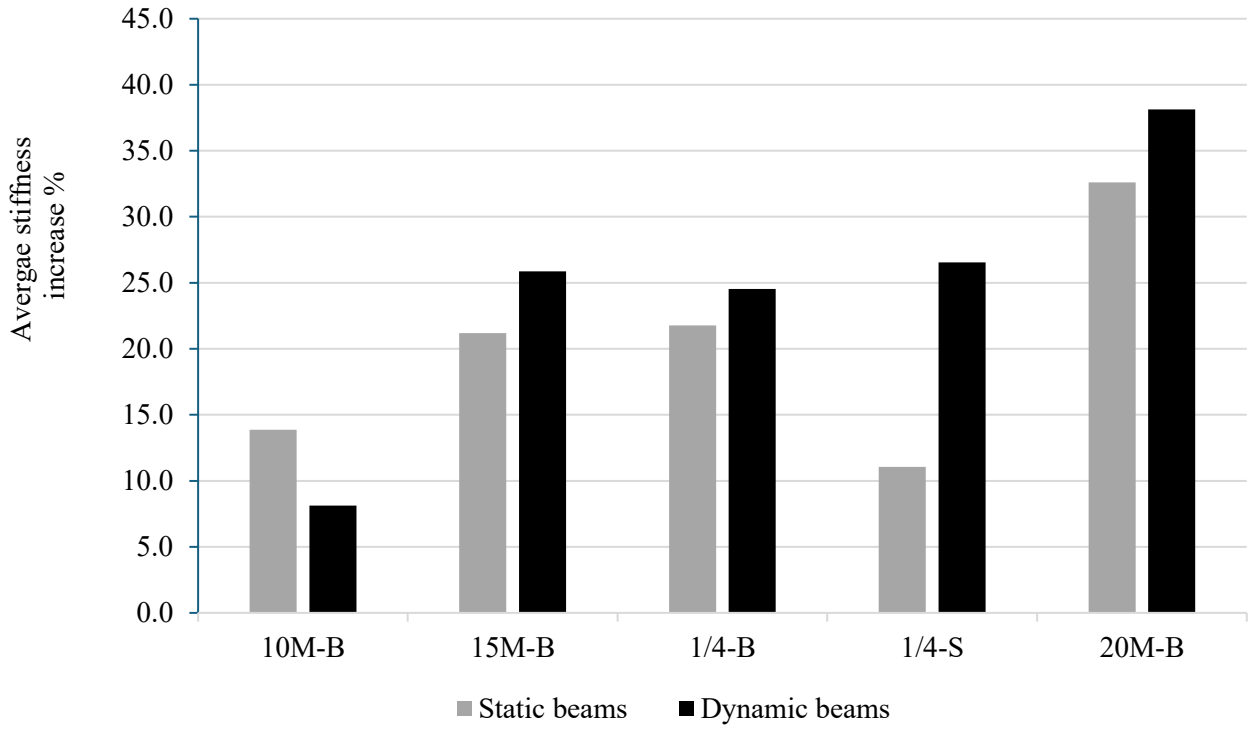

Figure 6.9: Average stiffness increases comparisons.

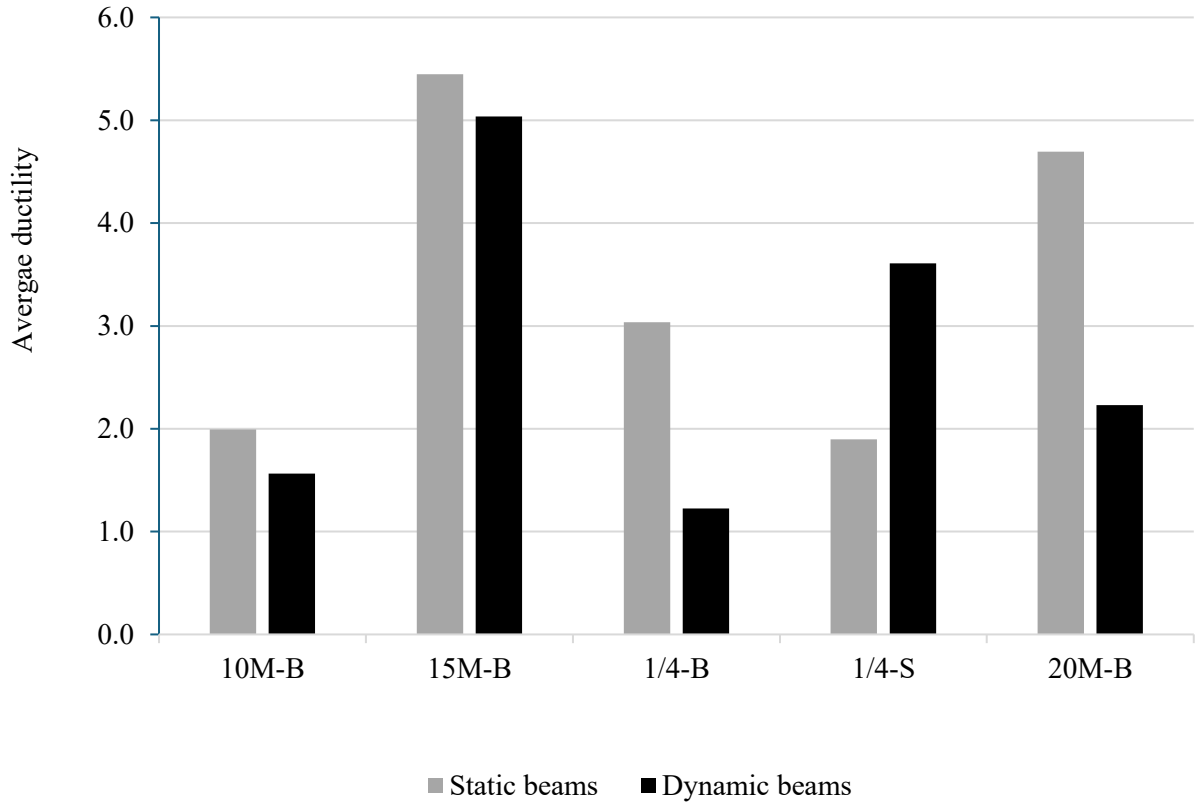

Figure 6.10: Average ductility comparisons.

As shown in Figure 6.9, both reinforced beams tested statically and dynamically show increase in stiffness after reinforcing them. Similar to the average strength comparison, the discrepancy in the stiffness comparisons were also observed between static and dynamic beams. However, a slight increase in stiffness was observed for dynamics beams than static ones except for R-10M-B. This may be attributed to the accuracy or difficulty associated with calculating the stiffness for beams were tested dynamically, as the resistance-displacement curves were not smooth similar to those of beams tested statically. Furthermore, the stiffnesses for beams tested dynamically were lower than those of static beams before reinforcement with steel found in Chapter 4. In addition, the highest increase in stiffness was for specimens reinforced with 20M rebars (R-20M-B1 and D-

20M-B1) with a value of 32.6% and 38.1%, respectively, followed by specimens R-PL-B for static beams and specimen D-PL-S1 for dynamic beams with a value of 21.8% and 26.5%, respectively, while the lowest increase in stiffness was for specimen R-PL-S1 for static beams with a value of 11.1% and specimens D-10M-B for dynamic beams with a value of 8.1%. As shown in Figure 6.10, a higher discrepancy in ductility was observed in the data between static and dynamic beams, the average ductility for specimens reinforced with 15M rebars (R-15M-B and D-15M-B) is the highest with a value of 5.4 and 5.0, respectively, followed by specimen R-20M-B1 for static beams and D-PL-S1 for dynamic beams with a value of 4.7 and 3.6, respectively, while the lowest average ductility was for specimens R-PL-S1 for static beams with a value of 1.9, and D-PL-B for dynamic beams with a value of 1.2.

For the failure mode, as mentioned in Chapter 4, both reinforced beams tested statically and dynamically exhibited ductile failure mode as well as crushing and buckling of the wood fiber at the compression side of the beam. As opposed to the static beams, all dynamic beams exhibited flexure crack failure at the maximum resistance of the beam. Additionally, cracks were noted at finger joints in certain instances. Cracks also appeared along the glue line of the beam, predominantly near the midspan. Moreover, due to the solid nature of epoxy, chunks of epoxy debris were observed following the test. Moreover, Figure 6.11 shows the damaged beams with 15M rebars; static (R-15M-1) and dynamic (D-15M-1), while Figure 6.12 shows the damaged beams with 20M rebars; static (R-20M-1) and dynamic (D-20M-1).

a) R-15M-B1

b) D-15M-B1

Figure 6.11: Damaged beams (15M) comparison static and dynamic.

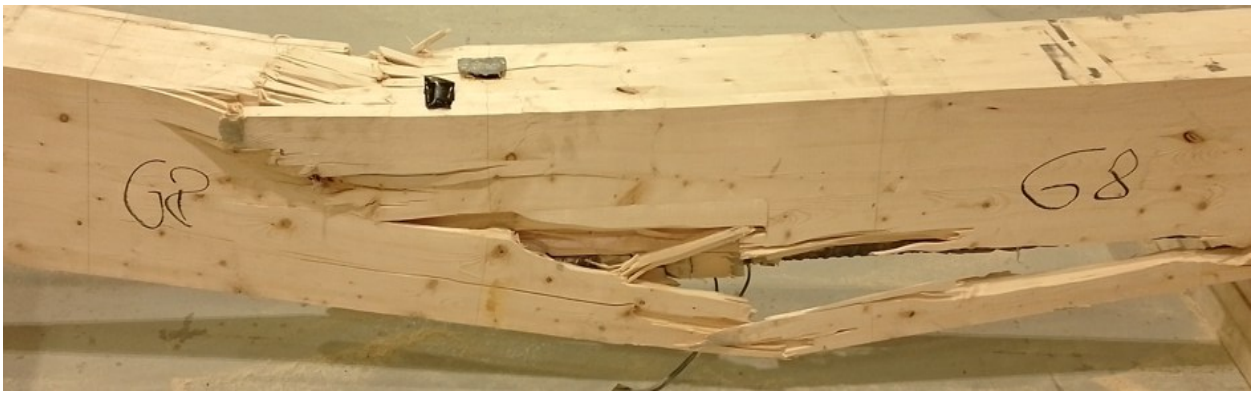

a) R-20M-B1

b) D-20M-B1

Figure 6.12: Damaged beams (20M) comparison static and dynamic.

As mentioned in Chapter 4, both specimens (R-20M-B1 and D-20M-B1) were expected to fail in shear due to their high reinforcement ratios, however, the beams reached their full flexure capacity. For the slip of the reinforcements, both beams reinforced with plates tested statically and dynamically exhibited slip failure at end sides of the beam, for beams reinforced with rebars, the slip was less occurring and pronounced. This may be attributed to the deformable surface nature of the reinforcement rebar (ribs), where the interlock mechanics provide additional bond force that

can help to prevent the rebar from slipping, while plates have smooth surface. The slip deformation for R-PL-B1 (static) and D-PL-B1 (dynamic) beams is shown in Figure 6.13.

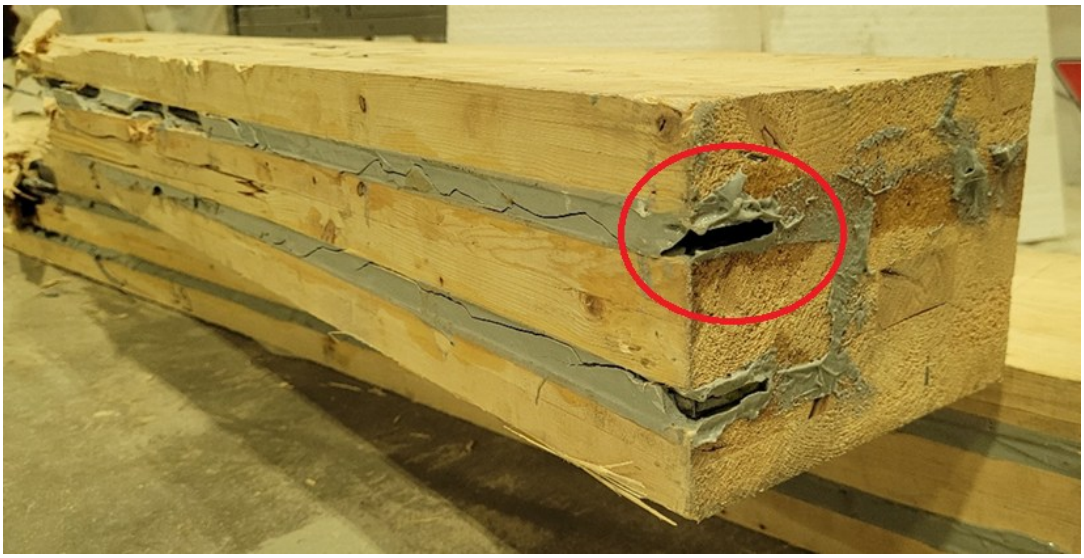

a) R-PL-B1

b) D-PL-B1

Figure 6.13: Slip damage (PL) comparison static and dynamic.

As shown in Figure 6.13, both beams reinforced with plates and tested statically or dynamically were vulnerable to slip failure at the ends of the beam. Furthermore, cracks were also observed along the glue line where the slippage happened.

6.4 Analytical results

As discussed in Chapter 5, it is not always possible to get reliable or correct data from the strain gauges, which in turn makes it difficult to find the increase in tensile strain at the bottom of the beam. For this reason, it is possible to consider a constant value for α such as 1.3 similar to (Gentile et al., 2002), as the authors used this value to model timber beams reinforced with NSM GFRP rebars. The comparison between experimental and theoretical predictions using the constant α value for beams tested statically is shown in Figure 6.14 and Figure 6.15, for maximum force and its corresponding displacement data, respectively.

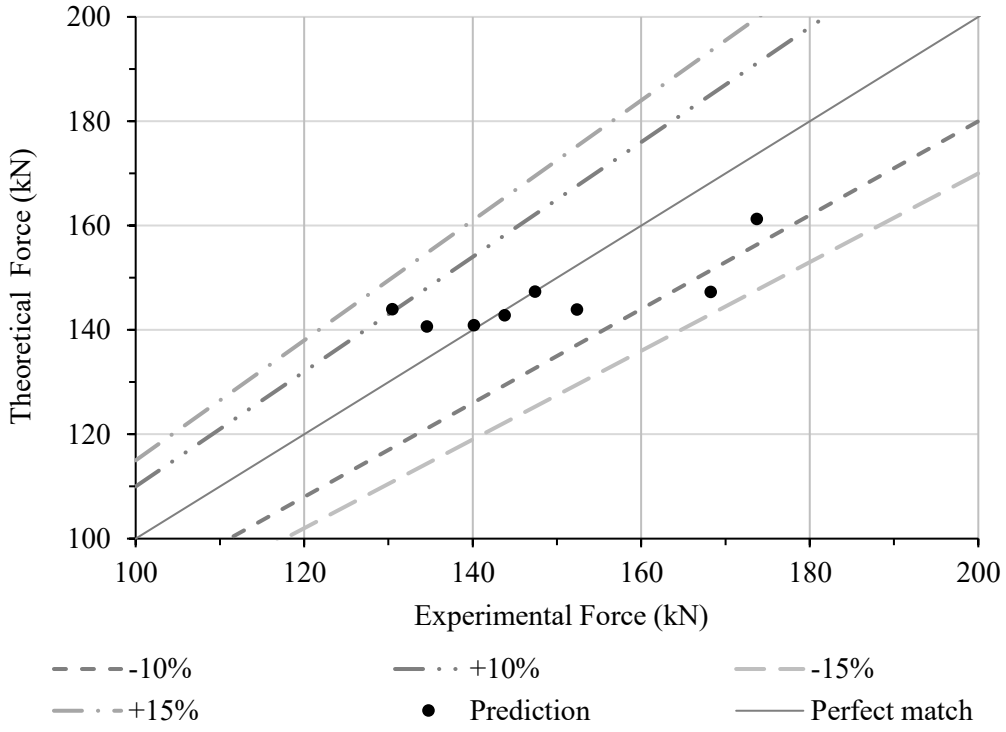

Figure 6.14: Force predictions (constant α) for beams tested statically.

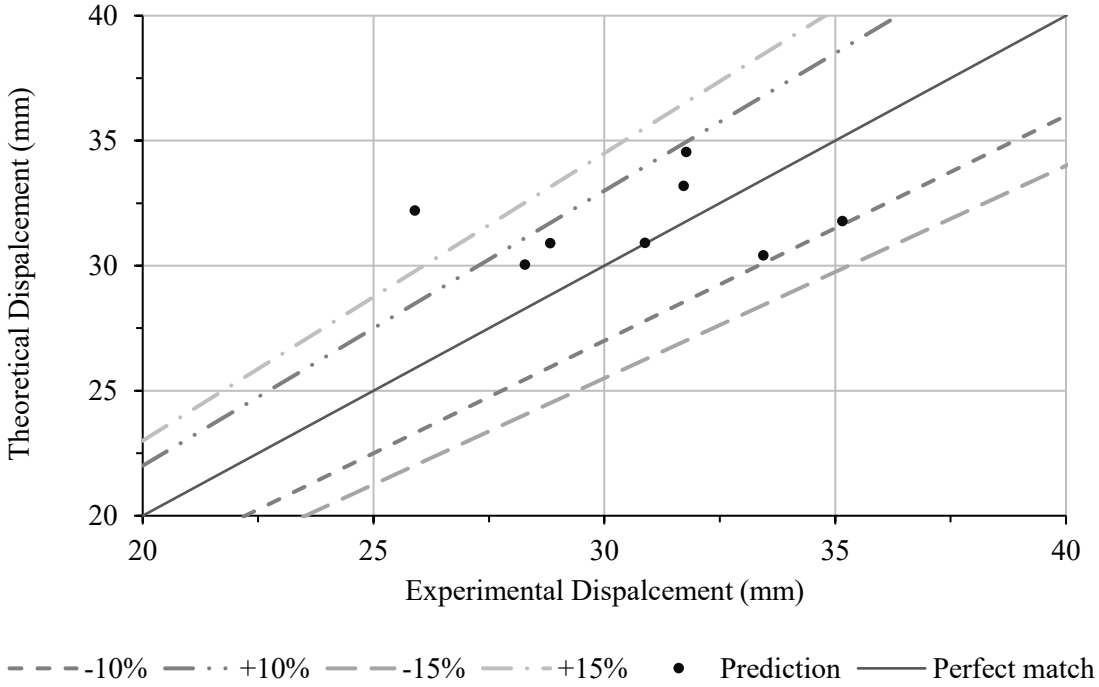

Figure 6.15: Displacement predictions (constant α) for beams tested statically.

As shown in Figures 6.14 and 6.15, using a single value of α as input for all reinforced beams shows acceptable results with average prediction ratios of 0.99 and 1.04 and COVs of 0.07 and 0.10 for force and displacement, respectively. However, more data points tend to fall outside the 10% and 15% error limits compared to the earlier prediction comparisons (Figure 5.7), where almost all prediction data was within the 10% error limit for both forces and displacements, and higher COV value is also observed when using a constant value of α especially for displacement. The comparison between experimental and theoretical results for beams tested dynamically using the constant α value is shown in Figure 6.16 and Figure 6.17, for maximum resistance and its corresponding displacement data, respectively,

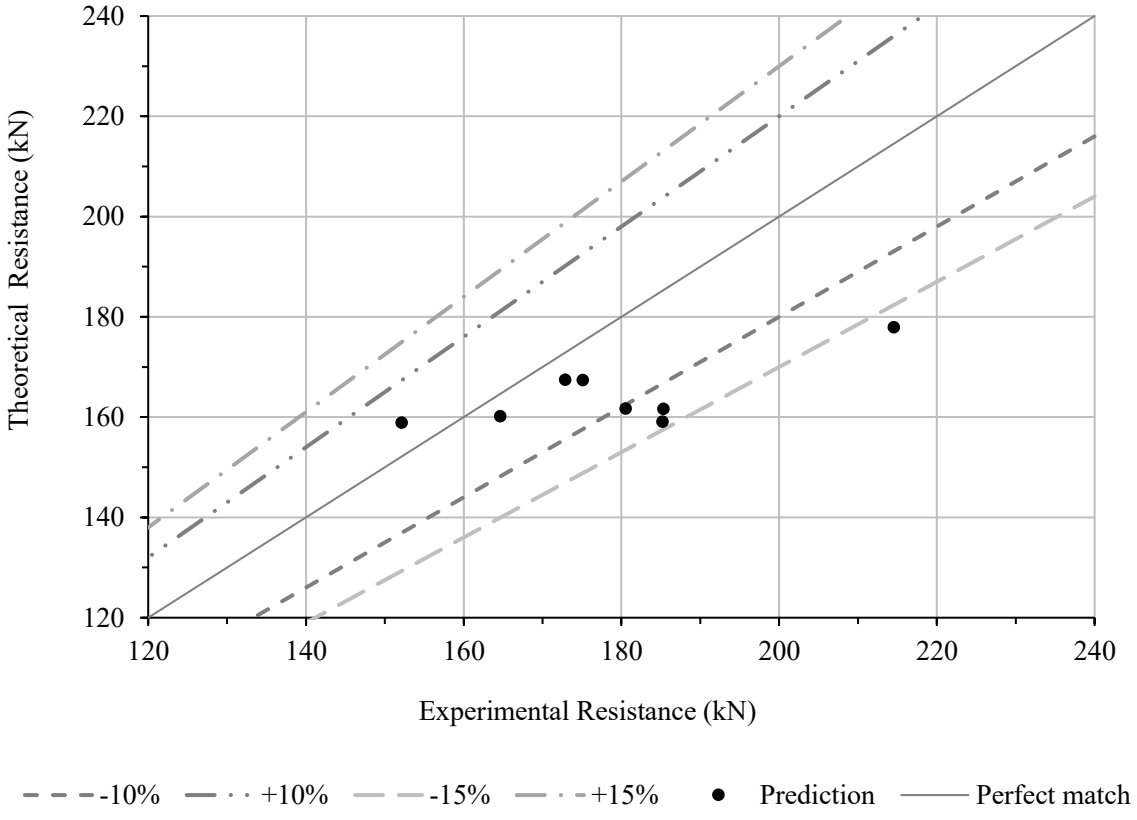

Figure 6.16: Resistance predictions (constant α) for beams tested dynamically.

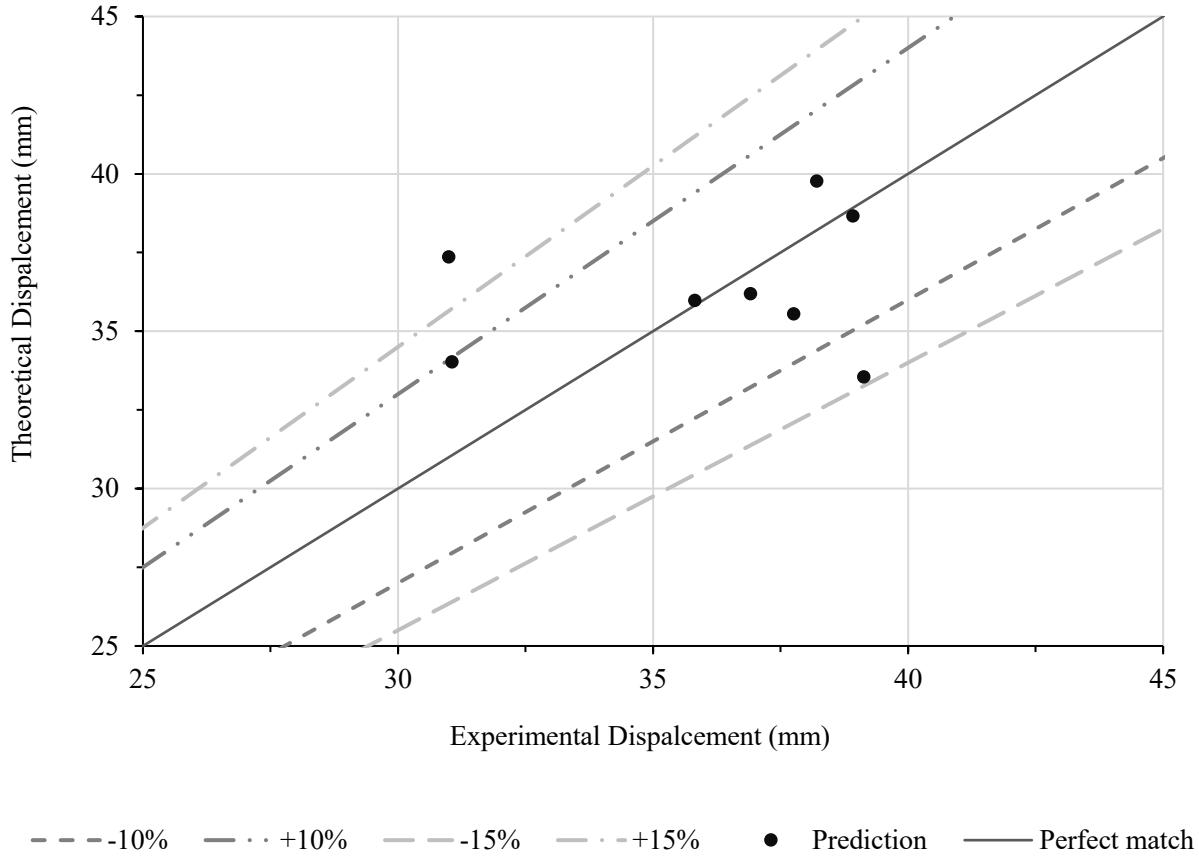

Figure 6.17: Displacement predictions (constant α) for beams tested dynamically.

Similar results were observed for the dynamically tested beams. Acceptable agreement was obtained for the average prediction ratios, with values of 0.92 and 1.01 for force and displacement, respectively, and COVs of 0.08 and 0.10. However, more data points tend to fall outside the 10% and 15% error limits compared to the earlier prediction comparisons (Figure 5.20), and higher COV values were observed when using a constant α. For specimen D-20M-B1, the α value was limited to 1.13, corresponding to the point of maximum moment in the sectional analysis (Chapter 5). Experimentally, after reaching peak load, the beam exhibited a sudden drop in capacity due to cracking on the tension side. This behavior was modeled by introducing a plastic hinge at mid-span, with all deformation assumed to be concentrated at that location (Section 5.2).

6.5 Design recommendation

The glulam beams with rebar and plate reinforcement exhibited significantly higher deformation capacity, with crushing and wrinkling of wood fibers observed on the compression side compared to unreinforced beams. This behavior resulted in a shift toward a more ductile failure mode. Nonlinearity was evident in the force–displacement curves prior to peak load, indicating that the compression fibers at the top of the beam exceeded their crushing stress. This was followed by the formation of tensile cracks, a sudden drop in load-carrying capacity, and subsequent residual flexural capacity. Both rebar- and plate-reinforced beams demonstrated improvements in strength compared to unreinforced beam under both static and dynamic blast tests, while stiffness increased when compared to the unreinforced beam.

Based on the output of the current study, a reinforcement ratio of approximately 1.6% (e.g., 15M rebar or an equivalent steel plate) offers a balanced option for improving strength, stiffness, and ductility while maintaining constructability and preserving desirable flexural behaviour. Ratios within the range of 1% to 2% showed significant enhancement in the performance, making this range suitable for most practical strengthening and retrofit applications. When reinforcement ratios exceeded 2.5%, the risk of shear failure dominating the failure mode is present. This transition is undesirable because shear failures are typically more brittle and less predictable, reducing the ductility and energy dissipation benefits associated with NSM strengthening. Higher reinforcement ratios require wider and deeper grooves, which reduce the net timber section, increase the likelihood of splitting along the groove corners, and complicate fabrication and installation. Such configurations also demand tighter quality control to ensure proper alignment, epoxy bonding, and anchorage performance. Moreover, due to potential rebar curvature and

placement imperfections, an epoxy cover of approximately 5 mm is recommended to ensure the rebar is fully embedded within the section, allowing proper bond development and minimizing the risk of unbonded areas or voids.

CHAPTER SEVEN: CONCLUSION AND RECOMMENDATION

7.1 Conclusion of the research

In this research, eight glulam beams reinforced with varying steel reinforcement ratios were employed for both static and dynamic testing. Opposed to external reinforcement methods, the NSM reinforcement method was utilized by hollowing out slots along the beam length, after which the steel reinforcements were placed inside these slots and attached to the wood with the aid of epoxy. The reinforcement ratios applied on the tension side of the beams included 10M, 15M, and 20M, representing 0.8%, 1.6%, and 2.5%, respectively. Additionally, steel plates were utilized to reinforce the glulam beams with the same ratio as the 15M reinforcement rebar. Moreover, the positioning of these plates was investigated, with horizontal placement on the side of the beam and vertical placement on its outer surface being compared to assess their respective behaviors. Vertical positioning was deemed more appropriate when access to the side of the beam is constrained. The present research study yields the following conclusions:

1. The NSM method, incorporating steel plates and rebars, demonstrated significant success, resulting in a substantial increase in strength ranging from 23.0% to 63.7% compared to unreinforced beams for statically tested beams. Additionally, the stiffness of the beams increased by 11.0% to 32.6% following reinforcement with the NSM method. Notably, the post-peak behavior of the reinforced beams exhibited improvement, with ductility ratios ranging from 1.1 to 6.4 for statically tested beams.

2. The reinforced beams displayed significantly greater deformation capacity compared to their unreinforced counterparts. This was characterized by the occurrence of wood fiber crushing or

wrinkling on the compression side of the beam, leading to a notable shift in the failure mode towards a more ductile failure at the compression face. The force-displacement curve exhibited nonlinearity prior to reaching the maximum force showing that the compression fibers at the top of the beam exceeded their crushing stress. After that a sudden decrease in load capacity occurred due to the formation of tensile cracks. As displacement is further increased, the damage on the compression side of the beam became more apparent.

3. The epoxy material exhibited satisfactory performance, showing no signs of debonding, or slipping between the wood and rebar during the testing period at the end sides of the beam. Instances of debonding were only observed near the specimens' ultimate failure. Moreover, all beams reinforced with plates displayed slip damage and failure between the reinforcement and the wood, or between the reinforcement and the epoxy layer, close to ultimate failure.

4. In dynamic tests, the addition of rebars and plates significantly enhanced both the stiffness and strength of the reinforced beams compared to the unreinforced ones. The strength and stiffness improvements ranged from 30.3% to 83.8% and from 7.8% to 38.1%, respectively, while the ductility ratios ranged from 1.2 to 7.2.

5. The epoxy material demonstrated excellent performance, with no instances of debonding or slippage observed between the wood and rebar at the end side of the beam in dynamically tested beams with rebars. However, specimen D-15M-B2 experienced a rebar plug-out failure during the post-peak phase, while all beams reinforced with plates exhibited slip damage during their post-peak resistance.

6. An analytical model based on layered-section analysis was developed to predict the behavior of reinforced beams, while steel reinforcement was simulated as concentrated elements at a point. This model encompassed three distinct stages of analysis: elastic, inelastic, and plastic hinge analysis. The analytical model demonstrated strong agreement with experimental data, covering strain, displacement, and force resistance results.

Despite extensive efforts to comprehensively understand the behavior of glulam members under static and blast loading, obtaining accurate and reliable readings from strain gauges across the entire strain-displacement curve was challenging. This challenge was particularly evident near the beam's maximum force and was further complicated by the premature failure of strain gauges, notably during the dynamic blast test.

7.2 Recommendations for Future Research

Based on the findings of this research, the following areas are recommended for further investigation under both static and dynamic (blast) loading conditions:

1. Span-to-Depth Ratios and Cross-Sectional Variations

Future studies should explore a range of span-to-depth ratios and cross-sectional dimensions to assess their influence on the effectiveness of the NSM reinforcement technique.

2. Alternative Reinforcement Materials

Investigate the use of alternative reinforcement materials such as GFRP and CFRP rebars or plates as potential substitutes for steel, with particular attention to their bond performance and energy dissipation characteristics.

3. Dual-Face Reinforcement

Examine the effects of reinforcing both the tension and compression face of the beam. This study focused solely on tension-side reinforcement; reinforcing both sides may yield further improvements in structural performance and strength.

4. Influence of Axial Loading

Assess the interaction between axial loads and NSM reinforcement performance, particularly for columns or beams in frames where combined loading conditions are expected.

5. Application to Other Engineered Wood Products

Extend the NSM reinforcement approach to other engineered wood products, such as LVL and Parallel Strand Lumber (PSL), to evaluate its broader applicability and performance across different material types.

6. Advanced Numerical Modeling Techniques

Use other analytical and numerical methods such as the Finite Element Method (FEM) to analyze the behavior of glulam beams. This approach can provide a more detailed understanding of local stress distribution, bond behavior, and potential failure mechanisms, complementing the experimental and sectional analysis results.

References

Alam, P., Ansell, M. P., and Smedley, D. (2009). Mechanical repair of timber beams fractured in flexure using bonded-in reinforcements. Composites Part B: Engineering, 40(2), 95–106.

Algassem, O., Li, Y., & Aoude, H. (2019). Ability of steel fibers to enhance the shear and flexural behaviour of high-strength concrete beams subjected to blast loads. Engineering Structures, 199, 109611.

Algassem, O., Li, Y., and Aoude, H. (2017). Influence of steel fibers on the shear and flexural performance of high-strength concrete beams tested under blast loads. IOP Conference Series Materials Science and Engineering, 246, 012011.

Alhayek, H., and Svecova, D. (2012). Flexural stiffness and strength of GFRP-Reinforced timber beams. Journal of Composites for Construction, 16(3), 245–252.

Alkhudery, H. H., Al-Tameemi, H. A., and Al-Katib, H. a. A. (2023). Experimental and theoretical investigation of the structural behavior of reinforced glulam wooden members by NSM steel bars and shear reinforcement CFRP sheet. Open Engineering, 13(1).

ASCE/SEI 59-22 (2022). Blast Protection of Buildings. ASCE/SEI 59-22, American Society of Civil Engineers, Reston, VA.

ASTM International. *ASTM D198-22: Standard Test Methods of Static Tests of Lumber in Structural Sizes.* West Conshohocken, PA: ASTM International, 2022.

ASTM International. *ASTM A370-24: Standard Test Methods and Definitions for Mechanical Testing of Steel Products.* West Conshohocken, PA: ASTM International, 2024.

APA – The Engineered Wood Association, TT-082B, (2012). True and apparent moduli of elasticity. In Technical Topics.

Bakalarz, M. M. (2024). Mechanical Properties of Full-Scale Wooden Beams Strengthened with Carbon-Fibre-Reinforced Polymer Sheets. Materials, 17(19), 4917.

Bakalarz, M. M., and Kossakowski, P. G. (2022). Strengthening of Full-Scale Laminated Veneer Lumber Beams with CFRP Sheets. Materials, 15(19), 6526.

Bakalarz, M. M., Kossakowski, P., and Tworzewski, P. (2020). Strengthening of Bent LVL Beams with Near-Surface Mounted (NSM) FRP Reinforcement. Materials (Basel), 13(10), 2350.

Barragán, O. G., and Jacob, J. (2007). Flexural strengthening of glued laminated timber beams with steel and carbon fiber reinforced polymers (Master's thesis), Department of Civil and Environmental Engineering, Chalmers University of Technology.

Barrett, J. D., and Lau, W. (1994). "Canadian Lumber Properties." Canadian Wood Council, Ottawa, Ontario.

Bazan, I. M. M. (1980). "Ultimate bending strength of timber beams," thesis pre sented to Nova Scotia Technical College, at Halifax, Nova Scotia, in partial ful fillment of the requirements for the degree of Doctor of Philosophy.

Biblis, E. J. (1965). Analysis of wood-fiberglass composite beams within and beyond the elastic region. Forest Products Journal, 15(2), 81-88.

Biggs J. M., (1964). Introduction to Structural Dynamics, New York, NY: McGraw-Hill.

Biscaia, H. C., Chastre, C., da Cruz, D. S., and Franco, N. (2017). Flexural Strengthening of Old Timber Floors with Laminated Carbon Fiber–Reinforced Polymers. Journal of Composites for Construction, 21(1).

Bohannan, B. (1964). Prestressed laminated wood beams. U.S. Forest Prod. Lab. Res. Paper FPL 8, USDA Forest Service, Madison, Wise, Jan., 32 pp.

Borgin, K., Loedolff, G. F., and Saunders, G. R. (1968). Laminated Wood Beams Reinforced with Steel Strips. Journal of the Structural Division, 94(7), 1681–1705.

Borri, A., Corradi, M., & Speranzini, E. (2013). Reinforcement of wood with natural fibers. Composites Part B Engineering, 53, 1–8.

Brunetti, M., Christovasilis, I. P., Micheloni, M., Nocetti, M., and Pizzo, B. (2019). Production feasibility and performance of carbon fibre reinforced glulam beams manufactured with polyurethane adhesive. Composites Part B Engineering, 156, 212–219.

Buchanan, A. (1990). Bending strength of lumber. Journal of Structural Engineering, 116(5), 1213–1229.

Buchanan, A. H., & Abu, A. K. (2017, January 30). Structural Design for Fire Safety. John Wiley & Sons.

Bulleit, W. M., Sandberg, L. B., and Woods, G. J. (1989). Steel-Reinforced glued laminated timber. Journal of Structural Engineering, 115(2), 433–444.

Burrell, R. P., Aoude, H., and Saatcioglu, M. (2015). Response of SFRC Columns under Blast Loads. Journal of Structural Engineering, 141(9).

Bérubé, A., and Doudak, G. (2023). Investigation of energy-absorbing connections for application in mass timber structures. Engineering Structures, 297, 117018.

Bérubé, A., and Doudak, G. (2024). Enhancing energy dissipation in glued-laminated timber assemblies using boundary connections. Structures, 65, 106744.

Coleman, G. E., and Hurst, H. T. (1974). Timber structures reinforced with light gage steel. Forest Products Journal, 24(7), 45-53.

Corradi, M., Borri, A., Castori, G., and Speranzini, E. (2016). Fully reversible reinforcement of softwood beams with unbonded composite plates. Composite Structures, 149, 54–68.

Corradi, M., Vemury, C. M., Edmondson, V., Pologanathan, K., & Nagaratnam, B. (2020). Local FRP reinforcement of existing timber beams. Composite Structures, 258, 113363.

CSA (2024). Engineering design in wood. CSA O86, CSA Group, Mississauga, ON.

CSA (2021). Carbon steel bars for concrete reinforcement. CSA-G30.18:21, Canadian Standards Association, Toronto, Ontario, Canada.

CSA (2023). Design and assessment of buildings subjected to blast loads. CSA S850, CSA Group, Mississauga, ON.

CSA Group. (2013). G40.20-13/G40.21-13. General requirements for rolled or welded structural quality steel/structural quality steel. Reaffirmed 2023. Toronto, Canada.

Côté, D., and Doudak, G. (2019). Experimental investigation of cross-laminated timber panels with realistic boundary conditions subjected to simulated blast loads. Engineering Structures, 187, 444-456.

De Jesus, A. M., Pinto, J. M., and Morais, J. (2012). Analysis of solid wood beams strengthened with CFRP laminates of distinct lengths. Construction and Building Materials, 35, 817–828.

De Luca, V., & Marano, C. (2012). *Prestressed glulam timbers reinforced with steel bars. Construction and Building Materials*, 30, 206–217.

Dusenberry, D., O. (2010). Handbook for blast-resistant design of buildings, J. Wiley, Hoboken, N.J.

Fiorelli, J., and Dias, A. A. (2003). Analysis of the strength and stiffness of timber beams reinforced with carbon fiber and glass fiber. Materials Research, 6(2), 193–202.

Gand, A. K., Yeboah, D., Khorami, M., Olubanwo, A. O., and Lumor, R. (2018). Behaviour of strengthened timber beams using near surface mounted Basalt Fibre Reinforced Polymer (BFRP) rebars. Engineering Solid Mechanics, 6(4), 341–352.

Gentile, C., Svecova, D., and Rizkalla, S. (2002). Timber Beams Strengthened with GFRP Bars: Development and Applications. Journal of Composites for Construction, 6(1), 11–20.

Glišović, I., Stevanović, B., Todorović, M., and Stevanović, T. (2016). Glulam beams externally reinforced with CFRP plates. Wood Research, 61(1), 141–154.

Glos, P. (1978). Reliability theory for timber structures: determination of compres sion strength behavior of glulam components from interaction of material prop erties. Heft 34/1978. Laboratorium fur den Konstrucktieven Ingenieurbau. Technische Universitat Munchen, Munich, Germany (in German).

Goodwin, J., Woods, J. E., & Hoult, N. A. (2022). Assessing the structural behaviour of glued-laminated timber beams using distributed strain sensing. Construction and Building Materials, 325, 126844.

Gul, M., Waseem, S. A., & Bhat, J. A. (2024). Experimental investigation on strengthening of glulam timber beams using cold-formed steel sections. *Structures, 66,* 106767.

Hammoud, A., Yan, J., Li, Y., and Aoude, H. (2021). Blast behavior of columns built with high-strength concrete and Grade 690 MPa high-strength reinforcement. Canadian Journal of Civil Engineering, 48(11), 1422–1439.

He, M., Wang, Y., Li, Z., Zhou, L., Tong, Y., & Sun, X. (2022). An experimental and analytical study on the bending performance of CFRP-Reinforced Glulam beams. Frontiers in Materials, 8.

Jacques, E. (2014). RCBlast. (Version 0.5.1). Ottawa, ON. Retrieved from http://www.rcblast.ca

Jacques, E. (2016). Characteristics of reinforced concrete bond at high strain rates. Ph.D. thesis, University of Ottawa, Ottawa, ON.

Jacques, E., and Saatcioglu, M. (2019). Bond-slip modelling of reinforced concrete lap splices subjected to low and high strain rates. Engineering Structures, 195, 568–578.

Jacques, E., Lloyd, A., Braimah, A., Saatcioglu, M., Doudak, G., and Abdelalim, O. (2014). Influence of high strain-rates on the dynamic flexural material properties of spruce–pine–fir wood studs. Canadian Journal of Civil Engineering, 41(1), 56-64.

Johns, K. C., and Lacroix, S. (2000). Composite reinforcement of timber in bending. Canadian Journal of Civil Engineering, 27(5), 899-906.

Johnsson, H., Blanksvärd, T., and Carolin, A. (2006). Glulam members strengthened by carbon fibre reinforcement. Materials and Structures, 40(1), 47–56.

Jordan Gandia (2019). Bast retrofit of Unreinforced Masonry Walls using EEC shotcrete. Thesis Dissertation, University of Ottawa, Ottawa, ON.

Krauthammer, T. (2008). Modern Protective Structures, Taylor & Francis Group, Boca Raton, FL.

Lacroix, D. (2017). Investigating the Behaviour of Glulam Beams and Columns Subjected to Simulated Blast Loading. PhD Dissertation, University of Ottawa, Ottawa, ON.

Lacroix, D. N., and Doudak, G. (2015). Investigation of Dynamic Increase Factors in Light-Frame Wood Stud Walls Subjected to Out-of-Plane Blast Loading. Journal of Structural Engineering, 141(6), 04014159.

Lacroix, D. N., and Doudak, G. (2018a). Determining the dynamic increase factor for Glued-Laminated timber beams. Journal of Structural Engineering, 144(9), 04018160.

Lacroix, D. N., and Doudak, G. (2018b). Effects of High Strain Rates on the Response of Glulam Beams and Columns. Journal of Structural Engineering, 144(5), 04018029.

Lacroix, D. N., and Doudak, G. (2018c). Experimental and Analytical Investigation of FRP Retrofitted Glued-Laminated Beams Subjected to Simulated Blast Loading. Journal of Structural Engineering, 144(7), 04018089.

Lacroix, D. N., Doudak, G., and El-Domiaty, K. (2014). Retrofit Options for Light-Frame Wood Stud Walls Subjected to Blast Loading. Journal of Structural Engineering, 140(4), 04013104.

Lacroix, S., Doudak, G., and McGrath, R. (2021). Blast performance of GFRP-reinforced wood studs and walls. Journal of Composites for Construction, 25(3), 04021015.

Lantos, G. (1970). The flexural behavior of steel reinforced laminated timber beams. Wood Science, 2(3), 136-143.

Laura Ciornei (2012) Performance of Polyurea Retrofitted Unreinforced Concrete Masonry Walls under Blast Loading. Thesis Dissertation, University of Ottawa, Ottawa, ON.

Lee, J. Y., Aoude, H., Yoon, Y. S., and Mitchell, D. (2020). Impact and blast behavior of seismically-detailed RC and UHPFRC-Strengthened columns. International Journal of Impact Engineering, 143, 103628.

Li, C., and Aoude, H. (2023). Behaviour of UHPFRC-retrofitted RC beams with varying strengthening configurations under single and repeated blast loading. Cement and Concrete Composites, 142, 105180.

Livas, C., Ekevad, M., and Öhman, M. (2022). Experimental analysis of passively and actively reinforced glued-laminated timber with focus on ductility. Wood Material Science and Engineering, 17(2), 129–137.

Lopez-Molina, A. M., and Doudak, G. (2019). Retrofit techniques for Cross-Laminated Timber (CLT) elements subjected to blast loads. Engineering Structures, 197, 109450.

Mark, R. (1963). Wood-aluminum beams within and beyond the elastic range. Part II: Trapezoidal sections. Forest Products Journal, 13(11), 508-516.

Mathuros, A., Thongchom, C., Van Hong Bui, L., and Jongvivatsakul, P. (2024). Monotonic and cyclic flexural performance of timber beams strengthened with glass fiber-reinforced polymer rods using near-surface mounted technique. Structures, 65, 106729.

MathWorks (2024) MATLAB R2024a, MathWorks: Natick, MA, USA.

McGrath, A., and Doudak, G. (2021). Investigating the response of bolted timber connections subjected to blast loads. Engineering Structures, 236, 112112.

Nassr, A. A., Razaqpur, A. G., Tait, M. J., Campidelli, M., and Foo, S. (2012). Experimental Performance of Steel Beams under Blast Loading. Journal of Performance of Constructed Facilities, 26(5), 600–619.

Njeem, W., Aoude, H., Martín-Pérez, B., and Jrade, A. (2022). Blast performance and analysis of reinforced concrete beams subjected to corrosion of the longitudinal reinforcement. Structural Concrete, 24(1), 239–256.

Oliveira, D., Viau, C., and Doudak, G. (2023a). Modelling the behaviour of heavy and mass timber members subjected to blast loads. Engineering Structures, 291, 116397.

Oliveira, D., Viau, C., and Doudak, G. (2023b). Behaviour of mass timber members subjected to consecutive blast loads. International Journal of Impact Engineering, 173, 104454.

Park, R., and Paulay, T. (1975). Reinforced concrete structures. John Wiley and Sons, Inc., New York, N.Y.

Peterson, J. (1965). Wood Beams Prestressed with Bonded Tension Elements. Journal of the Structural Division, 91(1), 103–119.

Plevris, N., and Triantafillou, T., C. (1992). FRP-Reinforced wood as structural Material. Journal of Materials in Civil Engineering, 4(3), 300–317.

Poulin, M., Viau, C., Lacroix, D. N., and Doudak, G. (2017). Experimental and Analytical Investigation of Cross-Laminated Timber Panels Subjected to Out-of-Plane Blast Loads. Journal of Structural Engineering, 144(2), 04017197.

Raftery, G. M., and Harte, A. M. (2011). Low-grade glued laminated timber reinforced with FRP plate. Composites Part B Engineering, 42(4), 724–735.

Raftery, G. M., and Kelly, F. E. (2015). Basalt FRP rods for reinforcement and repair of timber. Composites Part B: Engineering, 70, 9–19.

Raftery, G. M., and Whelan, C. V. (2014). Low-grade glued laminated timber beams reinforced using improved arrangements of bonded-in GFRP rods. Construction and Building Materials, 52, 209–220.

Rescalvo, F. J., Timbolmas, C., Bravo, R., Valverde-Palacios, I., and Gallego, A. (2021). Improving ductility and bending features of poplar glued laminated beams by means of embedded carbon material. Construction and Building Materials, 304, 124469.

Ross, R. J. (Ed.). (2010). *Wood handbook—Wood as an engineering material.* General Technical Report FPL-GTR-190. Madison, WI: U.S. Department of Agriculture, Forest Service, Forest Products Laboratory, 509 p.

Shu, Q., Li, Q., and Huang, S. (2022). Investigation on the bending capacities of the timber beams reinforced with aluminium plate. European Journal of Environmental and Civil Engineering, 27(4), 1447–1466.

Stern E.G., Kumar V.K. (1973). Flitch beams. Forest Products Journal, 23(5): 40-47.

Shekarchi, M., Vatani Oskouei, A., & Raftery, G. M. (2020). Flexural behavior of timber beams strengthened with pultruded glass fiber reinforced polymer profiles. *Composite Structures, 241,* 112062.

Theakston, F. M. (1965). A feasibility study for strengthening timber beams with fiberglass. Canadian Agricultural Engineering, 7(1), 17–19.

Thelandersson, S. and Larsen, H.J. (2003) Timber Engineering. John Wiley & Sons, West Sussex.

Triantafillou, T. (1997). Shear reinforcement of wood using FRP materials. Journal of Materials in Civil Engineering, 9(2), 65–69.

Triantafillou, T. C., and Deskovic, N. (1992). Prestressed FRP sheets as external reinforcement of wood members. Journal of Structural Engineering, 118(5), 1270–1284.

Thevarajah, B. E., Remennikov, A. M., Ngo, T. D., Guan, H., and Gilbert, B. P. (2025). *Impact behaviour of hybrid timber beams*. In *Proceedings of the 14th World Conference on Timber Engineering (WCTE 2025)* (pp. 473–482). Brisbane, Australia. DOI:10.52202/080513-0059.

Unified Facilities Criteria Program (2008). Structures to resist the effects of accidental explosions (UFC 3-340-02), United States of America Department of Defense, Washington, D.C.

US Federal Emergency Management Agency (FEMA) “Reference Manual to Mitigate Potential Terrorist Attacks Against Buildings” FEMA-426/BIPS-06, October 2011 Edition 2.

Van Der Woerd, J. D., Wagner, M., Pietzsch, A., Andrae, M., & Gebbeken, N. (2022). Design methods of blast resistant façades, windows, and doors in Germany: a review. Glass Structures & Engineering, 7(4), 693–710.

Van Le, T., Ghazlan, A., Ngo, T., Remennikov, A., Kalubadanage, D., and Gan, E. C. J. (2020). Dynamic increase factors for Radiata pine CLT panels subjected to simulated out-of-plane blast loading. Engineering Structures/Engineering Structures (Online), 225, 111299.

Viau, C., and Doudak, G. (2016a). Investigating the Behavior of Light-Frame Wood Stud Walls Subjected to Severe Blast Loading. Journal of Structural Engineering, 142(12), 04016138.

Viau, C., and Doudak, G. (2016b). Investigating the Behaviour of Typical and Designed Wall-to Floor Connections in Light-Frame Wood Stud Wall Structures Subjected to Blast Loading. Canadian Journal of Civil Engineering, 43(6), 562–572.

Viau, C., and Doudak, G. (2021a). Behavior and Modeling of Glulam Beams with Bolted Connections Subjected to Shock Tube–Simulated Blast Loads. Journal of Structural Engineering, 147(1).

Viau, C., and Doudak, G. (2021b). Energy-Absorbing connection for Heavy-Timber assemblies subjected to blast Loads–Concept Development and Application. Journal of Structural Engineering, 147(4).

Viau, C., Lacroix, D. N., and Doudak, G. (2016). Damage level assessment of response limits in light-frame wood stud walls subjected to blast loading. Canadian Journal of Civil Engineering, 44(2), 106–116.

Wdowiak-Postulak, A., Bahleda, F., and Prokop, J. (2023). An experimental and numerical analysis of glued laminated beams strengthened by Pre-Stressed basalt Fibre-Reinforced polymer bars. Materials, 16(7), 2776.

Weibull, W. (1939). "A statistical theory of the strength of materials." Proc. No. 151, Royal Swedish Institute of Engineering Research, Stockholm, Sweden.

Wight, N., Viau, C., and Heffernan, P. (2024). Behaviour of glued-laminated timber beams under impact loading. Canadian Journal of Civil Engineering.

Xu, Q, Chen, JF, Zhu, L, Li, X and Zhang, F (2012), Strengthening timber beams with near surface mounted carbon fiber reinforced polymer rods. in Proceedings of the 6th International Conference on FRP Composites in Civil Engineering, CICE 2012. International Institute for FRP in Construction (IIFC), 6th International Conference on FRP Composites in Civil Engineering, CICE 2012, Rome, Italy, 13/06/2012.

Yang, H., Liu, W., Lu, W., Zhu, S., and Geng, Q. (2016a). Flexural behavior of FRP and steel reinforced glulam beams: Experimental and theoretical evaluation. Construction & Building Materials, 106, 550–563.

Yang, H., Ju, D., Liu, W., & Lu, W. (2016b). Prestressed glulam beams reinforced with CFRP bars. Construction and Building Materials, 109, 73–83.

Yeboah, D., and Gkantou, M. (2021). Investigation of flexural behaviour of structural timber beams strengthened with NSM basalt and glass FRP bars. Structures, 33, 390–405.

Yusof, A., and Rahman, A.B. (2017). Flexural strengthening of timber beams using carbon fibre reinforced polymer. International journal of applied engineering research, 12, 348-358.

Yusof, A., and Saleh, A. L. (2010). Flexural strengthening of timber beams using glass fibre reinforced polymer. Electronic Journal of Structural Engineering, 10, 45–56.

Zhou Nianqiang and Shi Weixing 2017 IOP Conf. Ser.: Mater. Sci. Eng. 191 012043.

Appendix A: Analytical Data

A.1 Modulus of elasticity

The total deflection of the beam including shear deformation for four-point bending test where loads are applied at the third points of the beam's length, can be calculated using the following Equations A.1.

$$\Delta = \frac{23\ P\ L^3}{1296\ E\ I} + \frac{PL}{\kappa 6GA} \qquad Eq.A1$$

Where Δ is the total deflection at the midspan of the beam. P is the load, while L denotes the clear span length and E is the modulus of elasticity of the beam. I stand for the beam's moment of inertia. κ: shear factor equal to $5/6$ for rectangular beam. G is the shear modulus. A is the cross-section area of the beam, since all layups of the beam have the same stress grade across the depth. Similar to ASTM D198-22, to find the experimental shear-free modulus of elasticity (E_{sr}). Equation A1 can be written as

$$E_{sr} = \frac{23\ K\ L^3}{1296\ I\left(1 - \frac{KL}{5GA}\right)} \qquad Eq.A2$$

Where K represents the stiffness. I stand for the beam's moment of inertia. A is the cross-section area of the beam. G is the shear modulus. Due to the complexity to measure G, the value of G was taken as $E/16$ according to CSA O86, Where E was taken according to the manufacturer as either axial E_{axial} or shear-free in bending E_{true}, both having the same value of 13,100 MPa since the stress grade is uniform across the layup depth.

The value of E_{sr} for each beam before reinforcement for both static and dynamic tests are shown in Table A.1.

Table A.1: Modulus of elasticities for beams before reinforcement.

Static Beams	E_{sr}	Dynamic Beams	E_{sr}
Unreinforced	12224	-	-
R-10M-B1	13401	D-10M-B1	13730
R-10M-B2	12429	D-10M-B2	14014
R-15M-B1	13435	D-15M-B1	12345
R-15M-B2	14336	D-15M-B2	13295
R-PL-B1	13037	D-PL-B1	13211
R-PL-B2	13881	D-PL-B2	13056
R-PL-H1	13649	D-PL-H1	12520
R-20M-B1	13540	D-20M-B1	12187
Average	13326	Average	13045
COV	0.050	COV	0.050

Since G is equal to $E/16$, and all layups have the same grade across the depth. Substituting the G value in Equation A1. E_{sr} can be calculated from Equation A3. Similar equation form can be calculated for different type of load patterns such as distributed load along the beam's length (APA – The Engineered Wood Association, TT-082B, 2012).

$$E_{sr} = \left(\frac{23\ K\ L^3}{1296\ I} + \frac{16\ KL}{5\ A}\right) \qquad Eq.A3$$

Equations A2 and A3 produce very close values with average of 13326 MPa and 13301 MPa, respectively, for static beams, and 13045 MPa and 13048 MPa, respectively, for dynamic beams. This is due to the fact (E_{sr}) values obtained from Eq. A3 was very close to the manufacturer value

E_{true} (13100), which in turn produce similar G values, when dividing by 16. In addition, the effect of shear stress on the modulus of elasticity values was found to be low.

A.2 Values of the parameter (α)

The values of the parameter (α) introduced in Chapter 5, for each reinforced beam are presented in Table A.2 for beams tested statically and dynamically.

Table A.2: The values of the factor (α).

Static Beams	α	Dynamic Beams	α
R-10M-B1	1.18	D-10M-B1	1.18
R-10M-B2	1.25	D-10M-B2	1.53
R-15M-B1	1.46	D-15M-B1	1.32
R-15M-B2	1.23	D-15M-B2	1.31
R-PL-B1	1.02	D-PL-B1	1.39
R-PL-B2	1.42	D-PL-B2	1.30
R-PL-H1	1.30	D-PL-H1	1.06
R-20M-B1	1.20	D-20M-B1	1.09
Average	1.26	Average	1.27

A.3 Plastic hinge length

In the investigation of plastic hinge length, three assumptions were considered: the plastic hinge length was taken as equal to the beam depth (d), twice the beam depth (2d), and the span between the two-point loads, equivalent to one-third of the beam length (L/3). Two specimens, R-15M-R1 and D-15M-R1, were examined under these assumptions, as illustrated in Figure A.1 and Figure A.2, respectively.

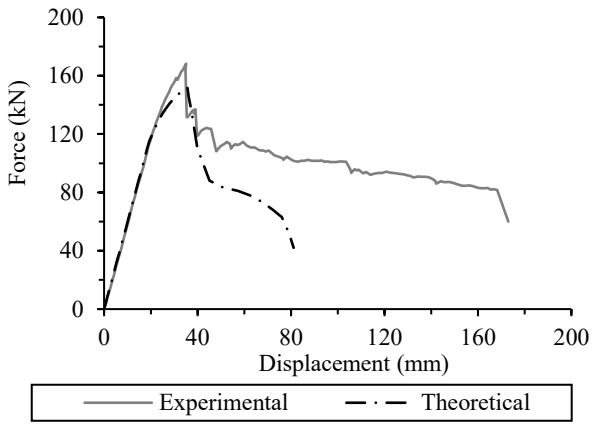

a) Plastic hinge as d

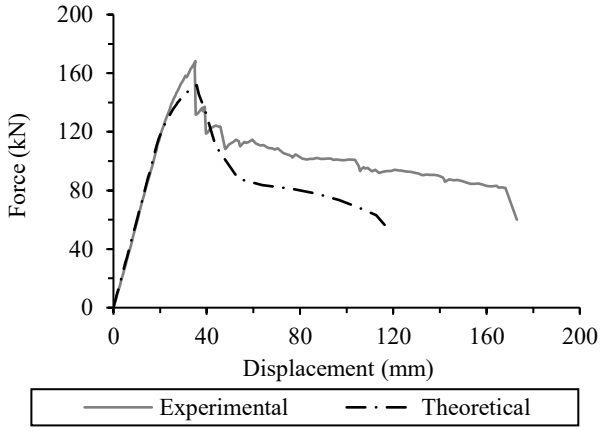

b) Plastic hinge as 2d

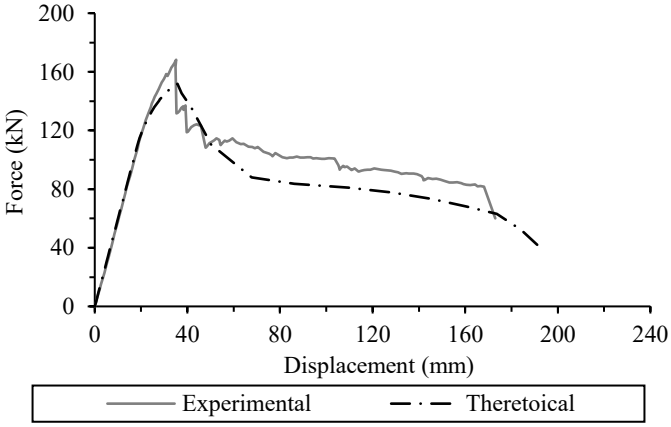

c) Plastic hinge as L/3

Figure A.1: Results for R-15M-B1

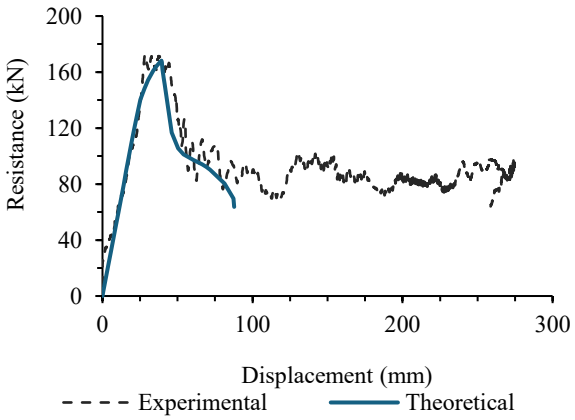

a) Plastic hinge as d

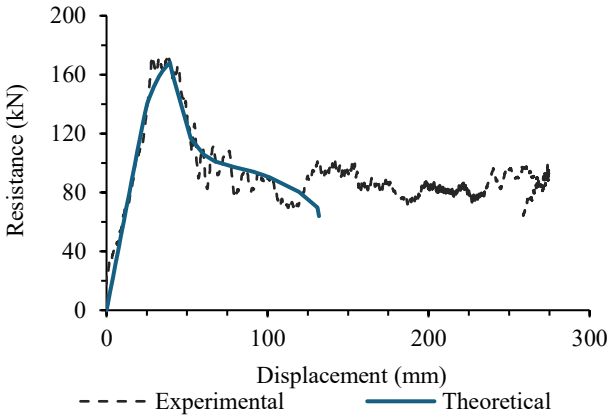

b) Plastic hinge as 2d

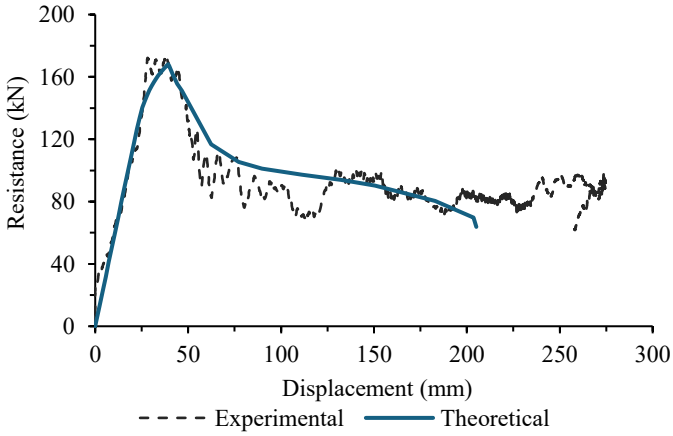

c) Plastic hinge as L/3

Figure A.2: Results for D-15M-B1

As this study is the first of its kind examining the post-peak behaviour analytically, the appropriate plastic hinge length is uncertain. However, the analysis indicates that assuming a plastic hinge length of L/3 yields better agreement with the observed results compared to using lengths equal to the beam depth (d) or twice the depth (2d) as shown in the above figures.

Appendix B: Static Analysis Data

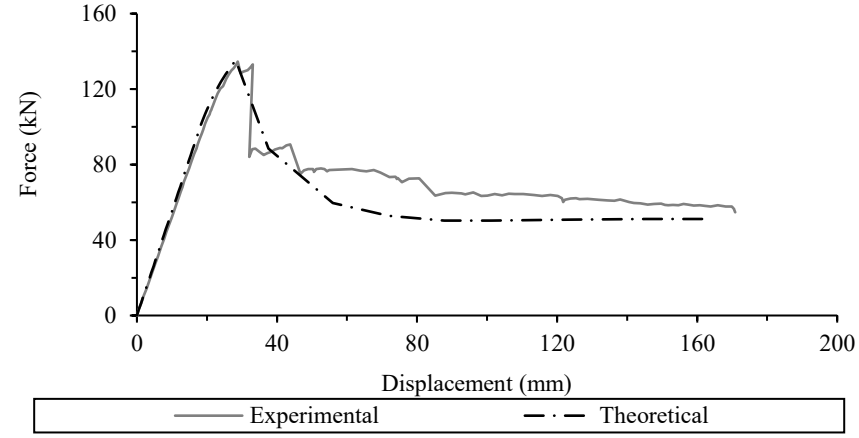

(a) Forces and displacements

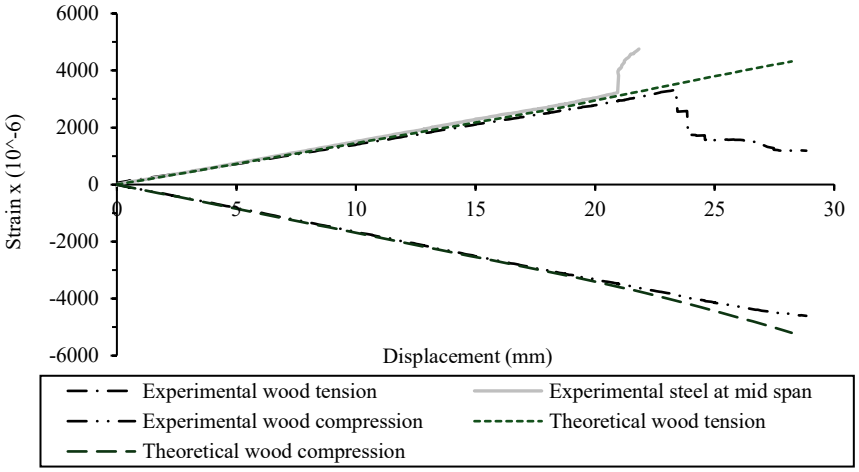

(b) Strains comparisons

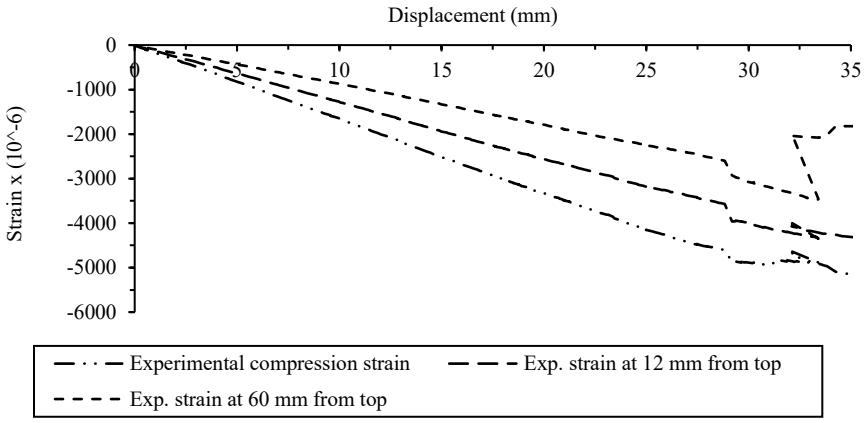

(c) Strains and displacements

Figure B.1: Results for R-10M-B1.

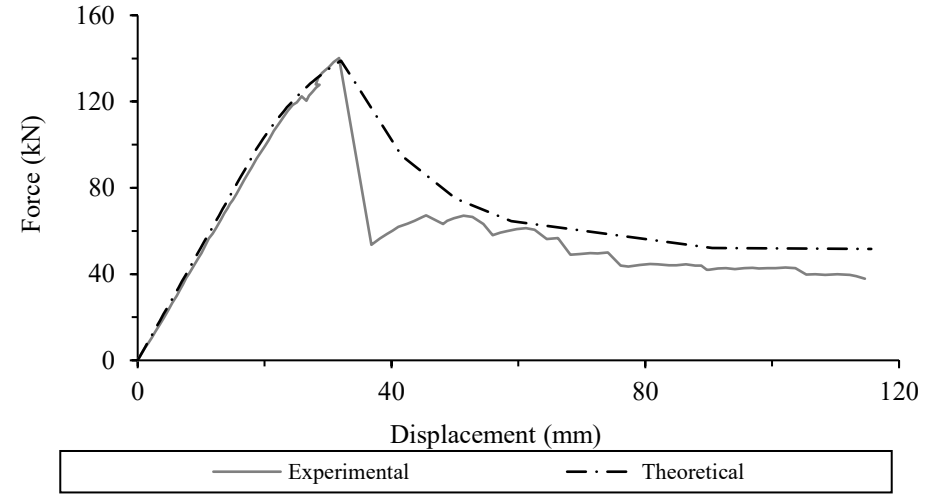

(a) Forces and displacements

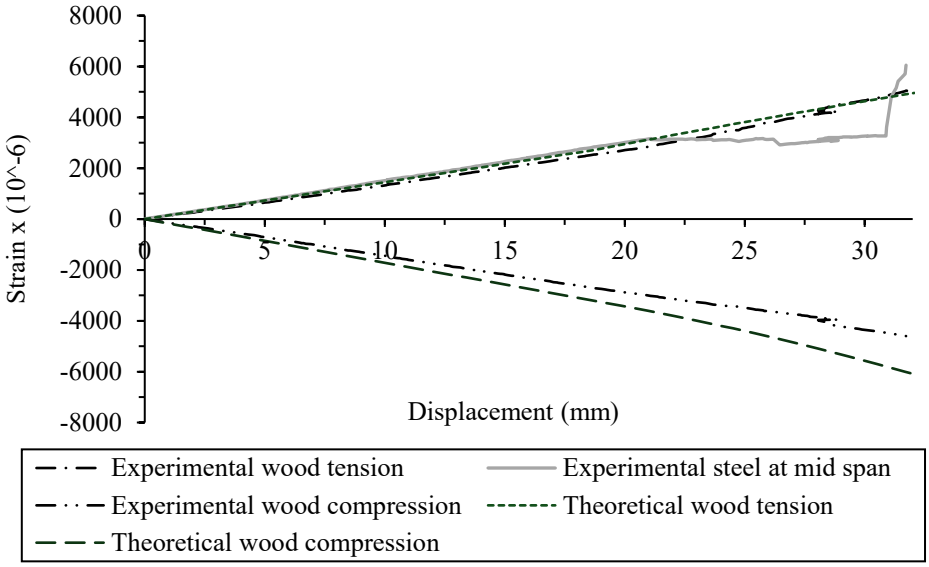

(b) Strains comparisons

Figure B.2: Results for R-10M-B2.

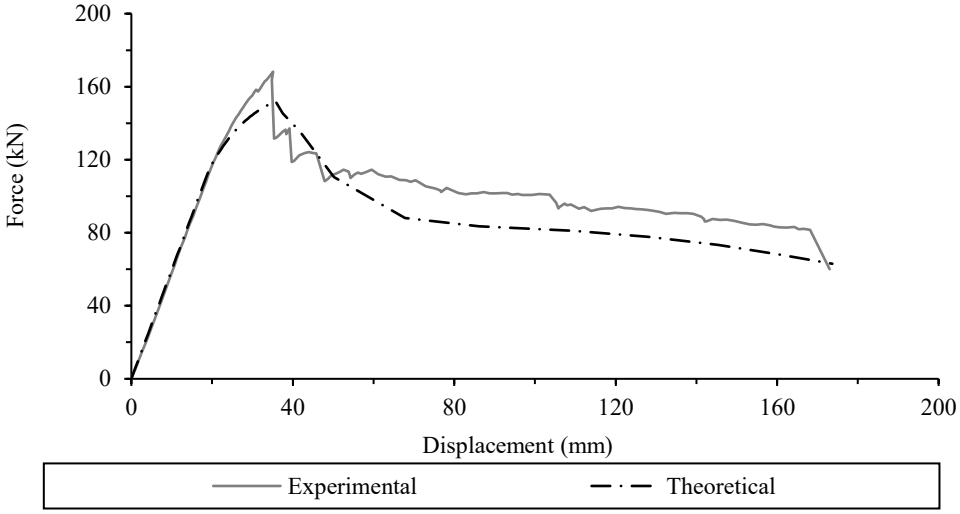

(a) Forces and displacements

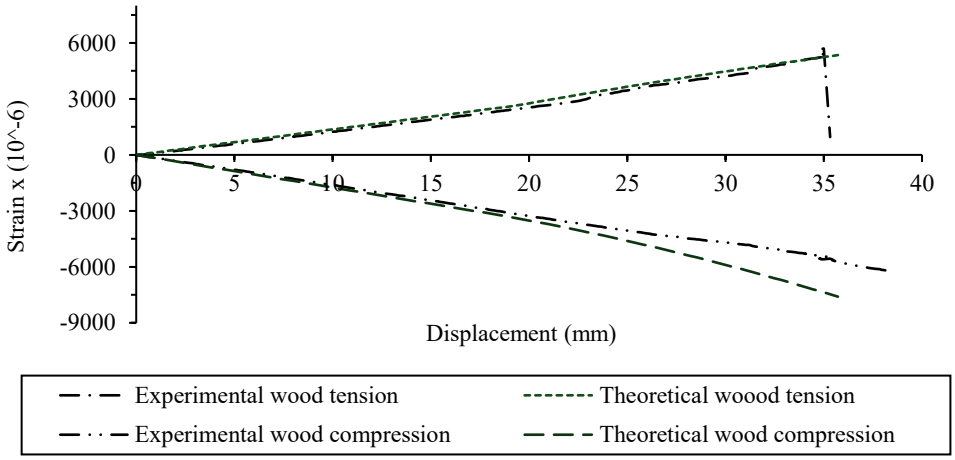

(b) Strains comparison

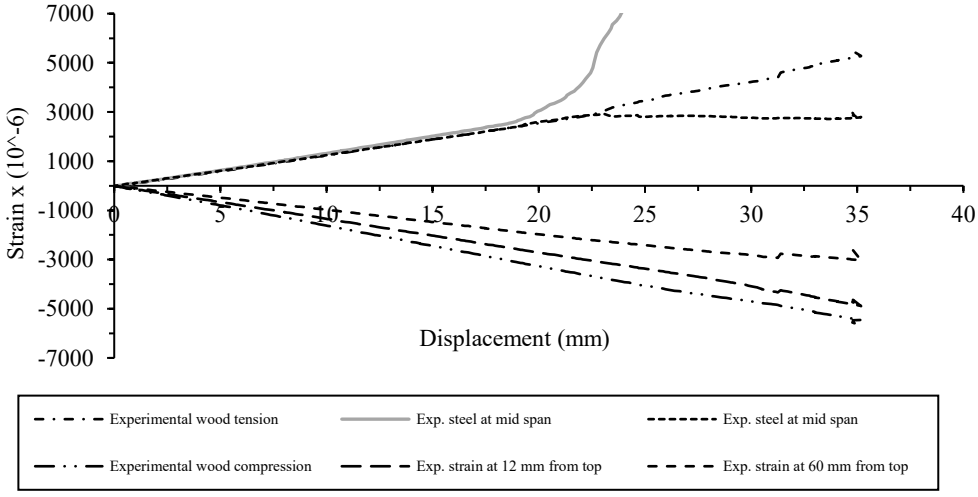

(c) Strains and displacements

Figure B.3: Results for R-15M-B1.

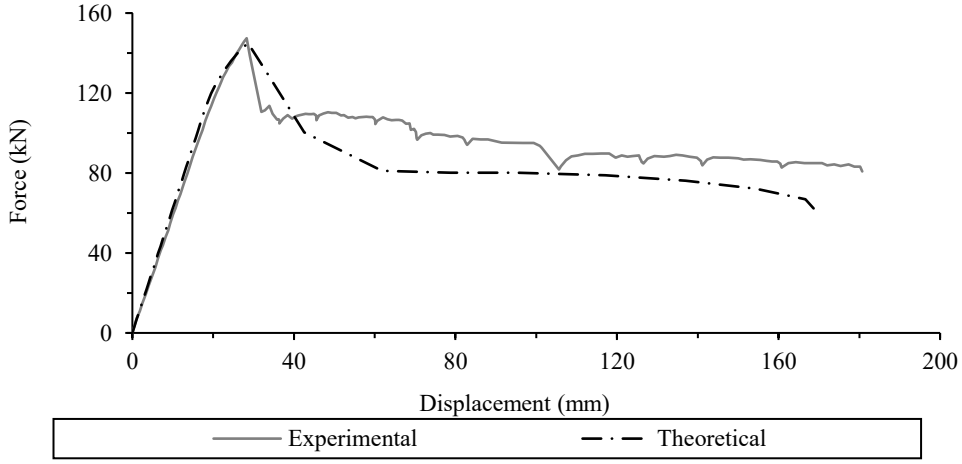

(a) Forces and displacements

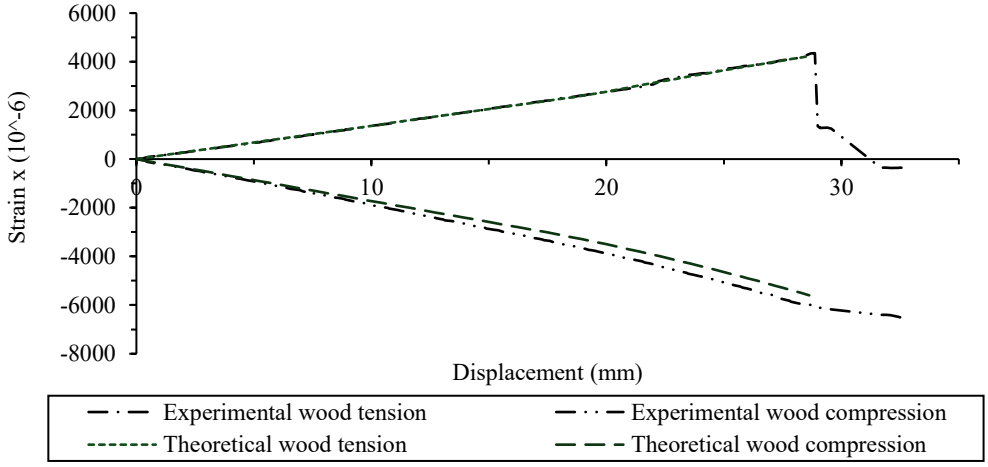

(b) Strains comparisons

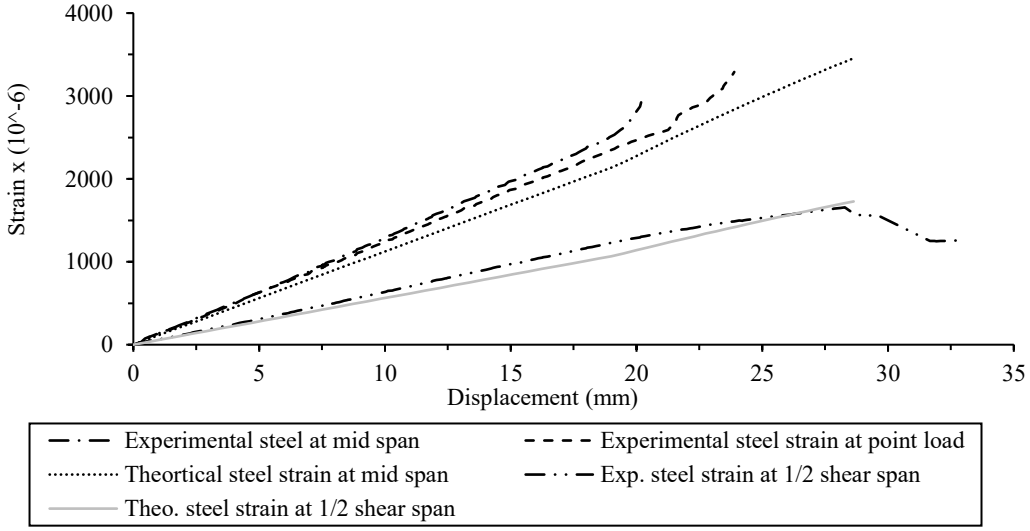

(c) Strains and displacements

Figure B.4: Results for R-15M-B2.

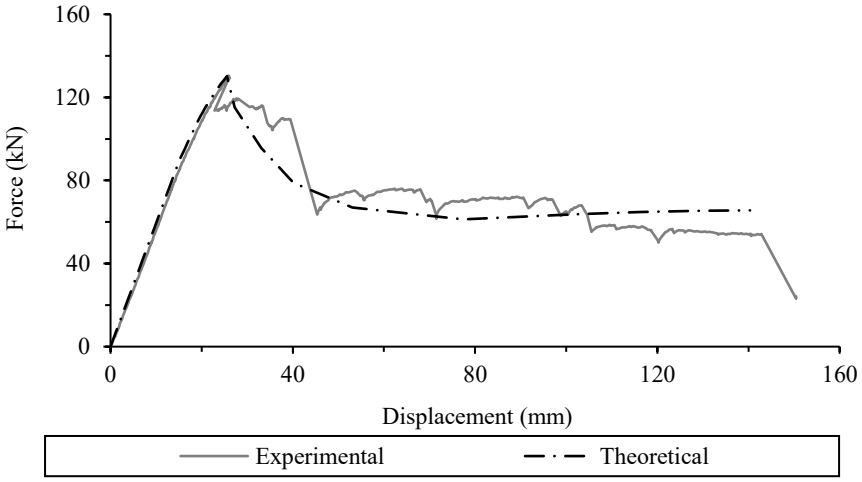

(a) Forces and displacements

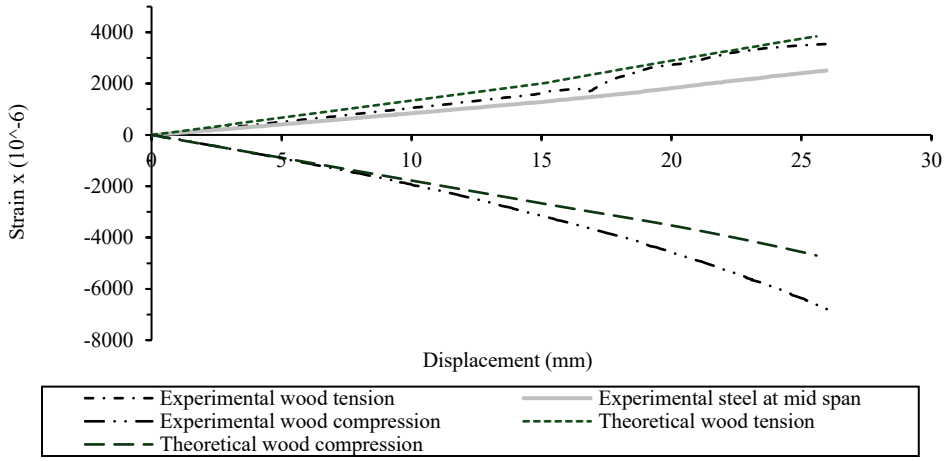

(b) Strains comparisons

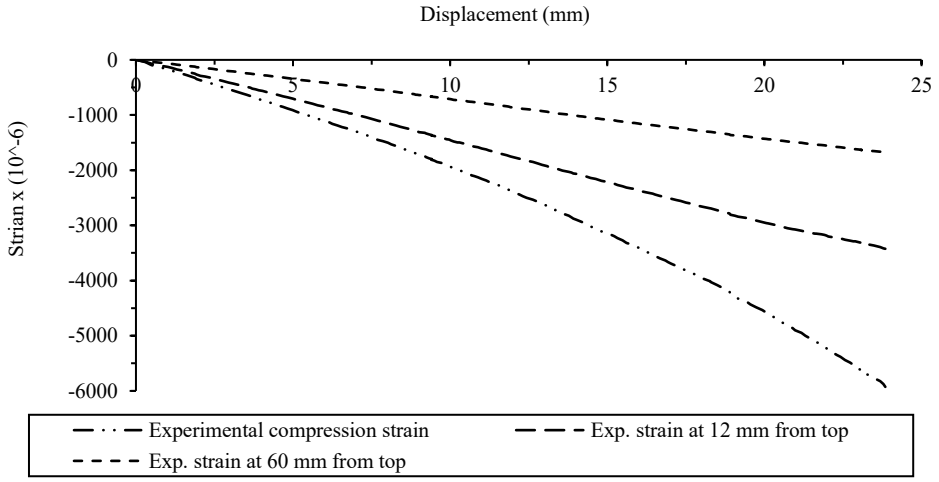

(c) Strains and displacements

Figure B.5: Results for R-PL-B1.

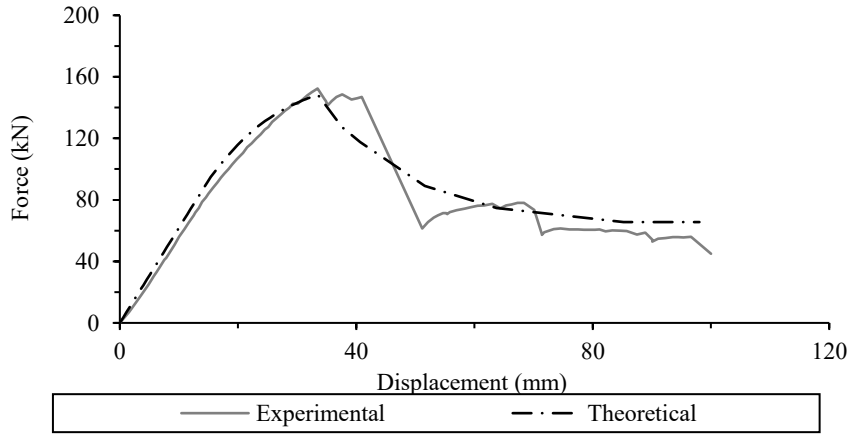

(a) Forces and displacements

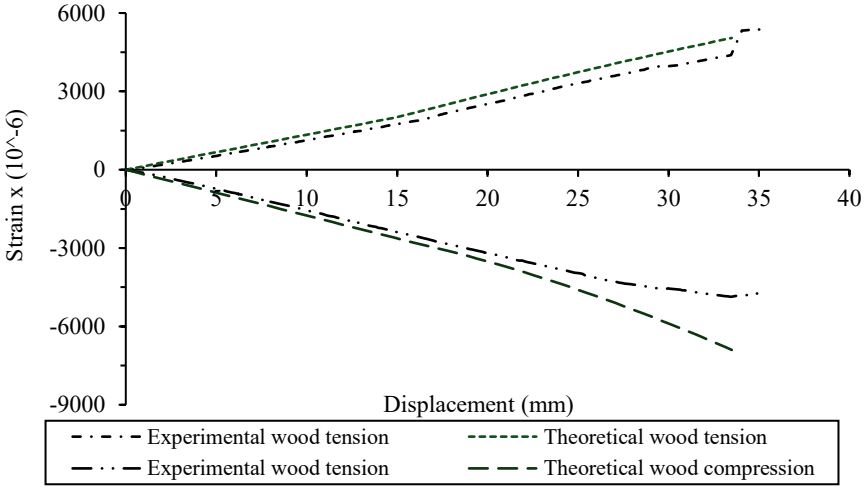

(b) Strains comparisons

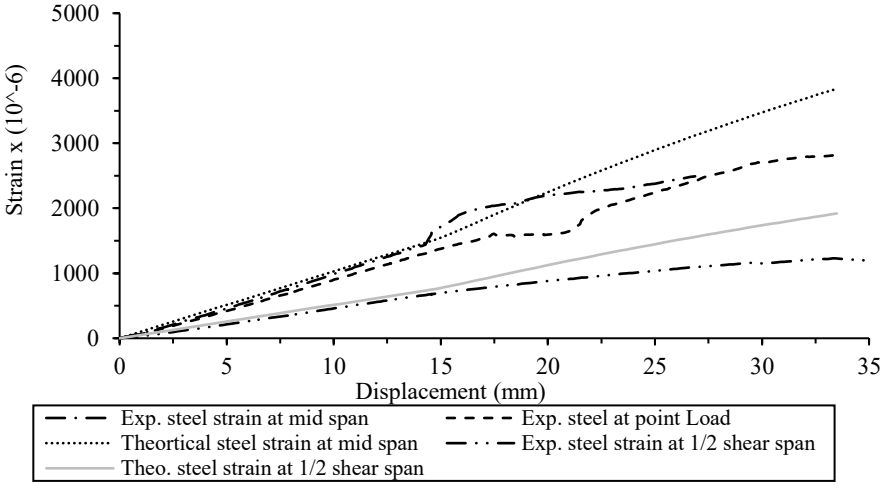

(c) Strains and displacements

Figure B.6: Results for R-PL-B2.

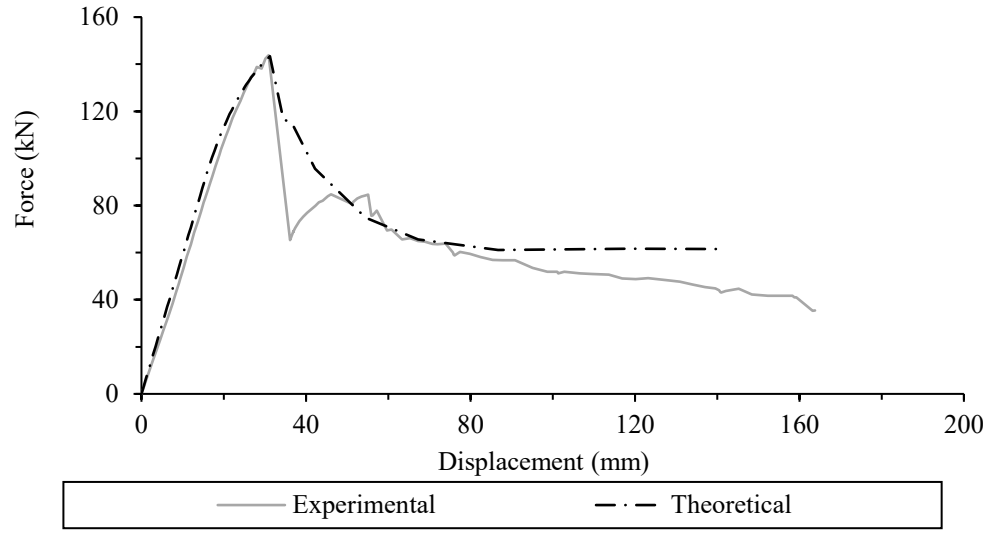

(a) Forces and displacements

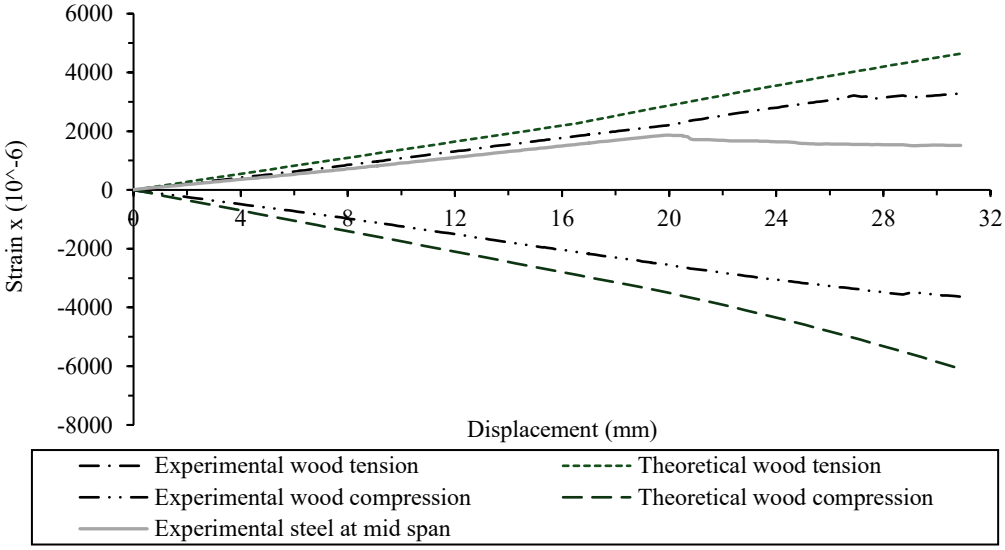

(b) Strains comparisons

Figure B.7: Results for R-PL-S1.

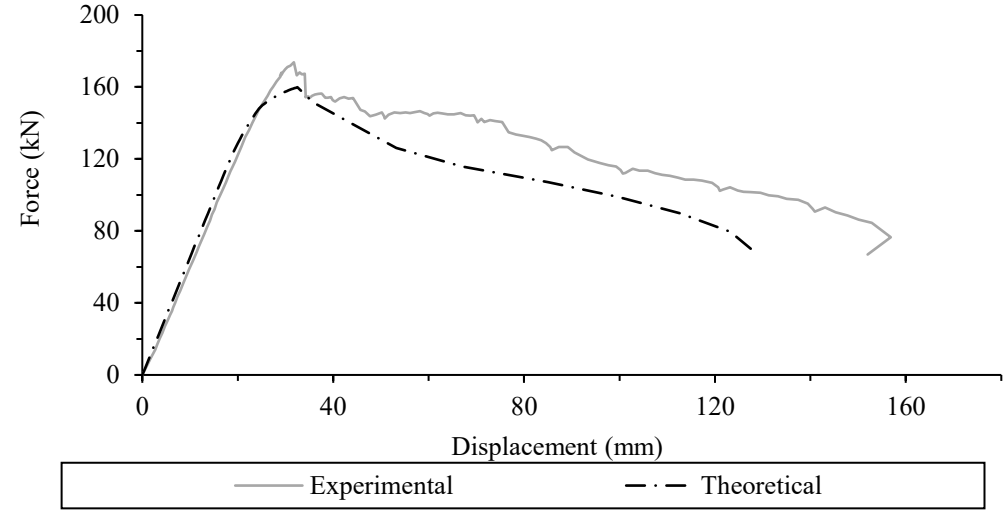

(a) Forces and displacements

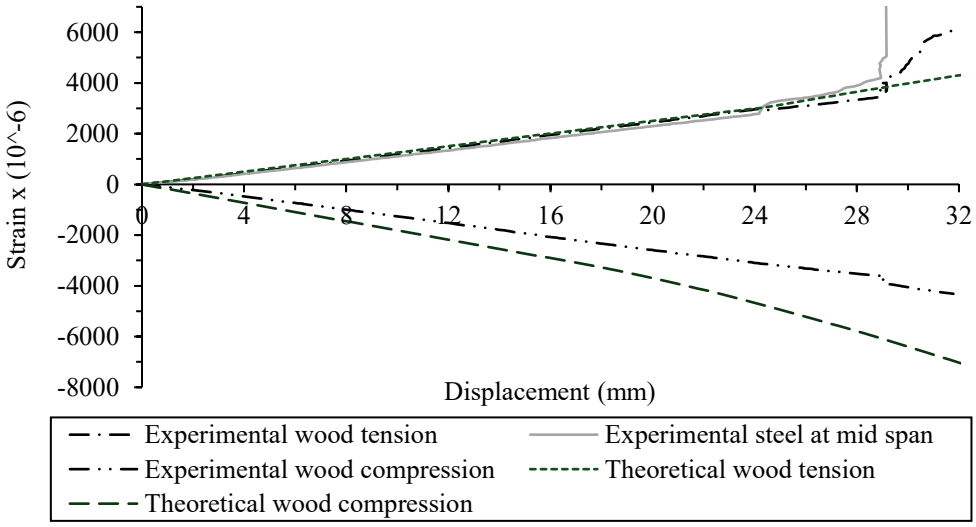

(b) Strains comparisons

Figure B.8: Results for R-20M-B1.

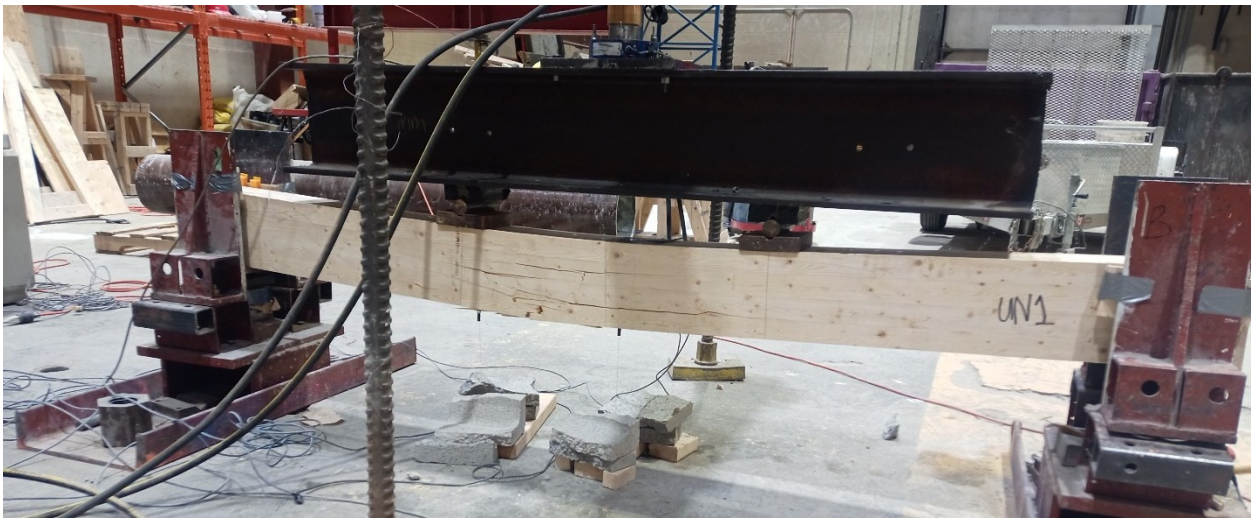

(a) During the test

(b) Tension side

(c) Compresion side

Figure B.9: Pictures for unreinforced beam.

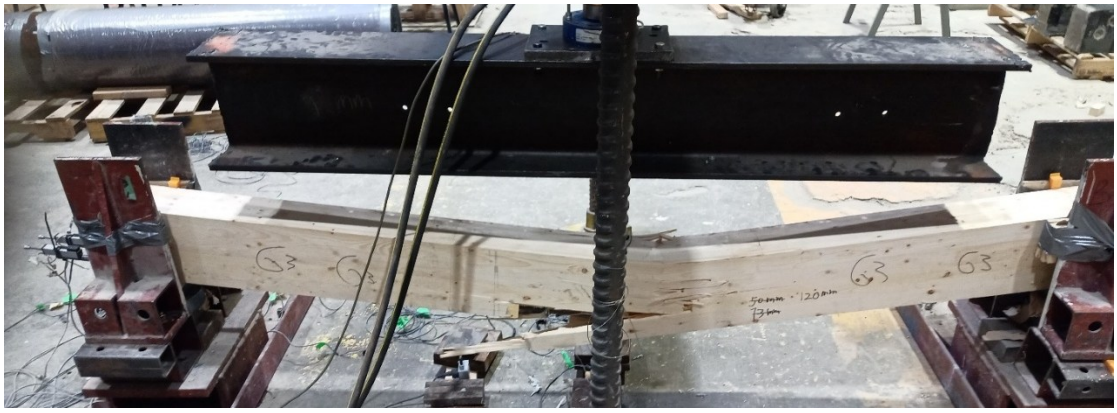

(a) After the test

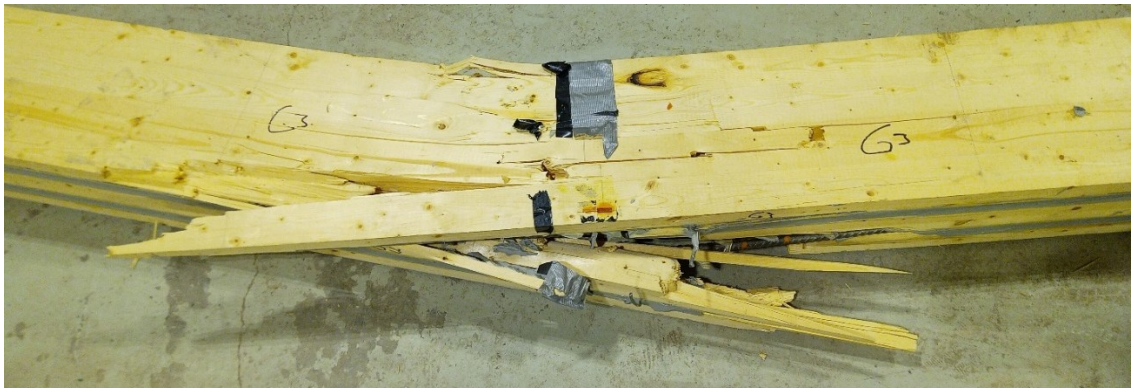

(b) Tension side

(c) Compresion side

Figure B.10: Pictures for R-10M-B1.

(a) During the test

(b) Tension side

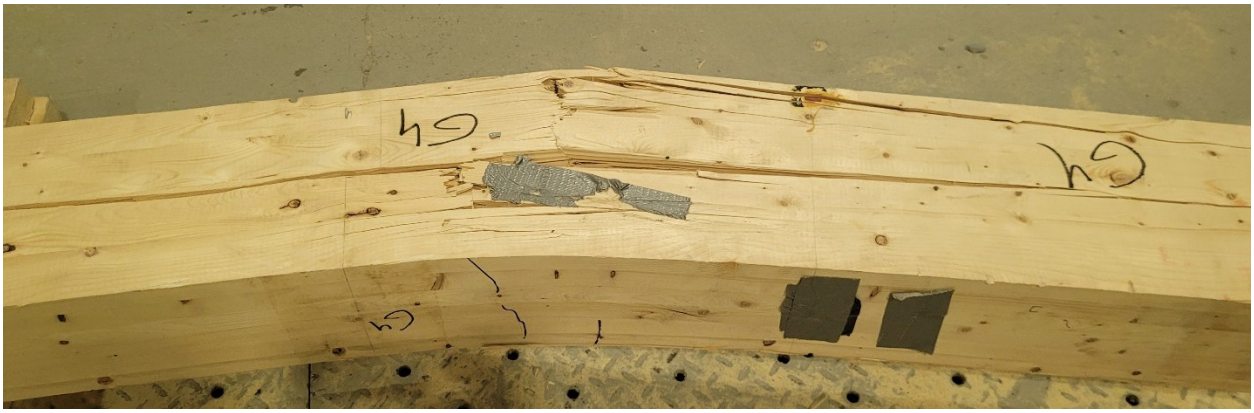

(c) Compresion side

Figure B.11: Pictures for R-10M-B2.

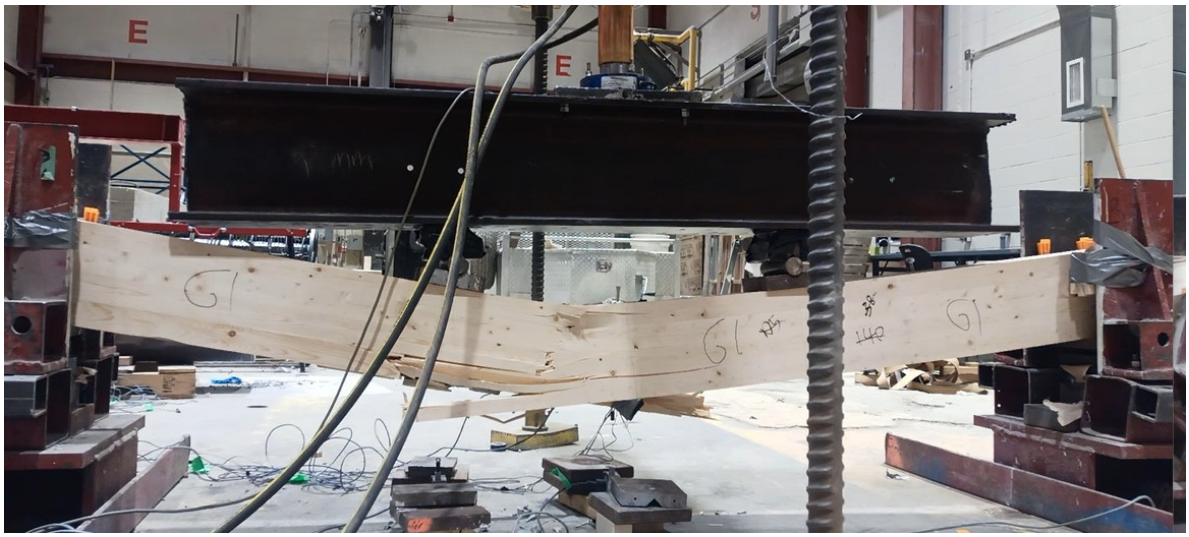

(a) During the test

(b) Tension side

(c) Compresion side

Figure B.12: Pictures for R-15M-B1.

(a) During the test

(b) Tension side

(c) Compresion side

Figure B.13: Pictures for R-15M-B2.

(a) During the test

(b) Tension side

(c) Compresion side

Figure B.14: Pictures for R-PL-B1.

(a) During the test

(b) Tension side

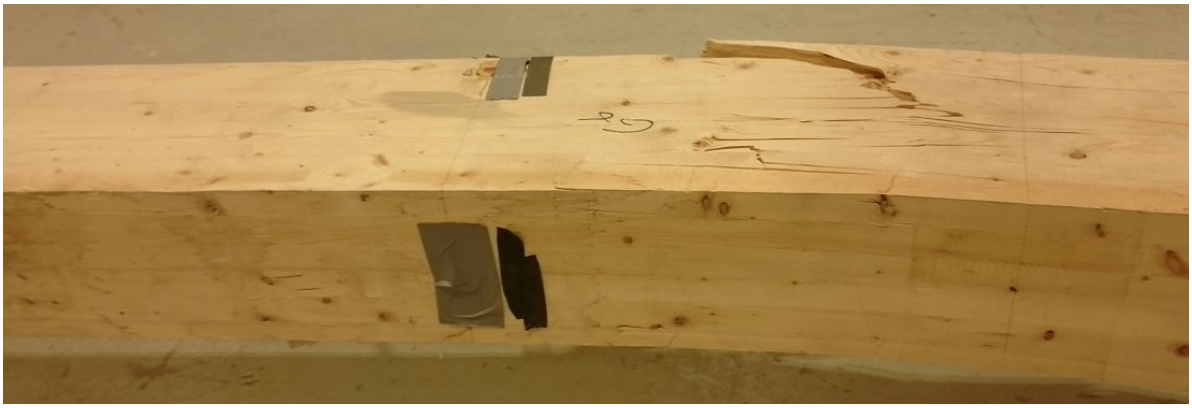

(c) Compresion side

Figure B.15: Pictures for R-PL-B2.

(a) During the test

(b) Tension side

(c) Compresion side

Figure B.16: Pictures for R-PL-S1.

(a) During the test

(b) Tension side

(c) Compresion side

Figure B.17: Pictures for R-20M-B1.

Appendix C: Dynamic Analysis Data

The results of the dynamic test are presented in this appendix, including pressure, impulses, dynamic reactions, and displacement histories. Additionally, this appendix documents the damage sustained by the beam during the test. The appendix also shows the screenshot of movement of reinforced beams under the blast test at rest, at maximum resistance ($R_{\max}$) and at the farthest position where the load transfer device (LTD) remains in contact with the sample (Δ_u).

The D-10M-B1 beam was tested on October 6, 2012, and subjected to a driver pressure of 530.9 kPa, resulting in a reflected pressure of 83.3 kPa and an impulse of 780.5 $kPa - ms$.

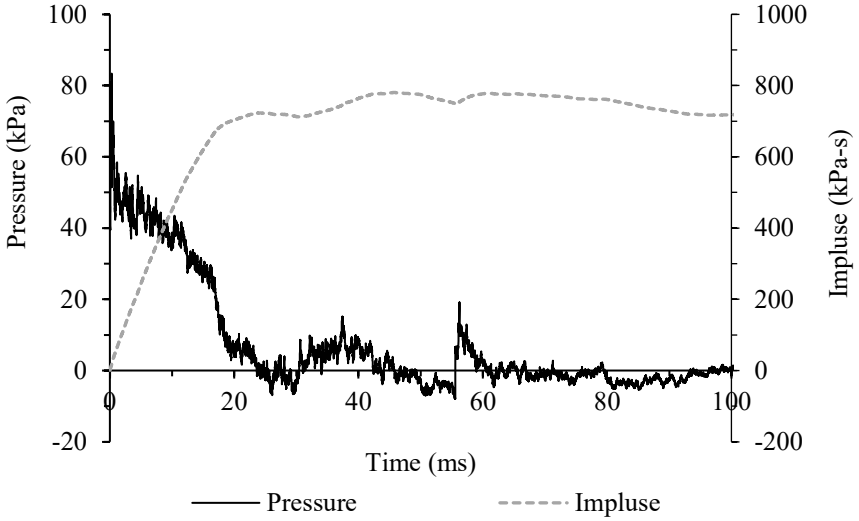

(a) Pressure and Impulse history

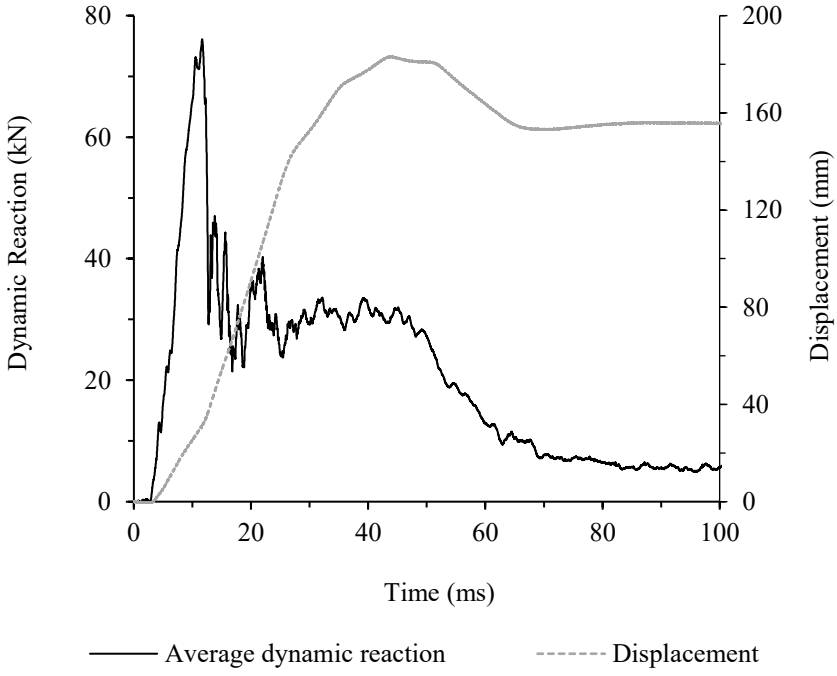

(b) Reaction and Displacement history

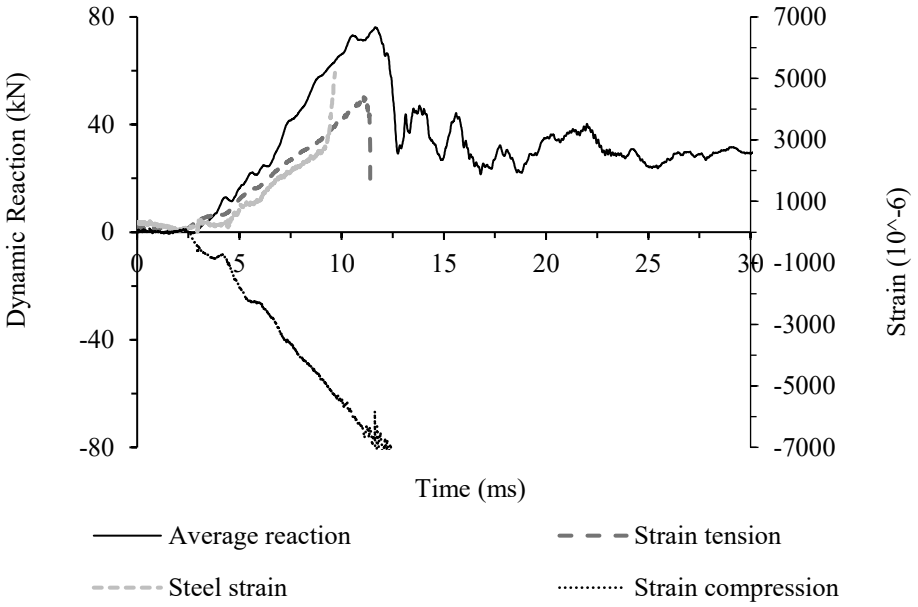

(c) Reaction and strains history

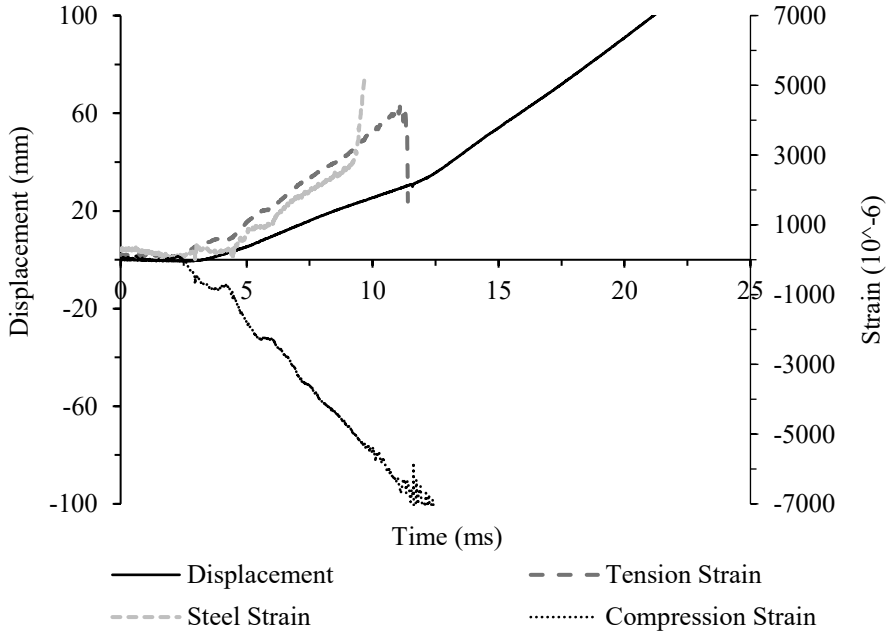

(d) Displacement and strains history

Figure C.1: Experimental data for D-10M-B1.

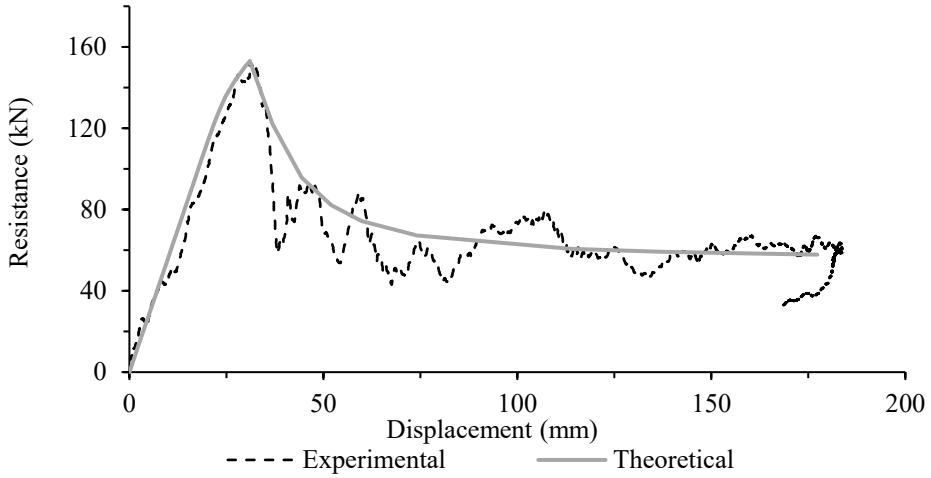

(a) Force-displacement curve

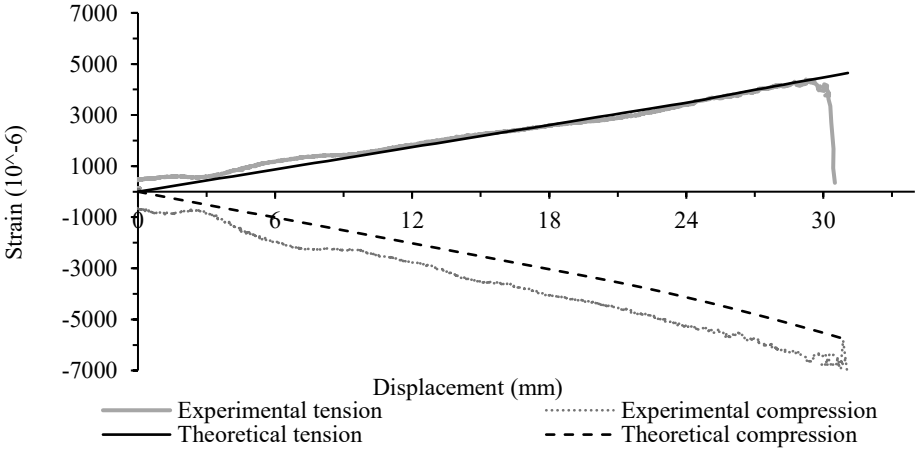

(b) Displacement-strain curve

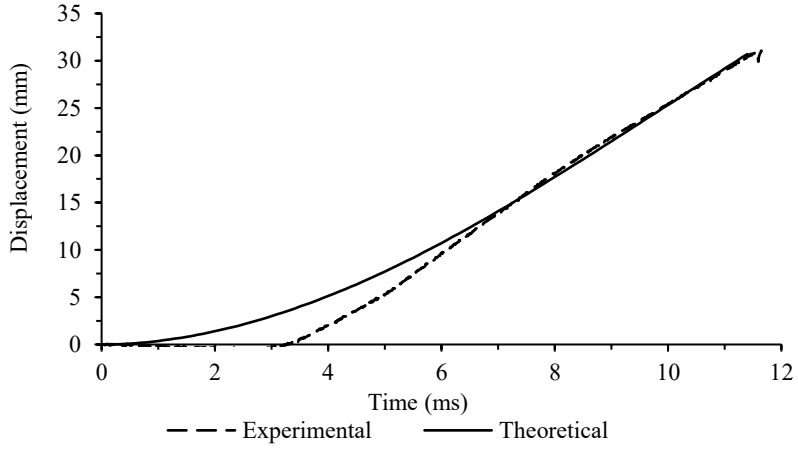

(c) Displacement-time curve

Figure C.2: Analytical and experimental data comparison for D-10M-B1.

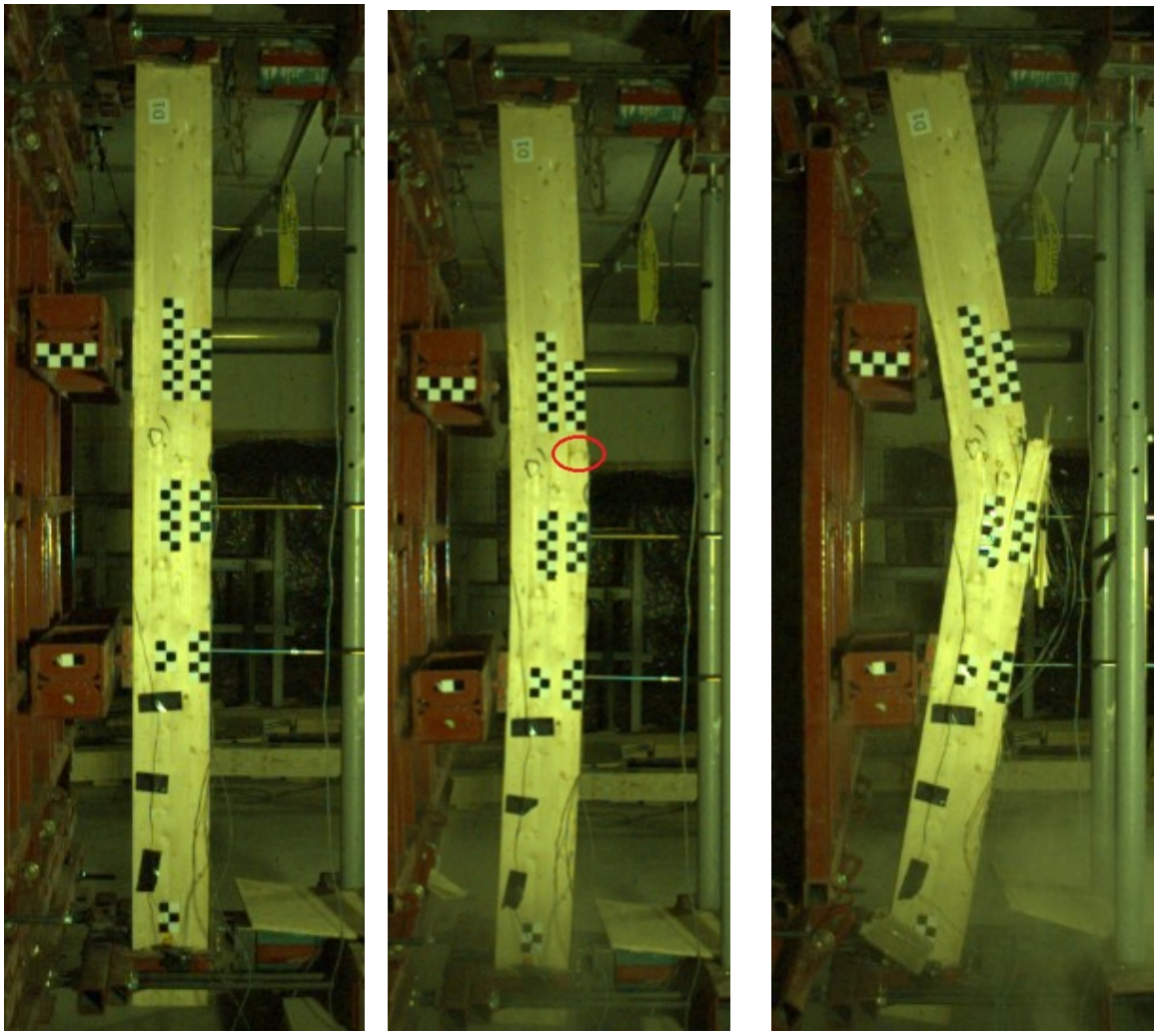

At Rest At R_{max} At Δ_u

Figure C.3: Dynamic test pictures for D-10M-B1.

(a) Before test

(b) After test

(c) Tension side

(d) Compression side

Figure C.4: Dynamic test pictures for D-10M-B1.

D-10M-B2 beam was tested on 14/Oct/2022 and subjected to driver pressure of 620.5 kPa, resulting in a reflected pressure of 88.8 kPa and an impulse of 912.4 $kPa - ms$.

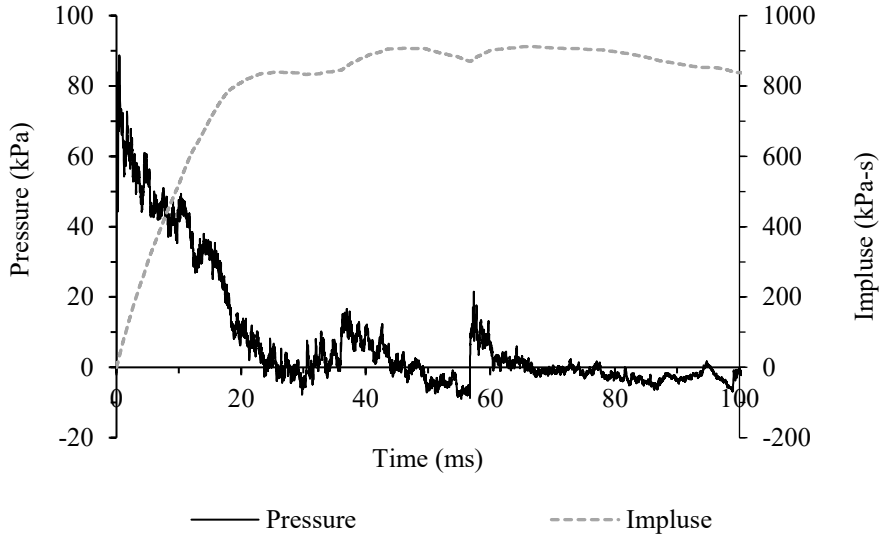

(a) Pressure and Impulse history

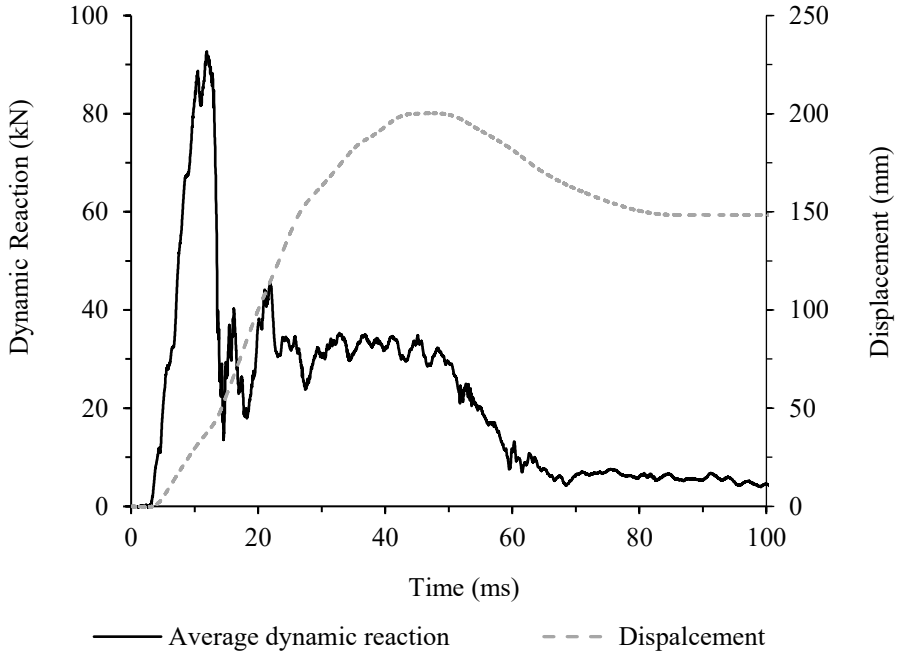

(b) Reaction and Displacement history

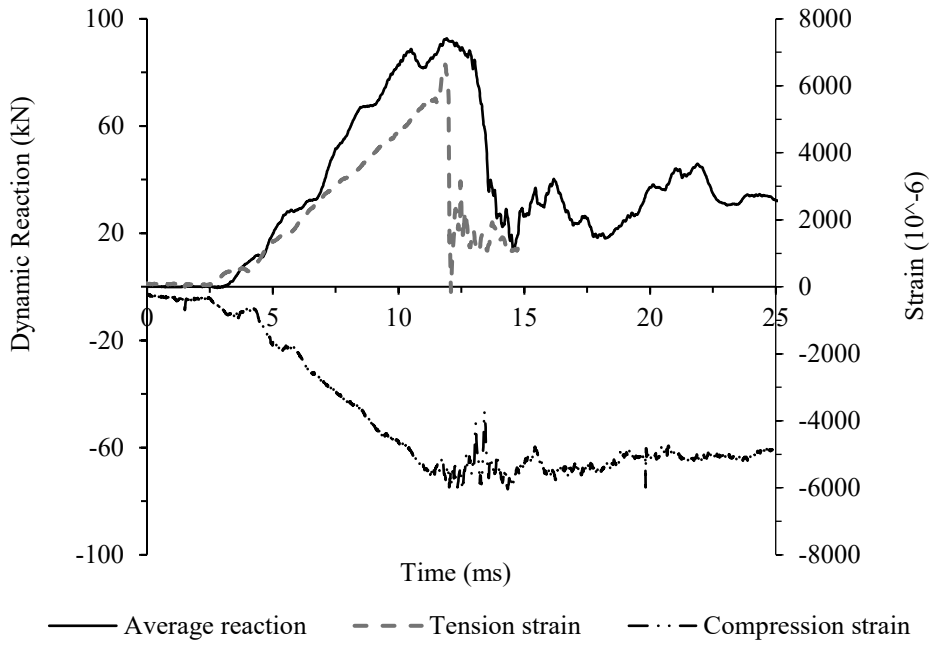

(c) Reaction and strains history

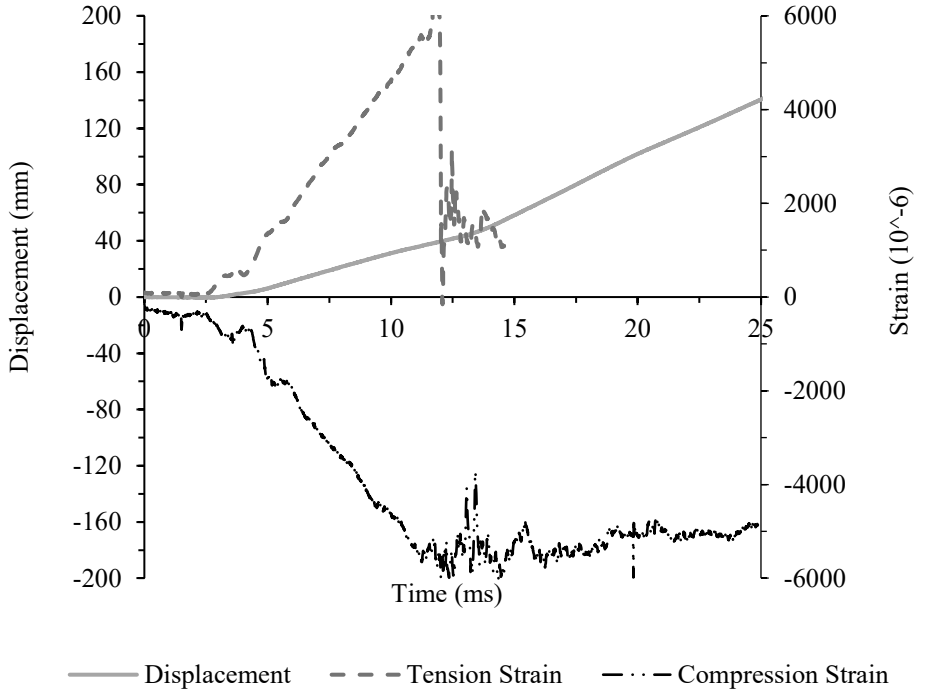

(d) Displacement and strains history

Figure C.5: Experimental data for D-10M-B2.

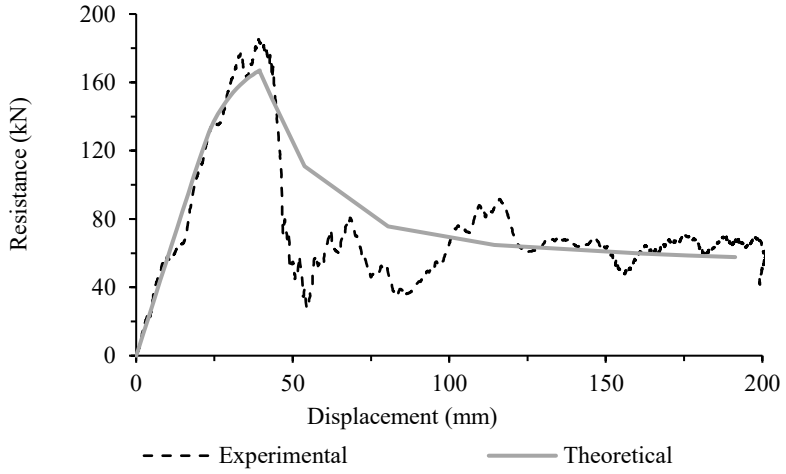

(a) Force-displacement curve

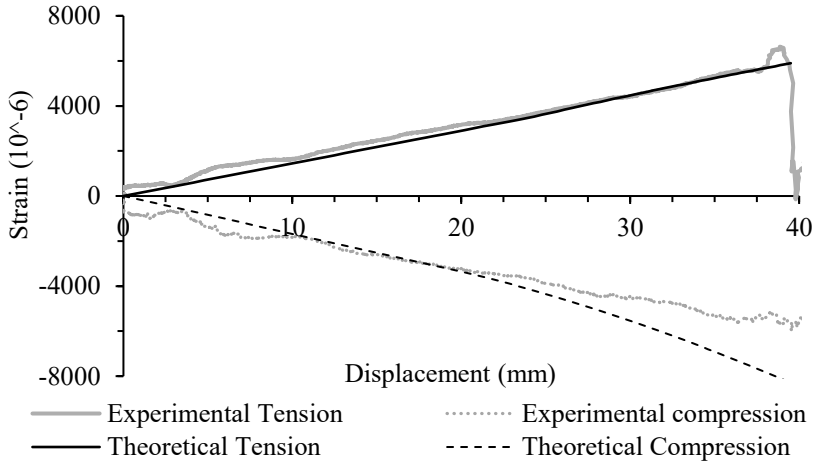

(b) Displacement-strain curve

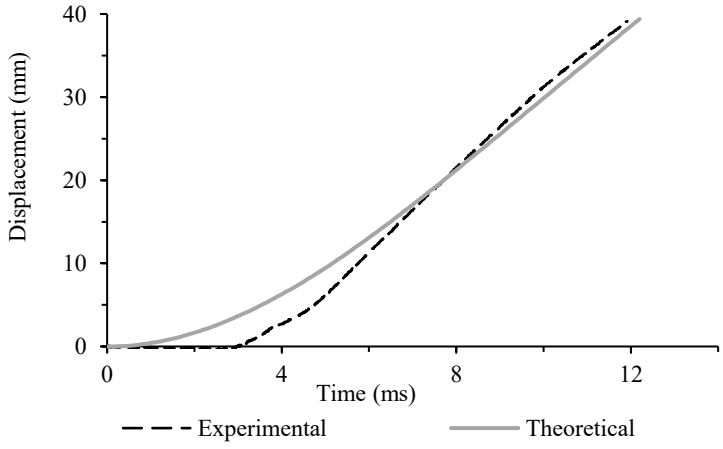

(c) Displacement-time curve

Figure C.6: Analytical and experimental data comparison for D-10M-B2.

At Rest At R_{max} At Δ_u

Figure C.7: Dynamic test pictures for D-10M-B2.

(a) Before test

(b) After test

(c) Tension side

(d) Compression side

Figure C.8: Dynamic test pictures for D-10M-B4.

D-15M-B1 beam was tested on 19/oct/2022 and subjected to driver pressure of 758.4 kPa, resulting in a reflected pressure of 89.3 kPa and an impulse of 1007.4 $kPa - ms$.

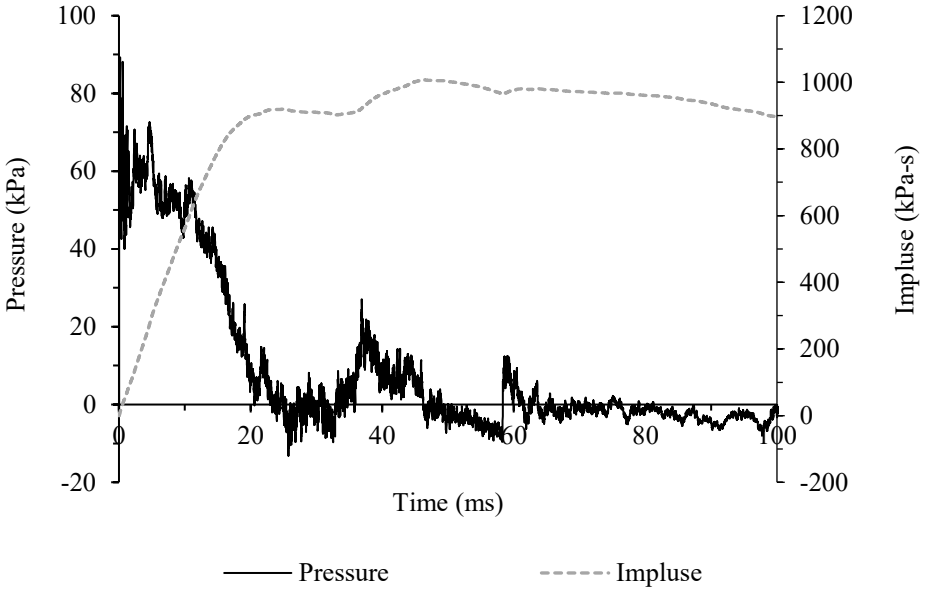

(a) Pressure and Impulse history

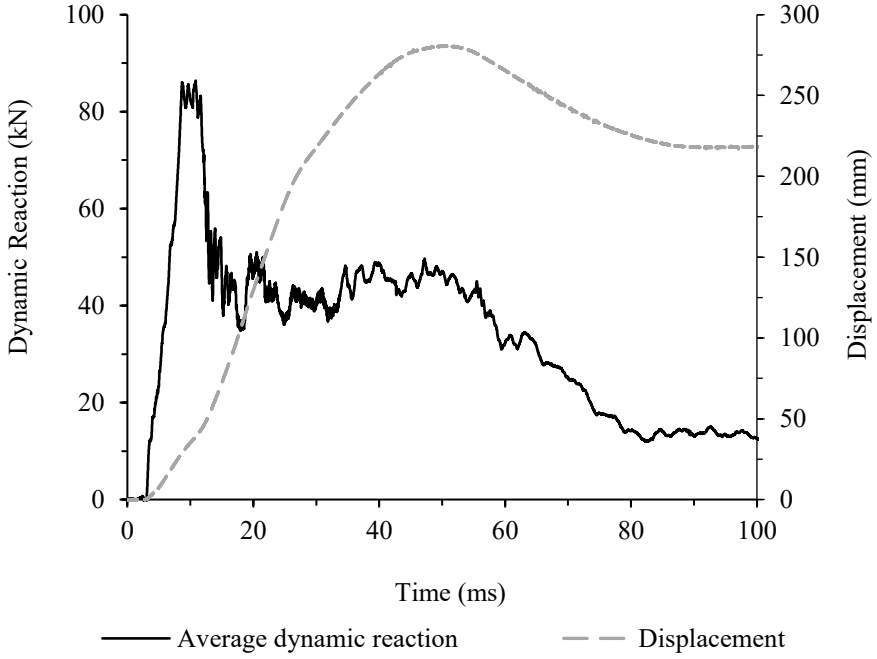

(b) Reaction and Displacement history

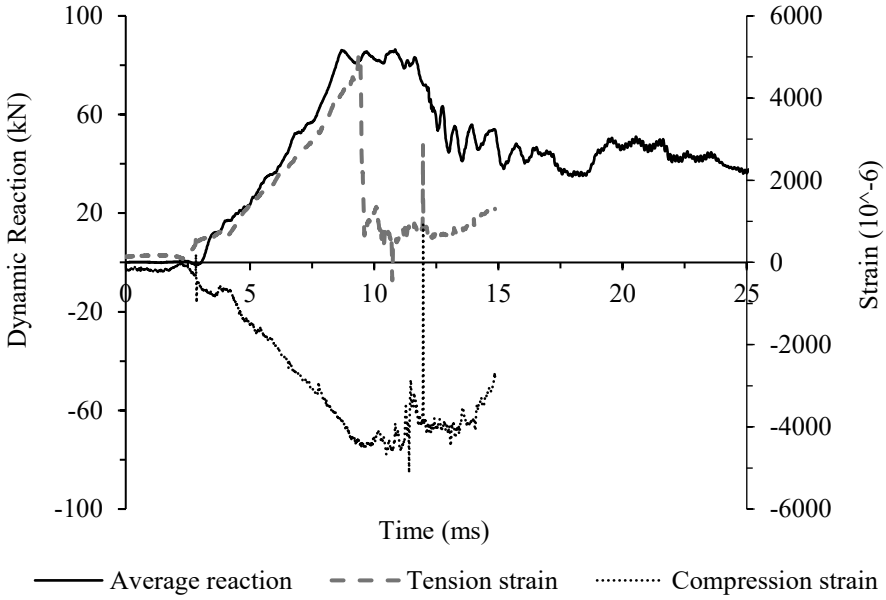

(c) Reaction and strains history

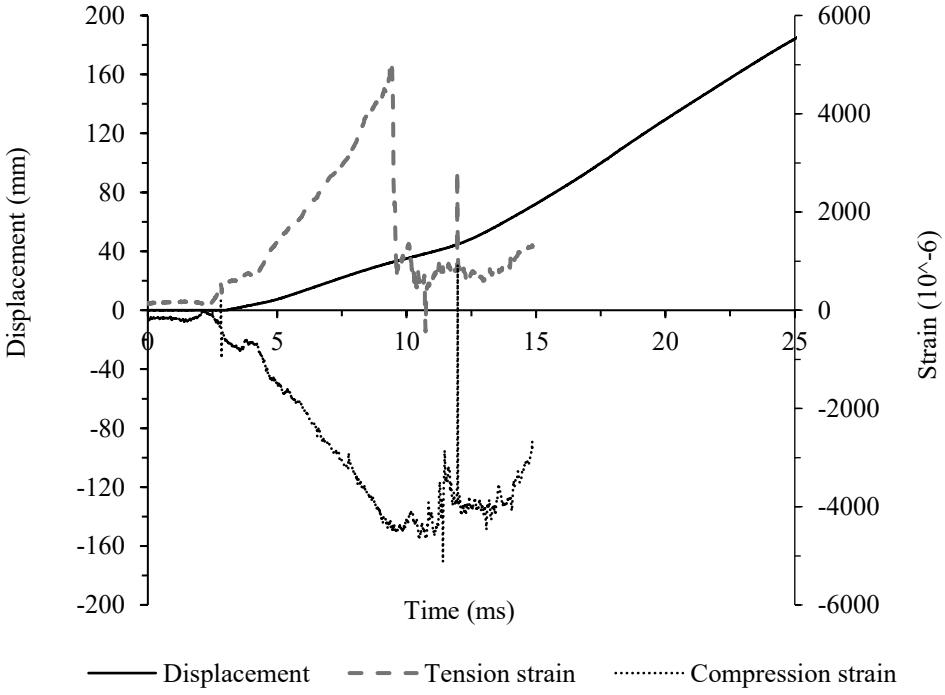

(d) Displacement and strains history

Figure C.9: Experimental data for D-15M-B1.

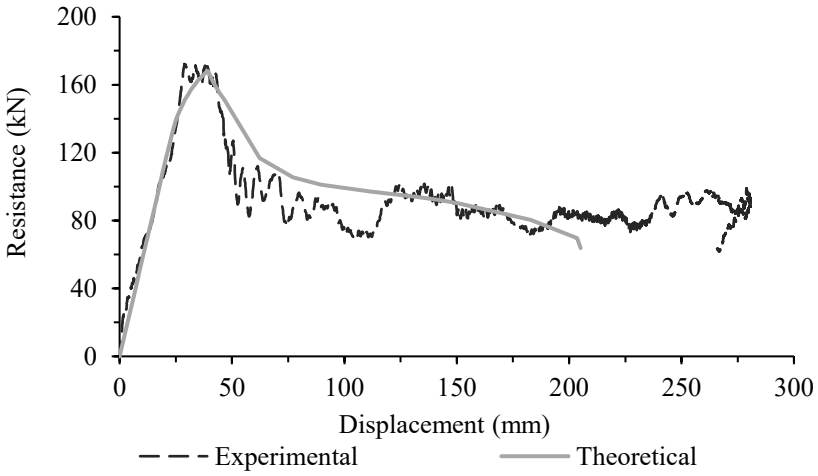

(a) Force-displacement curve

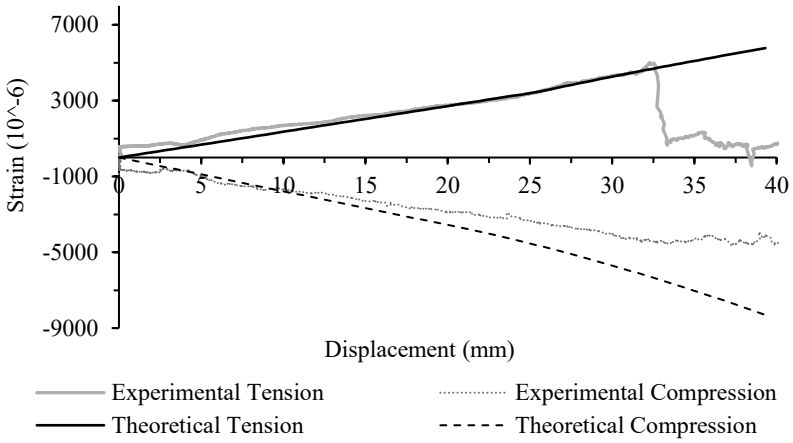

(b) Displacement-strain curve

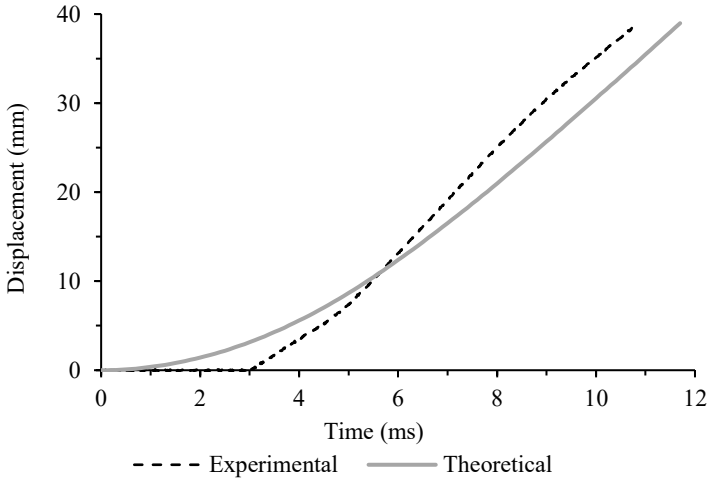

(c) Displacement-time curve

Figure C.10: Analytical and experimental data comparison for D-15M-B1.

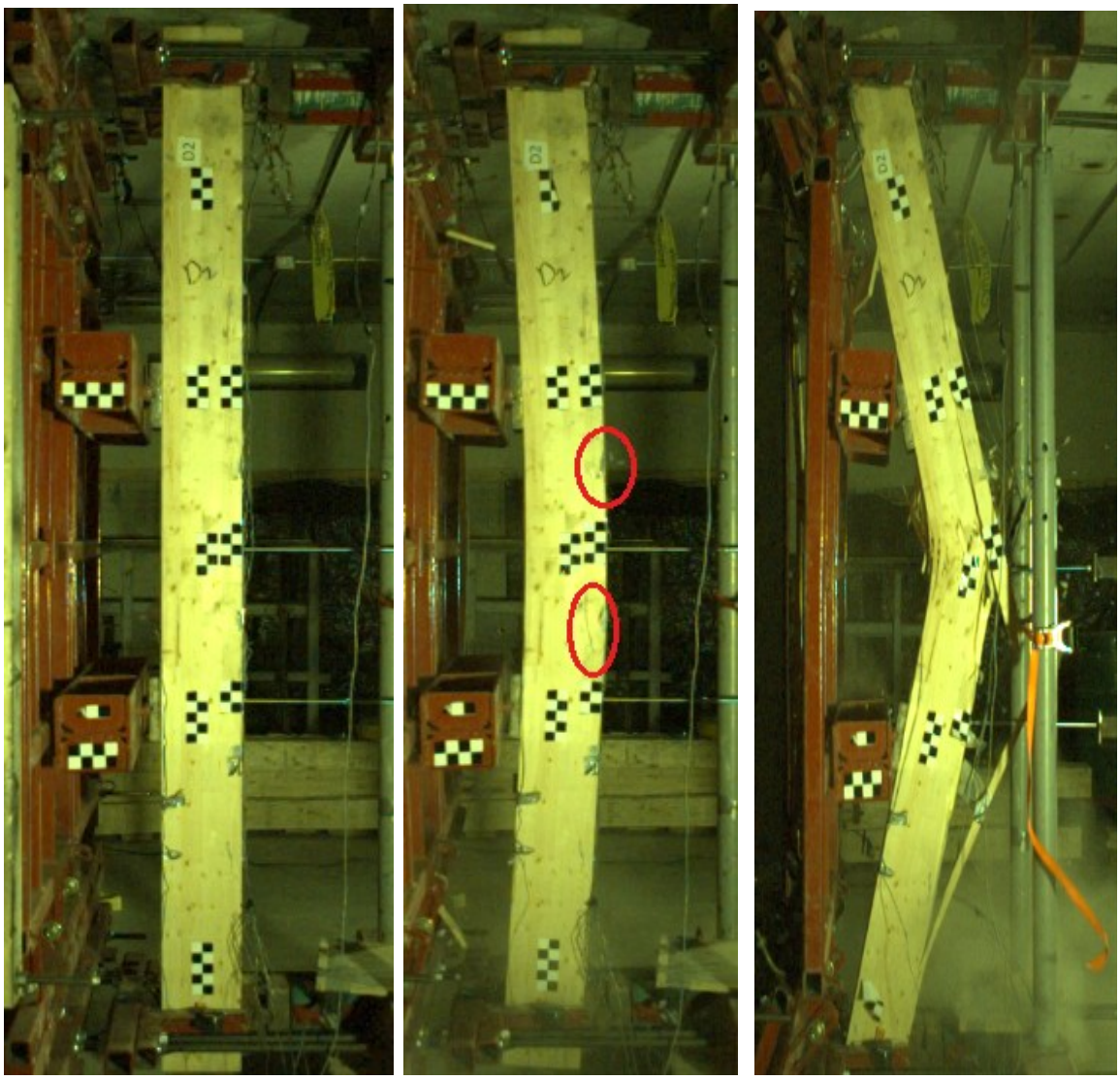

At Rest At R_{max} At Δ_u

Figure C.11: Dynamic test pictures for D-15M-B1.

(a) Before test

(b) After test

(c) Tension side

(d) Compression side

Figure C.12: Dynamic test pictures for D-15M-B1.

D-15M-B2 beam was tested on 28/oct/2022 and subjected to driver pressure of 717.1 kPa, resulting in a reflected pressure of 99.9 kPa and an impulse of 1012.0 $kPa - ms$.

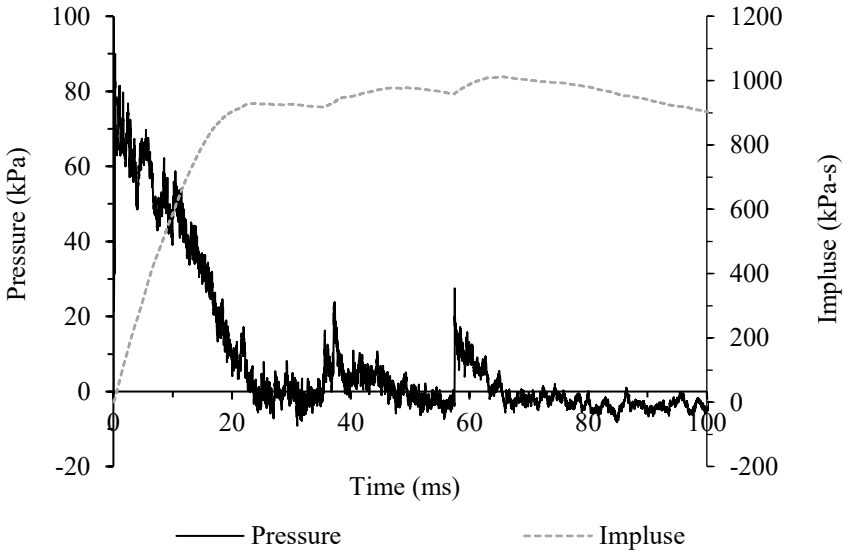

(a) Pressure and Impulse history

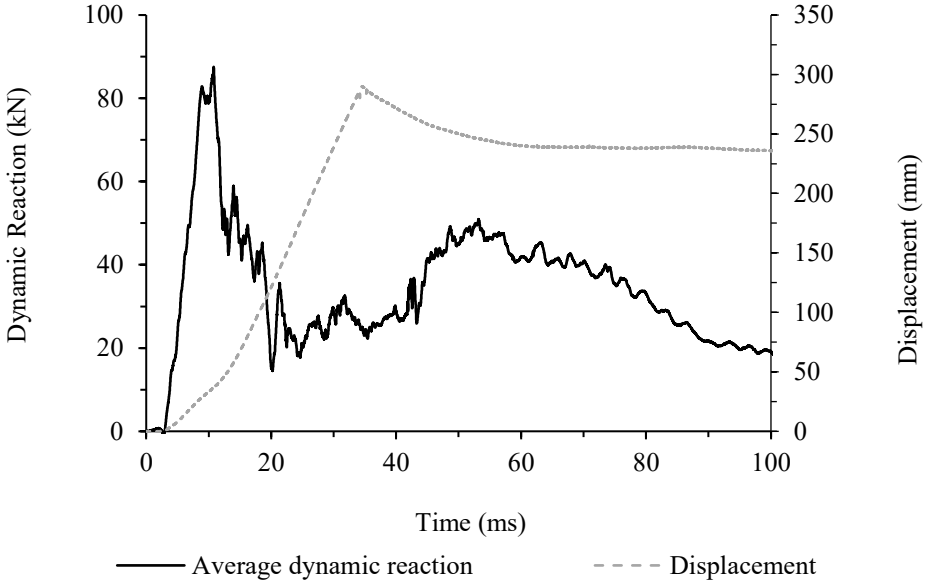

(b) Reaction and Displacement history

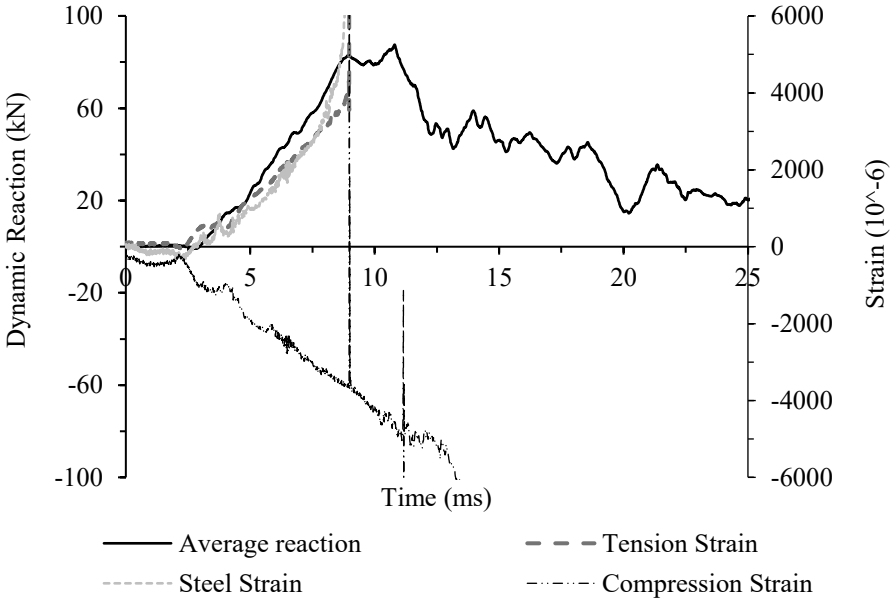

(c) Reaction and strains history

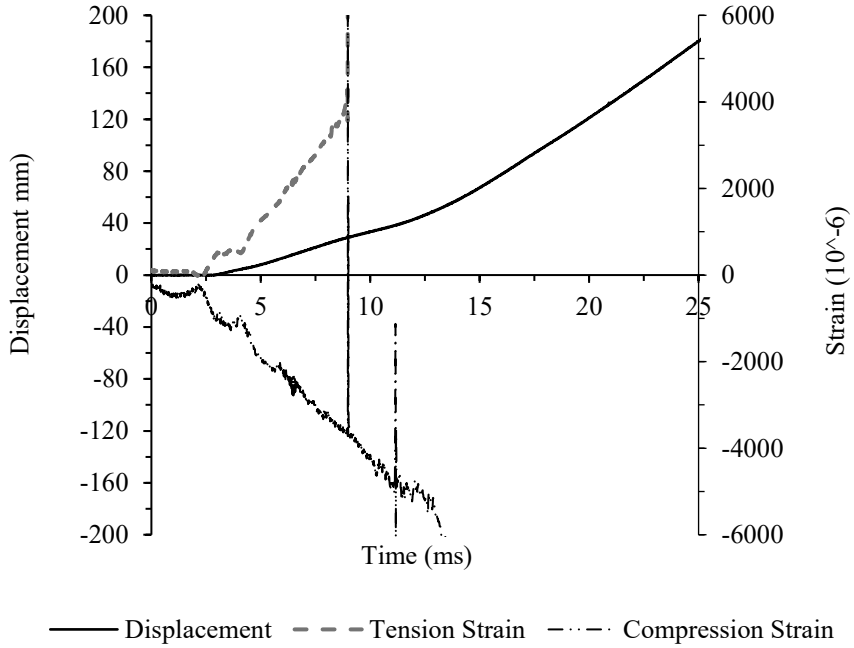

(d) Displacement and strains history

Figure C.13: Experimental data for D-15M-B2.

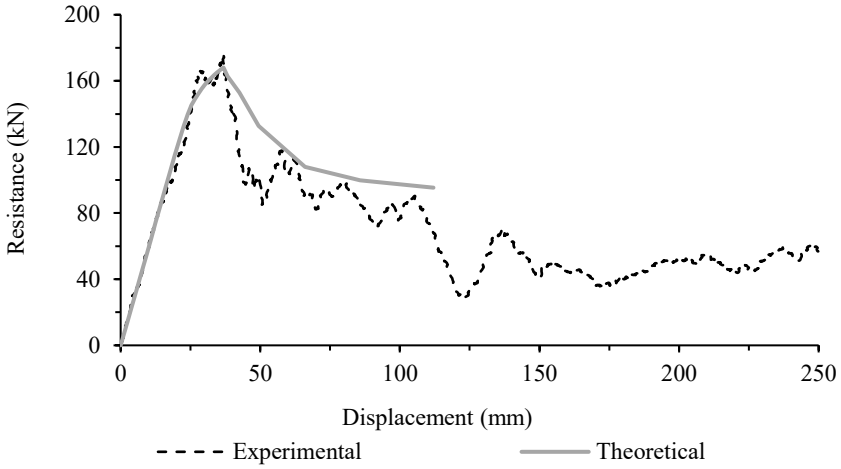

(a) Force-displacement curve

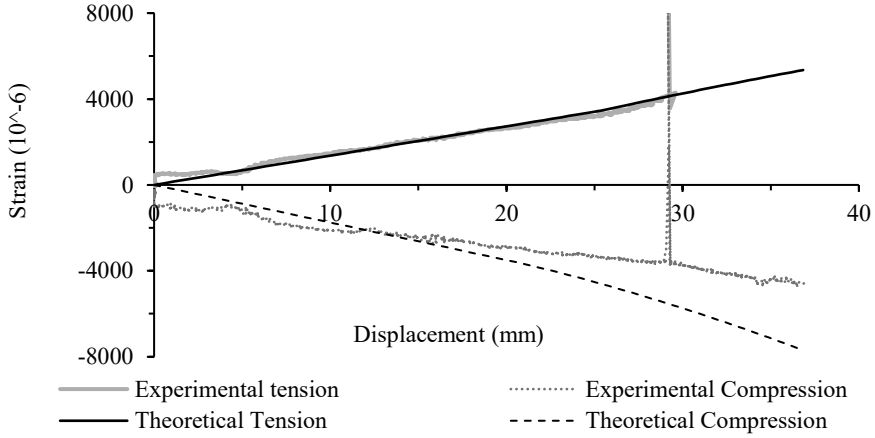

(b) Displacement-strain curve

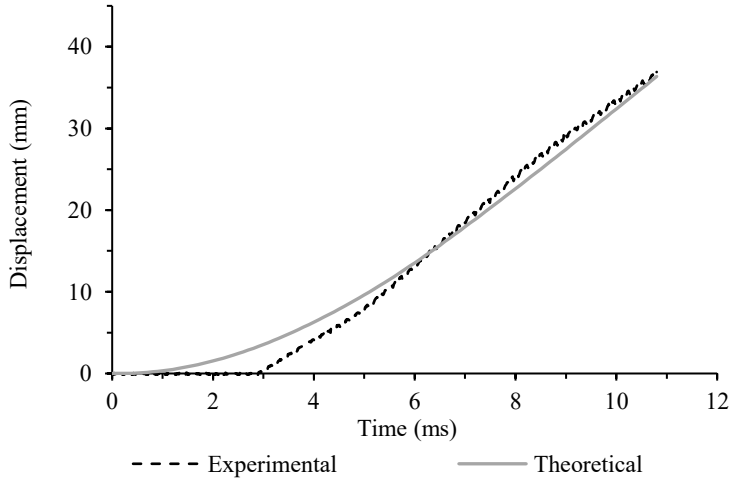

(c) Displacement-time curve

Figure C.14: Analytical and experimental data comparison for D-15M-B2.

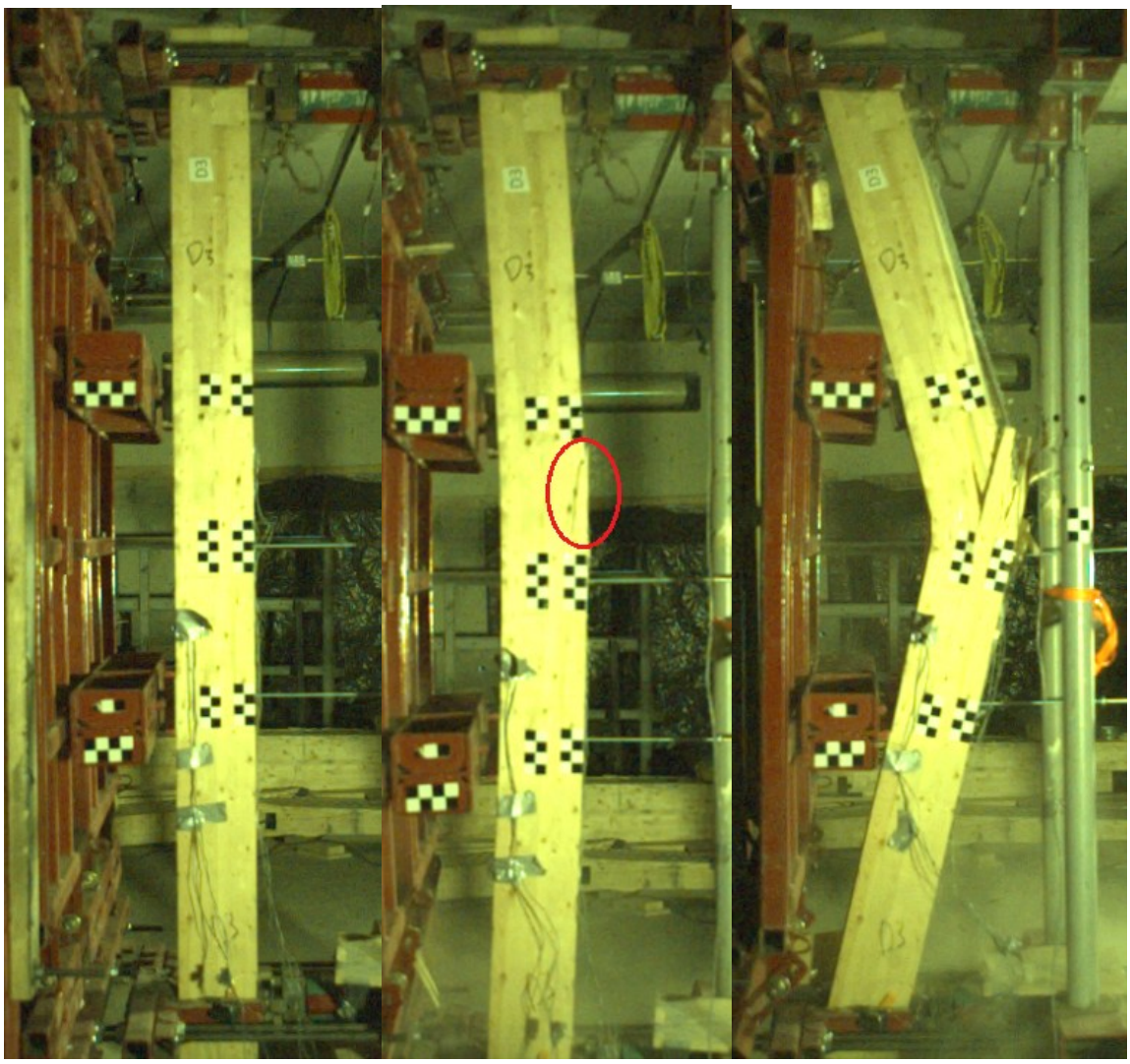

At Rest At R_{max} At Δ_u

Figure C.15: Dynamic test pictures for D-15M-B2.

(a) Before test

(b) After test

(c) Tension side

(d) Compression side

Figure C.16: Dynamic test pictures for D-15M-B2.

D-PL-B1 beam was tested on 3/Nov/2022 and subjected to driver pressure of 561.2 kPa, resulting in a reflected pressure of 72.0 kPa and an impulse of 795.9 $kPa - ms$.

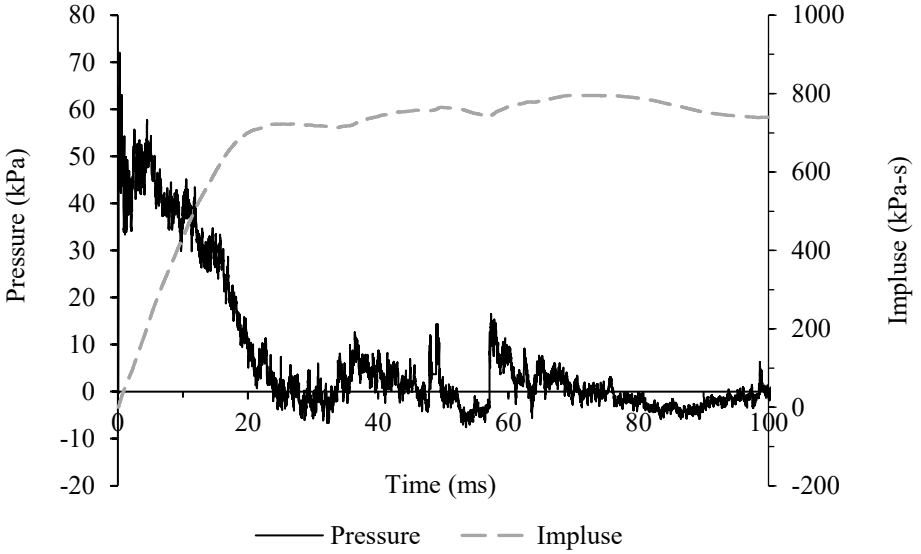

(a) Pressure and Impulse history

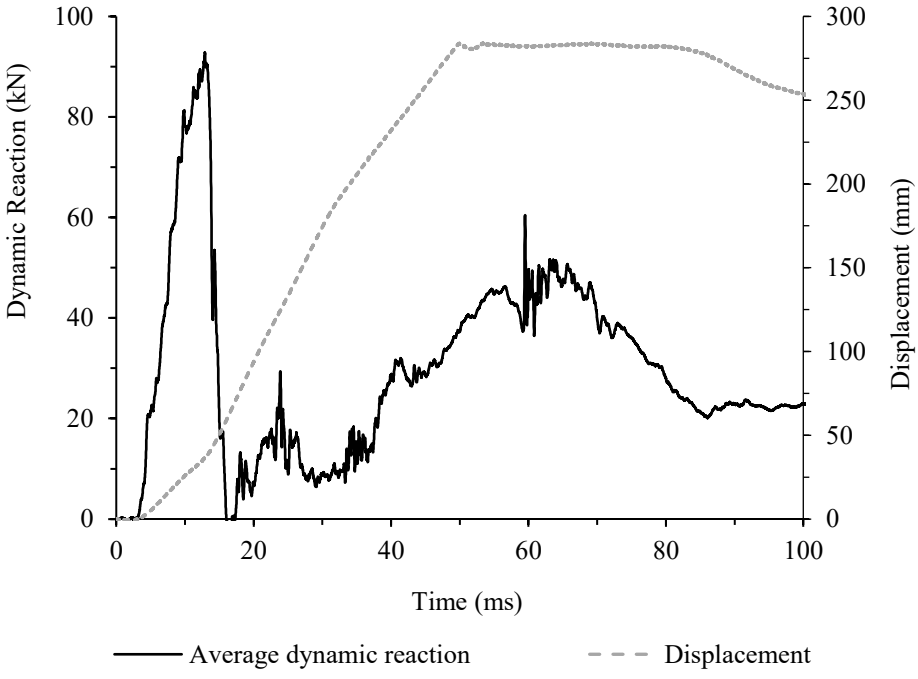

(b) Reaction and Displacement history

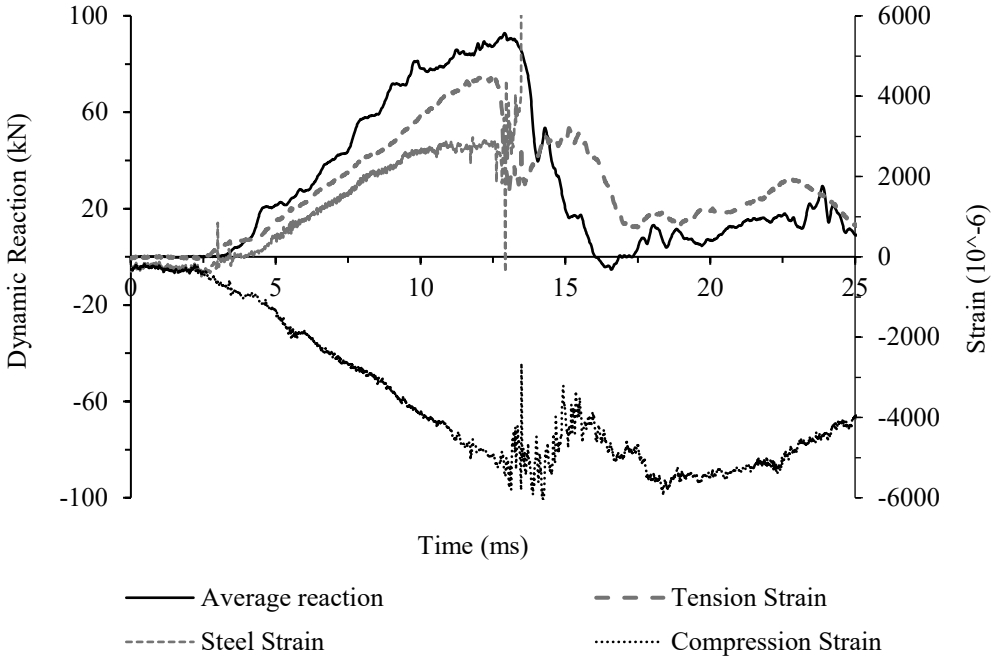

(c) Reaction and strains history

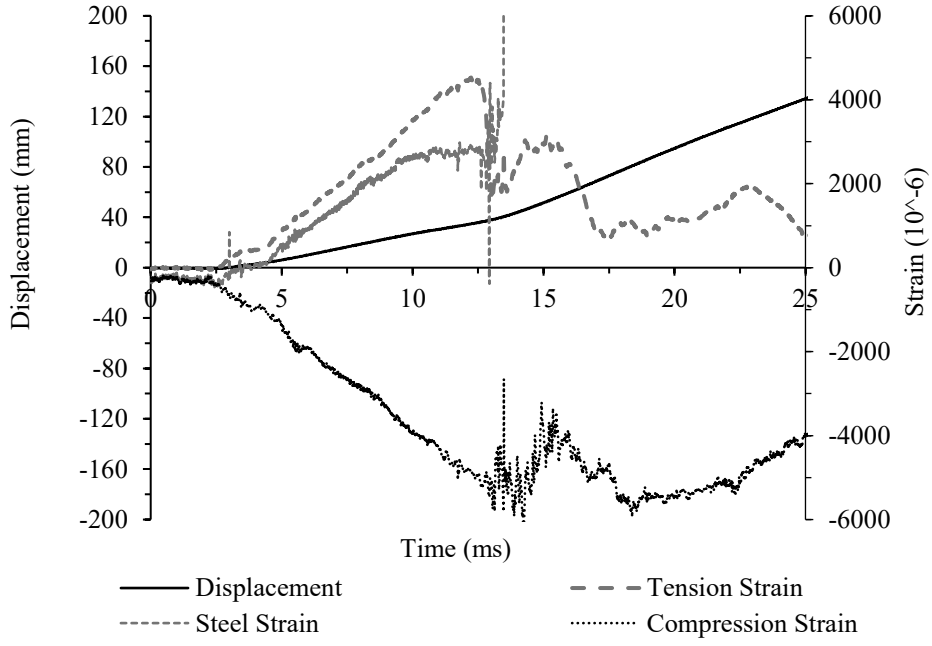

(d) Displacement and strains history

Figure C.17: Experimental data for D-PL-B1.

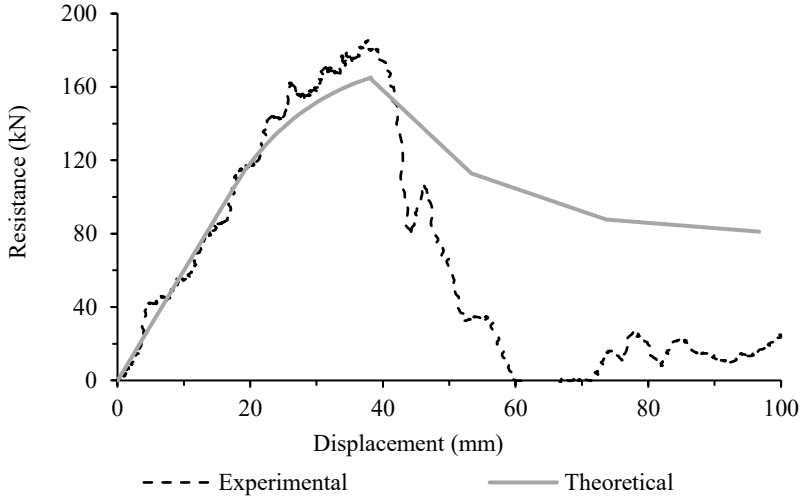

(a) Force-displacement curve

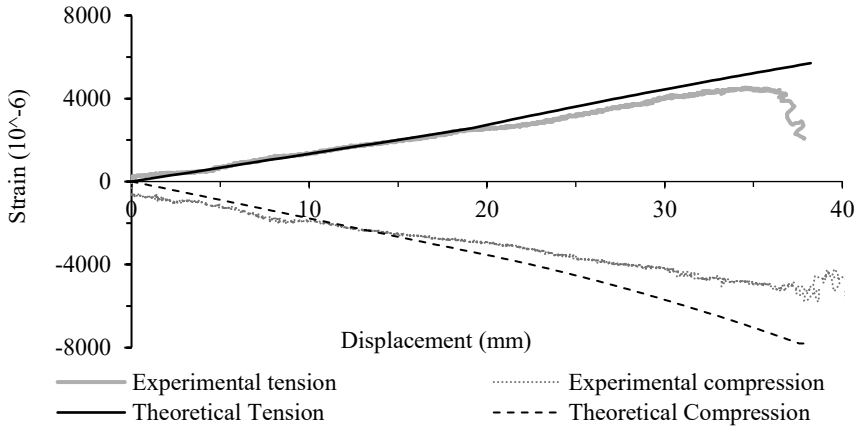

(b) Displacement-strain curve

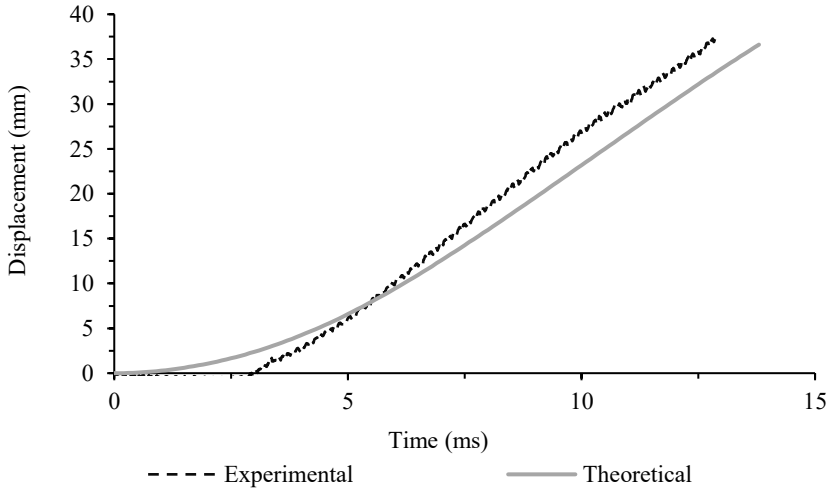

(c) Displacement-time curve

Figure C.18: Analytical and experimental data comparison for D-PL-B1.

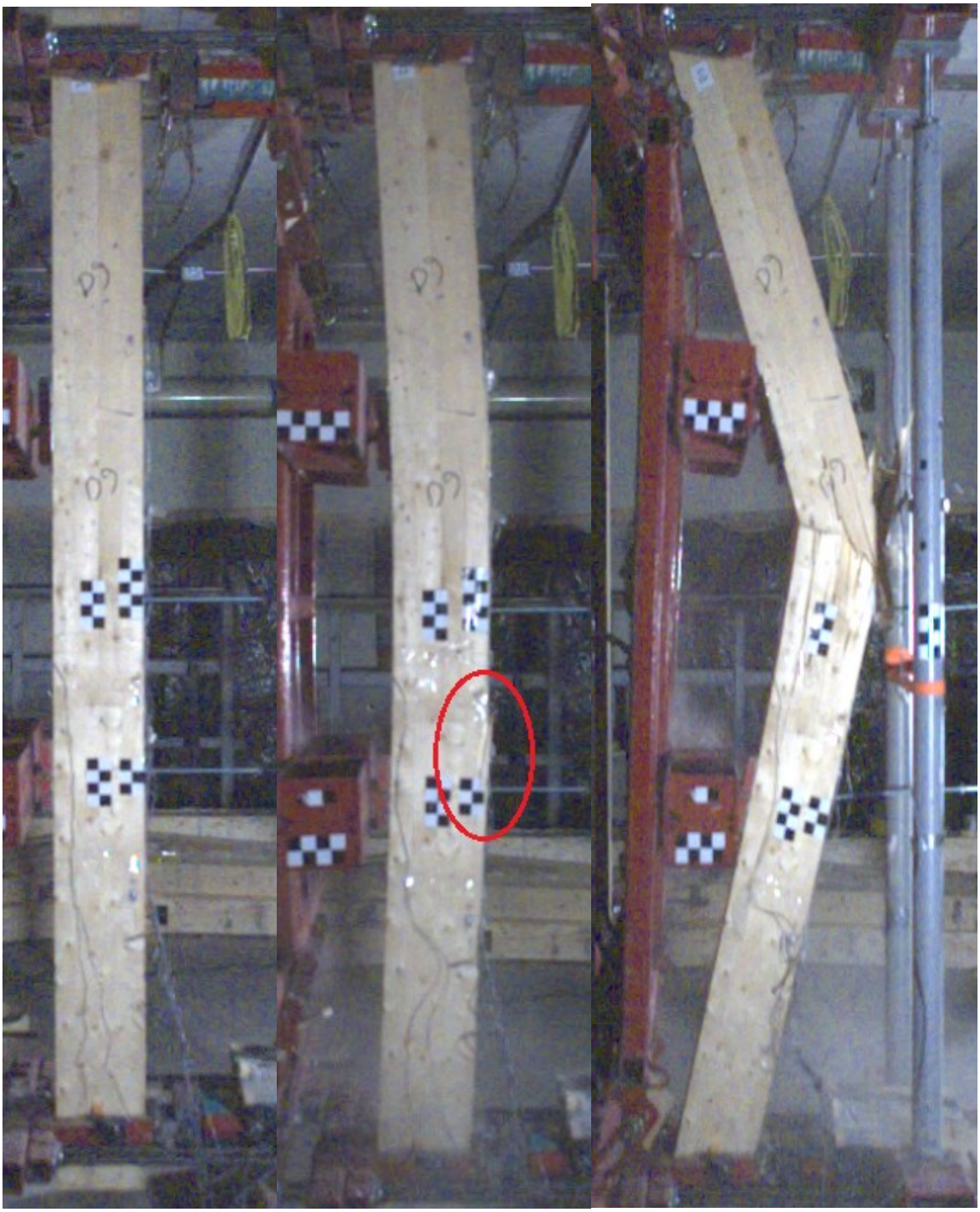

At Rest At R_{max} At Δ_u

Figure C.19: Dynamic test pictures for D-PL-B1.

(a) Before test

(b) After test

(c) Tension side

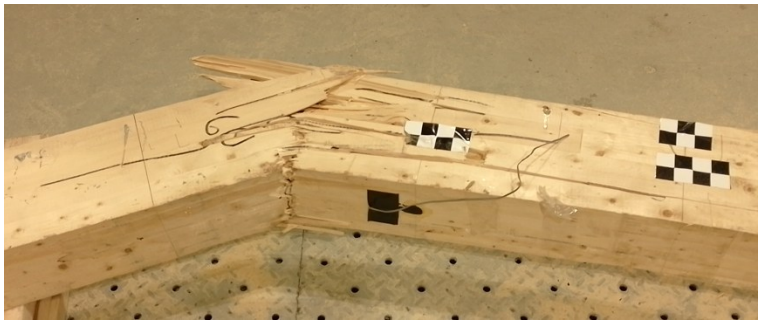

(d) Compression side

Figure C.20: Dynamic test pictures for D-PL-B1.

D-PL-B2 beam was tested on 10/Nov/2022 and subjected to driver pressure of 482.6 kPa, resulting in a reflected pressure of 78.8 kPa and an impulse of 712.4 $kPa - ms$.

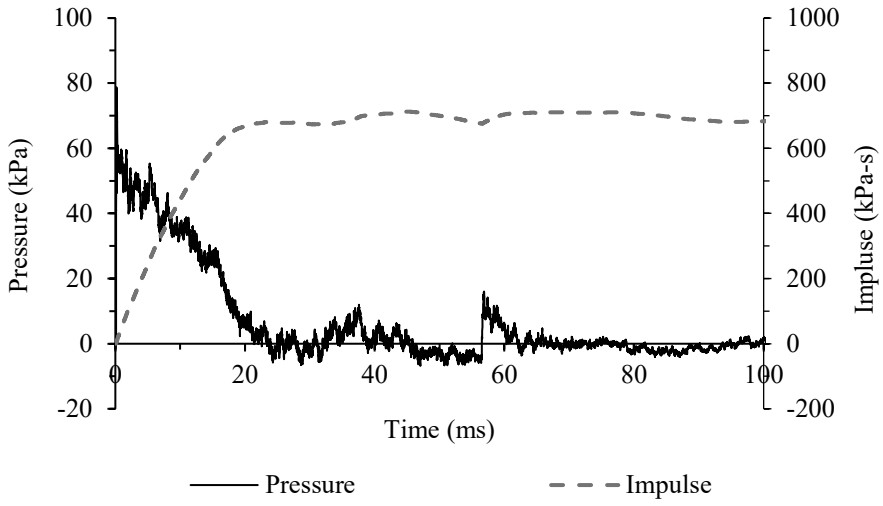

(a) Pressure and Impulse history.

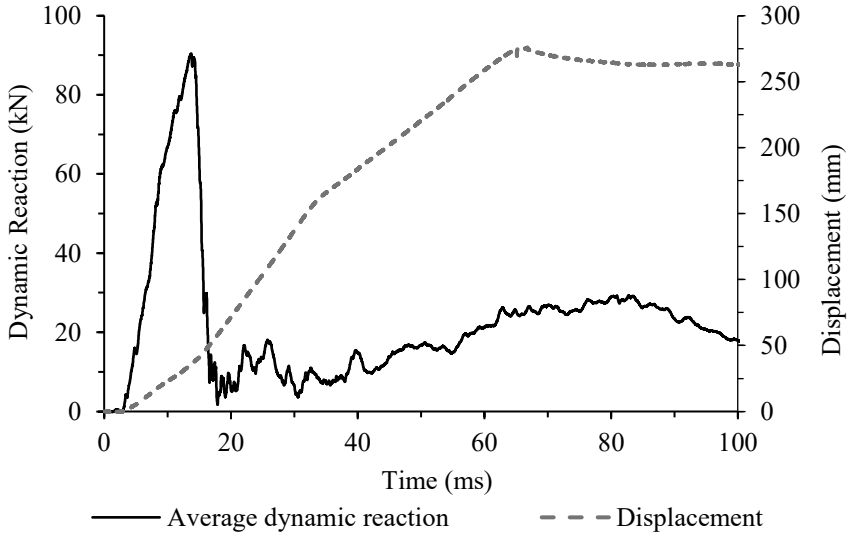

(b) Reaction and Displacement history

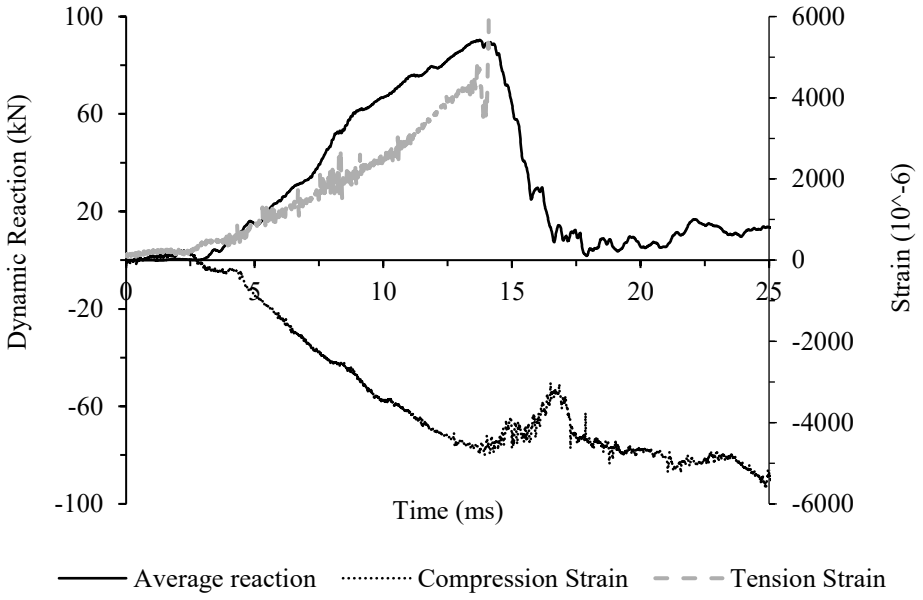

(c) Reaction and strains history

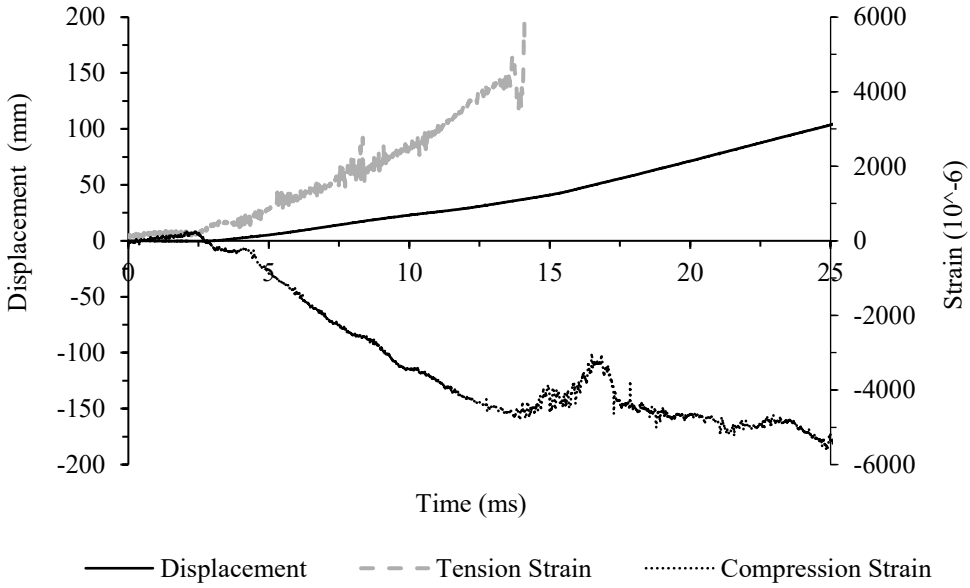

(d) Displacement and strains history

Figure C.21: Experimental data for D-PL-B2.

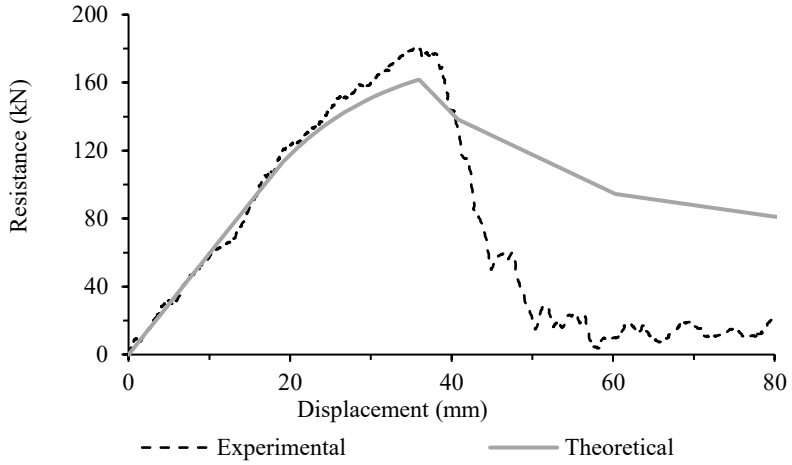

(a) Force-displacement curve

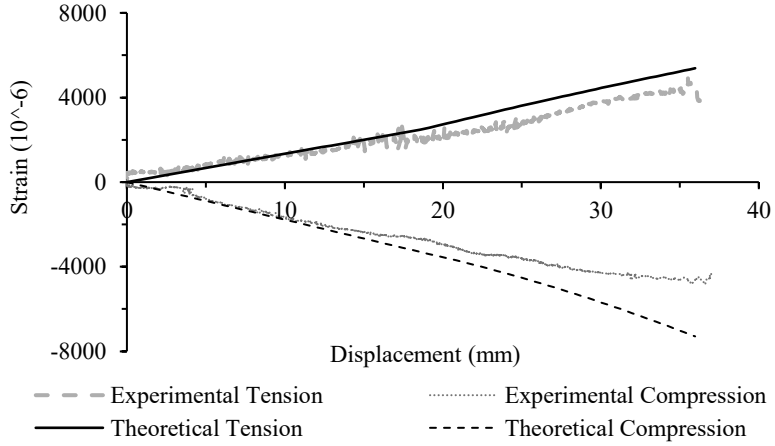

(b) Displacement-strain curve

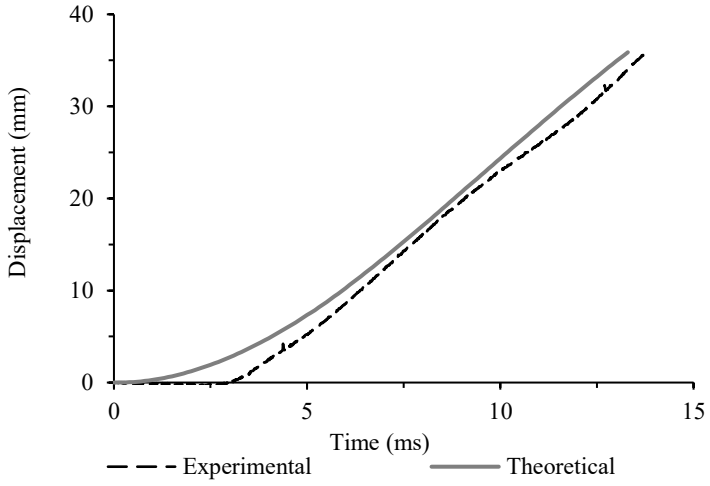

(c) Displacement-time curve

Figure C.22: Analytical and experimental data comparison for D-PL-B2.

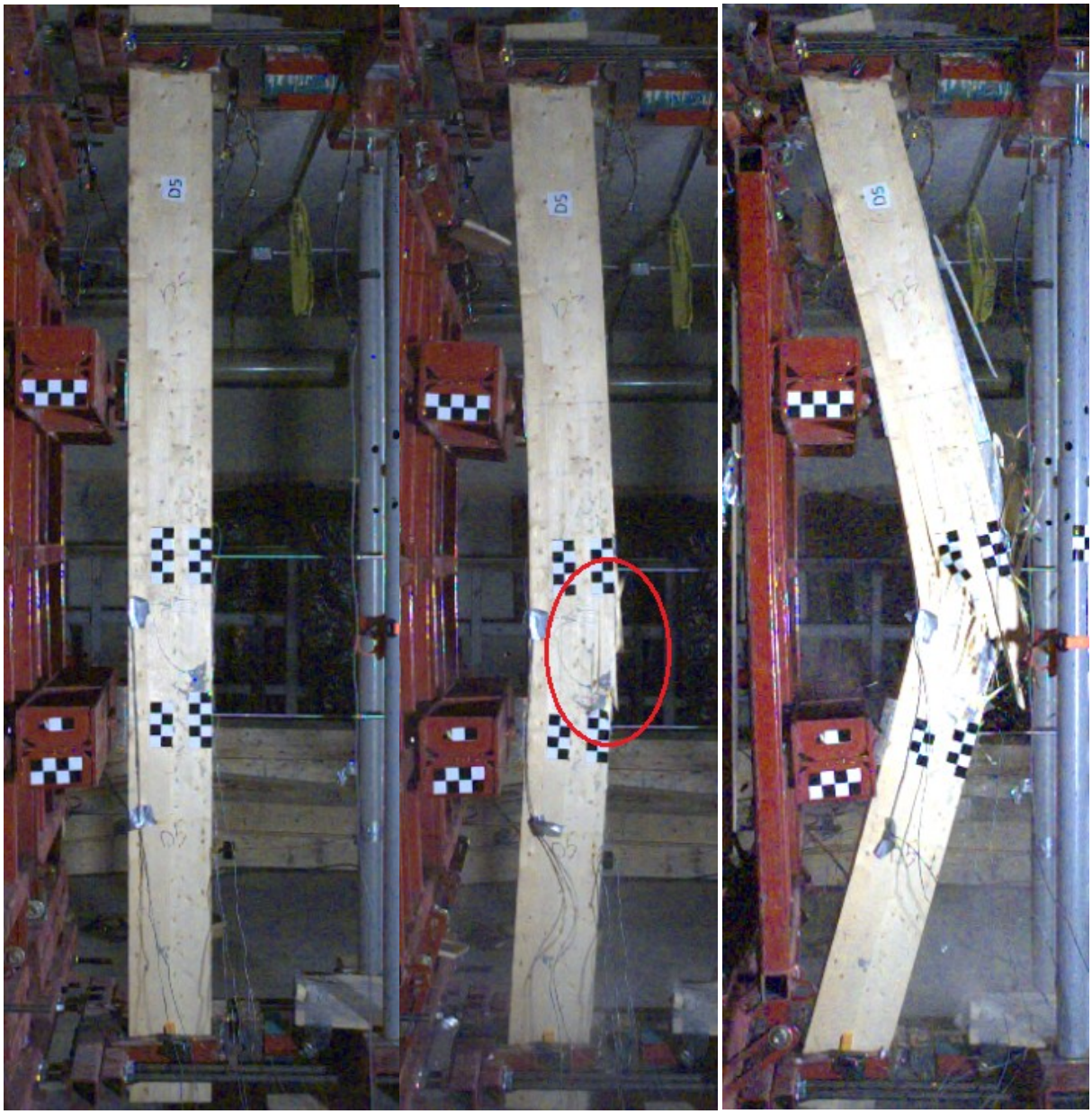

At Rest At R_{max} At Δ_u

Figure C.23: Dynamic test pictures for D-PL-B2.

(a) Before test

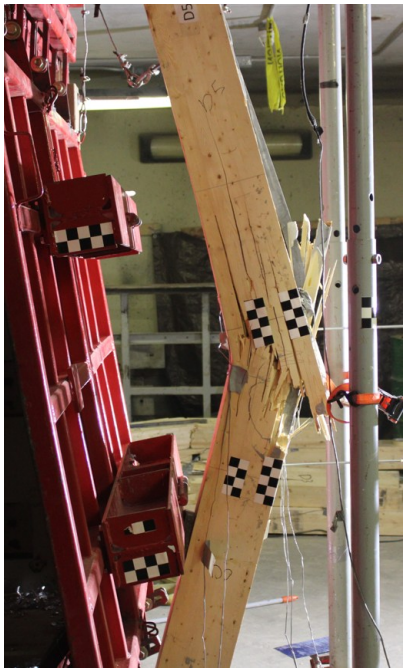

(b) After test

(c) Tension side

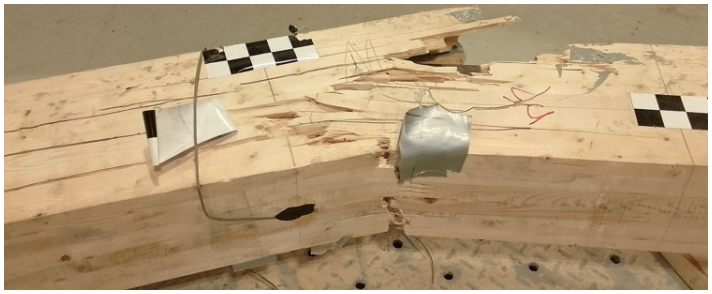

(d) Compression side

Figure C.24: Dynamic test pictures for D-PL-B2.

D-PL-S1 beam was tested on 17/Nov/2022 and subjected to driver pressure of 517.1 kPa, resulting in a reflected pressure of 73.2 kPa and an impulse of 755.0 $kPa - ms$.

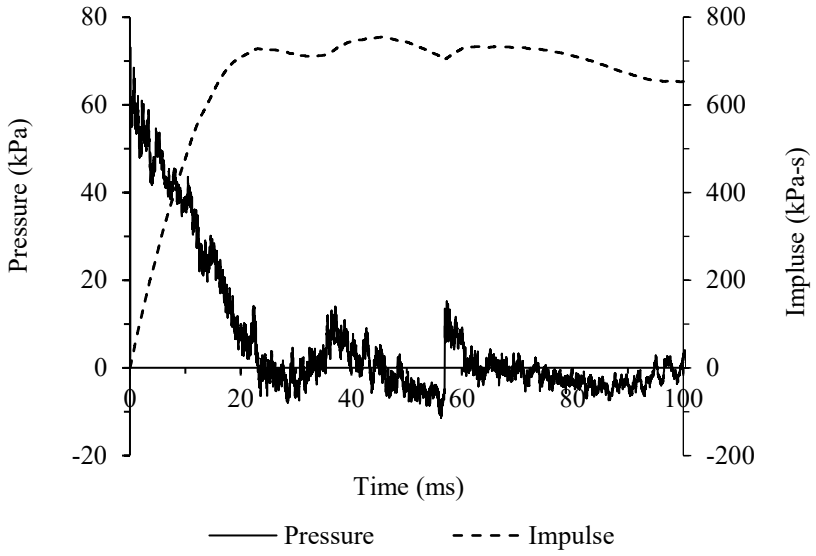

(a) Pressure and impulse history.

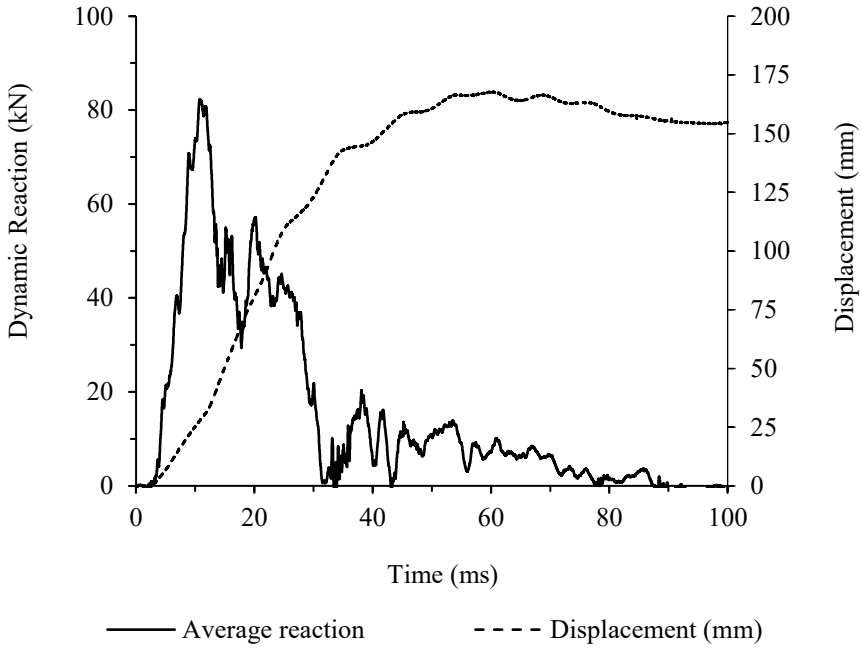

(b) Reaction and displacement history.

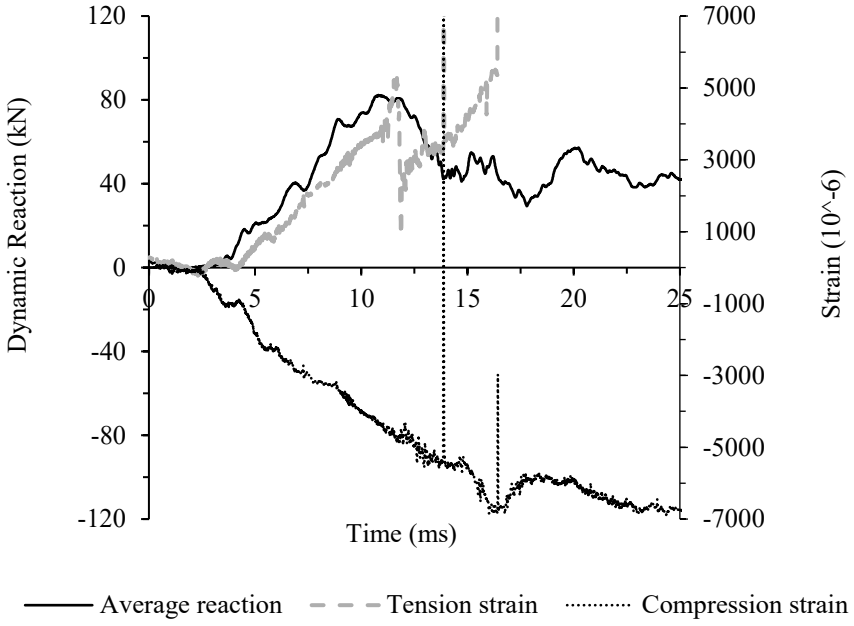

(c) Reaction and strains history

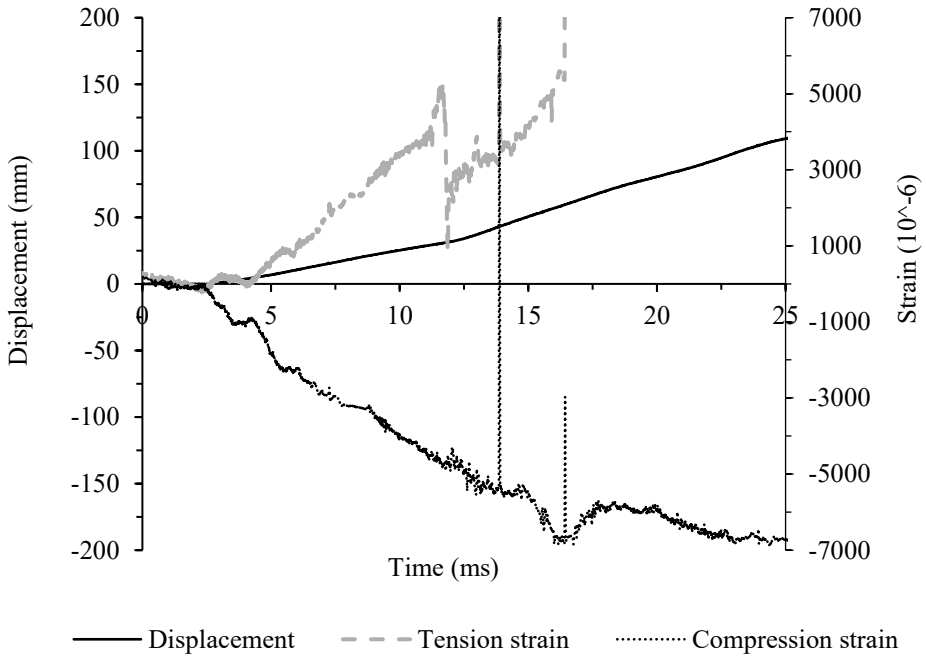

(d) Displacement and strains history

Figure C.25: Experimental data for D-PL-S1.

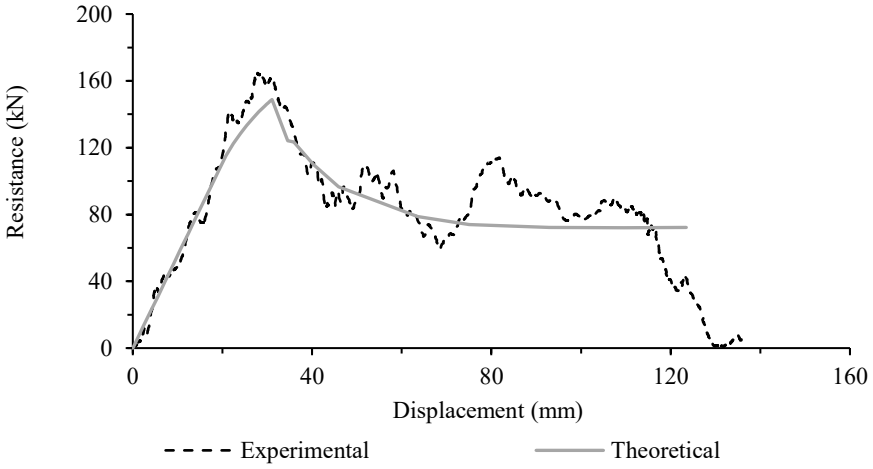

(a) Force-displacement curve

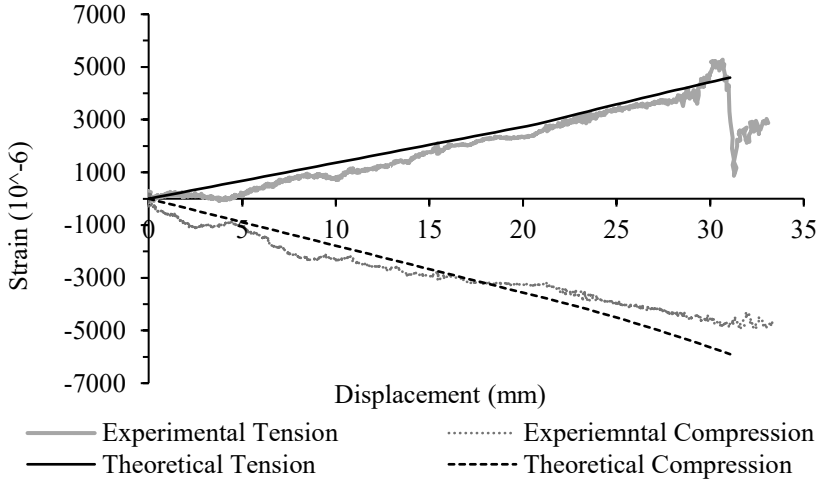

(b) Displacement-strain curve

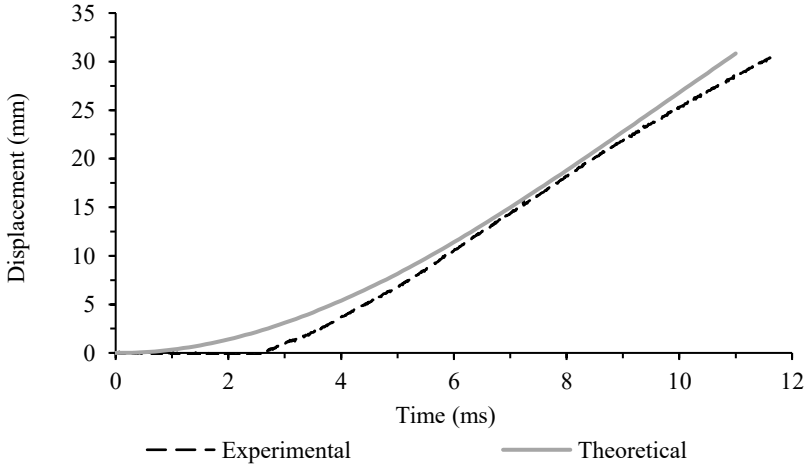

(c) Displacement-time curve

Figure C.26: Analytical and experimental data comparison for D-PL-S1.

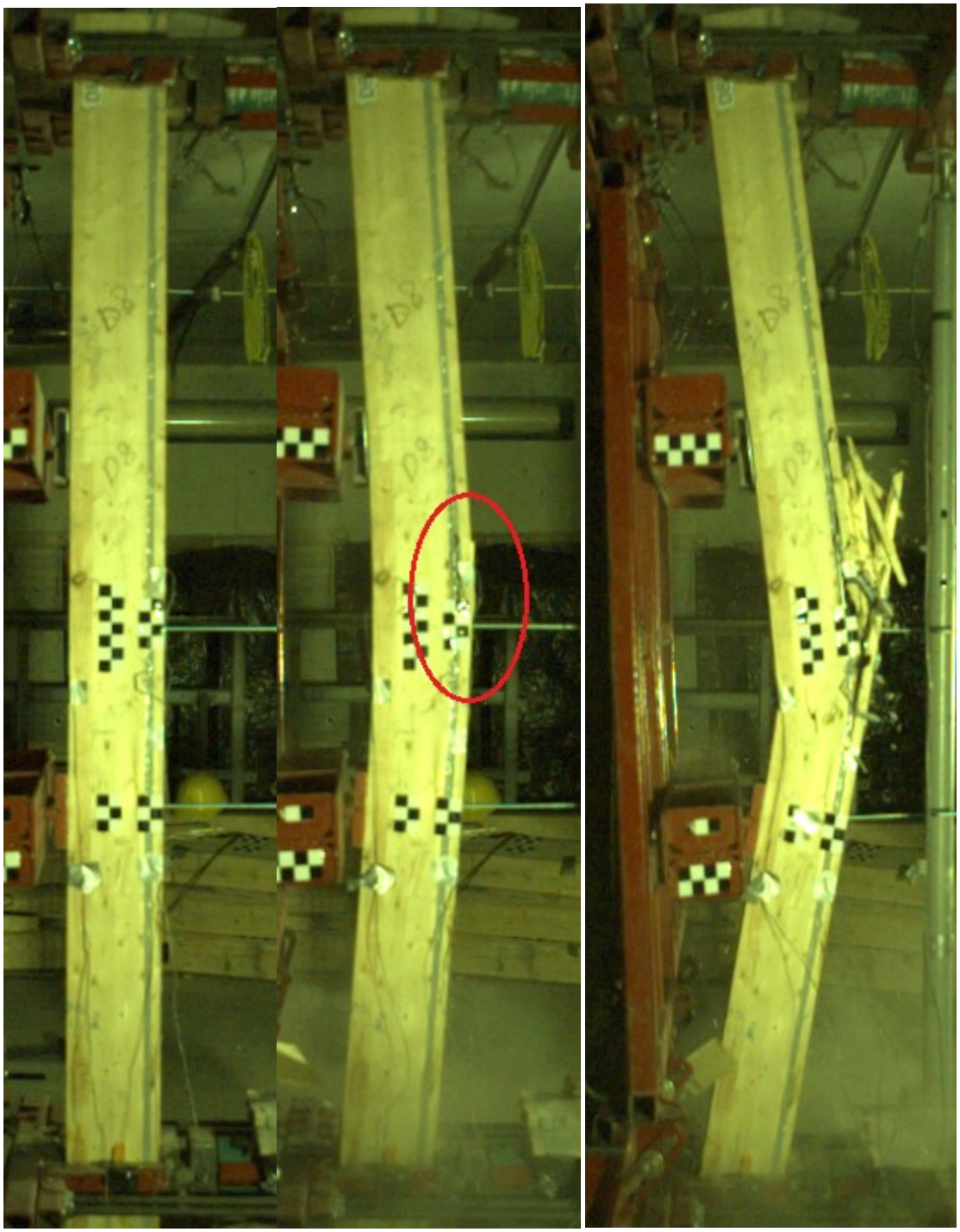

At Rest At R_{max} At Δ_u

Figure C.27: Dynamic test pictures for D-PL-S1.

(a) Before test

(b) After test

(c) Tension side

(d) Compression side

Figure C.28: Dynamic test pictures for D-PL-S1.

D-20M-B1 beam was tested on 24/Nov/2022 and subjected to driver pressure of 758.4 kPa, resulting in a reflected pressure of 105.7 kPa and an impulse of 961.6 $kPa - ms$.

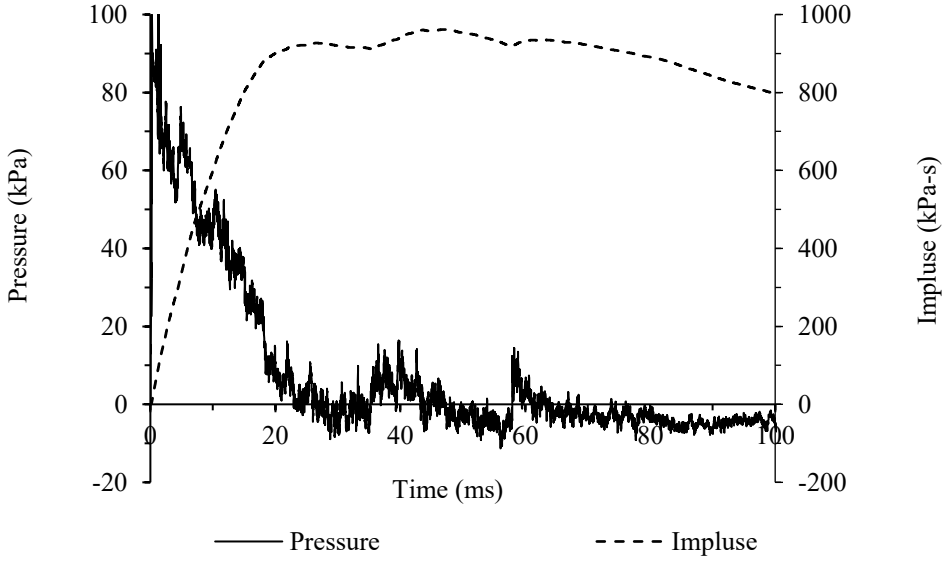

(a) Pressure and impulse history

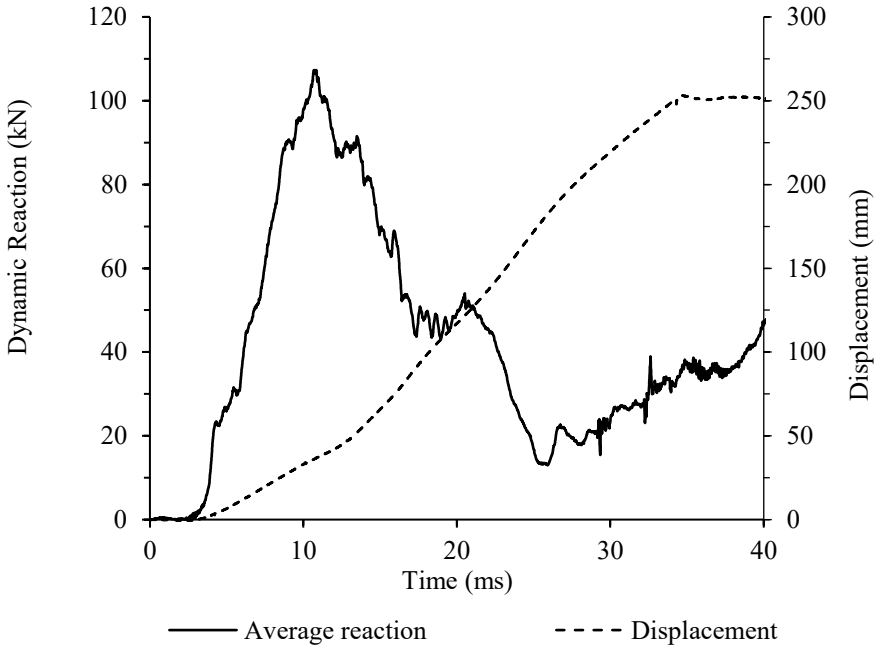

(b) Reaction and displacement history

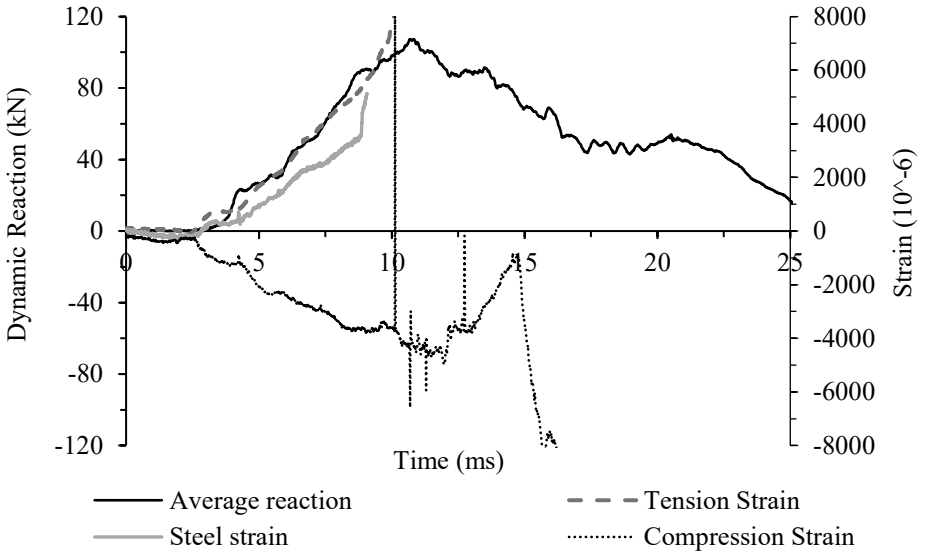

(c) Reaction and strains history

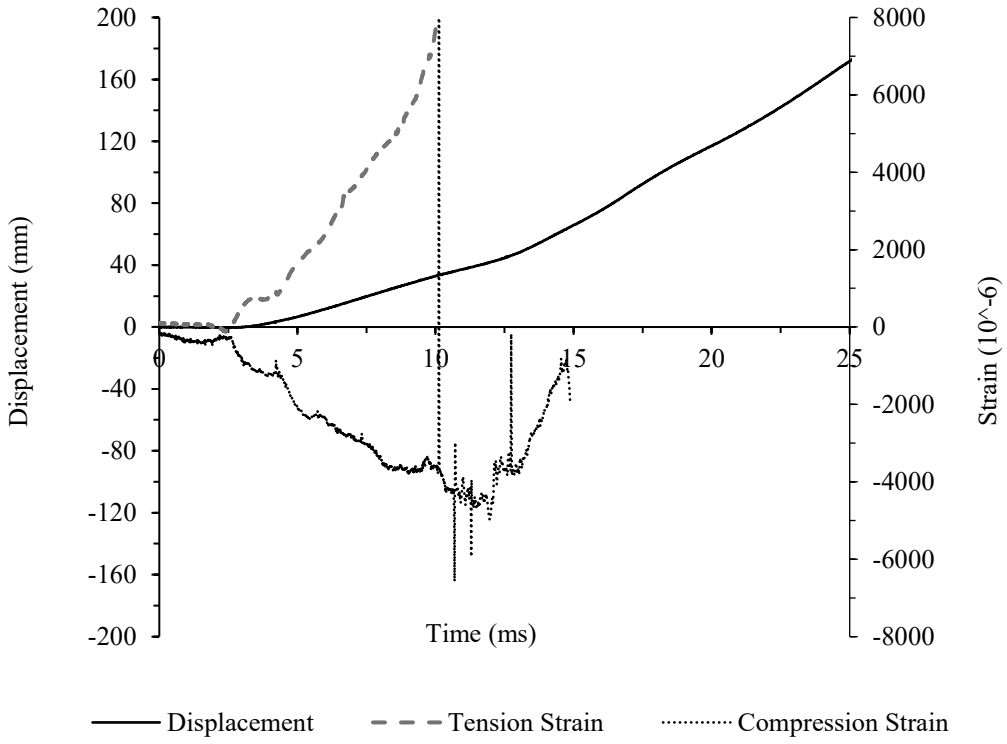

(c) Displacement-time curve

Figure C.29: Analytical and experimental data comparison for D-20M-B1.

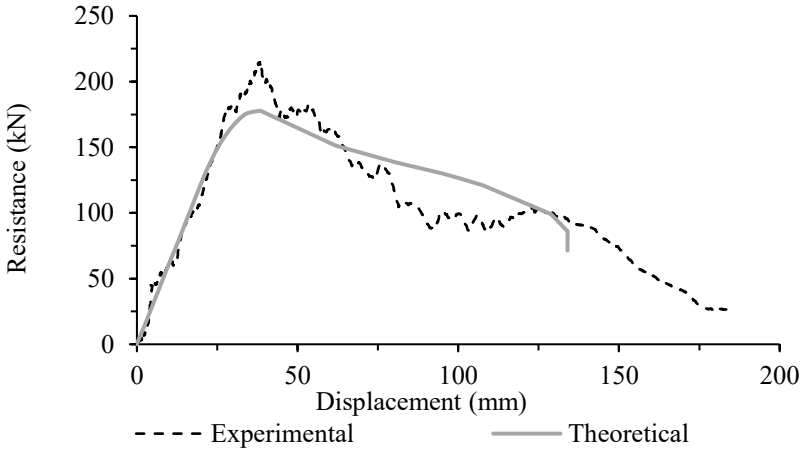

(a) Force-displacement curve

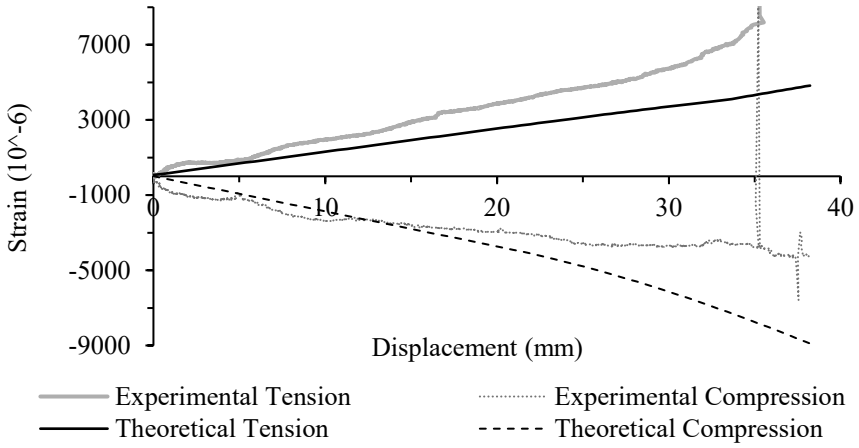

(b) Displacement-strain curve

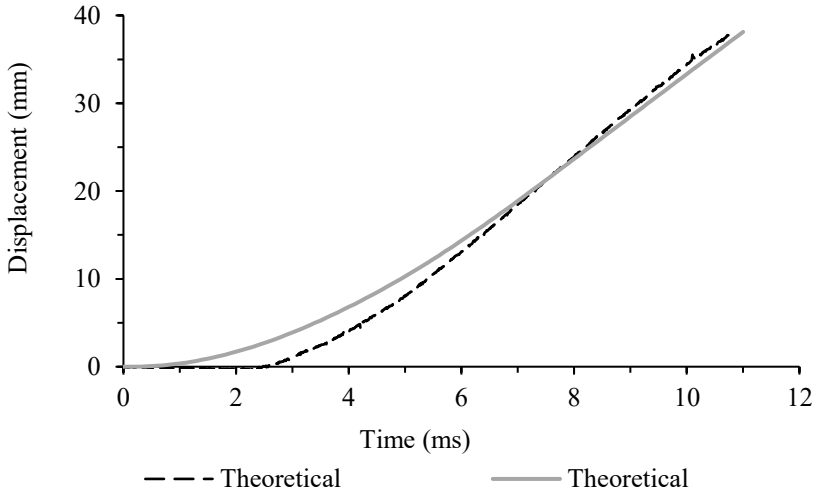

(c) Displacement-time curve

Figure C.30: Analytical and experimental data comparison for D-20M-B1.

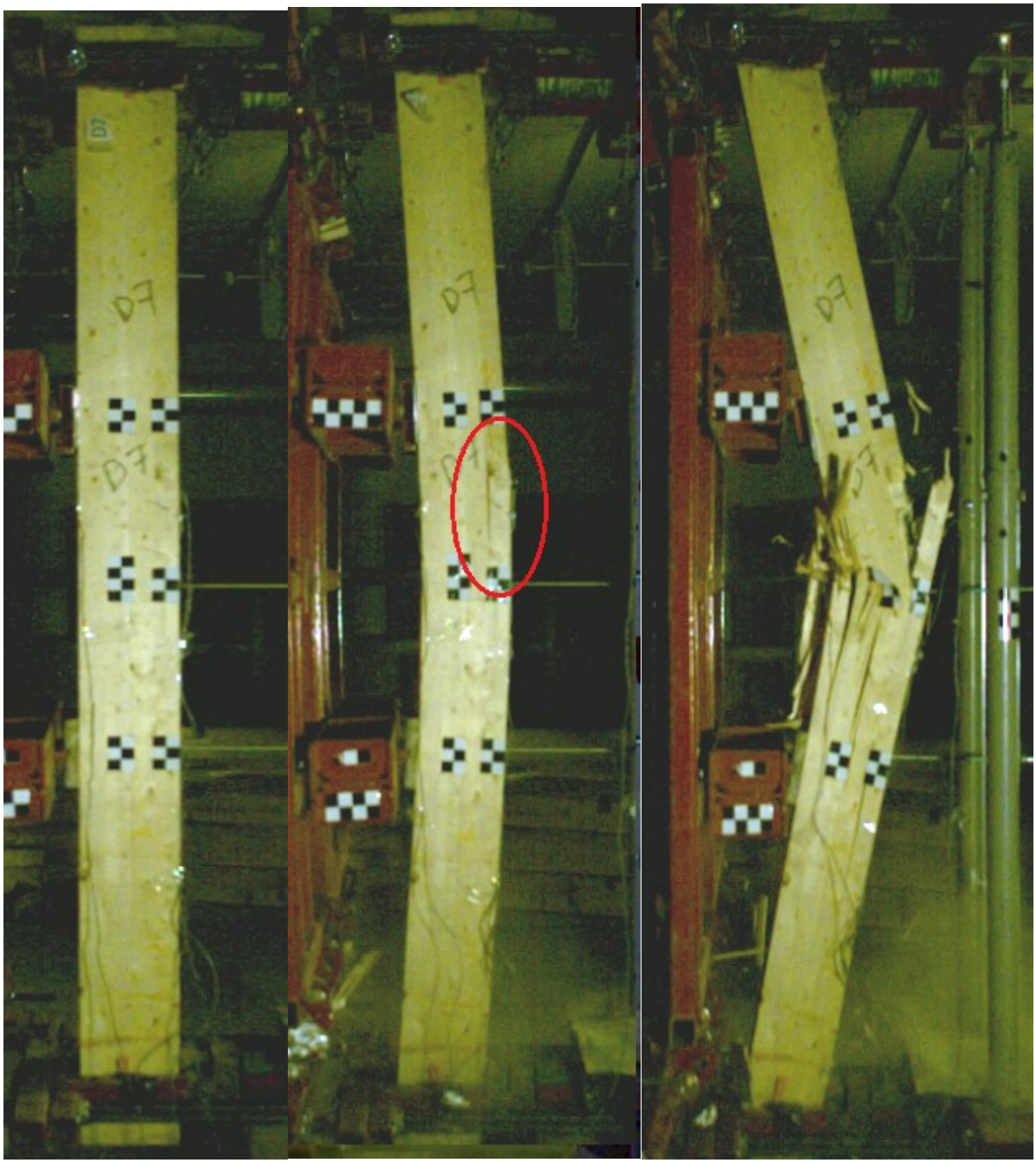

At Rest At R_{max} At Δ_u

Figure C.31: Dynamic test pictures for D-20M-B1.

(a) Before test

(b) After test

(c) Tension side

(d) Compression side

Figure C.32: Dynamic test pictures for D-20M-B1.

Appendix D: Parametric Study

A parametric study was conducted and is presented in this appendix. The modulus of elasticity (E_w) of wood was examined, excluding shear effects and assuming uniform material properties for all glulam sections reinforced with 15M rebar. The steel rebar properties were assumed to be the same as those listed in Table 3.1. Additionally, the α value was set to 1.4 for all reinforced beams. The force-displacement curve illustrating the effect of varying E_w is shown in Figure D.1.

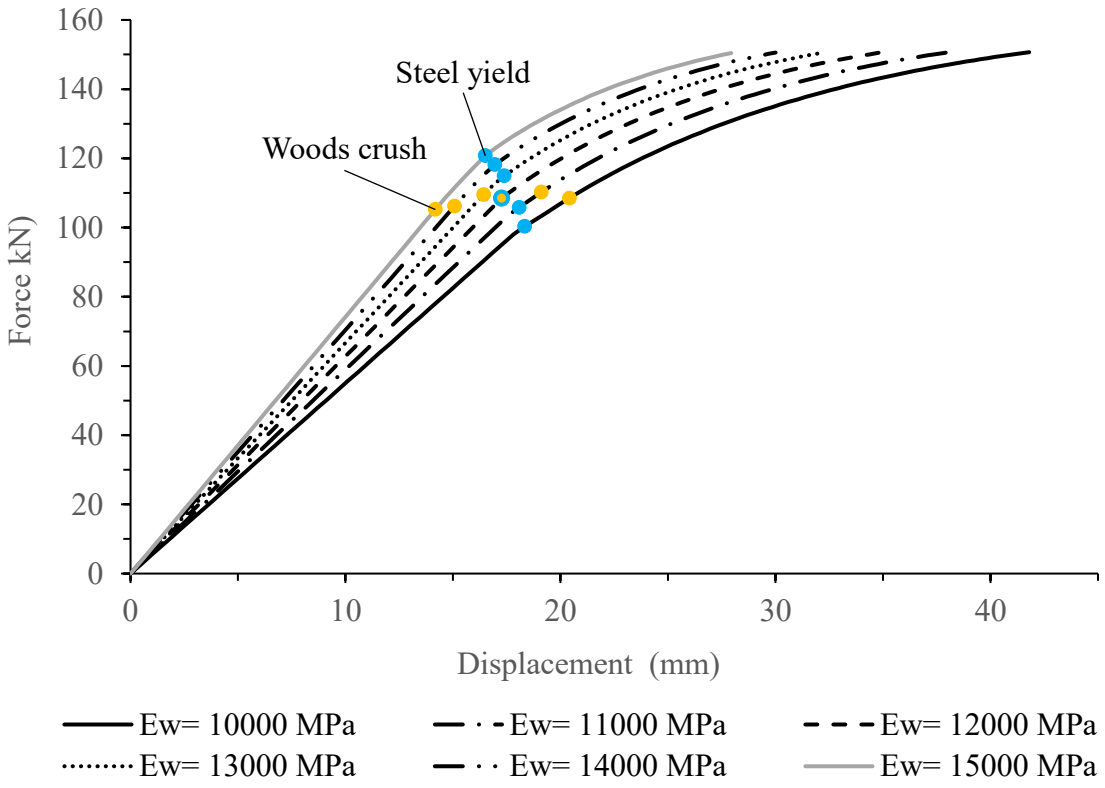

Figure D.1: Effect of E_w values on force-displacement curve.

As shown in Figure D.1, the maximum displacement increases at the same load level as E_w decreases. Additionally, steel yields at a lower load level when E_w is reduced. A comparison was also conducted for different reinforcement ratios (ρ) in glulam beams with identical material properties. To eliminate variations in steel rebar properties, the steel material properties were assumed to be constant, with a yield stress (σ_y) of 400 MPa and a modulus of elasticity (E_S) of 200 GPa. Furthermore, E_w was set to 13,100 MPa for all reinforced beams. The effect of grooves (wood removed for reinforcement placement) was also considered when determining the reinforcement ratio (ρ), assuming an approximate 1–3 mm spacing between the rebar edge and the surrounding wood, along with a 5 mm epoxy cover above the top surface of the rebar. The force-displacement curve for different ρ values is presented in Figure D.2.

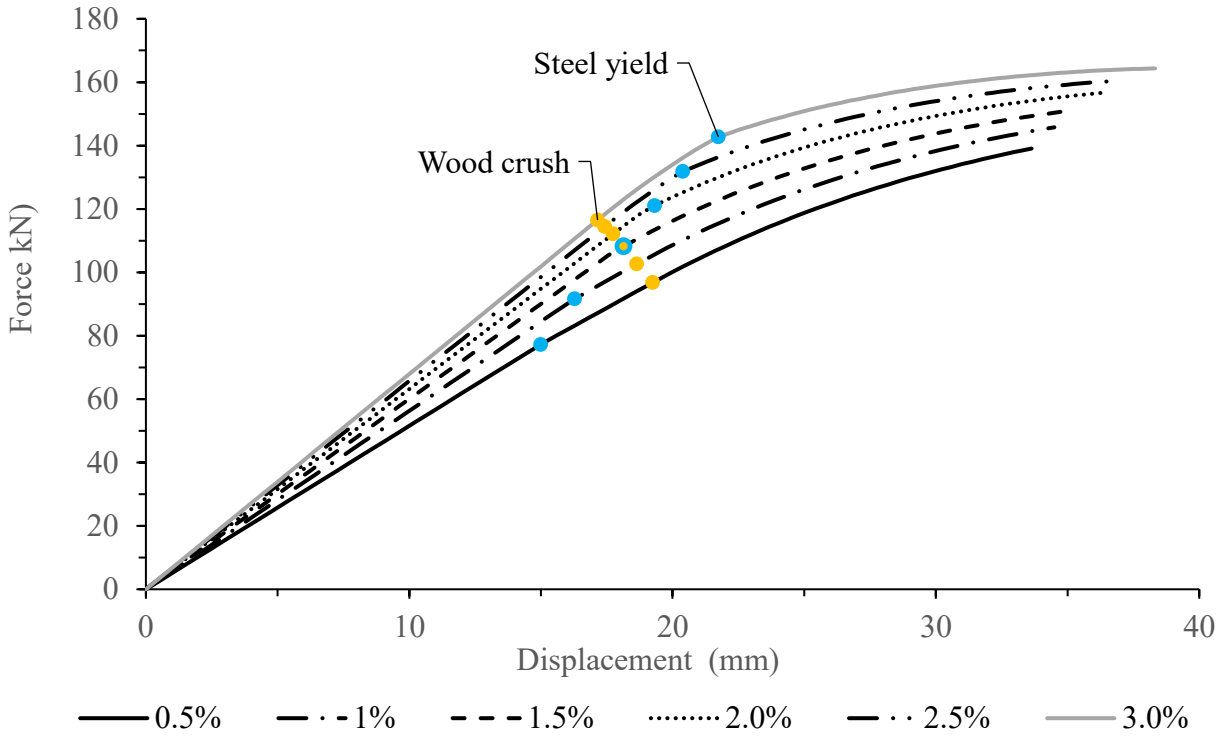

Figure D.2: Effect of ρ values on force-displacement curve.

As shown in Figure D.2, both displacement and force increase with a higher reinforcement ratio. Conversely, as the reinforcement ratio decreases, the steel yields earlier at lower load levels. Using a reinforcement ratio of 2% and the same material properties as previously described, the force-displacement curve for varying DIF is presented in Figure D.3.

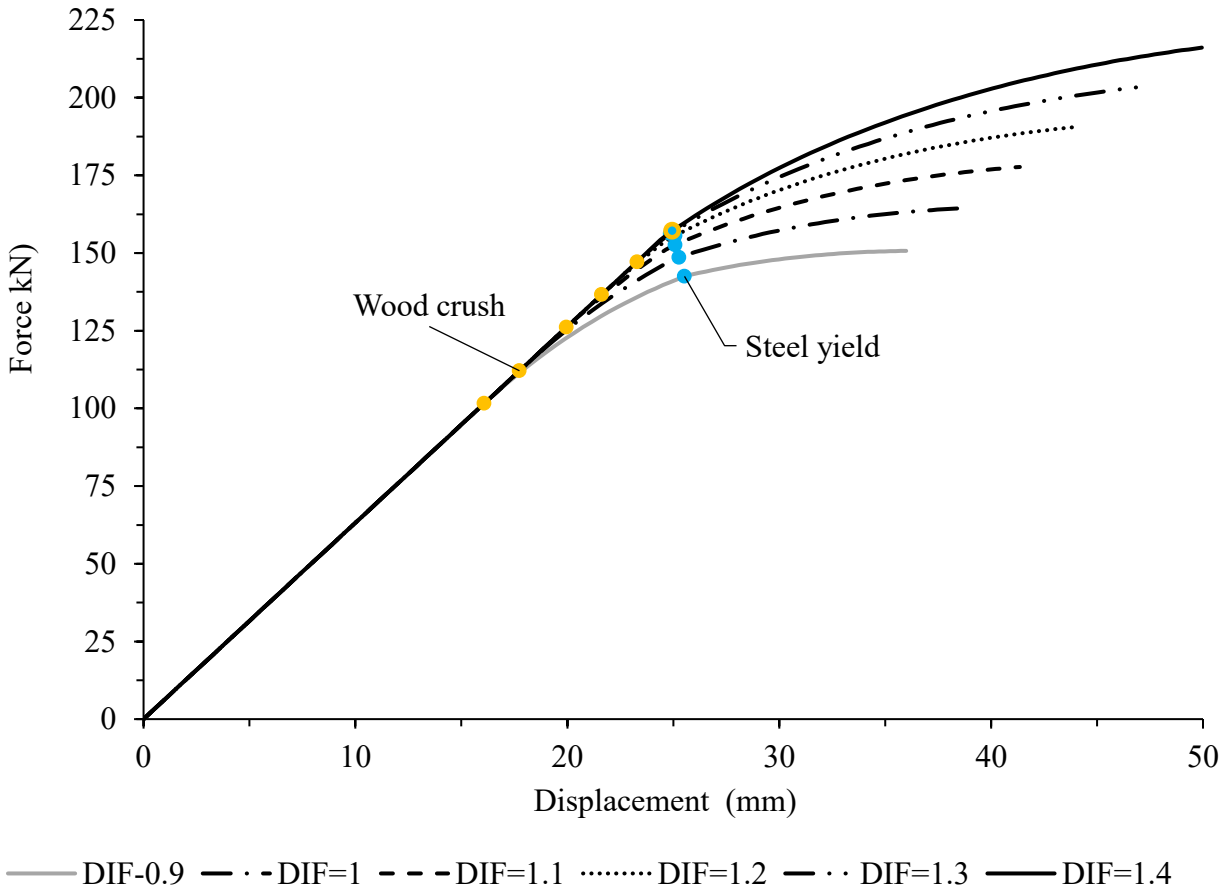

Figure D.3: Effect of DIF values on force-displacement curve.

As shown in Figure D.3, both displacement and force increase with a higher DIF. Additionally, as the DIF increases, wood experiences crushing at higher load levels.

Appendix E: Layered-section Analysis

Kinematics (plane sections)

Neutral axis depth c is measured from the top fiber. With top strain (ε_{top}) at a trial step, the curvature (κ) can be calculated as

$$\kappa = \frac{\varepsilon_{top}}{c} \qquad \textit{Eq. E1}$$

$$\varepsilon(z) = \kappa\,(c - z) = \frac{(c - z)\,\varepsilon_{top}}{c} \qquad \textit{Eq. E2}$$

where z is the layer centroid measured from the top (compression $z < c$, tension $z > c$).

l

Constitutive laws

Wood (piecewise linear, per Fig. 5.1)

$$f_w(\varepsilon) = \begin{cases} E_w\,\varepsilon, & \varepsilon_{wt} \le \varepsilon \le \varepsilon_{wc} \\ f_{wc} + m\,(\varepsilon - \varepsilon_{wc}), & \varepsilon_{wc} < \varepsilon \le \varepsilon_{uc} \end{cases} \qquad \textit{Eq. E3}$$

Steel (elasto-plastic, per Fig. 5.2)

$$f_s(\varepsilon_s) = \begin{cases} E_{st}\,\varepsilon_s, & |\,\varepsilon_s\,| \le \varepsilon_y \\ f_y, & |\,\varepsilon_s\,| > \varepsilon_y \end{cases} \qquad \textit{Eq. E4}$$

Layer/resultant forces

Discretize the timber section into $i = 1..N$ strips with areas $A_i$and centroids z_i.

$$F_{w,i} = f_w\big(\varepsilon(z_i)\big)\,A_i \qquad \textit{Eq. E5}$$

For each steel bar/plate j at depth $z_{s,j}$with area $A_{s,j}$,

$$\varepsilon_{s,j} = \varepsilon\big(z_{s,j}\big), \qquad F_{s,j} = f_s(\varepsilon_{s,j})\,A_{s,j} \qquad \textit{Eq. E6}$$

Section equilibrium (solve for c)

Force equilibrium:

$$\sum_{i=1}^{N} F_{w,i} \; + \; \sum_{j=1}^{n_s} F_{s,j} \; = \; 0 \qquad \textit{Eq. E7}$$

If (6) is not satisfied, update c(e.g., Excel Solver) and repeat (1) to (6) at the current ε_{top}.

Moment and curvature pair

Lever arms to the neutral axis: $y_i = z_i - c, \quad y_{s,j} = z_{s,j} - c.$

$$M \; = \; \sum_{i=1}^{N} F_{w,i}\, y_i \; + \; \sum_{j=1}^{n_s} F_{s,j}\, y_{s,j} \qquad \textit{Eq. E8}$$

Increment ε_{top} (e.g., $\Delta\varepsilon_{\text{top}} = 10^{-4}$), repeat to trace the M–κ curve.

Displacement from curvature

Distribute κ along the span under the applied bending moment diagram $M(x)$. For a symmetric four-point-bend test, the mid-span flexural deflection (Δ_b) via the moment-area/conjugate-beam method can be written as

$$\Delta_b \; = \; \int_0^{L/2} x\, \kappa(x)\; dx \qquad \textit{Eq. E9}$$

Include shear deformation (Δ_s) (Timoshenko):

$$\Delta_s \; = \; \int_0^{L} \frac{V(x)}{k\, G\, A_v}\; dx \qquad \textit{Eq. E10}$$

with $V(x)$ as shear force, shear-correction factor k(≈ 5/6 for rectangles), shear area A_v, and wood shear modulus G.

Total mid-span deflection

$$\Delta \; = \; \Delta_b + \Delta_s \qquad \textit{Eq. E11}$$

Notes for implementation

- Smaller $\Delta\varepsilon_{top}$ gives a denser M–κ curve but increases runtime.
- Treat NSM steel as concentrated elements at their centroids (Eq. E.6)